Investigation of the mechanisms of regulations, activation, and deactivation of Guanylate Cyclase, the endogenous NO-receptor, and NO-sensors

Byung-Kuk Yoo

PhD THESIS

presented by

Byung-Kuk YOO

On the subject of :

Investigation of the mechanisms of regulations, activation, and deactivation of Guanylate Cyclase, the endogenous NO-receptor, and NO-sensors

Defended on December 14, 2010

Michael Marden	Reviewer
Fabrice Rappaport	Reviewer
Pierre Nioche	
Jean-Louis Martin	
Michel Negrerie	Advisor

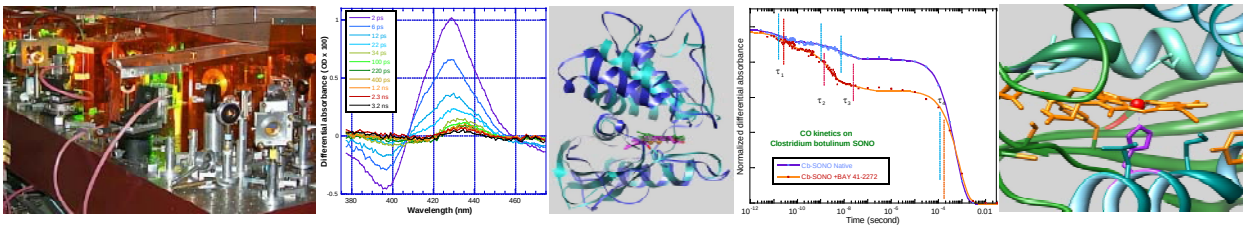

Acknowledgements

I was extremely lucky with **Michel** for four years in LOB because he was my lifesaver in France. He was an answering machine for all kinds of basic (mainly) and profound (sometimes) scientific questions on every single details during my PhD studies since 2007. He always gave me the answer affirmatively and deliberately, encouraging me to finish my PhD work without any problem and stress. Many thanks Michel !

Jean-Louis was the first person I met at the very first day in LOB and he welcomed me and introduced his state-of-art laboratory when I start 4 months internship in 2006. If he refused me permission at the beginning, this PhD work would not exist.

I could have not been able to purify my protein without the great help from **Isabelle**. We broke some rules by working on Saturday and even Sunday to accomplish our purification duties.

Our all measurements at longer time scales were done with the generous help of **Fabrice** in IBPC Paris. He also reviewed this thesis as a jury member with his sharp eyes.

SONO proteins that were investigated through my study were a gift from **Pierre** (Univ. Paris 5). He was one of my jury and I cannot publish this thesis without his help. Thanks for your generosity.

I was a lucky student because **Michael** (Univ. Paris 11) was a reviewer for my thesis. He gave me useful advices and encouragements for this thesis.

Marten and I sometimes met unexpectedly in the 30 Hz room and he always gave me some sharp comments on my subject. Most importantly, I feel sorry for him because I occupied TA laser too often to keep his research.

I very often attacked the office of **Jean-Christophe** who is armed with gigantic super computers. His magic hands enabled me to capture certain ideas from 3D structure revealed by his toys. I asked you so many times but you always said YES and this encouraged me to put a little step on molecular dynamics simulation stuffs and reduce the worries from complex mathematics and calculations.

I was supposed to be homeless without the unconditioned help of **Antigoni** in December 2010. I finally became a Parisian in 2010 after 4 years life of the minimum standard of living in 91 area with your magical help.

We published a beautiful paper in PNAS with the great idea with **Sergei** and he gave us the basic starting point for the band III measurements. I want to be trained by you for the time-resolved Raman techniques.

We had a great opportunity to work with **Sophie Bellon** at Genoptics using the SPR apparatus and I would like to thank for her help in experiments.

Latifa is another contributor for my homeless problem. I very often occupied the Shimadzu spectrometer, which bothered you sometimes. Sorry Latifa and many thanks for your consideration.

Jean-Marc and **Xavier** always stayed in the metal-smell area and gave us very useful tips and solutions. Mechanical and electronic problems could not hinder my research at all due to your strong and rigid supports.

Titre de sejour, Badge, conference money...etc..so many stuffs could not be a big obstacle for me since **Laure** and **Christelle** were always ready to help me with smile.

Mike, **Stefan**, and **Colin** gave us high quality proteins generously.

Doctor **Silvan** was my sports partner and latex advisor for my thesis.

Not in details but thanks for Liem, Alexander, Markus, Andras, Taku, Ursula, Mai-Thu, Sergei, Rivo, Mathias, Kevin, Patrick, Paul, Nicolas, Jongwoo, Junho, Younho, Jinyoun, Yiyin, Jean-Baptiste !

The generous French government allowed me to stay in France and do my scientific research and I would like to thank the people [Audrey Lemarechal, Michel Rosso, Claudette Dessertaine, Fabrice Baronnet] in EDX. Fondation pour la Recherche Médicale also supported me for extending my PhD fellowship.

I would like to thank for the people from the Sonann church in Paris.

Great thanks for my mothers, fathers, brother, and sisters (in law) and my eternal lifetime companion Hye Won.

Contents

Abbreviations

ATP	Adenosin triphosphate
AXCP	Cytochrome c' from *Alcaligenes xylosoxidans*
BAY	Bayer AG Pharma research
BAY 41-2272	[3-(4-Amino-5-cyclopropylpyrimidine-2-yl)-1-(2-fluorobenzyl)-1H -pyrazolo[3,4-b]pyridine]
BH_4	Tetra-hydrobiopterin
cGMP	Cyclic guanosin monophosphate
Cyt c	Mitochondrial cytochrome c
CCD	Charge-coupled device
DAS	Decay associated spectrum
DOS	Direct oxygen sensor
DHP	Dehaloperoxydase
DMSO	Dimethyl-sulfoxide
DTT	Dithiotreitol
eNOS	Endothelial nitric oxide synthase
Fe-PP IX	Iron proto-porphyrin IX
FAD	Flavin Adenine Dinucleotide
FMN	Flavin Mononucleotide
GTP	Guanosin triphosphate
GTP-γ-S	Thio(γ)-guanosin triphosphate
Hb	Hemoglobin
HD-β(190)	Heme domain of sGC β-subunit, comprising the first 190 amino-acids
HK	Histidine kinase
HPLC	High pressure liquid chromatography
IBMX	Isobutylmethyl xanthine
Mb	Myoglobin
Mb-(H93C)	His93Cys myoglobin mutant
Mb-(H64V)	His64Val myoglobin mutant

NADP	Nicotinamide Adenine Dinucleotide Phosphate
NADPH	Reduced NADP
NHA	N-hydroxy-arginine
NMA	N-methyl-arginine
NPS	Nitroprusside
PAS	Period circadian, Aryl hydrocarbon receptor nuclear translocator, Single minded proteins
PDB	Protein Data Bank
PMSF	Phenylmethylsulfoxide fluoride
PPi or Pi	Inorganic diphosphate or monophosphate
SEITU	S-ethyl-isothiourea
sGC	Soluble guanylate cyclase
SONO	Sensor of nitric oxide
SVD	Singular value decomposition
TA	Transient absorption spectroscopy
TEA	Triethanolamine
TR^3	Time resolved resonance Raman spectroscopy
Tris	Tris(hydroxymethyl) aminomethane hydrochloride
YC-1	5-[1-(phenylmethyl)-1H-indazol-3-yl]-2-furanmethanol

Chapter 1

Introduction

1.1 Signal transduction

The power of cells to receive and act on signals across the cell membrane is essential to life. Signal transduction is a conversion of electro-chemical information into a chemical change between cells and necessarily involves specific receptors[1]. The signal transduction from the extracellular area across the plasma membrane into the interior of cells is one of the most important events in the regulation of the life cycle of cell. Signals can be transmitted with the help of low molecular weight messenger substances that can transiently exist and involve the synthesis of second messengers. Intracellular signal transduction is mainly carried out by second messengers synthesized and and released by specific enzymes. One example of receptor enzyme is guanylate cyclase which catalyzes the intracellular second messenger guanosine $3'$, $5'$ - cyclic monophosphate (cyclic GMP, cGMP) from GTP in response to NO binding generated by extracellular signals. The discovery of the famous second messenger cGMP in 1961[2] provoked vigorous studies of numerous protein kinases and related substrates. Guanylate cyclase is the main protein in the center of our study and its regulation by NO and CO in terms of affinity, activity and coordination states shows an increasing complexity.

There are two types of guanylate cyclase that participate in signal transduction. One exists in two membrane-spanning forms that are activated by extracellular ligands but not nitric oxide. The other is a soluble enzyme that is activated by intracellular nitric oxide (NO) and this form is found in many tissues including smooth muscle of heart and blood vessels, regulating relaxation of blood vessels and thus blood pressure. A scheme of this process is displayed in Figure 1.1. The soluble guanylate cyclase (sGC), the focus of our research, binds the messenger NO with its heme whose properties were studied all along our work. Particular properties of the heme concerning NO binding will be investigated in NO-sensors and related

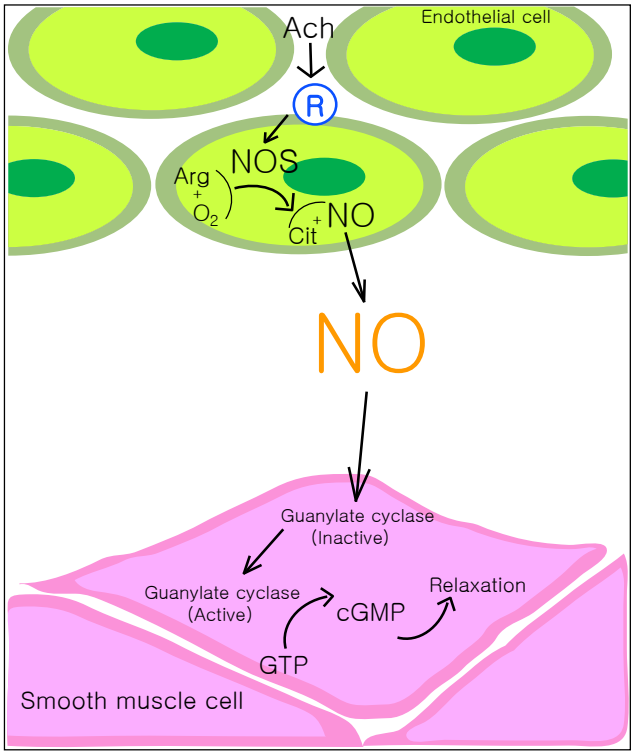

Figure 1.1: The relaxation of the smooth muscle cell and subsequent vasodilation. Agents such as acetylcholine (ACh) bind to their receptor (R) and stimulate the calcium-dependent activation of nitric oxide synthase (NOS). The subsequent production of NO diffuses to the underlying smooth muscle cells, activating guanylate cyclase and resulting in vessel relaxation.

proteins. sGC will be fully described in Chapter 2 and main properties of the heme and NO in the next sections of present chapter.

1.2 Metalloproteins and ligand binding

One-thirds of all proteins contain a metal in a specific position. In these metalloproteins, metal ions serve various functions in cells including transport, storage, and signal transduction. The most imperative function is to maintain the structural stability of the protein in the conformation required for biological activity and to participate in the catalytic processes of enzymes. Metal ions can take part in triggering and controlling the mechanisms by specifically altering the protein conformation upon binding various ligands. Ligands of metal ion (atoms or groups of atoms) chemically bound to the metal ion[3], generally donate an electron pair to the bond and becomes negatively charged or neutral. The number of such ligating atoms surrounding a central metal ion is designated as the coordination number of the metal ion.

The metal ion is coordinated by nitrogen, oxygen, and sulfur atoms of amino acids residues, which are constituents of the proteins. Thus, metals in biological systems such as

proteins function in a numerous ways. Sodium and potassium serve as charge carriers, for osmotic balance, and nerve impulses. Magnesium, calcium, zinc, and manganese function as structural elements in many enzymes. Copper is involved in electron transfer and dioxygen transport, although it is little in human body[1].

1.3 Heme proteins regulate their function by conformational change

Among these metals, Iron is the most abundant metal found in proteins and biological systems and iron-containing proteins can be categorized into two types depending upon the presence of porphyrin ligand systems. Porphyrin is a large heterocyclic organic ring harbouring a single metal ion in its central hole by four N-Fe bonds. The prosthetic group heme refers to an iron-porphyrin. Hemes are ubiquitous protein cofactors and quintessential components required for numerous biological functions of enzymes. Considerable fraction of porphyrin-containing metalloproteins have heme as their prosthetic group[4] and myoglobin and hemoglobin are the most known iron-containing heme proteins.

Iron alone in its ferrous state is extremely unstable because it is very reactive and provokes the generation of free radicals. Ferrous iron very easily oxidizes to ferric form (Fe^{3+}). Nature utilizes its ability to lower this reactivity by sequestering the iron between four nitrogens in pyrrole rings of the heme coordinated to the iron and become a coordination complex by giving electrons. The overall number of bonds is called the coordination number of the iron and there are still two possible coordination sites perpendicular to the free heme plane. Since two sides are exposed to other environment, variety of ligands can participate in making a bond to the heme iron. A chemical structure of protoporphyrin IX found in these globin-like proteins are displayed in Figure 1.2.

Essential to the function of the proteins, ligands make bond to particular amino acid residues or to prosthetic group forming the binding site. This binding of ligand induces a slight conformational change of the protein, which affects its function. For example, dioxygen (O_2) as the physiological ligand of hemoglobin (Hb composed of two pairs of $\alpha\beta$ dimers) binds to the heme iron at a free coordination sites. The function of Hb is based on the interactions between four subunits, which regulate the oxygen binding affinity of four hemes[5]. This allosteric process correlates with a conformational transition between a relaxed state (R state, low oxygen affinity) and a tense state (T state, high oxygen affinity). Thus Hb can efficiently bind oxygen at high partial pressure in lung tissue and release oxygen at low partial pressure in the cells, linked with the CO_2 concentration through the Bohr effect.

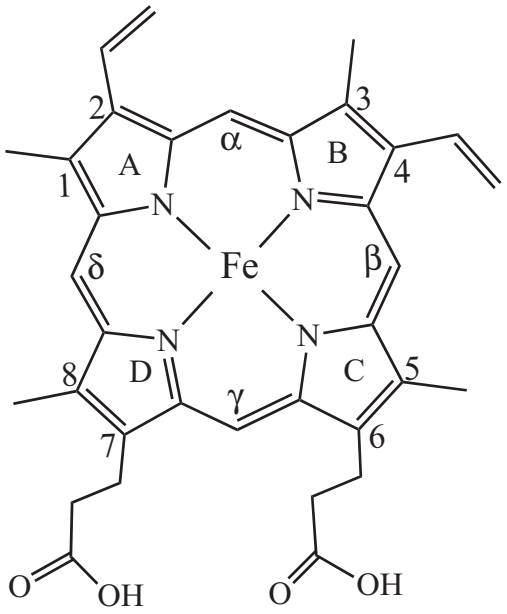

Figure 1.2: Iron-protoporphyrin IX, heme b found in hemoglobin, myoglobin, and most heme proteins

1.3.1 Heme protein and allosteric regulation

Heme-mediated allostery in hemoglobin was established in the early 1960s[6]. Hb has four subunits and exhibits combined effects upon binding a ligand caused by subtle changes in quaternary structure[7]. In 1965, J. Monod, J. Wyman, and J.-P. Changeux proposed a theoretical model of the concerted allosteric transitions (MWC model)[6]. In this model, a multimeric protein (not necessarily Hb) can exist in one of two different conformational states (two states model) and each subunit has both a binding site for an allosteric effector and an active site. However, various biochemical and biophysical studies are revealing new mechanisms for heme-driven conformational changes different from Hb mechanism, but which are still explained by the classical Hb model. Although protein allostery mediated by ligand binding looks straightforward, some sensor proteins have an extra complexity and require extension of MWC model.

1.3.2 Diatomics binding and the structural change of heme proteins

Heme proteins are specifically adapted to bind the biologically important diatomic molecules such as NO, CO, and O_2. Immense numbers of studies about heme proteins that sense these small gaseous diatomic molecules are reported. Their interactions with heme proteins cover a wide variety of physiological functions such as O_2 storage and transport, neurotransmission,

the immune response, the control of respiration, and vasoregulation. NO, CO, and O_2 binding to a heme protein may include four steps:[8]

- Displacement of endogenously bound side-chain to create an open distal pocket if the heme is 6-coordinate in resting state
- Ligand movement into the heme protein to form an intermediate in which the gas is trapped in the active site near the heme group
- Bond formation between heme iron and gaseous ligand
- Stabilization of the bound ligand by electrostatic interactions by distal side-chain(s)

The binding of NO may induce a fifth step: breaking of the bond between Fe^{2+} and the side-chain trans to NO. We will describe further this effect. The function of heme-based sensors is to react to the presence of NO, CO, and O_2 following their coordination to the heme. Numerous studies about sensor proteins have been performed[9, 10]. To date, three categories of sensors are characterized, as summarized in Table 1.1.

Effector	**Protein**	**Function**	**Source**
NO	**sGC**	**Conversion of GTP to cGMP**	**Mammalian brain, lung, aorta, etc.**
O_2	FixL	Kinase	Rhizobium meliloti Bradyrhizobium japonicum
O_2	DOS	Phosphodiesterase	Escherichia coli
O_2	PDEA1	Phosphodiesterase	Acetobacter xylinum
O_2	HemAT	Signal transducer for aerotaxis	Bacillus subtilis Halobacterium salinarum
CO	CooA	Transcriptional activator	Rhodospirillum rubrum
CO	NPAS2	Transcriptional factor	mammalian brain

Table 1.1: Heme-based gas sensor proteins (from the reference[11]). Abbreviations: sGC, soluble guanylate cyclase; DOS, direct oxygen sensor; PDEA1, phosphodiesterase protein A1; HemAT, heme-based aerotaxis transducer; NPAS2, neuronal PAS domain protein 2.

1.4 Nitric oxide and soluble guanylate cyclase

Nitric oxide will be discussed more deeply among these smallest biomolecules since our main target is the NO-receptor sGC. This molecule was chosen as the molecule of the year in 1992 since it is a fundamental biomolecule in the fields of neuroscience, physiology, and immunology. NO is a free radical and its molecular orbital diagram is depicted in Figure 1.3. There are three electrons in antibonding orbitals and eight electrons in bonding orbitals. The

electron occupying the highest energy level is in antibonding π^* orbital. It is an unpaired electron and this electronic configuration explains the high reactivity of NO molecule.

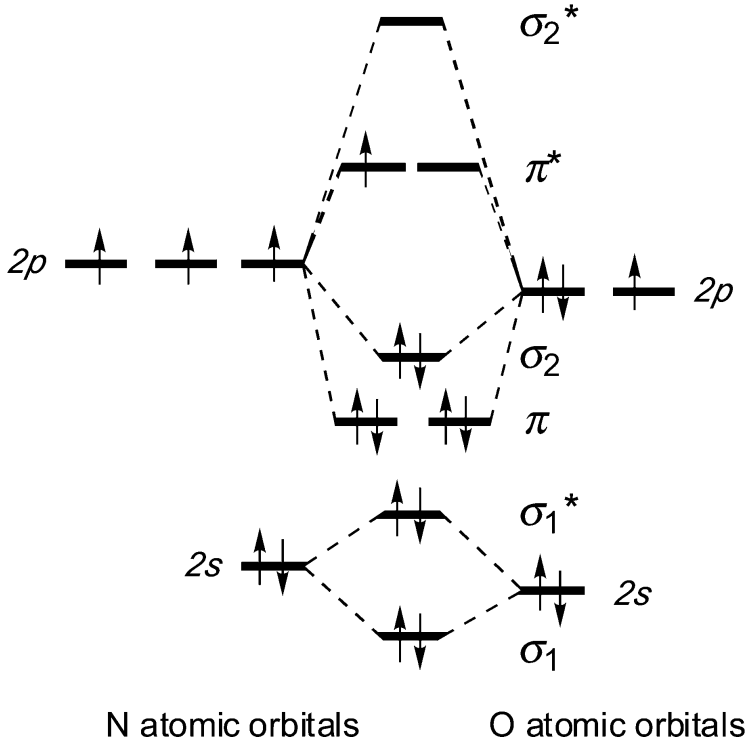

Figure 1.3: Molecular orbital diagram of NO.

Although NO is known as a toxic gas at high concentrations, its biological role as a messenger comes from its chemical properties. This diatomic gas molecule goes through the cell membranes just like oxygen or carbon dioxide without any support of carriers. NO can easily be oxidized to become nitrosonium ion (NO^+) and be reduced to be nitroxide (NO^-). Chemical and physical properties of NO and CO are displayed in Table 1.2. NO is unique among the diatomic biomolecules because it can bind to both ferric and ferrous heme iron due to its eletronic configuration. The affinity of NO for ferrous heme proteins is high due to the unpaired electron and on the order of 10^{11}–10^{12} M^{-1} for deoxyhemoglobin[12].

The endogenous NO receptor in cells is sGC which is activated by NO, triggering the elevation of cGMP concentration. sGC enzyme contains the same heme (protoporphyrin IX) as hemoglobin and myoglobin with iron in the ferrous state. Binding of NO with ferrous iron is reversible and this allows the sGC to switch off immediately after NO is removed. The partial rise in NO concentration can be readily translated into a cellular signal thanks to high affinity and fast diffusion. This signal is short-lived and localized because NO synthetized in endothelial cells can be decomposed by oxygen and heme proteins[13].

Property	Nitric Oxide	Carbon Monoxide	Reference(s)
Molecular weight	30.01	28.01	[14]
Solubility in water at 20 °C (mL/100mL)	4.6	2.3	[14, 15]
Binding affinity with iron	Fe^{2+}, Fe^{3+}	Fe^{2+}	[16]
Activation of sGC (cGMP production rate, fold)	400	4	[16]
Source	NO Synthase	Heme Oxygenase	[17]
Radical species	$NO^{\cdot}$, NO^{+}, NO^{-}	None	[15]

Table 1.2: Chemical and biological properties of NO and CO

Generally, NO-bound heme proteins such as Mb and Hb form 6-coordinate complexes with His and NO as axial ligands. However, sGC becomes 5c-NO at the last step as shown in Figure 1.4. When NO binds to the distal side of sGC, it exerts a strong repulsive trans effect on the proximal His-iron bond. This trans effect induces the less tightly bound histidine to be dissociated. This event is essential for the function of sGC. An intermediate of 6c-NO-His sGC forms transiently and right after the bond between iron and His breaks producing 5c-NO species[18, 19]. This rupture of the proximal Fe-His bond triggers the conformational change and it propagates along the whole protein structure. This is the very first and most important event for the explanation of the activation of sGC. Further other steps must be elucidated in order to put a bridge between the bond breaking/forming and increased catalytic activity. Our experiments interest about sGC focuses on the heme since it constitutes the triggering starting point. The coordination chemistry of heme linked to protein allostery is the main point of our study.

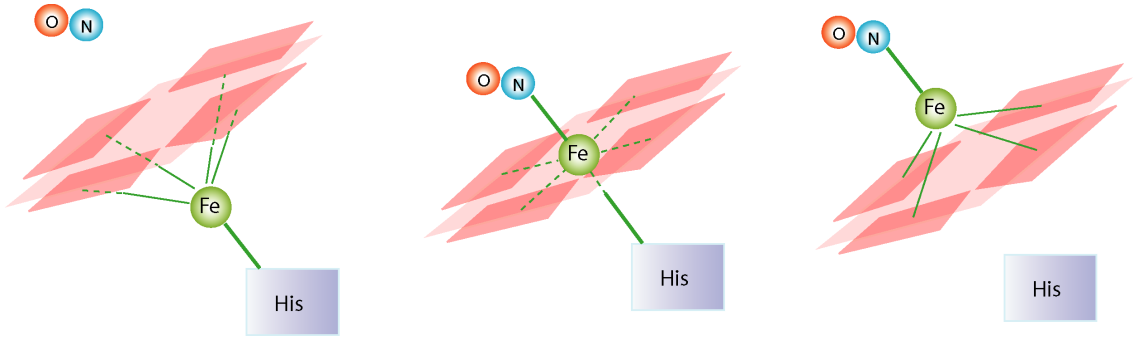

Figure 1.4: The activation of sGC with NO.

Conformational changes in a protein may be altered as a result of an allosteric event and changes between equilibrium states are usually investigated by X-ray crystal structural studies. But very often this critical information is not available due to difficulty of crystallizing the protein. For example, the crystal structure of our target protein sGC is missing. Furthermore, a complete understanding of protein functioning requires a dynamic view of

the transition between equilibrium states. When we consider the allostery in sGC, three important questions need to be answered.

1. How the dynamics and transitions are controlled by allosteric effectors?
2. How many transition of the protein conformational states?
3. Where sGC activators bind?

For the first, we investigated the dynamics of diatomics (NO and CO) in the absence and presence of various allosteric effectors in Chapter 2. Moreover, we extend the measurable timescales from second to femtosecond in order to answer the second question because the binding of NO to sGC can have more than two different allosteric transitions. To answer the third question, we compared entire sGC with NO-sensors and the isolated heme domain in Chapter 3.

1.5 Probing heme protein-ligand interactions by transient absorption spectroscopy

Our target belongs to heme proteins that have been largely studied by various kinds of optical methods. Since heme proteins structural properties are readily translated in their characteristic UV/Vis spectra, we will use transient absorption spectroscopy for investigating the transitions induced by diatomic interaction with sGC and related proteins.

1.5.1 Probing heme proteins by absorption

The spectral fingerprints of UV/visible absorption of the heme depend on many physical properties such as iron oxidation state (ferric or ferrous), peripheral substituents, nature of external ligands, coordination state, spin state, strain exerted on the heme, and amino acid residues at the vicinity of heme. Thus absorption spectroscopy is an excellent tool for physical studies of heme protein function. Metalloporphyrins would be of D_{4h} symmetry if they exhibited planar structures and the electronic transitions of metalloporphyrins are derived from the π-molecular orbitals (MOs). The highest occupied MOs (HOMOs) have a_{1u} and a_{2u} symmetry and are similar in energy, whereas the LOMO is doubly degenerate (e_g). Hence, we can consider two states with same symmetry and close energy, which are due to strong configuration interactions. Consequently, the transition dipoles combine in two ways and resultant transitions can be additive or subtractive[20]. This represents a strong electronic transition at near 400-435 nm (Soret) and a substantially weaker one at near 550

nm (Q band), respectively as exemplified in Figure 1.5 for Mb. Mb is one of *b*-type hemes in which only one axial coordination site is occupied by a unique histidine residue (proximal site). The ratio between the oscillator strengths of the Soret- and Q-bands is about 10.

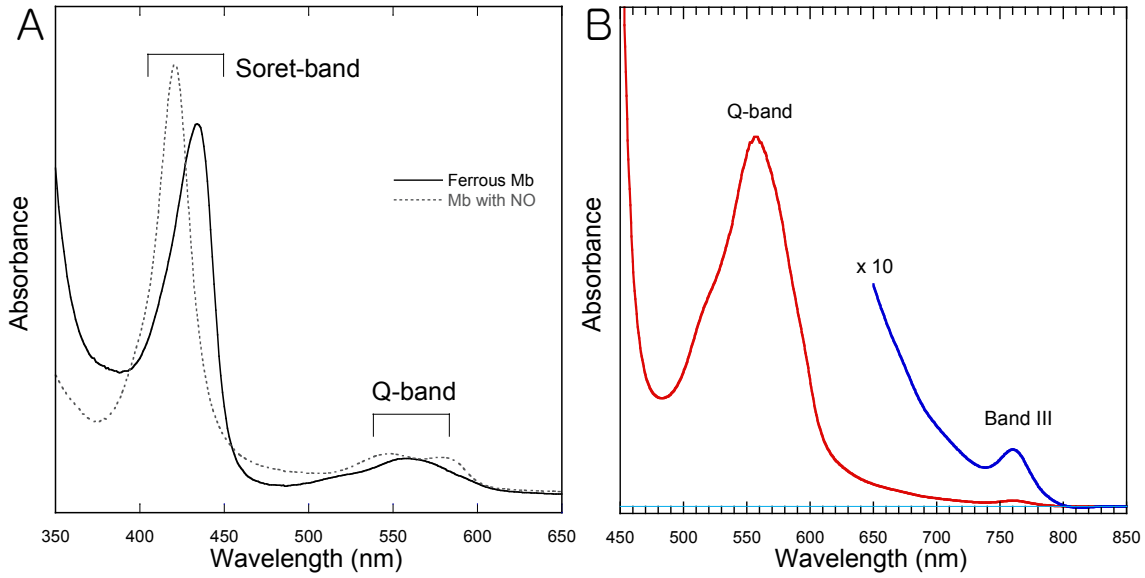

Figure 1.5: A) Absorption spectra of the Mb in the reduced (solid line) and NO-bound form (dotted line), B) Absorption spectra of the reduced Mb in near-IR region.

The absorbance spectrum of Mb (Figure 1.5) is dominated by two porphyrin π-π^* transitions and one very weak charge-transfer transition. Far beyond the Q-band in the near IR region at 760 nm, there is a extremely small peak which is only seen for the reduced form of Mb or Hb. As a marker band of protein conformation relaxation after photodissociation of the heme-ligand complex, band III can also be used as a marker of iron position. This band III of Mb and Hb will be discussed more deeply in Chapter 7.

1.5.2 The power of Transient Absorption (TA) spectroscopy

Time-resolved spectroscopies allow us to detect transient steps from the release of NO from heme to the unliganded relaxed protein. This is not only a problem of measuring kinetic traces, but of identifying all the transient species involved during the process. This is not trivial if we consider that for example 97 % of photodissociated NO geminately rebind to the heme of sGC in 7.5 ps[21] and that the 3 % remaining population are involved in the deactivation of sGC and must be identified. Thus, it is crucial to determine the structural events and the associated energy barriers following ligand release and preceding ligand binding. The time scale of the diatomic ligand motion within the protein core is in the picosecond to microsecond range. However, if the starting system is an aqueous solution with a non-ligated

heme-protein and an unbound diatomic (O_2, CO or NO), it is impossible to record a binding step faster than ~ 0.1 ms because the diffusion of interacting molecules in solution occurs much slower than the intramolecular structural events to be probed. To overcome this limitation, one must start from the well-defined system consisting of a heme protein liganded with a diatomic to its heme.

The photodissociation of a diatomic ligand from the heme with a fast laser pulse allows to displace the equilibrium and to simulate the thermal release of NO; in other words, we set the probability of ligand detachment to 1. Then, because NO can either rebind geminately (from the heme pocket or from a docking site in the protein) or can migrate within the protein core and finally to solution from where it may rebind to sGC in longer time, one can monitor the entire dynamics of NO from the solution to the heme and the subsequent heme coordination changes. This technique gives access to all steps, provided that we can measure the entire time range (1 ps to 1s) with enough sensitivity. Therefore, in some particular studies, we have completed the ps-ns measurements with ns-μs-ms measurements. TA technique is described in Chapter 9 (Materials and Methods). TA spectroscopy thus constitutes the main tool in our studies for the identification of molecular steps during the interaction between NO and sGC, probing the heme coordination and spin states, which relies on transient spectra and their evolution.

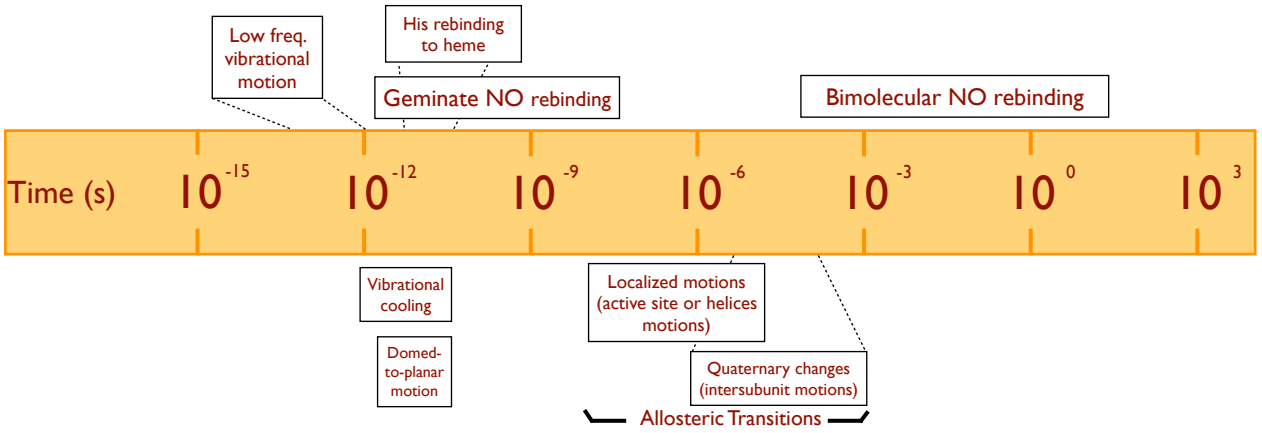

Figure 1.6: The timescales and their relevance to physical and biological changes.

Figure 1.6 briefly summarizes the timescales of the dynamic processes of our interest. Through this thesis, we explored the dynamic transitions of our target protein (sGC) in this time range using transient absorption spectroscopy. This valuable tool covers many biological processes, which span from femtosecond to nanosecond this time range is explored by means of optical delay between lasers. With the collaboration with another team at IBPC, we also explored other timescales from the microsecond to second time domain by means of electronic

delay between lasers. We thus investigated the dynamics of NO interacting with sGC in the broad time-range from 1 ps to 0.1 s, using two different transient absorption setups. This allowed us to monitor the entire NO dynamics and structural steps. The other processes that we detected are also indicated in Figure 1.6. Histidine rebinding to sGC and AXCP will be demonstrated in Chapter 2 and 4. Domed-to-planar motion together with band III measurements will be discussed in Chapter 7.

We extend our research to other relative heme proteins. Various studies of these proteins will be discussed after Chapter 2. The dynamics in the entire sGC will be compared to those of isolated beta-subunit of sGC and those of bacterial NO-sensors in Chapter 3. In Chapter 4, we chose a NO-binding protein whose structure is different from sGC. Cytochrome c' from *Alcaligenes xylosoxidans* (AXCP) will be a good model study for sGC because it has similar coordination properties with sGC. We will try to probe a fundamental transition for the deactivation mechanism of sGC using AXCP. Consequently, we will introduce a myoglobin mutant (H93C) which has similar trans effect found in sGC and it will be used as a model for 4-coordinated and 5-coordinated hemes due to the difference of coordination compared to wild type Mb. We will discuss NO geminate rebinding of the enzyme NO-synthase whose dynamics is different from sGC but which is the source of NO, so that its dynamics should be fundamentally different and which can be modulated by numerous effectors. Lastly, we have measured the absorption change of band III of myoglobin and hemoglobin, for measuring the time constant of heme-iron motion after NO binding. In each case, we place our results in the context of allostery.

Chapter 2

The endogenous receptor of nitric oxide: Soluble guanylate cyclase

2.1 Introduction

Soluble guanylate cyclase (sGC) is the endogenous nitric oxide receptor in mammals and is the main protein on which we focus our research. The rapidly diffusible messenger NO and the activation of sGC by NO are involved in several physiological processes, including vascular pressure regulation, lung airway relaxation, and neural communication[22]. The functioning of the endogenous NO-receptor sGC is crucial in several diseases, which comprises cardiovascular, pulmonary and renal pathologies. Thus sGC is a potential pharmacological target of great interest for various diseases. NO signaling pathway is also involved in apoptosis[23] and in tumor progression[24, 25], and sGC inhibition is of great interest for studying and fighting against tumor progression. Therefore, depending upon the pathology to be addressed, both cGMP production and inhibition are of therapeutic importance. A small number of stimulators of sGC except NO exist so far, including some artificial compounds and improving them or discovering new compounds requires the deep knowledge of their mode of action on sGC regulation at molecular level[26].

sGC as an enzyme catalyzes the formation of the second messenger cGMP from GTP upon NO binding. The heterodimeric protein possesses two subunits: the catalytic α-subunit harboring the GTP binding site and the regulatory β-subunit which contains the heme prosthetic group necessary for NO stimulation. When NO binds to sGC, the covalent bond between the heme iron and the proximal histidine is broken. This cleavage is the very first event of the molecular switch from NO binding to cGMP release. This internal molecular event is assumed to trigger a structural change within the protein, which induces the increase

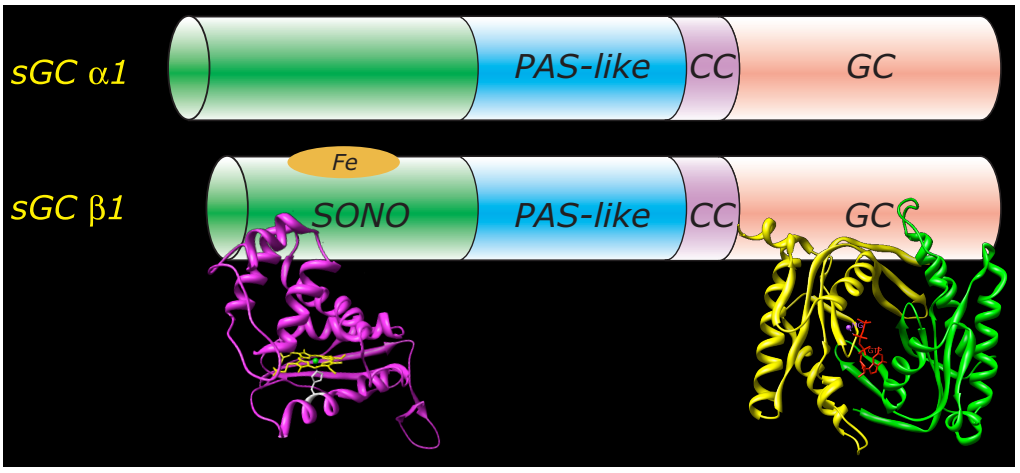

Figure 2.1: Guanylate cyclase architecture. Heme domain is designated as SONO and catalytic domain as GC, based on the two respective crystal structure determinations.

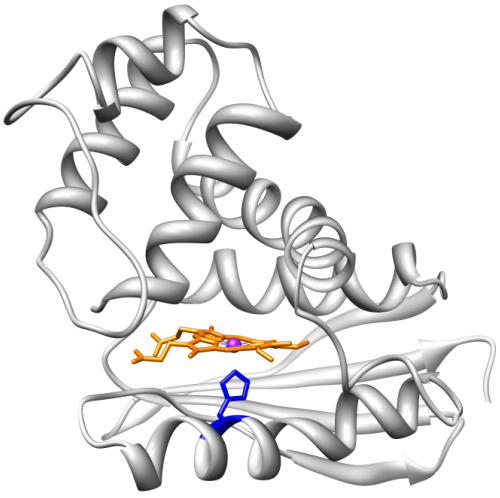

Figure 2.2: Homology model of the heme-binding domain (1-190) of the human sGC β-subunit obtained using MODELLER from the homologous bacterial *Tt*-SONO[27]. His105 residue is displayed in blue. Figure is generated using Chimera.

of catalytic activity. However, the entire mechanism of sGC functioning from the cleavage of His-Fe bond to the formation of cGMP is unknown.

sGC is a heterodimeric protein which contains one heme prosthetic group per heterodimer which is constituted by α (M_r = 74,000) and β (M_r = 69,000) subunits that are evolutionarily related homologues and have structural similarity and the most commonly studied isoform is the $\alpha1\beta1$ protein. The heme is located in the N-terminal part of $\beta1$ subunit designed as "Nitric Oxide Binding" domain. The ferrous heme iron is liganded with the histidine 105 residue (His105) of the $\beta1$ subunit. $\beta1$ subunit is composed of the NO/CO-binding heme domain, a PAS-like domain, a coiled-coil region[28], and a cyclase domain. When NO binds to the heme iron, the bond between iron and His105 is broken to induce catalytic activation. Proposed schematic description of sGC is displayed in Figure 2.1 with partial crystal structures of two domains, found separately[27, 29].

Although sGC is the endogenous NO receptorconstitutively expressed in the cytoplasm of many mammalian cells, the full three dimensional crystal structure has not been found yet although four decades has been passed since the discovery of sGC because of the difficulty of expressing quantities suitable for crystallization. Moreover, the role of NO signaling in bacteria is not well understood though the function of NO in humans is established. However, the discovery and crystal structure determination of prokaryotic homologues of sGC brought us a valuable insight for understanding sGC deeply. Nioche et al. succeeded in discovering the link between NO signaling in humans and bacterial NO sensing mechanisms[27]. They proved that some bacteria harbor a NO sensing protein (SONO, sensor of NO) with dramatic resemblance to the NO-binding heme domain of sGC. Figure 2.2 is based on the resolved crystal structure of a prokaryotic heme-binding protein of *Thermoanaerobacter tengcongensis* with sequence homology (19 %) to the sGC heme-binding domain using MODELLER[30]. The details of practical process for the homology modelling by MODELLER are described in Chapter 9.

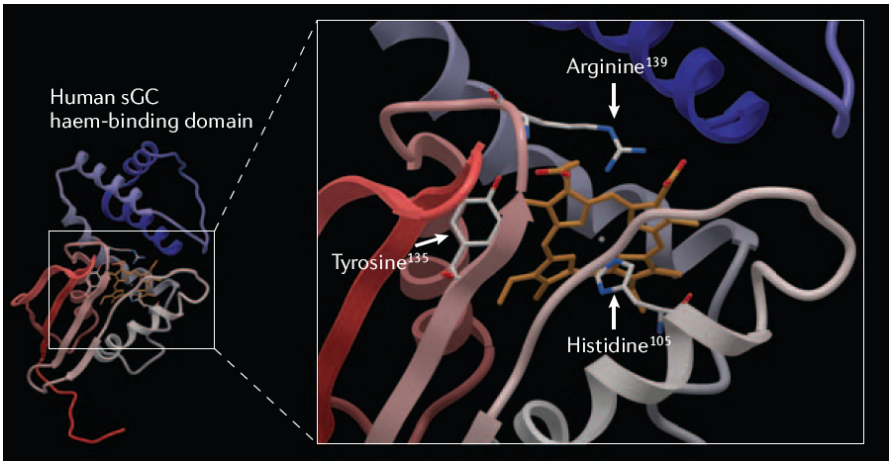

Figure 2.3: Detailed view of heme domain of the human sGC. Amino acid residues corresponding to the coordination of the heme are shown in the right with enlarged view. Image is taken from the reference[26].

From the vertical view, another detail near heme pocket is described in Figure 2.3. The important histidine (His105) as the axial ligand is located perpendicularly the heme and two other amino acid residues such as arginine (Arg139) and tyrosine (Tyr135) constitute the sGC heme binding motif[26]. Although recent progresses based on the structural analyses of homologous proteins allow us to compare heme domains, more fundamental and mechanistic studies need to be done on sGC itself thoroughly. This thesis mainly focuses on the sGC and major questions to be answered are detailed in the next section.

2.2 Questions to be addressed by our research

sGC is an allosteric protein, with the ability of influencing the properties of GTP binding site by ligating a diatomic to a remote site located in another subunit of the protein. A small number of sGC stimulators other than NO exist so far, including some artificial compounds[26] and improving them requires the deep knowledge of sGC regulation at molecular level. The binding of NO breaks the iron-histidine bond and, since the sensing heme part is harbored on a different subunit than the site of GTP conversion, we assume that there is a **cross-talk** between both subunits. This means that a structural change is necessary for allosteric regulation, and molecular steps must be identified to decipher the activation and deactivation mechanisms.

In the first section, we will investigate the NO-independent activation of sGC through the synergistic action of CO and effectors. The benzylindazole YC-1 is the first sGC stimulator which played a role as a lead structure to give birth to other improved sGC stimulators from diverse pharmaceutical companies. One optimized activator is BAY 41-2272 from Bayer AG and was chosen for our research on NO-independent sGC activation.

Secondly we have studied the deactivation process of sGC. The deactivation of sGC is one of the most important points in NO signal transduction. The rate for the dissociation of NO from the activated 5c-NO species ($k_{off} \approx 10^{-3} s^{-1}$) was determined by measuring the time for returning to the basal activity[31]. Another group reported a faster rate constant for the deactivation of sGC ($k_{off} \approx 3.7\ s^{-1}$) in cells[32]. However, we will show that histidine rebinding occurs on the picosecond time scale ($\sim$ 70 ps) both for a bacterial cytochrome c'[33] and sGC and this implies that other molecular processes take place in deactivation in different time scales. For these reasons, time-resolved spectroscopy is a tool of choice for studying such a NO-receptor coupled to an enzyme. The elucidation of activation of sGC by NO and its deactivation mechanisms requires to decipher the elementary molecular steps. This constitutes the subject of our work, which focuses on the heme domain rather than on the catalytic domain albeit we investigated the entire dimeric protein.

Thirdly, we have searched for a possible inhibitor of sGC by direct interaction with hypericin, which is very new in the field of sGC research and we preliminarily identified an unknown endogenous ligand of sGC in pulmonary cells by surface plasmon resonance method. We have studied elementary molecular mechanisms in heme proteins related (bacterial NO-sensors) or not (myoglobin mutant, cytochromes) to sGC. The heme reactivity and properties were thus compared with sGC with respect to different protein folds. Of particular interest is the analysis of substrate analogs and inhibitors to NO-synthase, the endogenous source of NO to target sGC. Finally, in Chapter 7, we have used transient absorption spectroscopy to

investigate a very fundamental process in heme-NO interaction: the motion of the iron atom upon NO binding.

2.3 Activation of soluble guanylate cyclase by artificial activators

Although YC-1 and BAY 41-2272 alone stimulate sGC in an NO-independent manner, they have an increased effect in synergy with CO. Therefore, we studied these effectors in the presence of CO to detect any effect on CO dynamics. YC-1 can participate in weakening the histidine-iron bond when NO or CO is bound[34]. An interaction of YC-1 with the catalytic domain of sGC was suggested by mutation studies[35]. Two cysteine residues in the α-subunit are hypothesized to be involved in the binding of BAY 41-2272[36]. On the other hand, it was reported that YC-1 can only interact with heme domain part of sGC by Denninger and coworkers[37]. Thus, the interaction of YC-1 (or BAY 41-2272) at the interface of both subunits and in catalytic domain of sGC has been reported but the precise binding site and mechanism are still in question.

Numerous efforts have been devoted to purify sGC from various native sources[38–42] as well as the expression and purification processes from recombinant sources[43–50]. Between two methods, we chose the first way to prepare sGC for our experiments. All the details for purification step are described in the materials and methods section (Chapter 9). The enzyme sGC was purified from fresh beef lung directly in the reduced form and reveals a characteristic Soret absorption maximum at 431 nm (Figure 2.6(a)).

After adding NO (1 % NO gas phase; 20 μM in aqueous phase) into the solution, the Soret band shifts to 399 nm on formation of the 5c-NO species. Originally, the ferrous sGC has a 5c-His heme and upon NO binding to its trans site, the iron-histidine bond is broken due to the strong trans effect induced by NO leading to the formation of a five-coordinate nitrosyl complex. However, binding of CO yields a 6-coordinate heme that only marginally increases the activity (5-fold). Thus, the bond between heme iron and His105 cannot be cleaved by CO alone, or in a so small proportion that cannot be detected (Figure 2.4).

In the cell, the event of breaking the bond between iron and histidine is crucial for the full activity; however, sGC can be partially activated in the presence of an allosteric activator YC-1 ([3-(5'-hydroxymethyl-2'-furyl)-1-benzylindazole], Figure 2.5) and fully activated in the presence of both YC-1 and CO. The first description of the synergistic activation of YC-1 in the presence of CO was reported in 1994[51]. Based on YC-1 structure, some pharmaceutical companies such as Bayer AG and Abbot Laboratories have synthesized a series of

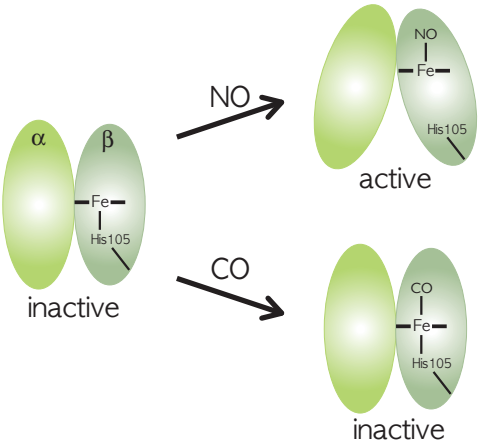

Figure 2.4: Model of NO-induced activation of sGC. Iron of the heme is coordinated to His105 of the β-subunit of sGC. CO alone cannot activate sGC.

NO independent activators of sGC as drug candidates (Figure 2.5). Setting YC-1 as a lead structure, scientists at Bayer AG (Wuppertal, Germany) reported the most promising new sGC activators pyrazolopyridine such as BAY 41-2272 [5-Cyclopropyl-2-[1-(2-fluoro-benzyl)-1H-pyrazolo[3,4-b]pyridine-3-yl]pyrimidine-4-ylamine][36] out of a series of thousands of synthesized derivatives[52]. Compared to YC-1, BAY compounds are more potent and do not inhibit the phosphodiesterase activity at therapeutic doses[53]. A-350619 from Abbot laboratories also activates sGC and has an effect on the penile erection in a rat model[54]. Among these non-NO sGC stimulators, we chose the compound from Bayer AG BAY 41-2272 and we will compare its effect on sGC with that of YC-1.

Organic nitrates and other NO releasing compounds that stimulate sGC have been found for the treatment of cardiovascular and related diseases but these molecules suffer from the nonspecific side reactions due to NO released in non-target cells and a tendency for tolerance to develop with prolonged usage. Thus YC-1 and BAY 41-2272 that activate sGC in a NO-independent manner may give favorable therapeutic improvements[26]. It is well demonstrated that YC-1 and BAY 41-2272 can increase the cGMP production rate together with CO, which is endogenously produced[55], but not necessary with NO.

In the presence of these allosteric effectors, CO can stimulate sGC to nearly the same extent as NO alone[56]. The interaction of these effectors (YC-1 or BAY 41-2272) with the CO-bound sGC can be investigated by time-resolved spectroscopic methods by measuring CO dynamics. Kitagawa *et al.* found that a weak population of 5c-CO-sGC could be present with 6c-CO-sGC, produced by the effectors, using resonance Raman approach[57]. However, the quantitative estimation of the amount of 5c-heme species is still missing but could be investigated by an absorption method. Therefore, with femtosecond transient absorption, we will attempt to obtain a quantitative estimate of species induced by these activators together with transitions between these species. Our aim is to understand how activators influence sGC substrate by probing the sGC-CO interaction and what is the basis for synergistic activation.

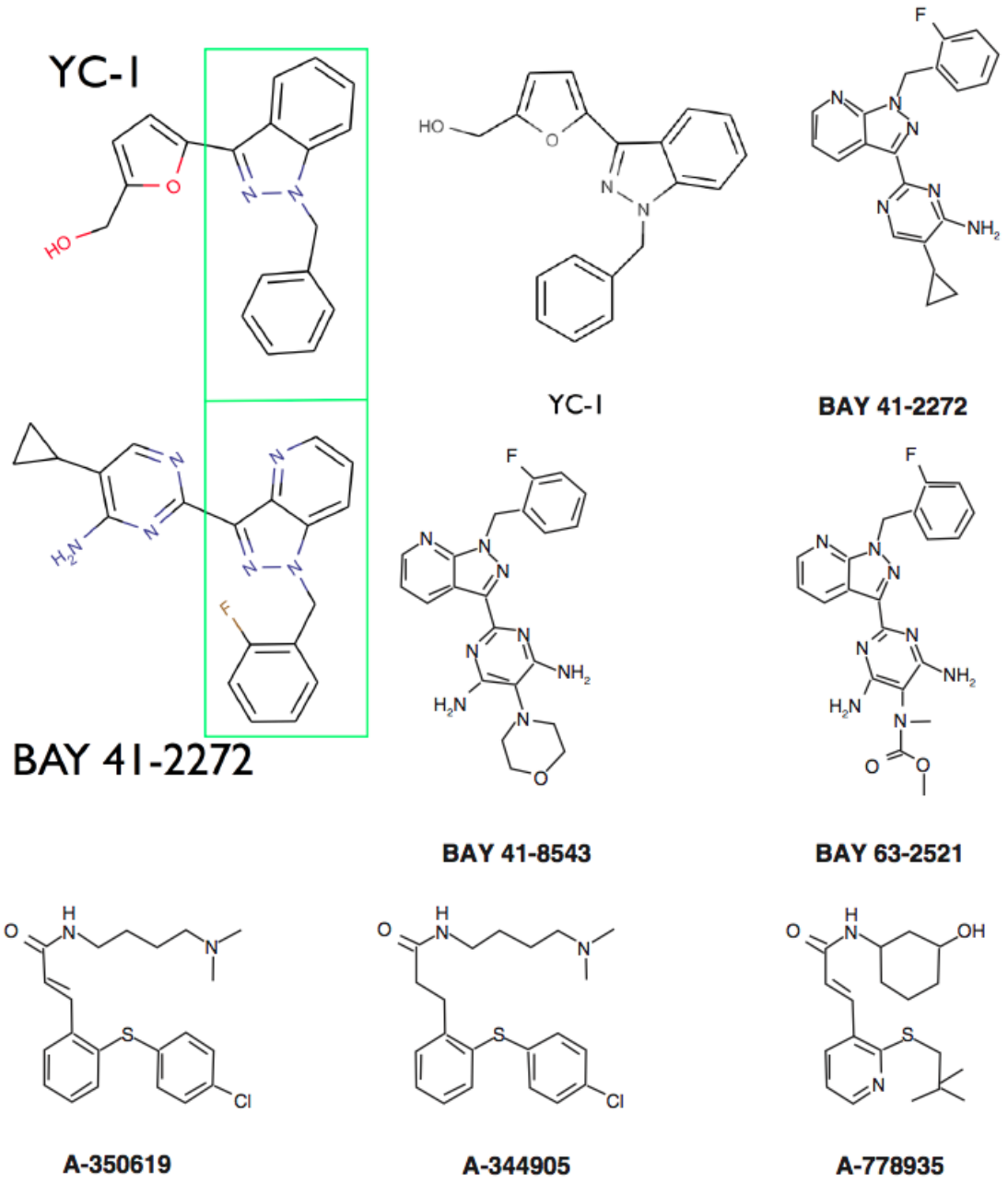

Figure 2.5: Nitric oxide independent stimulators of sGC. Two chemicals of our interest (BAY 41-2272 and YC-1) are enlarged and green square indicates the similar moiety of each compound. YC: Yung Shin Pharmaceutical, BAY: Bayer AG, A: Abbot Laboratory. Image is taken from reference[56].

The leading idea here is that if a heterogeneous population of sGC-CO exits, then the different species will behave differently upon CO photodissociation and could be identified by their respective photoproduct.

2.3.1 Synergistic activation of sGC with CO in the presence of effectors

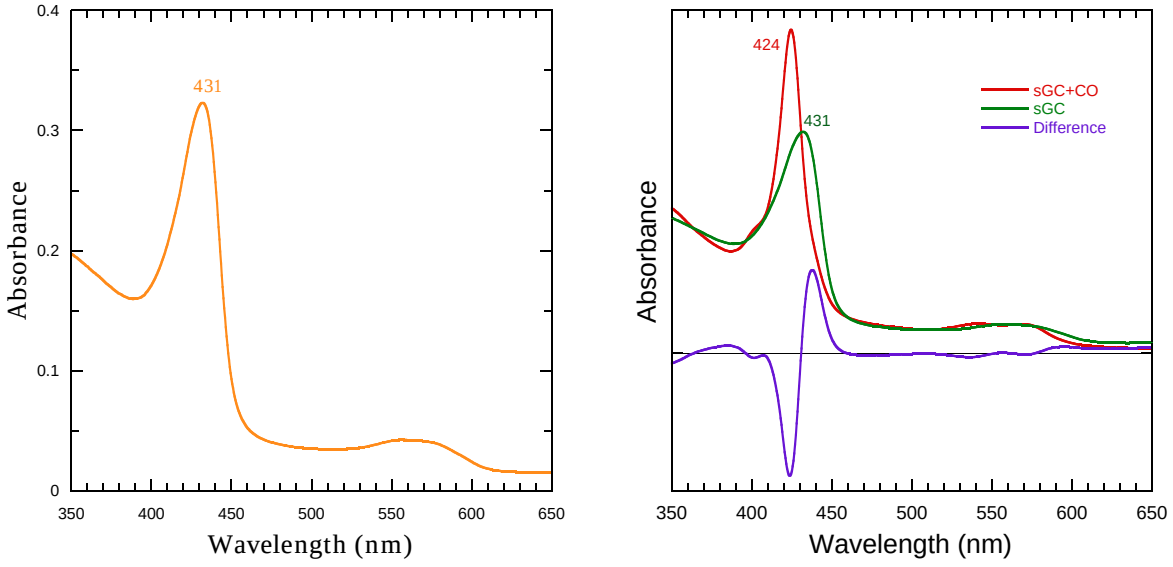

(a) Ferrous sGC

(b) Ferrous sGC ± CO

Figure 2.6: (a) The signature of the NO binding site: static absorption of sGC purified from bovine lung. Concentration of sGC was about 25 μM. Native sGC purified from bovine lung shows an absorption maximum at 431 nm, indicative of the 5-coordinate ferrous heme. (b) Absorption spectra of sGC in the absence and presence of CO. Difference spectrum is also included. [sGC] = 25 μM, [CO] = 100 % in gas phase.

The Soret band is shifted from 431 to 424 nm in the presence of CO bound to native sGC protein (Figure 2.6(b)). Upon addition of YC-1 and BAY 41-2272, Soret maximum at 424 nm shifts to 421 nm in the presence of two effectors as shown in Figure 2.7. The maximum of peak further shifts to 419 nm in the presence of GTP-γ-S as shown in Figure 2.7-B. These observations are in accordance with the previous published results[58]. Since there was no effect of DMSO alone on spectrum (solvent for YC-1 and BAY 41-2272) at 3-5 % concentration in buffer, we consider that Soret shift is attributed only to the interactions between YC-1 and sGC-CO complex.

We incubated YC-1 and BAY 41-2272 in sGC solution overnight. The molar concentration of BAY 41-2272 is same as YC-1 although it has a higher solubility than YC-1. Because of the low aqueous solubility of both YC-1 and BAY 41-2272, a minimum concentration (3-5

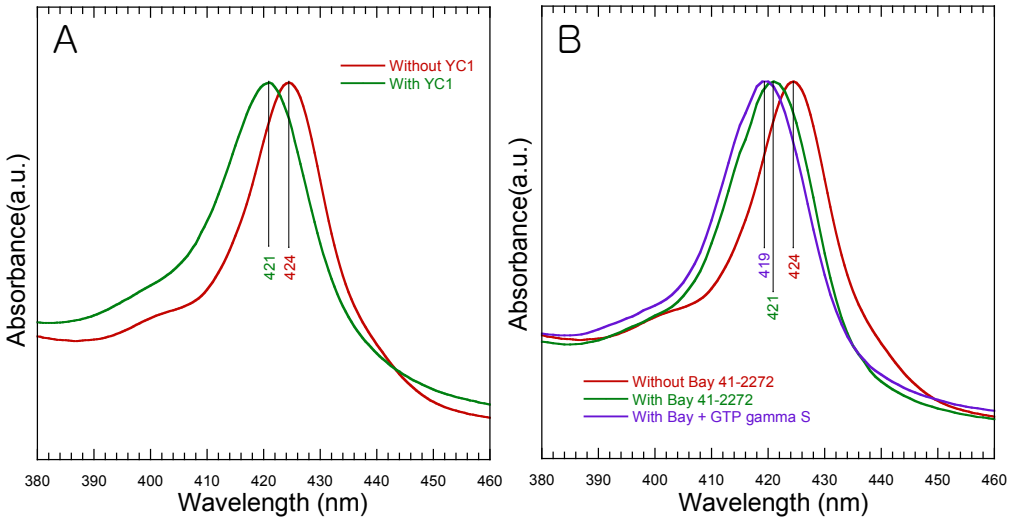

Figure 2.7: Soret band of sGC-CO in the absence and presence of A) YC-1, B) BAY 41-2272 and GTP-γ-S. [YC-1, BAY 41-2272] = 250 μM, [GTP-γ-S] = 1 mM. Clearly spectral shifts occur for all effectors. [DMSO] = 3-5 %.

%) of DMSO is required to keep the solubility. To know the real BAY activator concentration, we measured the absorption spectra of BAY 41-2272 as a function of [DMSO] with water contents as shown in Figure 2.8. We clearly see that the real concentration of BAY 41-2272 drops below 45 % of DMSO (we actually saw some particles whose amount increased when decreasing DMSO). Since we used DMSO at 3-5 % for dissolving BAY 41-2272, we assume that the real concentration of BAY 41-2272 is (0.016/0.57)[BAY] $\simeq$ 6 μM if [BAY] is 200 μM in pure DMSO. However, because the undissolved BAY particles remained in solution during overnight incubation, we assume that there was no depletion of BAY in the closed system so that [sGC-BAY] is larger than 6 μM, but the real BAY concentration in sGC solution is not precisely measured and we cannot assume that sGC is saturated.

2.3.1.1 BAY 41-2272 bound to sGC

We performed TA measurements of sGC incubated with BAY in the presence of CO. Firstly for BAY compound alone, the raw difference spectra at successive time delays after photolysis of CO are displayed in Figure 2.9-A. The maximum of induced absorption centered at 435 nm decreases without significant shift from 2.5 ps to 5 ns. However the minimum of bleaching centered at 419 nm shifted to the red. This spectral change is paralleled by the shift of isosbestic points from 404 nm to 409 nm and at longer wavelengths from 453 to 462 nm (Figure 2.9-A). These shifts indicate that at least three species (two processes) are involved in the kinetics. To disentangle each contribution precisely, we performed singular value decomposition (SVD) of the time-wavelength matrix and found two distinct spectral

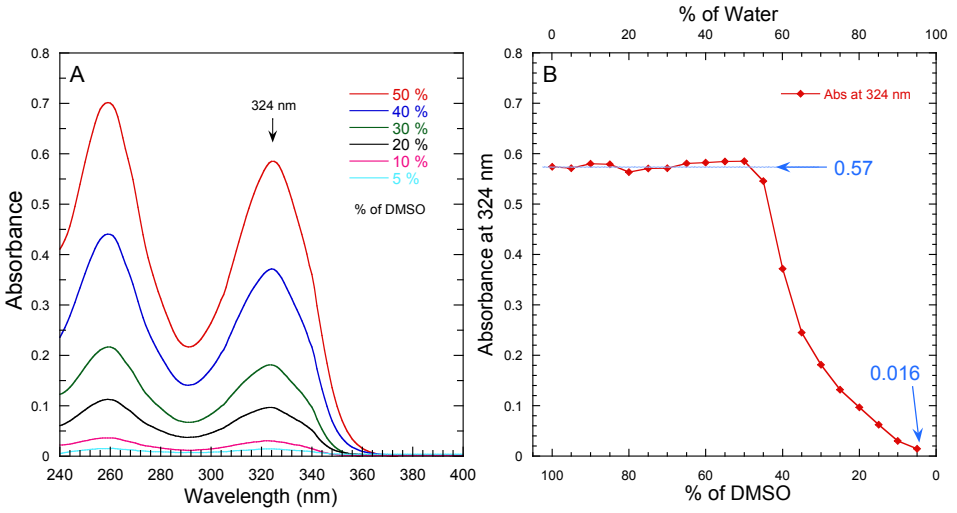

Figure 2.8: A) Absorption spectra of BAY 41-2272 at a concentration of 200 μM in pure DMSO as a function of concentration of DMSO, B) Absorbance at 324 nm depending on the ratio between water and DMSO.

species as shown in Figure 2.9-B. The detailed meaning and process of SVD calculation is described in Chapter 9. Each process has its own SVD values which can be interpreted in different ways. For example, SVD1 component does not always convey same biological information because this method is a mathematical process. The singular values of the first three SVD components are presented in Table 2.1. The third SVD component will be neglected in first approximation and the SVD4 and higher components are not displayed because they correspond to correlated noise (laser instability).

Species	**SVD1**	**SVD2**	**SVD3**
sGC/CO	1.046	0.02624	0.01594
sGC/CO/YC1	0.5026	0.02649	0.006954
sGC/CO/BAY	0.7275	0.07175	0.02065
sGC/CO/BAY/GTP-γ-S	0.4383	0.05814	0.01362

Table 2.1: First three singular values for sGC-CO in the absence and the presence of effectors. These values, depending on absorption coefficients concentration and pump energy, cannot be compared between species, but only their ratio. For example, SVD1 is dominant for sGC alone and decreases in the presence of YC-1. SVD1 and SVD2 are equivalent in presence of BAY whereas SVD2 is dominant if GTP-γ-S is added.

The SVD1 component corresponds to geminate rebinding of CO to the 5c-sGC species as shown by the minimum of bleaching at 420 nm together with the maximum of the induced absorption at 435 nm similarly with steady-state difference spectrum. In SVD2 the bleaching and induced absorption peaks at different wavelengths represent contribution of CO rebinding

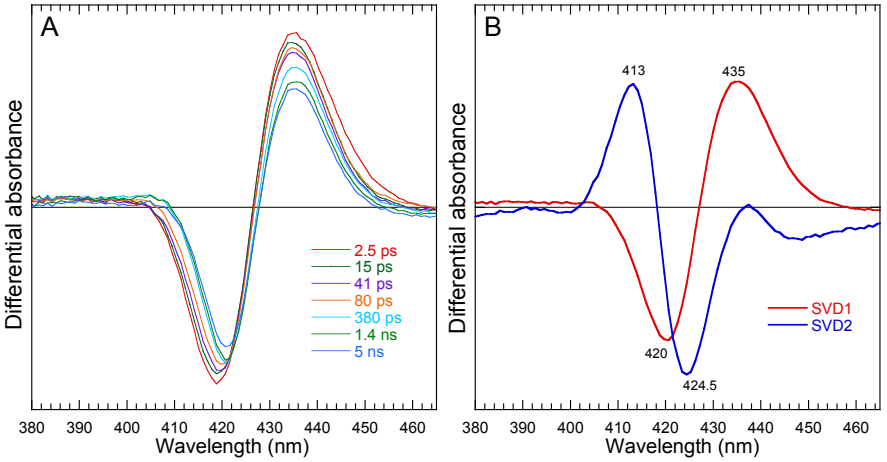

Figure 2.9: A) Raw transient spectra of sGC-CO with BAY 41-2272, B) Two spectral components obtained from SVD analysis for sGC-CO with BAY 41-2272. Geminate rebinding of CO component to 6c-CO (SVD1) is clearly separated from that to 5c-CO (SVD2).

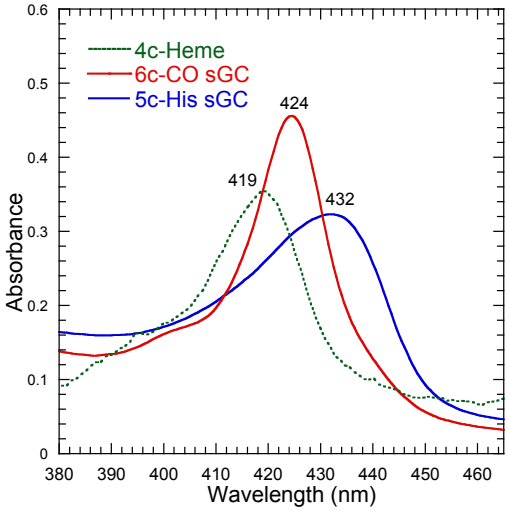

Figure 2.10: Calculated spectrum of 4c-heme (green, dotted) from raw transient spectrum of sGC after NO photodissociation and its comparison with equilibrium spectra of ferrous unbound sGC and 6c-sGC with CO as a ligand. The absorbance scale does not apply to the 4c-heme spectrum, which has been scaled for comparison.

to a different species. Induced absorption at 435 nm (SVD1) was assigned to the formation of 5c-His heme species but that at 413 nm (SVD2) can be due to the formation of 4c-heme as a starting hypothesis. This will imply that the bleaching at 424.5 nm would be attributed to the 5c-heme-CO.

We calculated the absolute spectrum of the 4c-heme of sGC generated after the photolysis of NO because we know that NO transiently produces a 4c-heme after dissociation, using the spectrum at 8 ps to minimize the contribution of excited state decaying in $\sim$ 3.5 ps. The contribution of non-photolyzed species was removed by weighted subtraction of spectrum before photolysis. The 4c-heme is compared with the unbound ferrous sGC absolute spectrum and 6c-CO bound sGC as shown in Figure 2.10. The Soret maximum peak is located at 419 nm and its shape is broader than the spectrum of 6c-sGC-CO. SVD1 component can

be directly compared with the difference spectrum between 6c-sGC-CO and 5c-His sGC as shown in Figure 2.11-A. Both bleaching and induced absorption parts are well overlapped with the static difference spectrum obtained from absolute spectra (Figure 2.10). Thus, we can ascertain that SVD1 component in Figure 2.9-B is due to the CO rebinding to the 5c-His-sGC species.

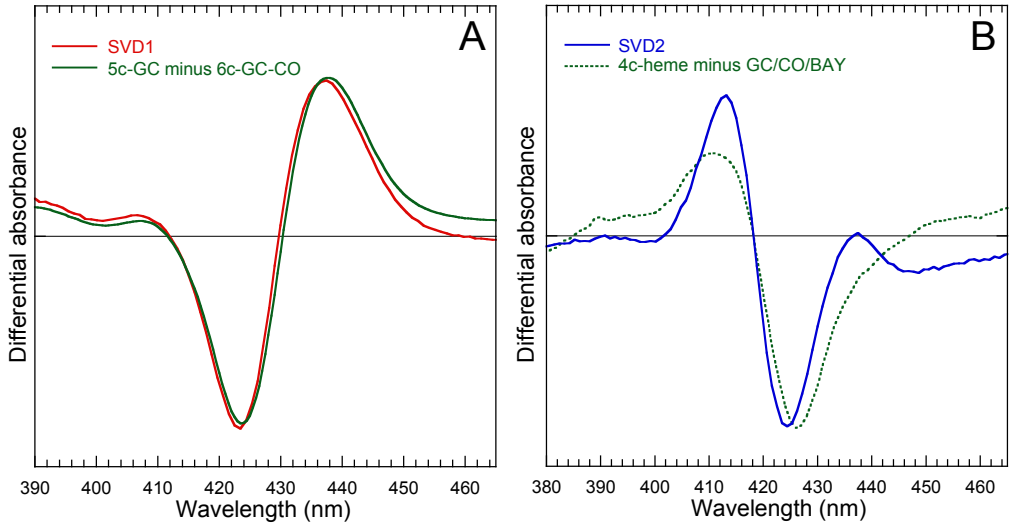

Figure 2.11: Comparison of A) equilibrium difference spectra of 5c-His sGC and 6c-sGC-CO with SVD1 component (Figure 2.9-B), B) difference spectra of 4c-sGC and sGC/CO/BAY with SVD2 component (Figure 2.9-B). The SVD2 spectrum was inverted (X(-1) for comparison with the static difference.

In the same manner, SVD2 component is the outcome from the subtraction of transient 4c-heme spectrum and photolyzed sGC/CO/BAY as shown in Figure 2.11-B. Using known static 6c-CO spectrum with BAY compound and calculated spectrum of 4c-heme, the difference spectrum is compared with SVD2 component. Because we cannot separate 5c-CO and 6c-CO spectra, which are contained in steady-state sGC spectrum, the bleaching part in Figure 2.11-B does not perfectly match. SVD2 can thus be assigned to the formation of 5c-CO species, CO rebinding to the 4c-heme.

Figure 2.12 shows the two main SVD kinetics associated with the corresponding SVD spectra. Two distinct kinetics were fitted with minimum number of exponential components of a multi-exponential function and it turned out that four exponential components were required to fit the data, their amplitudes are displayed as a distribution columns in Figure 2.13-A. Then, the difference TA spectra associated with each mono-exponential decay (Decay Associated Spectra, DAS) were calculated by:

$$DAS_i = \sum_j A_{i,j} S_j \Delta A_j^{SVD}(\lambda)$$

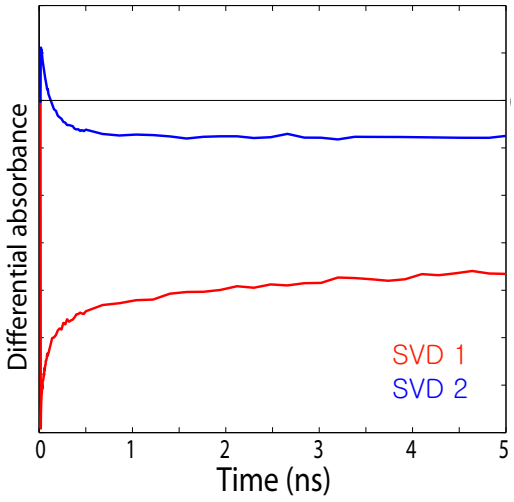

Figure 2.12: Kinetics of two SVD components of sGC/CO/BAY.

where $A_{i,j}$ is the amplitude of the ith decay in the jth SVD spectral component $A_j^{SVD}(\lambda)$ whose singular value is S_j. Thus, every transient spectral species can be characterized by its DAS_i which corresponds to a particular decay time τ_i. Since the raw transient spectra for sGC with CO in the presence of BAY compound contain different spectral contributions, we found distinct spectra associated with each decay component as shown in Figure 2.13-A. Because we want to measure the difference of amplitudes induced by the addition of effectors, we fixed the decay times from SVD calculations to perform DAS analysis.

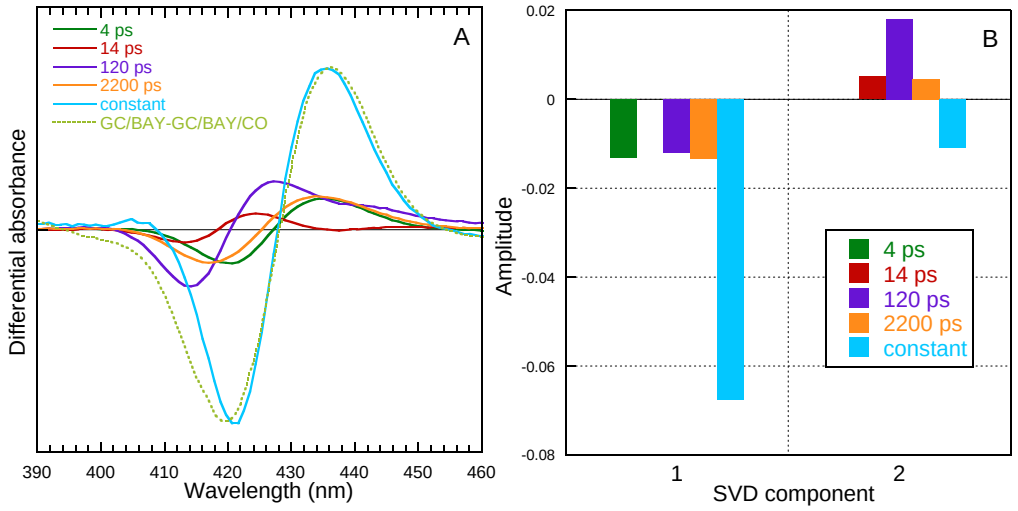

Figure 2.13: A) Amplitudes of individual exponential decays within the SVD kinetic components for sGC/CO/BAY, B) Difference TA spectra associated with each exponential decay components. Static difference spectrum (dotted line) is compared with DAS spectra.

The equilibrium difference spectrum is compared with all spectra. It is distinctly different

from the spectrum of 6c-sGC/CO as shown in Figure 2.14-A due to the contribution of 5c-CO-sGC decaying with 120 ps. The spectrum of sGC/CO/BAY (green, dotted) contains two species whose evolution is described by two DAS (120 ps, constant) and for this reason its spectral shape is broader than that in absence of BAY effector. The spectrum corresponding to the 120 ps decay (purple) is clearly separated from the spectrum associated with the constant (blue). The effect of BAY compound is clear if we consider the DAS of sGC/CO in the absence of any effector as shown in Figure 2.14. DAS (120 ps) disappears in the absence of BAY so that this contribution is assigned to the BAY compound. This fast component (14 ps) does not exist in case of sGC/CO and we assign the characteristic bleaching at 414 nm to the contribution of 4-coordinate sGC. Because the spectrum is similar to that of DAS (14 ps), DAS (120 ps) can correspond to CO rebinding to 4c heme. This explanation will be further discussed in case of sGC/BAY/GTP-γ-S. Lifetime of 4 ps is typically the contribution of excited state decay. For sGC/CO in the absence of activators, the contribution of other DAS components is very small, showing that equilibrium is almost toward 99 % of 6c-CO in this case.

2.3.1.2 Interaction of sGC with CO

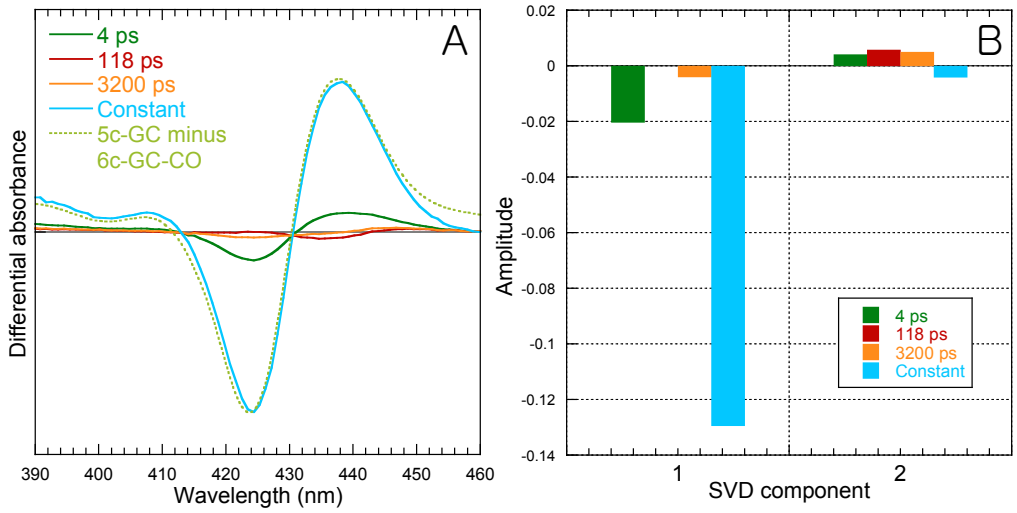

Figure 2.14: A) Difference TA spectra associated with each exponential decay components of sGC-CO in the absence of effectors. Static absorption spectrum is compared with DAS spectra, B) Amplitudes of individual exponential decays within the SVD kinetic components.

When we consider sGC/CO without any activator, the equilibrium difference spectrum is well matched with the constant DAS as shown in Figure 2.14-A and the amplitude of constant DAS is dominant and different from that of sGC/BAY species. The amplitude of DAS (118 ps) in Figure 2.14-B is much smaller than DAS (120 ps) in the presence of BAY

activator (Figure 2.12-B). The absolute difference spectrum is narrower due to the absence of contribution of species induced by the binding of activator.

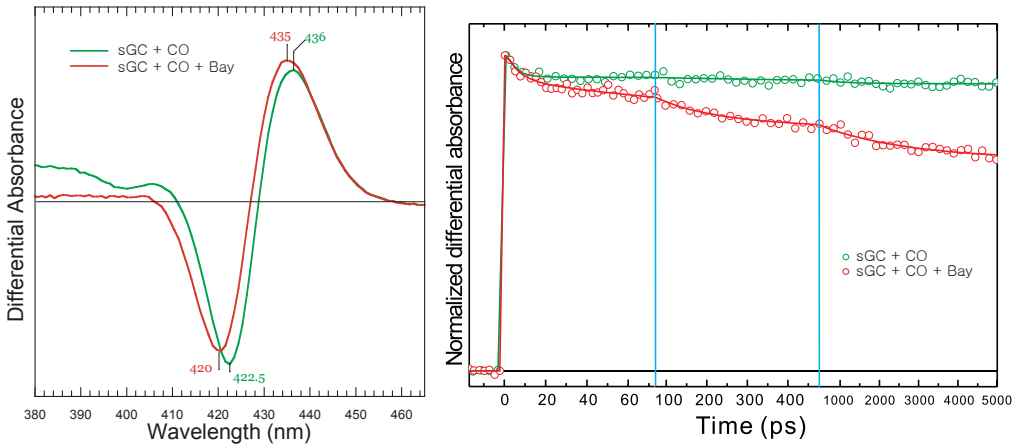

Figure 2.15: Comparison of SVD 1 component in the absence and presence of effectors. A) Spectral and B) kinetic components associated with the transient spectra of Figure 2.9-A are compared with those of sGC-CO without BAY 41-2272.

We compared the two main spectral components in the absence and presence of BAY compound to demonstrate the effect directly as shown in Figure 2.15. Previously it is reported that the rebinding of CO to sGC is similar with Mb[21]. CO alone does not rebind to sGC on a short time scale just like Mb as observed here. The spectral SVD1 component in the presence of BAY 41-2272 demonstrates shifted wavelengths of maximum and minimum compared to that of sGC alone as shown in Figure 2.15-A. Fast rebinding phases of CO to sGC in the presence of BAY 41-2272 are observed, on the other hand, sGC/CO without BAY 41-2272 has little decay phase (Figure 2.15-B). The kinetics associated with the main SVD1 component, which corresponds to CO geminate recombination was fitted with a multi-exponential function and is given in Table 2.2.

The assignment of the different transient species will be summarized in the latter section together with other effectors. Most important finding in this section is the 5c-CO population induced by BAY compound yielding a transient 4c-heme. Its existence was verified by comparing the kinetics without effector. In the following section, we will explore the dynamics of sGC with an extra substrate analogue of GTP in the presence of BAY compound.

2.3.1.3 Binding of BAY 41-2272 in the presence of GTP-γ-S

The substrate analogue of GTP, guanosine-5′-(γ-thio)triphosphate tetralithium salt (GTP-γ-S, Figure 2.16) has similar binding properties as GTP but it cannot be hydrolyzed due to the presence of the sulfur atom. GTP alone has no effect on the CO-bound sGC as reported

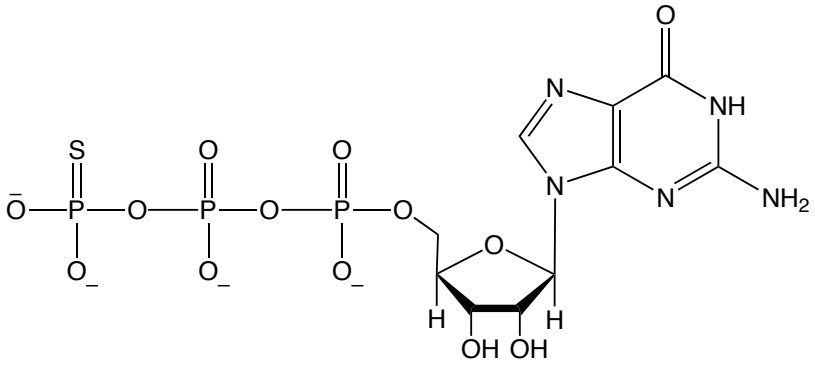

Figure 2.16: Chemical structure of GTP-γ-S.

by resonance Raman spectroscopy[59], however, GTP-γ-S has an effect in the presence of YC-1[60]. Therefore, we incubated GTP-γ-S with the CO-bound sGC in the presence of BAY 41-2272 and measured the transient absorption with the same condition as in its absence.

The raw difference spectra at successive time delays after photolysis of CO are displayed in Figure 2.17-A. We clearly notice a more pronounced effect induced by GTP-γ-S, in line with the greater shift observed in steady-state spectra (Figure 2.7). Similarly with Figure 2.9-A but more important spectral shifts of the bleaching from 417 nm to 421 nm are shown with a larger shift of isosbestic points. The maxima of induced absorption centered at 434 nm decreases with minor changes in shape from 2.5 ps to 5 ns. These shifts and the movement of isosbestic points indicate that more than two species are involved in the transient kinetics, similarly with CO-bound sGC in the presence of BAY 41-2272.

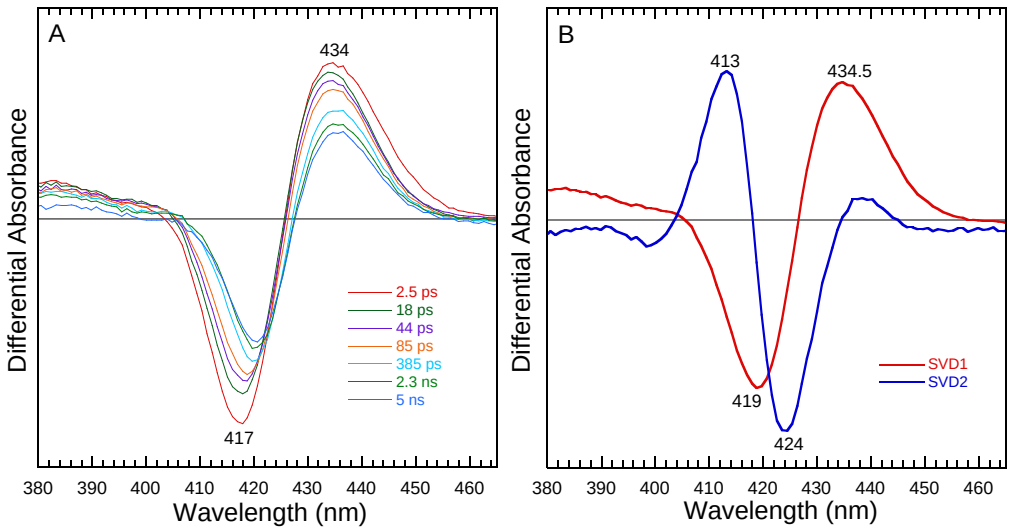

Figure 2.17: A) Raw transient spectra of sGC-CO in the presence of BAY 41-2272 and GTP-γ-S, B) Two spectral components obtained from SVD analysis, which are clearly separated.

Figure 2.18-B presents DAS for the sGC/CO/BAY/GTP-γ-S. In the same way for the sGC-CO, we fitted the SVD kinetics for sGC with effectors as shown in Figure 2.18-A and found five DAS components and one constant whose amplitudes are displayed in Figure 2.18-E. Overall, the time constants are similar with sGC/CO/BAY with minor difference (Table 2.2). The equilibrium difference spectrum is compared with all spectra and the tendency is the same as sGC/CO/BAY. We compared the longest component (1677 ps) and constant term with each corresponding static absorption difference spectra. Figure 2.18-C compares the 1677 DAS component with equilibrium spectrum (both are normalized) and both bleaching parts are well overlapped each other. We also compared the constant DAS component with equilibrium spectrum without BAY compound. In Figure 2.18-D, DAS of constant (blue) is closer to the static spectrum of sGC minus sGC/CO/BAY although the bleaching part contains the contribution of BAY compound. Static spectrum is broader because it contains BAY compound but the absorption part is well matched with DAS component of constant. From these results, we can separate two different contributions of CO rebinding to sGC, with and without BAY. The longest component (1677 ps) corresponds to the CO rebinding to sGC but the constant corresponds to the CO rebinding to the relaxed sGC.

The third component (84 ps) is faster and relative amplitude is larger than that of DAS (120 ps) in sGC/CO/BAY. The larger amplitude of DAS (84 ps) compared to that of sGC/CO/BAY is due to the synergistic activation of BAY and GTP-γ-S. The presence of GTP-γ-S increases the effect of BAY and increases the proportion of 5-coordinate sGC/CO complex and consequently of 4c-heme transient. The spectrum corresponds to the 84 ps is clearly separated from the spectrum of the constant DAS (Figure 2.18-B). We can assign this spectrum to the effect of BAY and GTP-γ-S on sGC-CO just as explained previously for sGC/CO/BAY case. DAS (4.7 ps) that is typically the contribution of excited state decay. One particular time constant (426 ps) was found and this is due to an increased contribution of CO rebinding to activated sGC due to GTP-γ-S, and not shown for other species.

When comparing the spectral SVD1 components in the presence of BAY and GTP-γ-S SVD1 spectrum shows shifted wavelengths of both maximum (435 nm) and minimum (419 nm) compared to that of sGC alone but the effect is larger than expected from the static absorption measurement (Figure 2.19-A). The rebinding phase of CO to sGC in the presence of BAY and GTP-γ-S is more pronounced than in the presence of GTP-γ-S as shown in Figure 2.19-B. All decay components of CO geminate recombination are compared in Table 2.4. Compared to sGC/CO/BAY, faster and dominant components (84 ps and 1.7 ns) were found with lower constant term, revealing that GTP-γ-S increases the proportion of 5c-CO sGC and activated sGC.

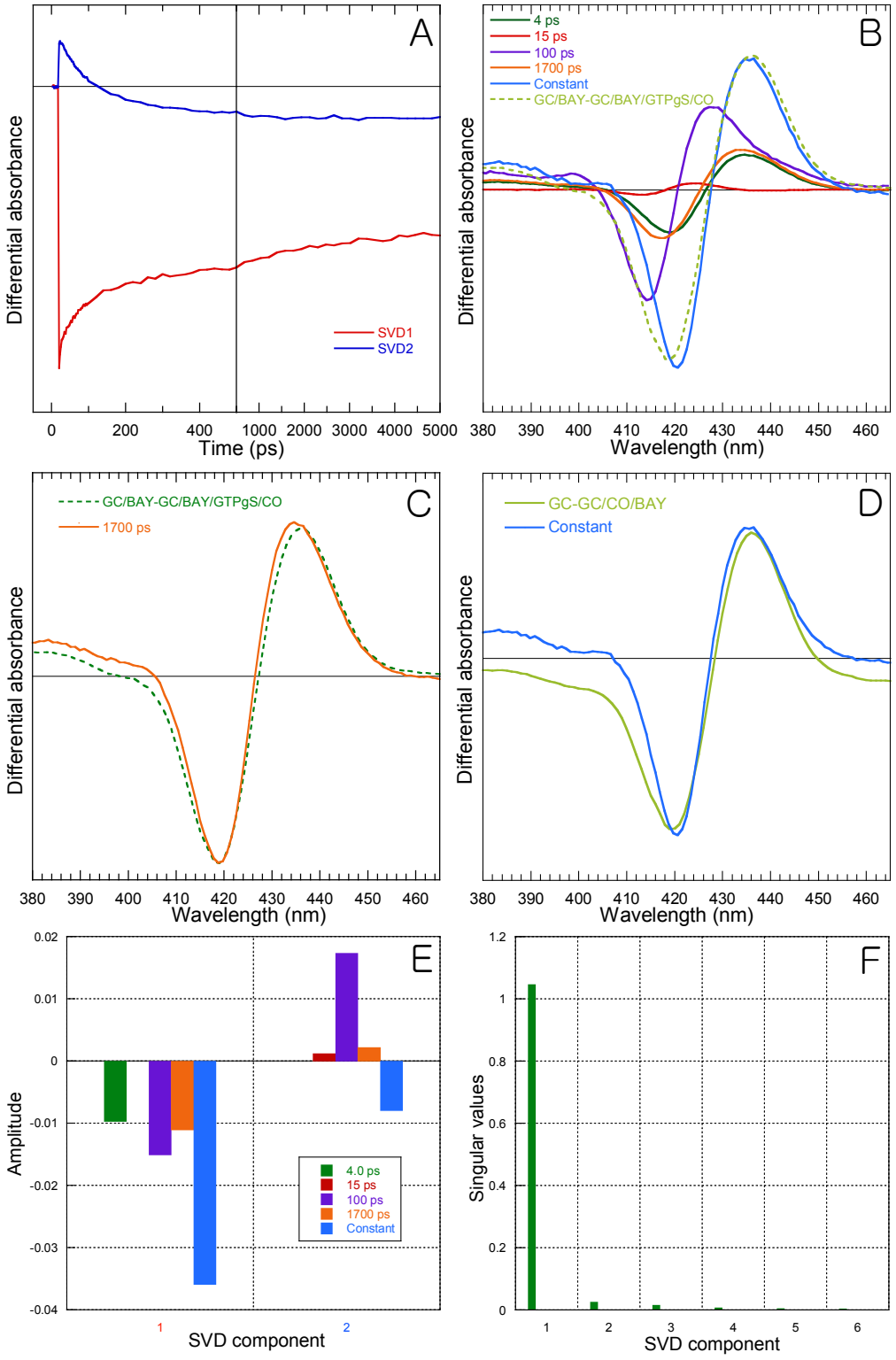

Figure 2.18: A) Kinetics of two SVD components for CO interaction with sGC/BAY/GTP-γ-S, B) Difference TA spectra associated with each exponential decay components. Static absorption spectrum is compared with DAS spectra, particularly with C) DAS (1677 ps), D) DAS (constant) in the absence of BAY (both are normalized), E) Amplitudes of individual DAS within the SVD kinetic components, F) Singular values for each SVD component.

Species	**DAS$_1$**	**A$_1$**	**DAS$_2$**	**A$_2$**	**DAS$_3$**	**A$_3$**	**C**	**A$_4$**
	ps		*ps*		*ns*			
sGC/CO	-	-	118	*0.02*	3.2	*0.01*	cst	*0.97*
sGC/CO/BAY	14	*0.06*	120	*0.19*	2.2	*0.13*	cst	*0.62*
sGC/CO/BAY/GTP-γ-S	15	*0.03*	100	*0.35*	1.7	*0.15*	cst	*0.47*

Table 2.2: Relative amplitudes of DAS for each species.

After we detect the fast CO rebinding to sGC in the presence of two effectors, we wonder whether slower transitions are changed and we measured kinetics from microsecond upto subsecond time range. Microsecond experiments were performed by using a setup at IBPC as described in reference[61]. We employed 532 nm and 6 ns pump pulses and the absorbance was probed at 437 nm. Figure 2.20 shows the comparison of CO kinetics in the two different conditions. From the large difference of the amplitude at 5 ns previously observed (Figure 2.19-B), we expected a similar difference of the amplitude at longer time range. As expected, we found a fast decay component at the "early" times (20 ns) and slower decay components (Table 2.3).

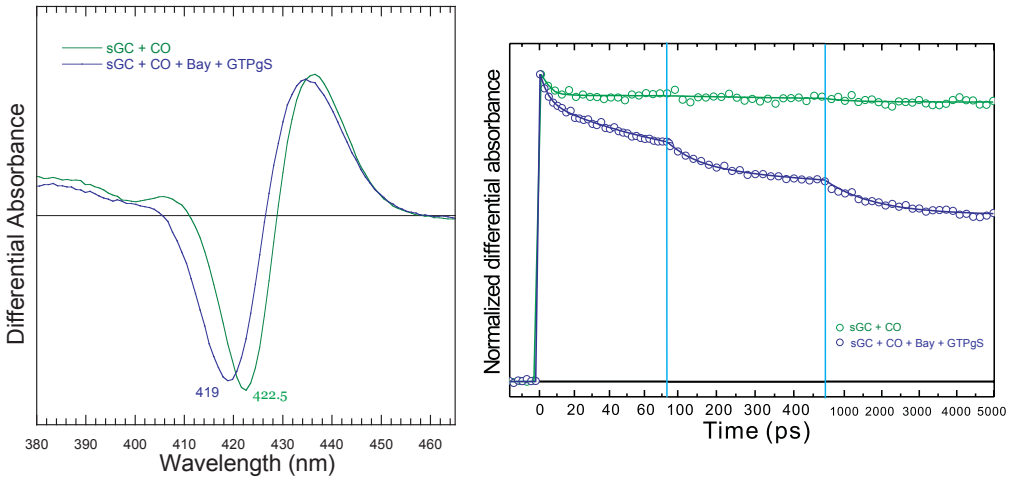

Figure 2.19: Comparison of SVD 1 component in the absence and presence of effectors. A) Spectral and B) kinetic components associated with the transient spectra of Figure 2.9-A are compared with those of sGC-CO without BAY 41-2272.

The transient spectra that we measured on the isolated heme domain did not change at three delay times (+12 ns, +25 ns and + 1 μs) showing that only one process occurred at time > 12 ns. Whereas the initial amplitude of μs-kinetics was smaller in the presence of BAY/GTP-γ-S, we normalized the two curves to make apparent the differences in amplitude of components. The major difference is the presence of a 50 μs component induced by the simultaneous presence of activation BAY and substrate analog GTP-γ-S, and the increased

amplitude of the 20 ns decay. This is due to the increase of energy barrier for CO exiting the heme pocket (20 ns) and from the protein core into the solution (50 μs). These changes of energy barriers are a direct consequence of the change of allosteric state of sGC, induced by BAY/GTP-γ-S. We will also compare this microsecond kinetics for the isolated heme domain β (1-190) of sGC and prokaryotic SONOs in the following chapter. All together the ps-ns kinetic data, our microsecond measurements revealed allosteric transitions in sGC induced by stimulators and substrate. We now describe the effect of the effector YC-1 analogous to BAY 41-2272 and then we will describe a general model from all the data on sGC/CO interaction in the presence of effectors.

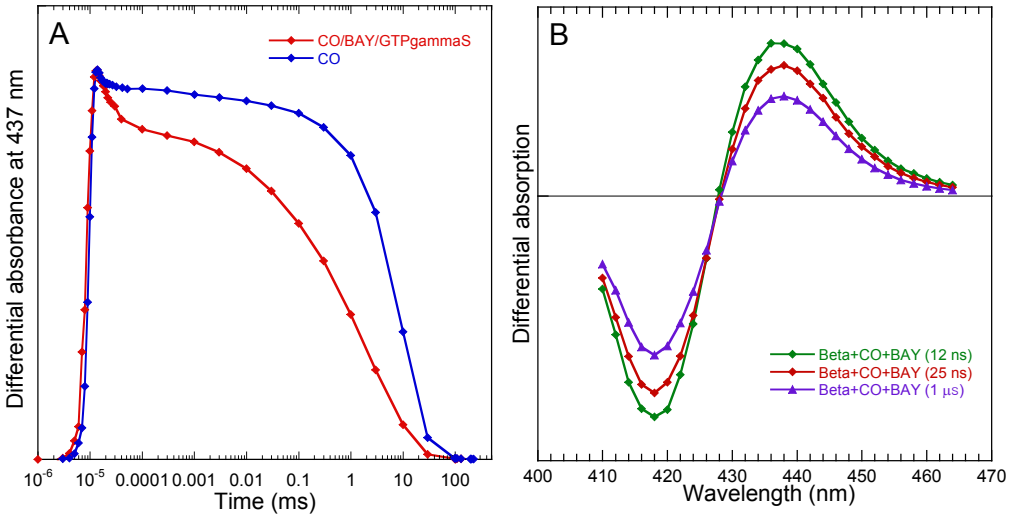

Figure 2.20: A) Comparison of the CO rebinding to sGC kinetics at 437 nm in the absence and presence of BAY 41-2272 and GTP-γ-S. Two curves were normalized. B) Transient spectra at three different times in the presence of the activator bound to the isolated heme domain.

Species	τ_1	A_1	τ_2	A_2	τ_3	A_3	τ_4	A_4	τ_5	A_5	Constant
	ns		*µs*		*µs*		*ms*				
sGC/CO	-	-	1.5	*0.04*	-	-	0.3	*0.07*	11	*0.89*	*0*
sGC/CO/BAY/GTP-γ-S	20	*0.30*	2	*0.06*	50	*0.13*	0.7	*0.22*	7	*0.29*	*0*

Table 2.3: Fit parameters of kinetics in Figure 2.20.

2.3.1.4 YC-1 bound to sGC

Lastly, we performed measurements with the same protocols for CO-bound sGC in the presence of YC-1 analogous to BAY. The raw transient spectra and two dominant SVD components are displayed in Figure 2.21-A.

The TA spectra are dominated by the bleaching of the ground state Soret band centered at 419 nm and the induced absorption centered at 435 nm. The minimum peak of bleaching is shifting to the red together with the isosbestic point movements until 2 ns. Similarly with BAY, SVD1 component corresponds to the CO rebinding to the 5c-His-sGC and SVD2 component is due to other species (Figure 2.21-B). The shape of SVD2 is the result of 4c-sGC minus 5c-CO-sGC. Thus SVD2 spectrum represents the CO rebinding to 4c-heme. We can infer that the 5c-CO heme has a Soret position close to that of 6c-CO heme. Although the tendency is same, the difference is smaller than BAY 41-2272. This proves that BAY 41-2272 has a stronger effect on the CO-bound sGC or a larger affinity than YC-1, provided their solubilities are similar.

Figure 2.21-D presents the DAS data for the sGC/CO/YC-1. In the same way as previous data, we fitted the SVD kinetics (Figure 2.21-C) and found four time constants and one constant term. The amplitudes are displayed as distribution columns in Figure 2.21-E. The dominant constant DAS corresponds to the geminate rebinding of CO to the 5c-His-sGC species. DAS (124 ps) represents other contribution distinct from the constant DAS and this component is similar with sGC/CO/BAY species. DAS (4.5 ps) is the contribution of excited state decay. We compared the spectral and kinetic SVD1 components of CO-bound sGC in presence of YC-1 with those in absence of YC-1 in Figure 2.21-F. A spectral shift and rebinding phase is also found for YC-1 similarly to BAY. Fitted parameters are displayed in Table 2.4 together with BAY data in the next section. Thus the effector YC-1 has exactly the same effect as BAY 41-2272, but the proportion of 5c-CO and 6c-CO is different in both cases, shifted toward 5c-CO with BAY. A general model is discussed in the following section.

2.3.1.5 Discussion: the action of three allosteric activators for sGC-CO

SVD1 component corresponds to the geminate recombination of CO to the 5c-heme iron and all the species have same DAS components but with different amplitudes. In contrast, SVD2 component represents CO recombination to the 4c-heme as identified by its transient spectra. YC-1 is hypothesized to stimulate sGC by weakening the proximal His105-iron bond of CO-bound complex[34]. The formation of 5c-heme for CO-bound sGC in the presence of YC-1 is demonstrated in our results and the amount of 5c-CO depends upon the nature of the effector and upon the simultaneous presence of the analog substrate GTP-γ-S. Very recently, Kitagawa et al found the weak 5c-CO-heme in addition to the 6c-CO-heme produced by the effectors but could not quantify their ratio[57]. Therefore, we calculated the amount of 5c-CO-sGC with the amplitude of DAS components. Montfort et al observed a 17 ns geminate phase of CO with the two thirds of sGC[62] in the presence of BAY in the time scales from ns to

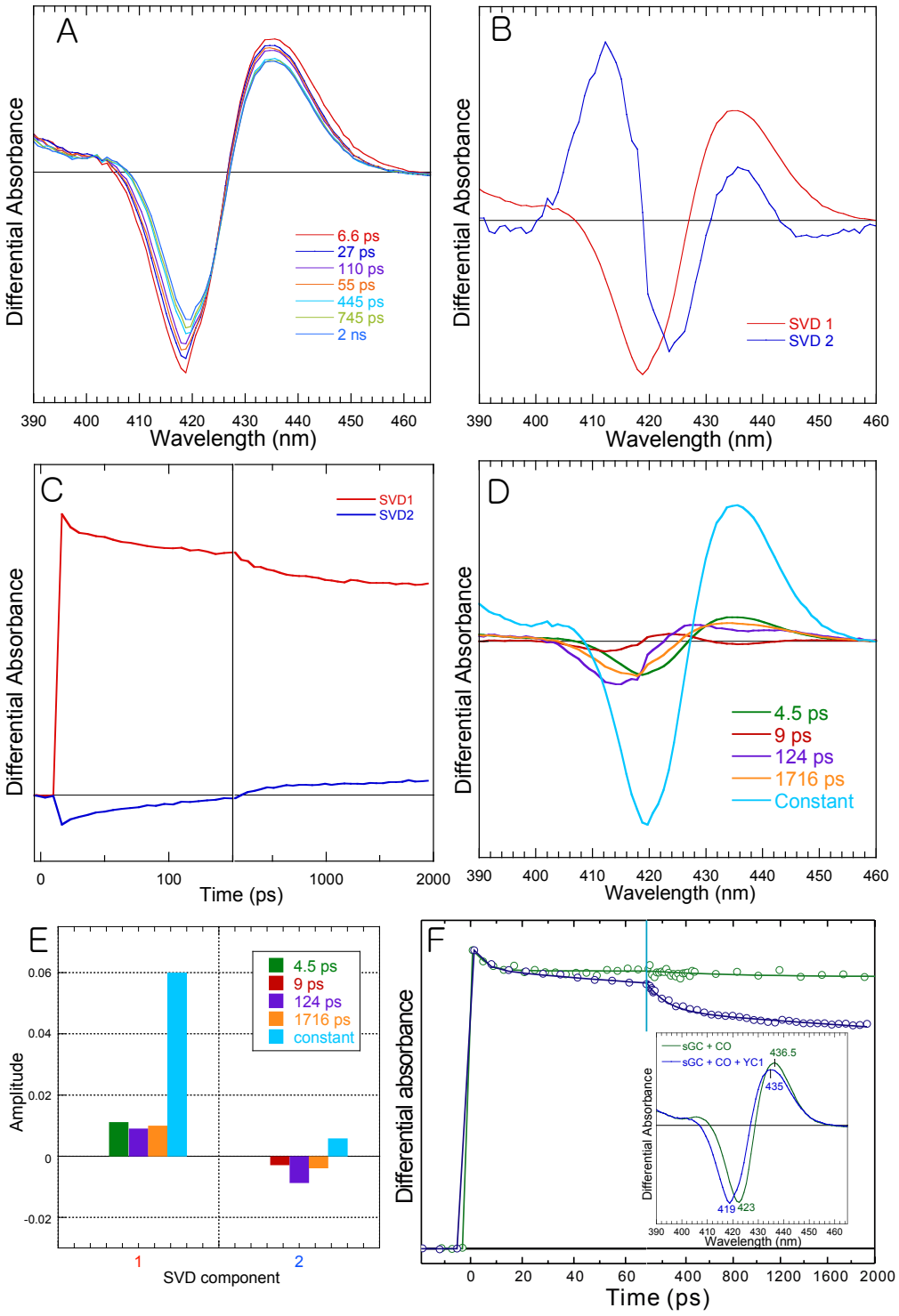

Figure 2.21: A) Raw transient spectra of CO-bound sGC with YC-1, B) Two spectral components obtained from SVD analysis. SVD1 component is clearly separated from SVD2, C) Kinetics of two SVD components of sGC/CO/YC-1, D) Difference TA spectra associated with each exponential decay components, E) Amplitudes of individual exponential decays within the SVD kinetic components, F) Comparison of SVD1 kinetic components for sGC/CO in presence and absence of YC-1 (inset: spectral components).

sub-seconds. Their conclusion is that two effectors can induce a change in sGC conformation that blocks escape of CO as we demonstrated here.

Species	DAS_1	A_1	DAS_2	A_2	DAS_3	A_3	C	A_4
	ps		*ps*		*ns*			
sGC/CO	-	-	118	*0.02*	3.2	*0.01*	cst	*0.97*
sGC/CO/YC-1	9	*0.04*	124	*0.09*	1.7	*0.10*	cst	*0.77*
sGC/CO/BAY	14	*0.06*	120	*0.19*	2.2	*0.13*	cst	*0.62*
sGC/CO/BAY/GTP-γ-S	15	*0.03*	100	*0.35*	1.7	*0.15*	cst	*0.47*
Interpretation	CO rebinding to 4c-heme		CO rebinding to 4c-heme		CO rebinding to 5c-His		CO rebinding to 5c-His$^{\circledast}$	

Table 2.4: Relative amplitudes of DAS for each species. $^{\circledast}$: Relaxed 5c-His heme.

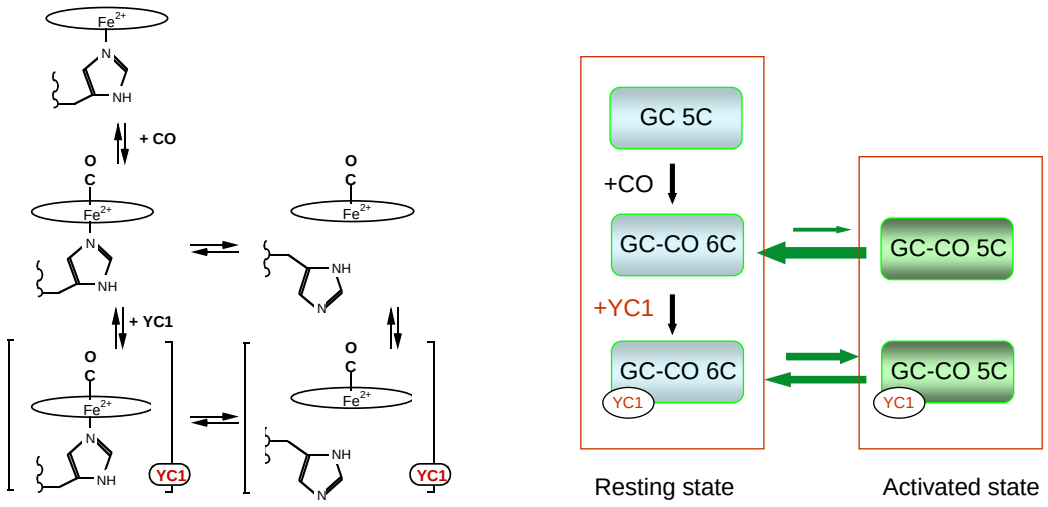

(a) Mechanistic model (b) Allosteric model

Figure 2.22: (a) Mechanistic model for the synergistic activation of sGC induced by CO and YC1. Two populations exist in the presence of CO (5c-CO and 6c-CO heme). The equilibrium is shifted toward 5c-CO in the presence of activators. (b) Allosteric model: the relative size of the arrows represents the displacement of equilibria induced by CO and the activators. The corresponding catalytic activity is indicated in the right column.

Table 2.4 summarizes all the DAS components and their amplitudes together with the interpretation for each species. The very fast (9-15 ps) components correspond to the CO rebinding to 4c-heme. This component can be compared with that of sGC/NO, which is 7.5 ps. The second components (few hundreds of picosecond) can be also assigned to the CO rebinding to 4c-heme. Especially for the sGC/CO/BAY/GTP-γ-S, an extra longer component was found and can be due to the presence of GTP-γ-S. The longest and constant term can be interpreted as CO rebinding to 5c-His-sGC but different allosteric state. The nanosecond components (1.7-3.2 ns) were detected because of the effector-bound sGC is allosterically different from the effector-free sGC.

Taken together, our data strongly indicate that YC-1, BAY 41-2272 have two effects: 1) they provoke a conformational change of sGC that reduces the escape of CO from the heme pocket, 2) the binding of effectors to sGC facilitates the breaking of the iron-histidine bond, increases the proportion of a 5c-heme liganded with CO and therefore increases the activated GC just like NO activation. These effects are more pronounced if the substrate analog GTP-γ-S is bound to the active site of α-subunit. This is summarized in Figure 2.22, which shows two different activation states of sGC by CO for which 6c-heme and 5c-heme can exist simultaneously. Therefore, we can explain the increased activity induced by allosteric activators by the formation of 5c-CO species, simultaneously with an allosteric transition of the 6c-CO species, both species being enzymatically activated.

2.4 Activation by NO and deactivation of soluble guanylate cyclase: the complete NO dynamics

The complete catalytic mechanism underlying the role of sGC which controls the cleavage of GTP to the formation of cGMP is still unknown. In order to have a molecular basis for developing a potential drug toward the sGC, it is essential to understand the activation and deactivation mechanisms. One major unknown mechanism of the NO-cGMP signal transduction is the deactivation of sGC. We define deactivation of sGC as the transition from the NO-activated state generating cGMP to the non-activated state and the deactivation can be obtained by dissociation of bound NO, not considering here the possibility of deactivated state in the presence of NO due to unknown endogenous allosteric effectors. Very often, the rate of NO dissociation from the heme is one of the principal indexes for measuring the deactivation of the sGC enzyme. Previously two studies reported that YC-1 could slow down of the deactivation process of purified sGC with NO complex[63, 64]. YC-1 participates in prolonging the half-life of sGC-NO complex. However the origin of this effect of YC-1 on the behavior of the enzyme is not clear. Our approach is to detect the transient species of sGC-NO complex alone and sGC-NO complex in the presence of YC-1 in picosecond time scales to estimate the effect of YC-1 on NO dynamics interaction with sGC. Then we will measure the dynamics of dissociated NO in a broad time range in order to detect all transients during the interaction of sGC with NO.

2.4.1 Histidine rebinding

His105 is the most important and the very first amino acid residue in transmitting NO binding information in sGC because it is directly coordinated to the heme iron and the

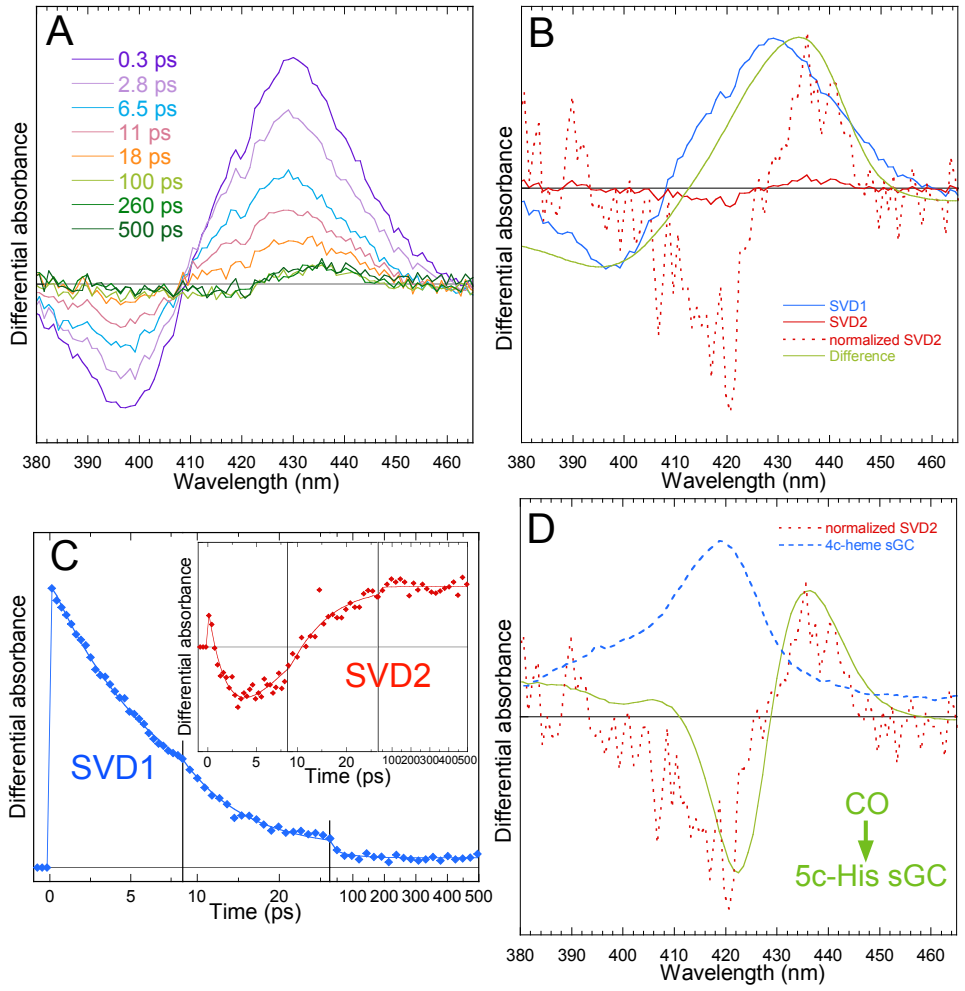

Figure 2.23: A) Raw transient spectra of sGC-NO upto 500 ps, B) The two spectral components obtained from SVD analysis are compared with the steady-state difference. NO rebinding component is clearly separated from the histidine rebinding component, C) Kinetics of SVD1 and SVD2 (inset) components, D) SVD2 is compared with SVD1 component in case of CO.

Fe^{2+}-His bond breaks upon NO binding triggering activation.After dissociation, the geminate rebinding of NO represents 97 % of the species and we can hypothesize that the remaining 3 % will become 5-coordinated with His. In spite of its importance, it is extremely hard to detect the 3 % contribution of His rebinding. Remarkably we succeeded to detect the histidine rebinding using our TA setup in case of cytochrome c'[33] and we measured similarly sGC up to 0.5 ns. Two main SVD spectral components are displayed in Figure 2.23-B representing two different spectral contributions compared with the equilibrium difference spectrum of unliganded minus 5c-sGC-NO (Figure 2.24-A). The main spectral component (SVD1) having the highest singular value corresponds to the NO geminate rebinding, which is in accordance with the previous result[21]. It has a characteristic bleaching recovery centered at 396 nm

and broad induced absorption centered at 428 nm. The induced absorption part of second component (SVD2) centered at 435 nm is the characteristic wavelength due to the formation of 5c-His species. This SVD2 spectral component corresponds to histidine rebinding to the 4-coordinate heme. We fitted these two kinetics SVD components with bi-exponential function whose parameters are displayed in Table 2.5. The contribution of excited state decay (2.5 ps) was excluded from this table.

Species	τ_{gem}	A_1	τ_{His}	A_2	**C**	A_3
	ps		*ps*			
SVD1	7.5	*91 %*	56	*5 %*	cst	*4 %*
SVD2	7.2	*73 %*	68	*2 %*	cst	*25 %*

Table 2.5: Fit parameters of SVD1 and SVD2 components for sGC-NO species.

We compared the kinetics of SVD1 and SVD2 to separate the contribution of different species. Figure 2.23-C shows the kinetics of SVD1 and SVD2 (inset) respectively. The first trace follows the bleaching part near 396 nm and the second trace does the induced absorption part near 435 nm in Figure 2.23-A. Almost NO rebinds to the heme extremely fast with dominant populations (97 %) but certain amounts of NO cannot[21]. The contribution that appears at longer time scales is shown as a minor decay of induced absorption particularly at the wavelength of 435 nm, which is the indicating wavelength for histidine rebinding. Apparently, the kinetics of SVD2 is clearly slower than that of SVD1 as shown in Figure 2.23-C. The fitted intrinsic time constant of this histidine rebinding process of SVD2 was determined as 68 ps. Very recently, 5c-His heme formation from the 4-coordinate species was detected for the cytochrome *c*/cardiolipin complex [65]. Time constant (60 ps) for the histidine rebinding process is very similar with that we measured in sGC but the amplitude is larger (11 %).

2.4.2 Does the allosteric activator YC-1 influence NO dynamics and histidine rebinding?

In a similar way with CO-bound sGC, YC-1 (200 μM) was added to the sGC enzyme to know whether there is any effect or not. After measuring the transient absorption, we performed an SVD analysis, which resulted in two spectral components as shown in Figure 2.24-B. The main component corresponds to geminate rebinding of NO as shown by the decrease of the bleaching at 395 nm. The SVD2 component whose intensity is lower appears with different wavelength maximum and minimum than SVD1, revealing a different process. The second component represents the contribution of His rebinding to sGC since induced

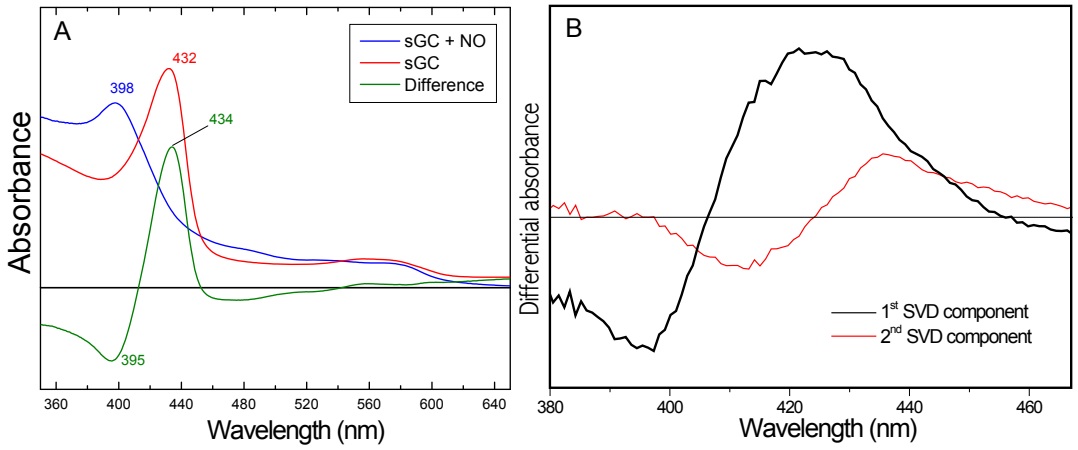

Figure 2.24: A) Static absorption of sGC in the absence and presence of NO. B) Two spectral components obtained from SVD analysis. Geminate rebinding of NO component (SVD1) within sGC heme pocket is clearly separated from the histidine rebinding component (SVD2) in the presence of YC-1.

absorption is located at 435 nm as previously seen. Once NO left the heme binding site, His105 rebinds, leading to the structural change towards the resting state. Thus, thermal equilibrium is sufficient to account for the deactivation of sGC whatever the fate of NO.

We compared two spectral aspects of sGC/NO and sGC/NO/YC-1 and found the similar tendency for both cases. This shows that YC-1 does not influence the rebinding between the heme iron and His105 but influence on somewhere in the system. Although we found the synergistic effect of CO in the presence of YC-1, we do not find any similar effect with NO alone because NO exerts a trans effect on $\sim$ 100 % of 6c-NO, contrary to CO due to its electronic nature. This result is a direct proof to show the allosteric effect of YC-1 on the sGC.

2.4.3 The dynamics of NO interacting with sGC

2.4.3.1 Activation and deactivation of sGC: the structural transitions induced by NO dynamics

Understanding the signaling pathway more deeply requires the knowledge of the kinetic constants such as k_{on} and k_{off} for NO binding and release. This gives us direct implications for phamaco-kinetic evaluation. The detailed picture of the structural changes induced by NO binding to sGC and affecting its activity are still unknown[27]. The reaction rate for NO binding to sGC is extremely fast and the conventional stopped-flow methods have a temporal resolution restricted to 2 ms[45] which is too slow to detect the transient species following NO binding.

We have previously observed that after NO dissociation from the heme, NO recombines geminately to the reactive 4-coordinate heme with a very high probability (τ = 7.5 ps; 97 % of dissociated NO). For understanding NO-sGC interactions, the dynamics of the 3 % NO not rebinding may continue to interact with sGC on longer time scale and we therefore focused on this population of molecules. We investigated the dynamics of NO interacting with sGC by time-resolved absorption in a time-range from 5 ns to 0.1 s. Since the population to be probed is very small with respect to the total sGC population, we have used a spectroscopic system at Institut de Biologie Physico-Chimique (IBPC)[61] which ensures the detection of signal variations as small as $\Delta OD/OD < 10^5$. Because NO can either rebind immediately after photodissociation (geminately from heme pocket or from a docking site in the protein) or migrate within the protein core and finally to solution, from where it may rebind to sGC in longer time (bimolecular rebinding), we can monitor the entire NO dynamics and structural steps from the solution to the heme if we explore a broad time range, as described below. We applied the same sample that was used for picosecond TA measurements to the following studies.

2.4.3.2 NO rebinding phases and heme iron-histidine bond cleavage: nanosecond to second dynamics after NO dissociation

The broad time range ns-μs-ms kinetics (Figure 2.25) recorded at eight wavelengths begin with a peak whose intensity is higher at 435 nm and which corresponds to the fast formation of 5c-His sGC due to NO photodissociation and its immediate decay. This assignment is supported by the transient spectrum at 10 ns whose maximum absorbance is located at 435 nm (Figure 2.26(a)). The initial rise after CO dissociation from Mb, a diatomic which does not rebind geminately to Mb (Figure 2.26(b)) shows exactly the same shape as sGC-NO kinetics, proving that this rise is only due to photodissociation. Because the NO geminate recombination to the 4-coordinate heme is ultrafast (τ_{gem} = 7.5 ps), numerous cycles of photodissociation-recombination can occur for the same molecules during the duration of the pulse (6 ns) used in this kinetic measurement. This phenomena, already observed for cytochrome c'[66, 67], results in a higher apparent dissociation yield so that kinetics in subsequent decades appear with a higher amplitude relative to the initial peak than in measurements using a femtosecond excitation pulse. This turns to be an advantage for detecting the small signal observed in the previous time-range and we can clearly separate all contributions in this kinetics. The repetitive dissociation-recombination cycles, much faster than the pulse duration, induce an initial peak response which is the convolution of excitation and probe pulses, as seen in Figure 2.25-(b), which can be fitted to a gaussian function whose

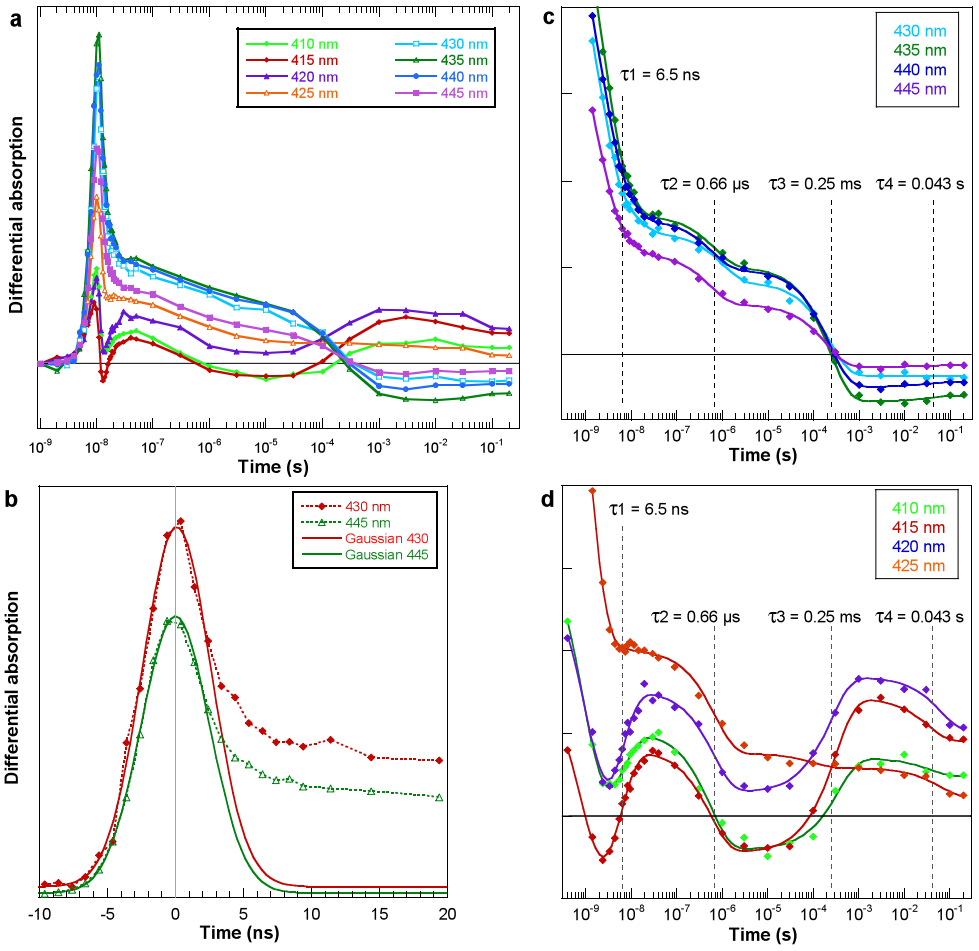

Figure 2.25: Nanosecond to second dynamics after NO dissociation. (a) Raw kinetics over eight orders of magnitude recorded at different wavelengths. Differential absorption is plotted with respect to its value before photodissociation. (b) The initial rise and immediate decay of the signal correspond to the convolution of the two laser pulses and were fitted to a gaussian function whose width at half maximum is 6 ns at two different wavelengths. (c) Global fit of the kinetics at indicated wavelengths. The fitting function is a sum of five exponentials $\sum A_i exp(-t/\tau_i)$ + C which includes the decay side of the convolved pulses as an exponential with τ_{pulse} = 1.4 ± 0.4 ns (Table 2.6). The four time constants indicated by the vertical dashed lines correspond to individual coordination events. Before fitting, the origin of time was positioned according to the gaussian fit in panel b. (d) Same as in panel c at indicated wavelengths. [NO] = 20 μM.

width is that of the laser pulses. The maximum of this gaussian determines the time origin in the subsequent analysis.

There is an immediate decay, starting within, but departing from the temporal profile of the faster gaussian pulse shape and easily distinguished at wavelengths 430-445 nm (Figure 2.25-(b)). This starting decay is simultaneous to an absorbance increase at wavelengths 410-420 nm (Figure 2.25-(a) and 2.25-(d)) and is followed by a complex evolution of the signal.

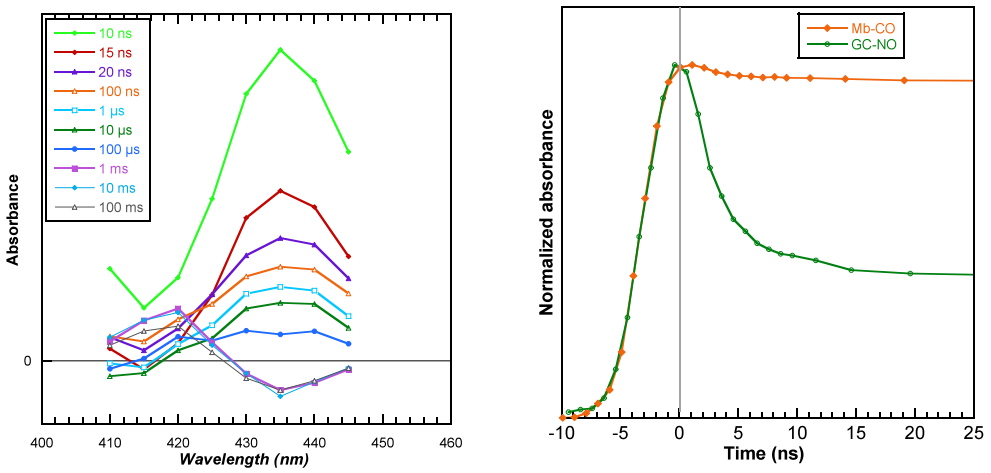

(a) Transient spectra

(b) Rise of two signals

Figure 2.26: (a) Transient spectra at 10 ns, 1 μs, 100 μs etc. constructed from kinetic data (b) The rise of the two signals due to photodissociation of NO from sGC and CO from myoglobin (the later does not rebind geminately) were normalized and superimposed to show that photodissociation is faster than the pulse width and that the rise is only due to photodissociation of diatomics and follows the pulse duration.

The kinetics after the initial pulse were globally fitted to a sum of four exponential components (obvious at 410-420 nm) as indicated in Figure 2.25-(c) and 2.25-(d) corresponding to transitions in the heme coordination. All the parameters of the fits are indicated in Table 2.6.

Wavelength	**410**	**415**	**420**	**425**	**430**	**435**	**440**	**445**	**Average**
τ_1(ns)	5.8	4.8	4.8	7.0*	10	5.7	7.0	7.0	6.5 ns
A_1	*-635*	*-1184*	*-1243*	*30*	*529*	*1407*	*913*	*544*	
τ_2(μs)	0.55	0.55	0.66	0.70	1.00	0.68	0.59	0.55	0.66 μs
A_2	*625*	*545*	*543*	*546*	*496*	*512*	*497*	*508*	
τ_3(ms)	0.35	0.31	0.25	0.10*	0.22	0.23	0.22	0.19	0.25 ms
A_3	*-483*	*-818*	*-611*	*76*	*939*	*1349*	*1174*	*623*	
τ_4(s)	0.037	0.033	0.065	0.060	*	0.040	0.035*	0.040*	0.043 s
A_4	*96*	*229*	*289*	*156*	*0*	*-65*	*-50*	*-18*	
Constant	209	393	443	98	-213	-407	-274	-103	

Table 2.6: Fitting parameters of the nanosecond to millisecond kinetics (Figure 2.25) according to $\sum A_i exp(-t/\tau_i)$ + C. The unit for amplitudes is OD $\times$ 10^6. Some parameters* are badly defined at particular wavelengths due to their low amplitudes.

The first one (time constant τ_1 = 6.5 ns) shows simultaneously a pronounced decay at 430-445 nm, due to disappearance of 5c-His heme, and an absorbance increase at 410-420 nm due to appearance of 6c-NO heme. We therefore assigned this transition to geminate rebinding of NO present within the protein core to 5c-His heme. The second transition discloses simultaneous decays at 430-445 nm (less pronounced than in first transition) and at

410-420 nm, and thus corresponds to the disappearance of 6c-NO heme. This transition (τ_2 = 0.66 μs) is assigned to the conversion 6c-NO → 5c-NO due to proximal histidine release. The third transition (τ_3 = 0.25 ms) occurs about 2.5 time decades later, again with a pattern of decay at 430-445 nm due to the disappearance of 5c-His heme, simultaneous with an absorbance increase at 410-420 nm due to the appearance of 6c-NO heme and is thus also assigned to NO binding to 5c-His, but bimolecular and not geminate in this slow kinetic range. The last transition (τ_4 = 43 ms) is assigned to the conversion 6c-NO → 5c-NO due to proximal histidine release after bimolecular binding (this conversion is not finished on our time range ending at 0.2 s as previously observed[19, 45]). Thus, our kinetic data clearly separate the geminate rebinding of NO being located within the protein core (same molecules that were photodissociated), and the bimolecular rebinding of NO coming from the solution, which was investigated from 1 ms to several seconds[19, 45]. Given the concentration we used [NO] = 20 μM, the conversion 6c-NO → 5c-NO occurs with a time constant (τ_4 = 43 ms) which fully agrees with the stopped-flow measurements as a function of NO concentration[19]. The rate of NO binding from the solution containing 20 μM NO to the 5c-His sGC (τ_3 = 0.25 ms) directly yields an association rate constant $k_{on} = 2 \times 10^8 M^{-1} \cdot s^{-1}$, in very close agreement with that measured in platelets ($3 \times 10^8 M^{-1} \cdot s^{-1}$) using a one-site model[68]. Stopped-flow measurement reported a time constant for 6c-NO → 5c-NO conversion larger (175 ms) than 43 ms[45] (obtained at higher [NO]): this difference is due to instrumental bias. Indeed our measurement starts in time range well below the time constant but is truncated at higher time delays (at 0.2 s), under-estimating the time constant, contrary to stopped-flow measurements truncated at ∼ 1 ms and recording larger time delays, over-estimating the time constant.

All transitions are listed in the Table 2.7 together with their corresponding rate. These sequences of transitions have several implications. Firstly, because histidine rebinding already occurred (τ_{His} = 62 ps; previous section) NO binding, either geminate or bimolecular, necessarily leads to the 6c-heme (with NO bound to the distal side, not proximal).

Bimolecular NO binding to 5c-His	$\tau_3 = 0.25$ ms	$k_3 = 2 \times 10^8 M^{-1} \cdot s^{-1}$
Conversion 6c-NO → 5c-NO	$\tau_4 = 43$ ms	$k_4 = 23\ s^{-1}$
Geminate NO rebinding to 5c-His	$\tau_1 = 6.5$ ns	$k_1 = 0.15 \times 10^9\ s^{-1}$
Conversion 6c*-NO → 5c*-NO	$\tau_2 = 0.66\ \mu$s	$k_2 = 1.5 \times 10^6\ s^{-1}$
His rebinding to 4c-heme	$\tau_{His} = 62$ ps	$k_{His} = 1.6 \times 10^{10}\ s^{-1}$
Geminate NO rebinding to 4c-heme	$\tau_{gem} = 7.5$ ps	$k_{gem} = 1.3 \times 10^{11}\ s^{-1}$
Structural relaxation sGC ↔ sGC*	$0.66\ \mu s < \tau_R < 250\ \mu s$	$4 \times 10^3\ s^{-1} < k_R < 1.5 \times 10^6\ s^{-1}$

Table 2.7: Rates of the transitions observed in kinetics

This assignment is further strengthened by the fact that kinetics at 425 nm (i.e. close to the isosbestic point at 424 nm between the spectra of resting 5c-His sGC and 6c-NO sGC) is

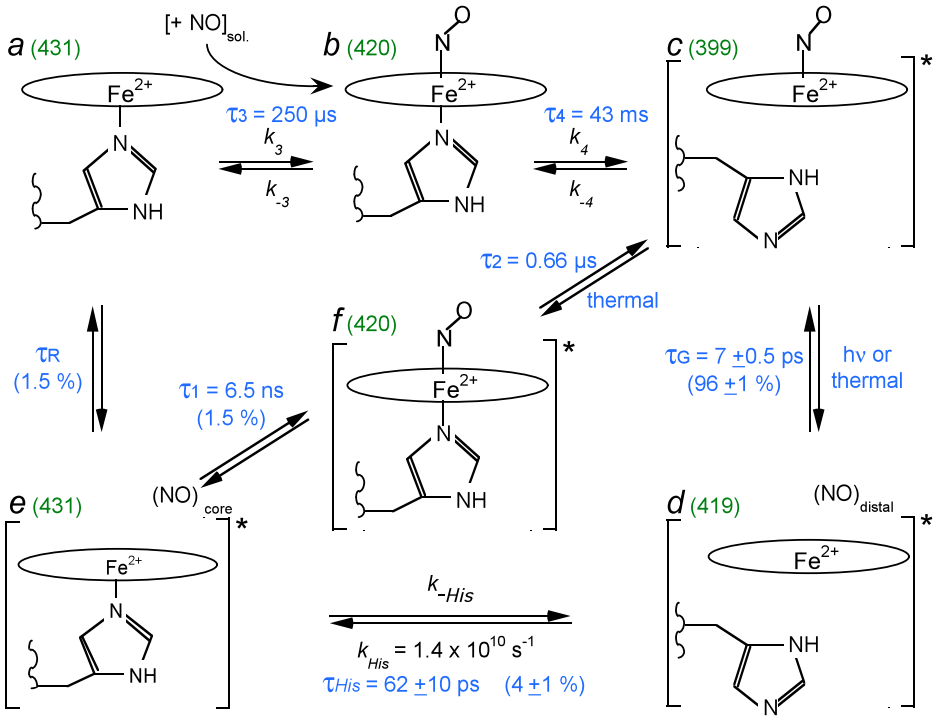

Figure 2.27: Model describing the species involved in these experiments. *a*: 5c-His sGC in the resting state. *b*: 6c sGC. *c*: 5c-NO sGC. *d*: 4c sGC after NO dissociation. *e*: 5c-His sGC in the activated state, immediately after His105 rebinding. *f*: 6c sGC in the activated state, immediately after NO geminate rebinding. The value in parenthesis adjacent to the letter label is the wavelength of the species and the star at the right bracket denotes the activated state of sGC. The starting species of the kinetic measurements is *c*. The time constants indicated are all those measured in the present experiments. For clarity, the corresponding rates are indicated in Table 2.7. In species *d*, NO is located within the heme pocket whereas in species *e*, NO is located in another docking site in the protein. Proximal NO binding is not included here because not necessary to explain our data. Formally, since the ratio of time constants is 62/7, we should expect the same ratio for the populations of species, determined by the probabilities of rebinding, that is to say by energy barriers. However the percentage of populations that we indicated from species d were obtained by differential absorption through SVD analysis. To exactly reflect the populations, one must take into account the absorption coefficient of all transient species, that are unknown. Thus, the proportion of populations is indicated with identical coefficients.

flat in the time range of τ_1 and τ_3 transitions. Secondly, because we measured two coordination changes with the same spectral behavior, both assigned to the conversion 6c-NO $\rightarrow$ 5c-NO, but on very different time-scales ($\tau_2 = 0.66$ μs and $\tau_4 = 43$ ms), this implies that in both cases the species 6c-NO are different and that a structural relaxation occurred between both. The implications of these observations are discussed below and a model for NO-sGC dynamic interaction is presented in Figure 2.27.

2.4.3.3 NO rebinding and histidine rebinding

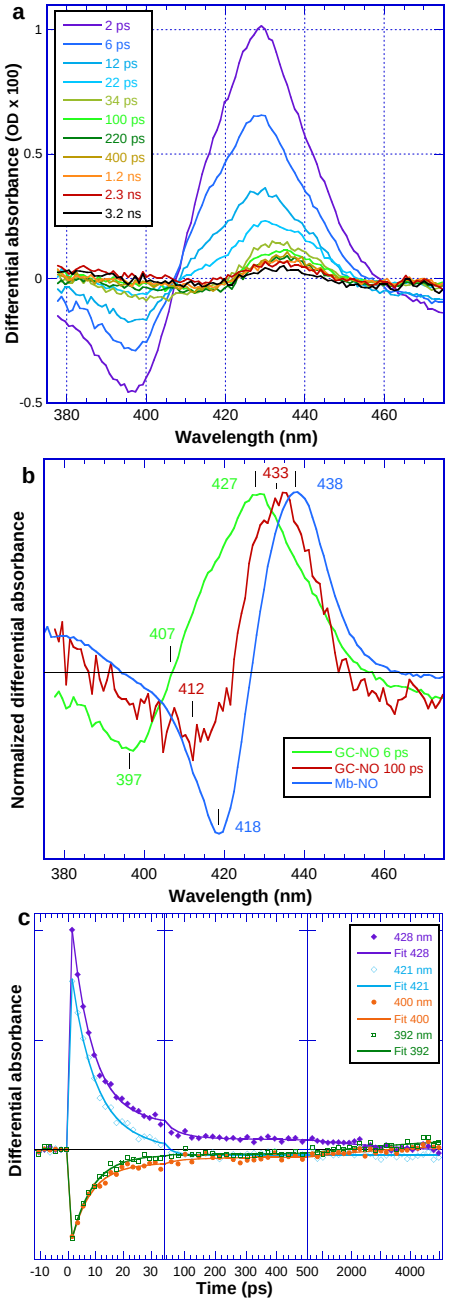

Figure 2.28: (a) Raw transient spectra at indicated time delays. (b) Comparison of normalized transient spectra at + 6 ps and + 100 ps after NO dissociation, revealing the difference in transient species, with that obtained from Mb. (c) Raw kinetics up to 5 ns at indicated wavelengths, fitted to a sum of three exponential components yielding the time constants in Table 2.8.

To support the kinetic profiles that we examined from microsecond setup, it is necessary to analyse the kinetic behaviors from the pico-nanosecond data as shown in Figure 2.28. Figure 2.28-(a) shows the raw transient spectra (5000 ps) and is pretty similar with the preceding data (500 ps) in Figure 2.23-A. Instead of analyzing SVD components, we compared the raw spectra at given times. Figure 2.28-(b) discloses two distinguishable spectra at the early (6 ps) and the late (100 ps) time respectively. This explains the different contributions of each species. Green trace corresponds to the NO rebinding to sGC to become 5c-NO sGC species. On the other hand, the red trace is the long-lived phase and it corresponds to the His rebinding to sGC and this trace is compared with Mb-NO transient spectrum.

From the raw transient spectra, we took 4 different kinetics and displayed them together with their fitted curves in Figure 2.28-(c). Decay time parameters taken from the kinetic traces at given wavelengths together with their fitted curves are summarized in Table 2.8. The averaged time constants were $\tau_1 = 7.5 \pm 0.5$ ps, $\tau_2 = 55 \pm 10$ ps and $\tau_3 = 5600 \pm 500$ ps. In the three windows the time interval was respectively 2 ps, 22.5 ps and 180 ps between spectra. Because of the 2 ps time interval in the first window, it was not necessary to add a fourth component to take into account the excited state decay of the heme, which is usually $\tau_{ex} = 2.5 - 3.5$ ps.

The τ_1 corresponds to the fast rebinding of NO to 4-coordinate heme and τ_2 can be assigned to the histidine rebinding component. The τ_3 can be assigned to the NO rebinding to become 6c-NO sGC and amazingly this time component is found in the microsecond data. These observations from two different TA setup allow us to investigate the NO behavior in sGC from the very beginning (few ps) to the second time scale.

Wavelength	**392**	**400**	**421**	**428**	**Average of τ's**
τ_1(ps)	7.7	7.1	8.2	7.3	7.5 ± 0.5 ps
A_1	*-0.0046*	*-0.0040*	*0.00482*	*0.0100*	
τ_2(ps)	-	58	32*	52	55 ± 10 ps
A_2	*0*	*-0.0004*	*0.0012**	*0.0014*	
τ_3(ps)	5565	6190	-	5042	5600 ± 500 ps
A_3	*-0.0010*	*-0.0010*	*0*	*0.0008*	
Constant	*0.0008*	*0.0006*	*-0.0002*	*-0.0003*	-

Table 2.8: Fitting parameters of the nanosecond kinetics to a sum of three exponentials according to $\sum A_i exp(-t/\tau_i)$ + C. The unit for the amplitude is OD. *Components badly defined at this particular wavelength which is very close (± 1 nm) to the isosbestic point. See Figure 2.28-b.

2.4.3.4 The hypothesis of NO-proximal binding

Since the discovery that NO binds to the proximal heme side in AXCP[69], numerous models of guanylate cyclase activation have been proposed which include the binding of NO to the proximal heme side[19, 58, 70–73] because stopped-flow revealed a dependence upon NO concentration[19] despite the lack of observation for such an activation step in sGC. After the fast geminate rebinding in the picosecond range, we have observed four phases in the nano- to milli-second time range. Thus, we must also consider the alternative explanation that incorporates proximal side binding alternative to the scheme in Figure 2.27.

After the 6-ns pulse, only two species remain: the 5c-NO due to picosecond NO geminate recombination and 5c-His due to His rebinding (Figure 2.25), both having the 4c-heme as intermediate. Due to the high reactivity of the 4c-heme, NO geminate rebinding is ultrafast (7.5 ps) and occurs necessarily to the same heme side from which NO was photodissociated. Thus, if proximal NO binding is to be detected in subsequent process, it must be preceded by formation of the 6c-NO species. Furthermore, the second step of NO binding to the proximal side is NO concentration dependent[74], the second NO coming from the solution to interact with the 5c-NO species (hypothetically replacing His105 displaced by trans effect of distal NO binding). This should occur in the 0.1 μs – 0.1 ms range (between the geminate rebinding and the bimolecular rebinding) and there is clearly no supplementary phase in this

time range (Figure 2.25-(c),(d)). Indeed, in AXCP the proximal 5c-NO complex forms via a dissociative mechanism and the lifetime of the heme dinitrosyl species is very small at room temperature[74] so that this species is expected to be detected below the microsecond range and cannot be detected by stopped-flow. Soret absorption spectra of dinitrosyl porphyrins were observed only in organic solvents[75, 76] with a maximum at 416-418 nm ($\varepsilon = 140 \times 10^3\ M^{-1}\ cm^{-1}$), separated from other species[75, 77]. Albeit the maximum can be shifted in organic solvents with respect to water buffer, supplementary kinetic components should appear if a dinitrosyl heme intermediate were involved. However, kinetics recorded with the highly sensitive detection system[61] disclose only two phases, which are the same at 410, 415 and 420 nm, and are assigned to 6c-NO and subsequent distal 5c-NO formation. This assignment comes from the fact that we have unambiguously identified the fast rebinding of His105 (70 ps) when NO does not rebind to the 4c-heme. This leads us to the conclusion that NO does not bind to the proximal side of sGC. Clearly, our data can be described with a one-site model[78], without phases that could be assigned to dinitrosyl formation or NO proximal binding; however, since our experiments probed only the heme, we cannot exclude the existence of a non-heme binding site[70, 79].

2.4.3.5 Structural allosteric transition

The binding of NO to the 5c-His, geminately in 6.5 ns and from the solution in 250 μs, induces the cleavage of the Fe-His bond in both cases, in a subsequent step with different time constant in both cases (0.66 μs and 43 ms). Thus, because the same structural event occurs with rates separated by more than 4 orders of magnitude, we must infer that sGC is not in the same structural (and allosteric) state in both cases, with a different strain exerted on the Fe-His bond. Consequently, this allosteric transition between both states occurs in the time range $0.66\ \mu s < \tau_R < 250\ \mu s$ (the structural allosteric transition rate τ_R does not correspond to k_{-6} in the model of reference[80] because this later rate includes both histidine rebinding and relaxation, but k_{-6} should be $< 0.25 \times 10^{-3}\ s^{-1}$). This time range for τ_R remarkably corresponds to the time constant measured for the R $\rightarrow$ T allosteric transition ($\tau_{RT} = 2$ - 20 μs) in the tetrameric hemoglobin[81, 82]. The structure of activated state (i.e. in the presence of bound NO) favors the release of proximal histidine with respect to the resting state, in absence of NO. By analogy with hemoglobin[7, 83] these states can be named respectively "relaxed" (R) and "tensed" (T). In the T state of hemoglobin, the constraints were demonstrated in conditions where the Fe-His bond could be broken upon diatomic binding[84].

2.5 Searching for an inhibitor of sGC

It is generally assumed that the rate of NO dissociation is the main reason for the deactivation of sGC. However other mechanisms may intervene: an unknown natural inhibitor seems present in pulmonary cells and can participate in the deactivation of sGC in particular circumstances[85]. Furthermore, modifications such as phosphorylation[86, 87] and nitrosation[88, 89] has been suggested as regulatory processes. Thus, it is very challenging to attempt to search for a natural effector or inhibitor of sGC activity. It is important to search for an inhibitor since sGC activation is also involved in apoptosis[24, 90, 91] and tumor growth[92–94]. sGC is essential for some cells to survive under regular growth conditions and defense against apoptotic inducements. Among the diverse inhibitors, only 1H-[1,2,4]oxadiazole [4,3-a]quinoxalin-1-one (ODQ), a well-known sGC irreversible inhibitor, was found to induce an increase in caspase activity or cytotoxicity, which was related to a loss of cell viability and a decrease in cGMP content[90]. However ODQ acts by oxidizing the heme and is not specific. Because hypericin induces a change in cGMP concentration in cardiomyocytes[95], we aimed at investigating its direct action on purified sGC. We also tried to identify a natural regulatory ligand present in the cell, which activate or deactivate sGC using surface plasmon resonance (SPR) method.

2.5.1 Hypericin

Hypericin [polycyclic aromatic 2,2′-dimethyl-4,4′,5,5′,7,7′-hexahydroxy-meso-naphthodianthrone] is a natural product isolated from the herb *Hypericum perforatum* generally known as St.Johns Wort[96] and its chemical structure of hypericin is displayed in Figure 2.29(a). It is commonly utilized as an antidepressant in phytomedicine, an anti-retroviral agent[97], a protein kinase-C inhibitor[98] and cytochrome P450 inhibitor[99] and may have other targets[97, 100] in signal transduction. Hypericin is also extensively studied for its possible action in photodynamic therapy[97].

Recently, it has been shown[95] that in frog atrial cardiomyocytes, hypericin increased the conductance of cardiac L-type Ca^{2+} channels by decreasing the cellular cGMP level by 69 % in atrial myocytes via a possible inhibition of sGC. Blocking of sGC activity by ODQ (13 μM), mimicked the effects of hypericin. The assays of this previous study were performed on the entire cytosol of cardiomyocytes, so that other proteins than sGC could interact with ODQ which is not specific. Thus, the direct action of hypericin is not yet ascertained and we aimed at verifying *in vitro* the direct effect of hypericin on purified sGC activity. We have incubated sGC isolated from beef lung with increasing concentration of hypericin and measured the cGMP produced in the presence of the NO-donor nitroprusside (see Box 2-1).

Box 2-1. Measurement of sGC inhibition by hypericin

sGC purified from beef lung was diluted in triplicates aliquots in TEA buffer to concentrations 20 nM or 10 nM.

Hypericin is from Molecular Probes.
1.25 μL of hypericin dissolved in DMSO was added to 50 μL of 20 nM or 10 nM sGC in TEA buffer so that the final concentration of Hypericin ranges from 0.1 μM to 200 μM.
The mixture hypericin/sGC incubated overnight in dark.
The final concentration of DMSO is 2.5 % in all tubes.
Controls:

1. DMSO alone at 2.5 % does not inhibit sGC.
2. Hypericin without sGC does not produces false negative or false positive in assay wells (no change of absorption in the absence of cGMP).

Assay of cGMP: see Part 9-2 Materials and Methods.
Volume of aliquot for GTP to cGMP conversion: 8 μL.
Volume of supernatant removed after precipitation: 8 μL.

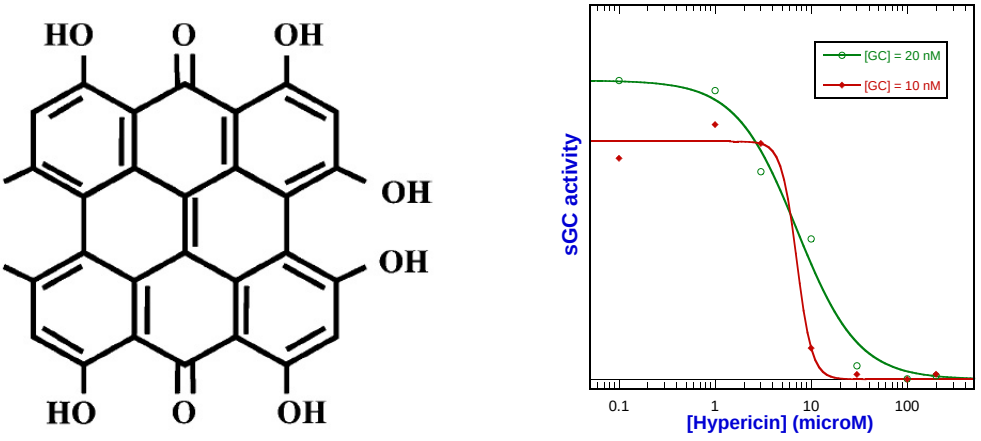

(a) Hypericin

(b) Inhibition by Hypericin

Figure 2.29: (a) Chemical structure of Hypericin and (b) Inhibition of the activity of sGC from beef lung by hypericin. $K_i = 7$ μM.

For two concentrations of sGC we obtained the value $IC_{50} = 7$ μM for the inhibition constant of hypericin toward NO-stimulated sGC activity (Figure 2.29(b)). This result confirms the previous hypothesis[95] based only on the observation that hypericin decrease the cGMP content in cardiomyocytes. The mode of action and binding site of hypericin are unknown

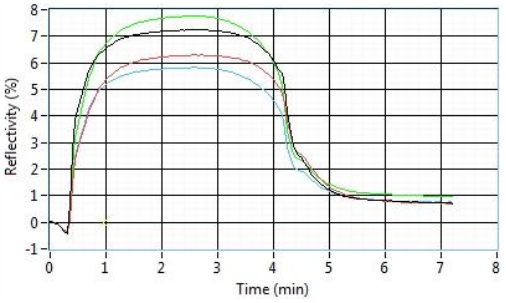

Figure 2.30: SPR curves for sGC in four different conditions. Black: sGC is spotted with 1.6 μM in the presence of 10 % glycerol. Red: sGC is spotted with 1.6 μM. Green: sGC is spotted with 0.8 μM in the presence of 10 % glycerol. Blue: sGC is spotted with 0.8 μM.

and further experiments must be undertaken to resolve these issues. Because it interacts with various proteins, hypericin cannot be used in itself as a sGC inhibitor, but because its IC_{50} reveals a rather good interaction (and maybe a more specific binding than for other proteins) hypericin mode of action must be studied and lead compounds can be derived from hypericin structure. The present data clearly shows that hypericin inhibits sGC and this is the first direct evidence of its effect.

2.5.2 Endogenous ligand of sGC in pulmonary cells

Although most of researches focus on the activation of sGC by NO, little is known about how the activation is restricted or controlled. Our attempt is to identify natural regulatory ligands present in the cell that activate or deactivate sGC. The *in vitro* deactivation rate is slower than that observed *in vivo*[32] leading to the hypothesis of the existence of a natural inhibitor of sGC. During the purification step of sGC from beef lung, we found that the enzymatic activity is lower in the crude cytosolic supernant than in the fractions obtained in the later steps. This suggests a possible presence of a sGC inhibitor which exists separately from other chromatographic steps. Previously an endogenous protein was reported as a possible inhibitor peptide but this hypothesis has never been confirmed[85].

Our approach to detect any binding molecule for the purified sGC is to utilize the highly sensitive technique based on surface plasmon resonance (SPR). We took the fractions from the supernatant during the purification process and the SPR measurements were performed at Genoptics, who has developed a new generation of SPR instrument. We performed preliminary experiments with several fractions obtained after the first chromatographic step (details of purification steps are described in Chapter 8). The purified sGC protein was immobilized on the surface of the plasmon prism chip and interacted with the entire cytosol cellular extract from bovine lung cells. Because the SPR signal is sensitive to the ionic strength, the prism was first equilibrated with buffer containing the same concentration of solutes (except protein) than the fraction to be measured. Raw data for one fraction obtained from SPR method are displayed in Figure 2.30. Thanks to Genoptics' technology, the analysis of large

number of fractions was automated efficiently. We observed the interaction between sGC and an unknown compound present in the early-eluted fractions (14-18) as shown in Figure 2.31 (blue). This compound eluted at lower NaCl concentration than sGC (Figure 2.31) and was not bound to sGC during anion exchange separation and thus has much less negative surface charges. As a future project, after the detection by SPR, the identification of interacting ligand will be performed by mass spectroscopic method (MALDI-TOF) directly on the same chip, choosing the spots which have the highest interacting profile.

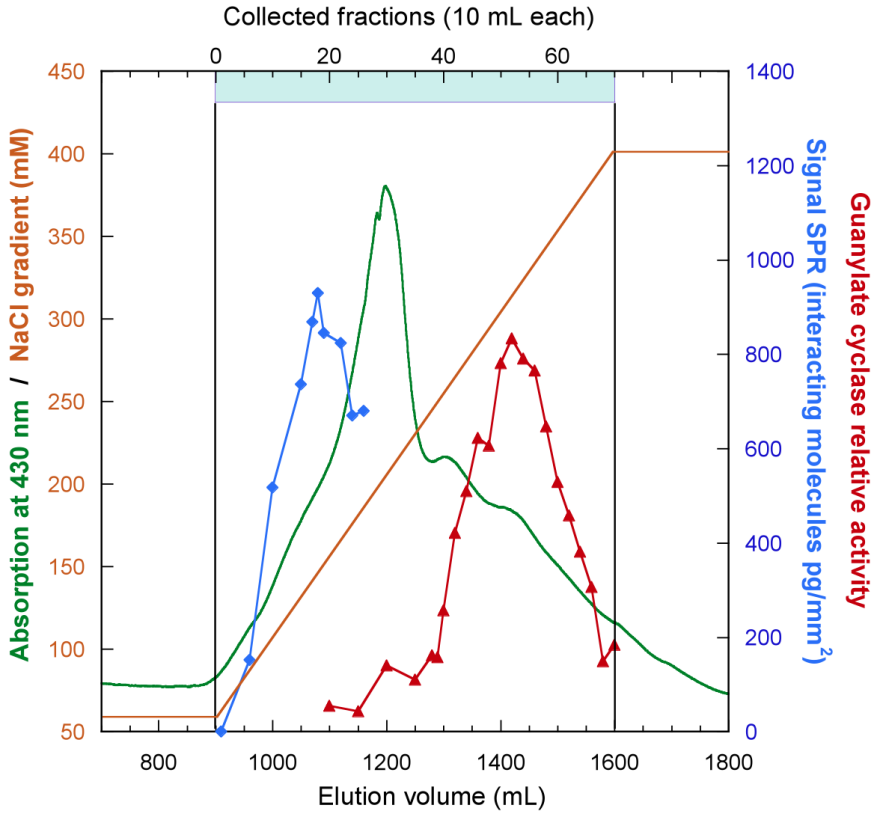

Figure 2.31: Guanylate cyclase activity and SPR signal from lung cells cytosol (blue) interacting with sGC immobilized on a chip are superimposed with the chromatogram profile (green). The assay for sGC (red) was performed in individual fractions (cGMP formed from GTP per min at 37°C for 10 μL of sGC solution in presence of a NO-donor). Individual fractions from Sepharose column (10 mL) were injected in SPR apparatus for interaction followed by a washing step. The ship was previously equilibrated with buffer at the same NaCl concentration than the fraction. The SPR signal is expressed as picograms of molecules bound to the ship per mm^2. The error is $\pm$ 15 %. Each point is the measure from 20 sGC-spots on the SPR ship. A peak in fractions 17-19 reveals a molecule interacting with sGC, which is eluted before sGC from the Sepharose Fast-Flow column. NaCl Gradient is from 50 to 400 mM.

2.6 The comparison of sGC with other proteins

In this chapter, we explored sGC from purification to investigations by optical tools, mainly using transient absorption method. We uncovered the mechanism of synergistic activation of sGC by CO in the presence of two different activators: YC-1 and BAY 41-2272 by detecting 5c-CO transient species. We also established a complete mechanism of the sGC activation and deactivation by probing kinetics ranging from picosecond to second time scales. Lastly, we searched for a novel inhibitor (hypericin) for sGC for future unknown drug candidates and also detected an endogenous ligand that potentially regulates sGC using SPR method.

An obstacle to study the entire sGC is the absence of the structural information based on crystallographic data. Only sequence of 1-194 residues have been modelled as a heme binding domain[101]. Apart from sGC as NO-receptor from mammalian source, a conserved family of proteins named SONO (Sensor of Nitric Oxide) have been found in prokaryotes[27]. The isolation and crystallization of SONO homologous to sGC heme domain enables us to understand some structural aspects of sGC and to model the sGC heme (1-190) domain at molecular level. We have the opportunity to study these heme proteins, including human β1 (1-190) subunit of sGC and three different SONO proteins expressed in Pierre Nioche's laboratory, to be investigated the same way as sGC to explore particular aspect of molecular mechanism of sGC activation. How do heme proteins control 6- to 5-coordinate transition and how does the sGC get deactivated are important issues to be addressed. Using femtosecond time-resolved spectroscopy, we will compare in Chapter 3 the transient steps induced by the release of diatomic ligands from SONO with those identified in sGC.

sGC that serves as NO receptor has a structure which exerts a strain on the proximal histidine. This strain causes a weakening of the bond between the iron and histidine when NO binds at the distal side, a process known as a "trans effect". One good example is the bacterial cytochrome c' from *Alcaligenes xylosoxidans* (AXCP) and this heme protein also functions through trans effect albeit it has different structure from sGC. In Chapter 4, we will compare AXCP dynamics with sGC. The rate of formation of 6c-NO and the subsequent conversion to the 5c-NO species depend upon the concentration of NO. The first NO binds to the distal side and the proximal bond becomes weaker by trans effect. Right after, the second NO binds to the heme at the proximal side as the His120 dissociates from the heme[66, 102]. This mechanism in AXCP could be similar to the activation of sGC and we chose to study AXCP for this reason. One must recall that NO proximal binding is demonstrated in AXCP by the X-ray structure of the nitrosylated form, whereas in sGC proximal binding is only a working hypothesis based on the NO dependence of the formation of 5c-NO species. Moreover,

we will expand our study about the trans effect in Chapter 5 by introducing one myoglobin mutant (H93C), which also discloses similar trans effect. Both AXCP and H93C will thus be good examples to compare with the NO (CO) rebinding dynamics in sGC, which has an unique character due to the 4c-heme properties. This aspect of iron coordination with NO for both is similar but the whole protein structure is different. In the following chapters, various results on these heme proteins will be discussed in light of sGC dynamics.

2.7 Conclusion

1. The activators YC-1 and BAY 41-2272 change the allosteric state of sGC and facilitate His-Fe bond cleavage.
2. This effect is increased by the substrate GTP.
3. Proximal His rebinds in 62 ps after release of NO.
4. A structural relaxation occurs in sGC in the time range 0.7 μs to 250 μs.
5. Proximal binding of NO is not observed.
6. Hypericin inhibits sGC with $K_i = 7$ μM.
7. Endogenous ligand exists in the cytosol of pulmonary cells.

Chapter 3

The heme domain of sGC: Bacterial NO-sensors and β1 (1-190) subunit of sGC

3.1 Prokaryotic NO-sensors and the soluble guanylate cyclase

sGC is the endogenous NO receptor which is expressed in the cytoplasm of many mammalian cells. Unfortunately, the full three dimensional crystal structure of sGC has not yet been determined although four decades has been passed since the discovery of sGC. This is due to the difficulty of preparing the protein with the quality and quantities suitable for crystallization. sGC is a heterodimeric protein which contains one heme prosthetic group per heterodimer and its α and β subunits are evolutionarily related homologues and have structural similarity. The catalytic site consists of components from both subunits and is located at the interface of the two catalytic domains and catalyzes the conversion of GTP to cGMP and PPi (inorganic diphosphate). The heme is located in the N-terminal area of β1 subunit but not α1, despite their homology and the most common isoform is the $\alpha1\beta1$ protein. β1 subunit is composed of the NO/CO-binding heme domain module of sGC (called SONO, Sensor of Nitric Oxide), a PAS-like domain, a coiled-coil region, a cyclase domain (Figure 3.1).

The SONO heme domains were found in some bacteria as isolated domains and a recent breakthrough was the crystal structure determination of prokaryotic homologues of sGC[27, 103]. It has been possible to uncover the bacterial expression systems for the SONO and domain, which offer smaller proteins that are more easily crystallized. We had the opportunity

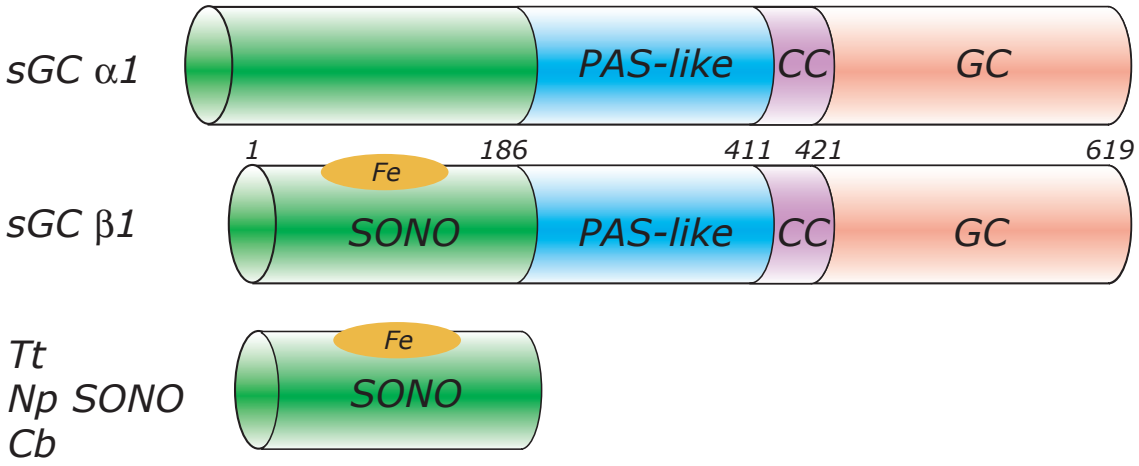

Figure 3.1: Three bacterial SONO domain is compared with the β1 subunit of the whole sGC architecture. Indicated numbers of amino acid are based on the sequence of the β-subunit of human sGC.

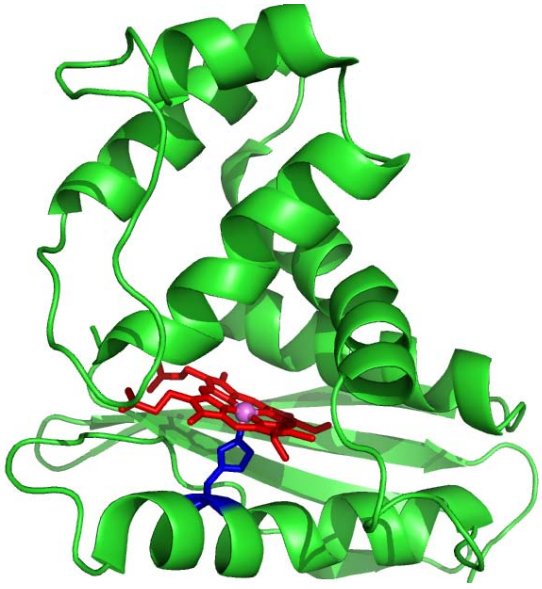

Figure 3.2: 3D structure of *Tt*-SONO. Ribbon diagram describes the residues of 181 amino acid residues of the protein. The heme prosthetic group and the proximal histidine (His102) coordinating its iron are shown respectively in red and blue. PDB ID is 1XBN and the figure was generated using Chimera.

to study three SONO proteins from different bacterial sources from Pierre Nioche's Laboratory who actually determined their crystal structure. The first SONO is from the strict anaerobe thermophile bacteria - *Thermoanaerobacter tengcongensis* (*Tt*) and the two known crystal structures of *Tt*-SONO revealed bound oxygen[27, 103]. The crystal structure of *Tt*-SONO (PDB ID: 1XBN) is displayed in Figure 3.2. Similarly with sGC, histidine is attached to heme iron at the proximal side and the vacant distal side is available for binding a ligand.

Tt-SONO shares a 18 % sequence identity with sGC and this value is up to 40 % for other SONOs. Although some insights were obtained from their structures[27, 72, 103] and some biochemical properties were defined[104, 105], the exact physiological role of the bacterial

SONO is still not clearly known[106]. In this Chapter, we will study the interaction of bacterial SONO's (whose precise function of SONO's is not yet known) with NO and CO for understanding their own properties that we will compare to the isolated heme domain of sGC β-subunit, and then to the entire dimeric sGC. We must remember that isolating a protein domain allows to restrict a mechanism under study to some elementary steps, but at the same time, can perturb this mechanism, so that some particular properties could not be directly transposed to the same domain within the entire protein.

3.2 Interaction of NO with sGC-related bacterial NO-sensors

Pierre Nioche and coworkers run genome screening of *Clostridium botulinum* to discover a potential ortholog of the human sGC which has NO-binding heme domain. A multiple sequence alignment of SONO proteins with human sGC is shown in Figure 3.3 to show the homologies of them compared with sGC. They determined a gene that encodes a two-domain protein in which the N-terminal domain shares 15 % sequence identity with the first 186 amino acids of β1 subunit of sGC. They demonstrated that SONO from *C. botulinum* was indeed expressed in growing *C. botulinum* cells by applying the technique of the reverse transcription-polymerase chain reaction (RT-PCR). By using *E. coli* as the host cell they overproduced the protein which constitutes the N-terminal heme domain with 186 amino acids from the *C. botulinum* DNA source. Spectroscopic measurements readily identified the presence of heme after the purification. EPR spectroscopy determined histidine coordination of the heme iron in the purified protein[27], with a typical three line spectrum as the blueprint of five-coordinate heme-NO complex. Remarkably, ferrous *Cb*-SONO is stable even under the exposure to air, similarly with the homologous mammalian sGC. In the same manner other SONOs were prepared from the bacteria *Thermoanaerobacter tengcongensis* and *Nostoc punctiforme* with a slightly different number of amino acid residues. Proteins thus produced were over 98 % pure as determined by SDS-PAGE (Sodium Dodecyl Sulfate-Poly Acrylamide Gel Electrophoresis) and sent to us in ice to perform laser experiments.

In sGC, the binding of NO to heme, induced bond cleavage between histidine and heme iron, leading to a five-coordinate ferrous iron with NO triggering the activation of sGC by inducing a structural change of β-subunit and propagated through the interface between subunits. In previous Chapter, we found the mono-exponential and ultrafast (τ = 7.5 ps) behavior of NO in sGC. The purpose of our experiments for SONO proteins is to compare the dynamics of NO in SONO proteins with that of sGC in order to determine the corresponding

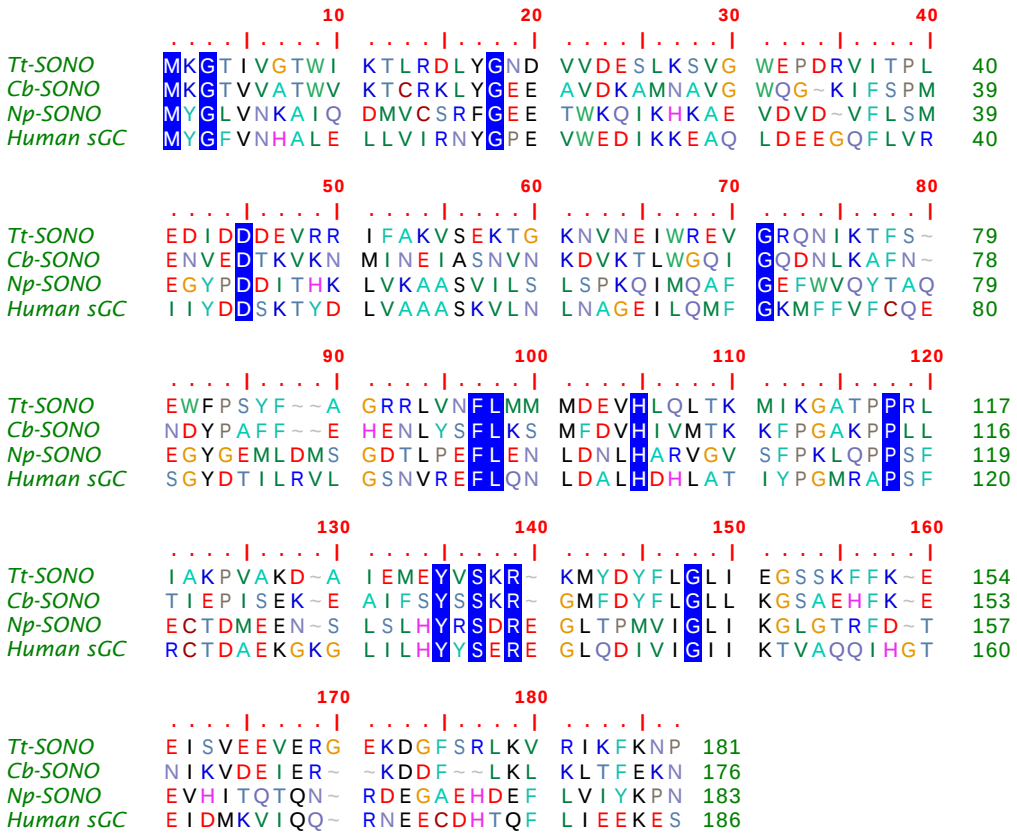

Figure 3.3: Multiple sequence alignment of three SONO domains and human sGC β1. Sequence numbering is that of *Tt*-SONO. Residues with absolute identity in the alignment are represented by blue blocks. The histidine residue coordinating the heme is represented by red block. Each SONO shares 18 % (*Tt*), 16 % (*Np*), and 40 % (*Cb*) sequence identity with the heme domain of sGC. Accession numbers are taken from Pubmed web source and as follows: *Tt*-SONO [*Thermoanaerobacter tengcongensis*, gi55670808], *Cb*-SONO [*Clostridium botulinum*, gi148381498], *Np*-SONO[*Nostoc punctiforme*, gi23129606], and Human β1 [Homo sapiens, gi2746083]. Alignments were generated using the BioEdit program.

energy barriers due to the entire protein structure or to the isolated heme domain. We also aimed at describing NO interaction with the bacterial sensors.

For SONO proteins, the proportion of 5c-NO and 6c-NO liganded forms depends upon the temperature and we tried to analyze this effect for each SONO in their sensing properties. Very interestingly for the comparison with sGC, they form a mixture of 5c-NO and 6c-NO liganded species, which is not found for sGC. We need to separate both contributions and analyze the parameters influencing their proportion. Since SONO covers only heme domain part (1-190) of sGC, the dynamics will be restricted to it but interconnection between heme domain and other domain of sGC may also influence the NO/CO dynamics. We will first study separately SONO from three bacterial species, and then we will compare SONO with their counterpart, the isolated heme domain β(1-190) of sGC.

3.2.1 sGC-related bacterial NO-sensor: *Tt*-SONO

The first SONO to be studied is from the strict anaerobe thermophile *Thermoanaerobacter tengcongensis (Tt)*, which has 39 % sequence identity with *Cb*-SONO. The SONO domain comprises an α-helical distal domain and β-strand-rich proximal domain with the heme between both (Figure 3.2), coordinated by the histidine 102 residue (Figure 3.4).

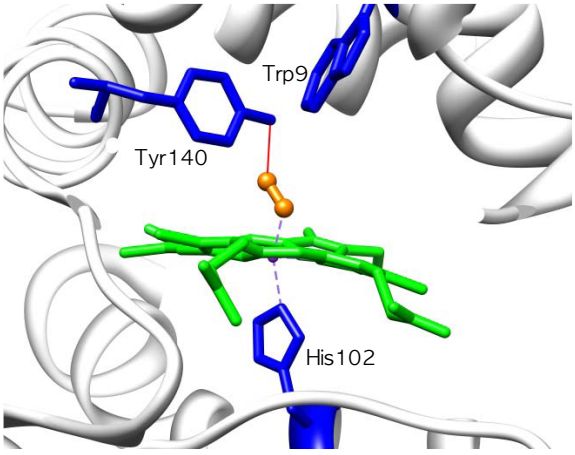

Figure 3.4: Close-up view of the heme prosthetic group (green) of *Tt*-SONO, histidine, tyrosine, tryptophan residues coordinating its iron with O_2 ligand (orange). Red line depicts that the phenolic OH of Tyr140 is within hydrogen bonding distance of the oxy ligand. His102 (proximal ligand of the heme Fe^{2+}), Tyr140, and Trp9 are shown in blue. PDB ID is 1XBN and the figure was generated using Chimera.

As purified, the raw protein sample has a Soret maximum at 416 nm and α/β bands at 592 nm and 555 nm respectively. Compared with absorption spectrum data of Hemoglobin, we can assume that this protein forms a Fe^{2+}-O_2 complex. As seen in Figure 3.4, *Tt*-SONO with O_2 as ligand has a 6c-oxy-His102 coordination structure.

Interestingly, at 72°C, this protein is still in bound form Fe^{2+}-O_2 similar to those of the heme-containing O_2 sensors[107] but it oxidizes to the ferric state, a property that we will use for preparing the NO/ *Tt*-SONO complex. This property of *Tt*-SONO is intrinsic because sGC does not bind O_2. In line with this behavior, *Thermoaneaerobacter tencongensis* is a strict anaerobe and has a physiological relevant temperature at $\sim$ 72°C in native conditions[108]. 90 μL of protein solution were placed in a cell, degassed and heated at 72°C in order to displace O_2. To reduce the protein, we used ascorbate at final concentration 5 mM. The static absorption spectrum of O_2-liganded form is displayed in Figure 3.5-A at RT and 72°C. Very small blue shift of Soret appears at 72°C but no shift is apparent for Q-bands. The spectra of unliganded reduced *Tt*-SONO exhibits Soret band at 431 nm and broad α/β band around 566 nm which are similar to those of sGC. This characteristic Soret maximum is assigned to the 5c-His heme after the consumption of O_2 by ascorbate solution.

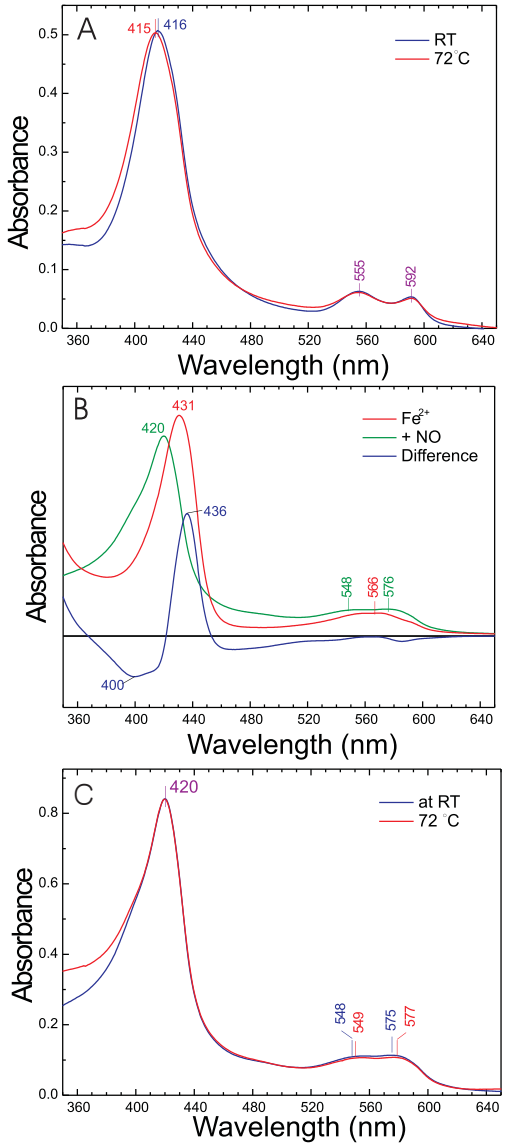

Figure 3.5: Electronic absorption and difference spectra of *Tt*-SONO species, α/β bands; A) O_2-bound (not degassed) at RT and 72°C, B) NO-bound, C) NO bound forms at RT and 72°C. [NO] = 20 μM.

Formation of NO-liganded *Tt*-SONO was conducted by the input of 1 % NO diluted in N_2 directly into the cell through the gas train at a total pressure of 1.3 bar (about 20 μM NO in the aqueous phase). Similarly, 100 % CO was introduced to the cell to obtain CO-liganded *Tt*-SONO. This resulted in a sharp Soret band at 424 nm and the extinction coefficient increased (Figure 3.5-C). Absorption peaks of Soret and α/β band of unliganded ferrous *Tt*-SONO are very similar with those of full-length bovine sGC. After the addition of NO, the Soret band shifts to 420 nm and the extinction coefficient decreased (Figure 3.5-B) as opposite with the case of CO. This specific Soret position of 420 nm indicates a major population of 6c-NO form of *Tt*-SONO by similarity with myoglobin and contrary to sGC, but the presence of a shoulder at $\sim$ 398 nm indicates a small population of 5c-NO complex at 72°C (Figure 3.5-B). The equilibrium difference spectrum of NO-bound species shows a maximum located at 436 nm and two different characteristic minimum peaks located at 400 and 416 nm. In Table 3.1, the spectroscopic parameters of *Tt*-SONO are summarized and compared with other relevant proteins. Before and after the kinetic measurements, we verified the static absorption spectra as shown in Figure 3.6-A and B. At 72°C, we found a slight evolution at lower wavelength (350 nm) and a shoulder at 400 nm. This is due to an increase of proportion of 5c-NO species during the laser experiment at high temperature.

Proteins	**Coordination**	**Soret**	**Q-band**
	Unliganded Fe(II)	nm	nm
sGC	5c-His	431.5	555
Tt-SONO	5c-His	431	566
	Fe(II)-CO complexes		
sGC	6c-CO	424	541/570
Tt-SONO	6c-CO	424	546/567
	Fe(II)-NO complexes		
sGC	5c-NO	398	-
Tt-SONO	6c-NO	420	548/575
Tt-SONO at 72°C	6c-NO/5c-NO	420, 398*	549/577
Myoglobin	6c-NO	420	547/582
	Fe(II)-O_2complexes		
Tt-SONO	6c-O_2	416	555/592
Tt-SONO at 72°C	6c-O_2	415	555/592
Myoglobin	6c-O_2	416	543/581

Table 3.1: *Tt*-SONO and other proteins. Peak positions of UV/Vis spectra of given proteins with/without gaseous ligands. *a shoulder at given wavelength.

We performed TA measurements right after measuring equilibrium spectra and the raw difference transient spectra after photolysis of NO are displayed in Figure 3.6-C. At RT the maximum of induced absorption is centered at 441 nm and the minimum of bleaching at 421 nm remains without any shift during first 5 ps. The bleaching at 421 nm is due to the dissociation of 6c-NO species. While the bleaching at 421 nm decreased rapidly, a second bleaching at 429 nm was becoming significant after 10 ps, paralleled by a considerable shift of the isosbestic point from 431 to 443 nm. A similar shift also appears around 390 nm in the same time range. These shifts indicate that two different processes are involved in the early time kinetics. The transient spectra are different when recorded at 72°C. Instead of the bleaching at 421 nm a broad bleaching centered at 400 nm appeared, due to the dissociated 5c-NO bound heme species yielding transient 4c-heme. The bleaching which appears at 429 nm is more pronounced than that at RT.

SVD calculation of the time-wavelength matrix data resulted in two main spectral components for both temperatures. At RT, SVD1 component represents the spectral process not evolving on this time-scale but should change in larger time-range. The SVD2 component corresponds to geminate recombination of NO, as shown by the double bleaching at 399 and 418 nm as shown in Figure 3.7-C. At 72°C, the broad bleaching located at 399 nm (Figure 3.7-B) is due to the dissociated 5c-NO heme species yielding 4c-heme. Unexpectedly, the induced absorption at 436.5 nm in SVD1 component appears, indicating that the transition

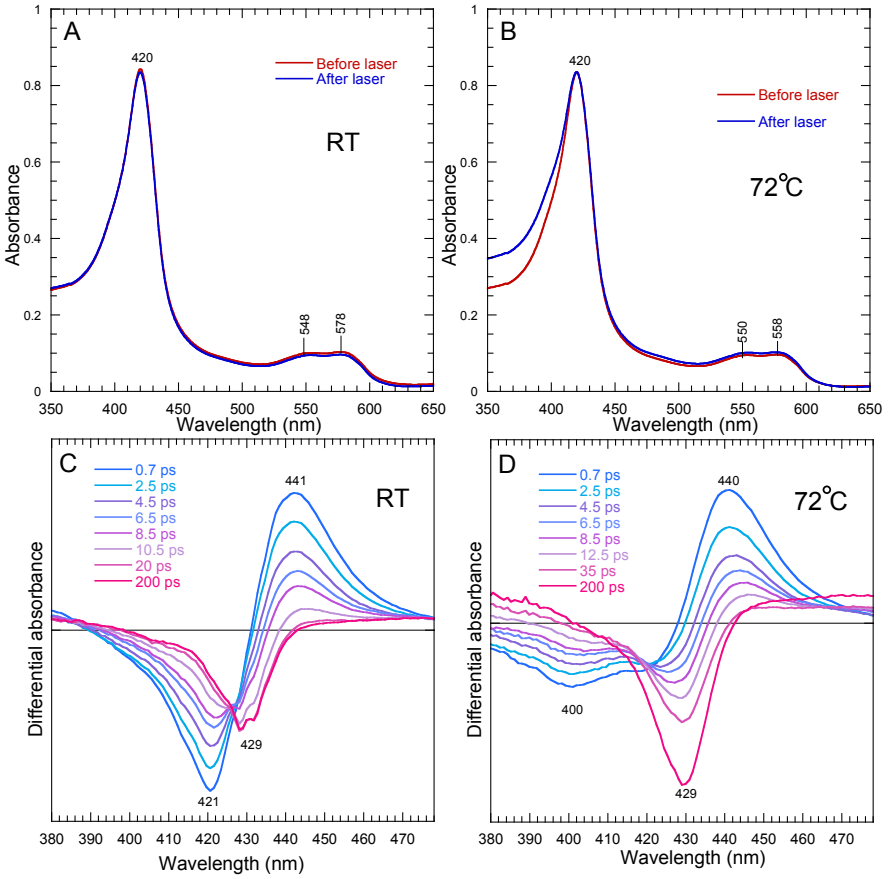

Figure 3.6: Static absorption spectra before and after laser experiments at A) RT and B) 72°C, C) Transient spectra (raw data) at different time delays after photodissociation of NO for ferrous *Tt*-SONO at RT and D) at 72°C. [NO] = 20 μM.

in *Tt*-SONO is different from sGC. Instead of 4c-heme as an intermediate, the spectra suggest a direct histidine rebinding in *Tt*-SONO. However, the small induced absorption of the transient 4c-heme can be completely "hidden" by the large bleaching centered at 421 and 429 nm.

We fitted the kinetic traces for each SVD component at two temperatures as displayed in Table 3.2. At RT, the kinetics associated with each SVD component was fitted with two decay components. 7.1 ps is dominant for SVD2 and this corresponds to the 5c-NO geminate rebinding. DAS (7.1 ps) shows a mixed contribution of 5c-NO and 6c-NO (Figure 3.7-A), indicating that both DAS and SVD spectra were not able to separate the pure contribution of each species at RT. At 72°C the kinetics associated with SVD1 component was fitted to a bi-exponential function (7.1 ps; A_1 = 0.80 and 84 ps; A_2 = 0.03) with a base line (A_3 = 0.17). The bleaching is dominant at 398 nm, contrary to RT and the contribution at 418 nm almost disappeared. Induced absorption is located at 432 nm and this value is very close to that of 5c-His species. For this case, DAS calculation allowed to separate the contribution

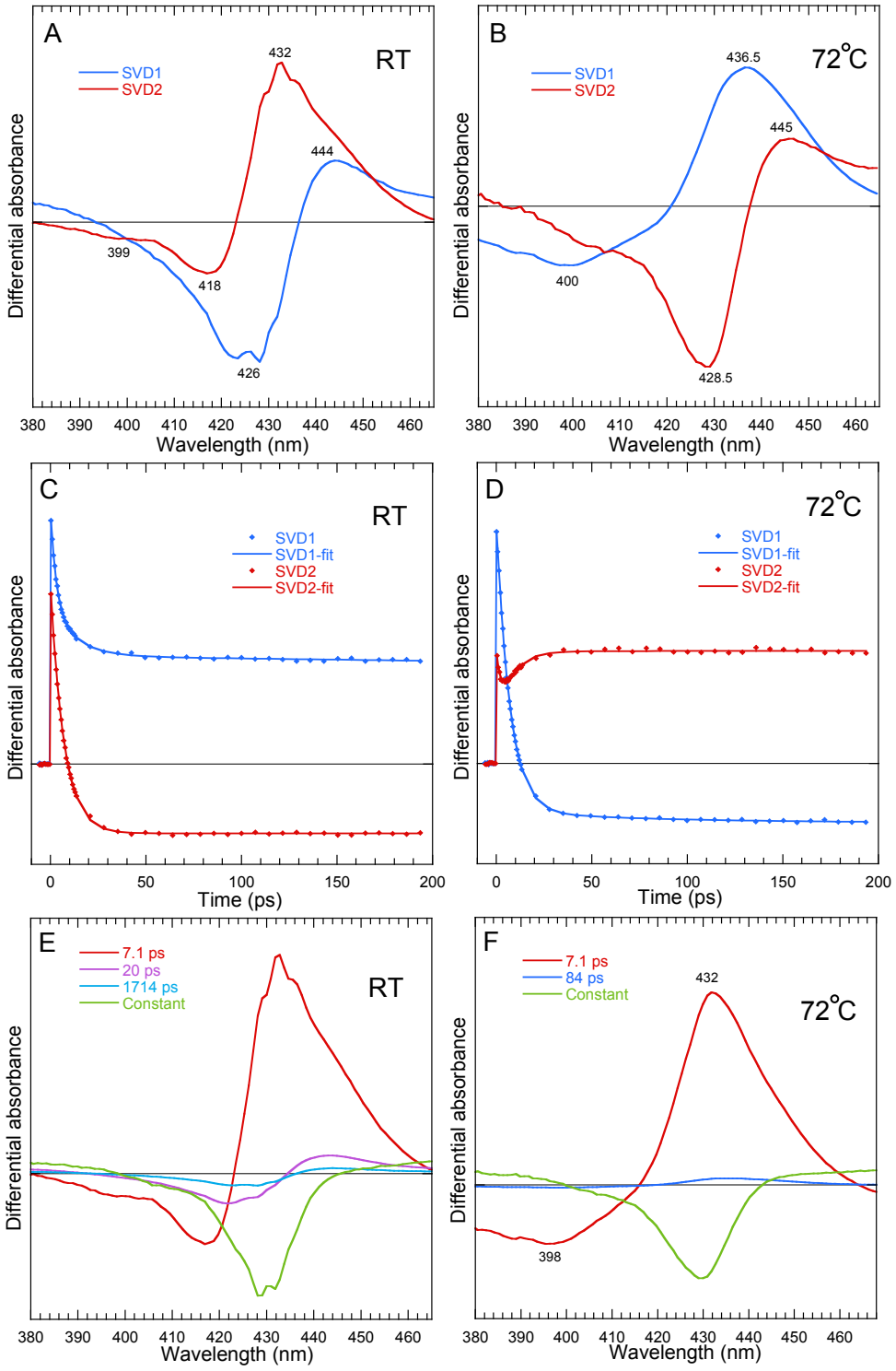

Figure 3.7: Two spectral components obtained after SVD analysis for the raw transient spectra of *Tt*-SONO at A) RT and B) 72°C. Two SVD kinetic components were fitted and displayed at C) RT and D) 72°C. Difference TA spectra associated with each exponential decay components for *Tt*-SONO at E) RT and F) 72°C. In panels A and B the spectrum SVD1 (RT) and SVD2 (72°C) are similar. We must note that SVD components are not numbered after their singular values, not their shapes. Consequently, SVD1 kinetics at 72°C (D) is similar to SVD2 kinetics at RT (c).

of each species. Importantly, the kinetics has other minor component of 84 ps ($A_2 = 0.03$) which exists only at 72°C with a constant value lower than at RT. The fast rebinding of NO ($\sim$ 7.1 ps) appears at both temperatures but with a larger amplitude at 72°C.

Temp.	Component	Singular value	τ_1	A_1	τ_2	A_2	τ_3	A_3	C
			ps		*ps*		*ns*		
RT	SVD1	0.9106	-	-	20	*0.26*	1.7	*0.10*	*0.64*
	SVD2	0.4744	7.1	*0.77*	20	*0.03*	-	0	*0.20*
72°C	SVD1	0.5723	7.1	*0.80*	84	*0.03*	-	-	*0.17*
	SVD2	0.7011	7.1	*0.05*	-	-	-	-	*0.95*

Table 3.2: Fit parameters of SVD1 and SVD2 components for *Tt*-SONO-NO species.

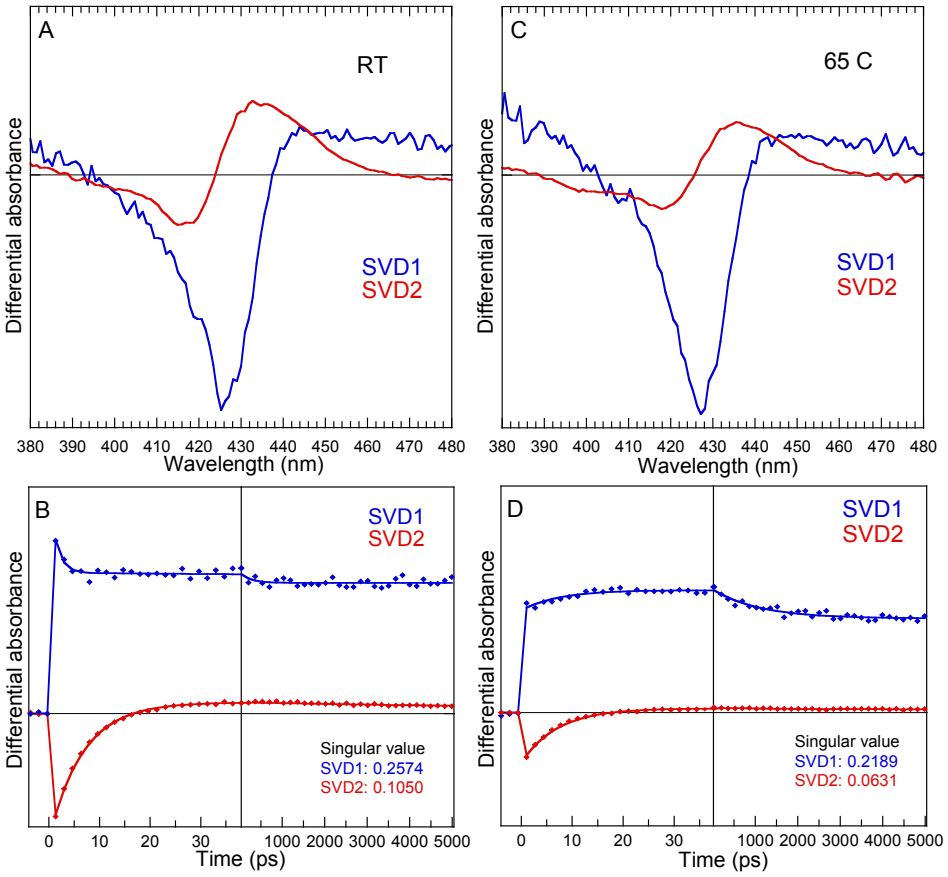

Figure 3.8: The two main SVD spectral and kinetic components after NO dissociation from Tt-SONO up to 5 ns at two temperatures. Panels A and B: 20°C. Panels C and D: 65°C. The corresponding singular values are indicated with the kinetics. SVD1 corresponds to NO geminate rebinding and SVD2 to oxidation after NO dissociation.

At this point we infer that there is another process, parallel with NO recombination. Because there is an increasing induced absorption at 390 nm at 72°C we conclude that heme

oxidation occurred following NO photodissociation. Is this oxidation reversible ? The comparison of steady-state spectra before and after laser measurements (Figure 3.6) shows that re-reduction occurred within 33 ms (period of laser pulses), maybe induced by NO rebinding (but we did not have enough *Tt*-SONO purified sample to investigate a μs-ms time-range). The slight increase at 400 nm in the steady-state spectra after laser measurement cannot be explained by oxidation since there is no decrease at 430 nm, no change in the α/β bands and is too small to account for the amplitude of transient measurement. The hypothesis of oxidation is in line with the appearance of the deep bleaching centered at 429 nm readily assigned to the ferrous unliganded 5c-His heme.

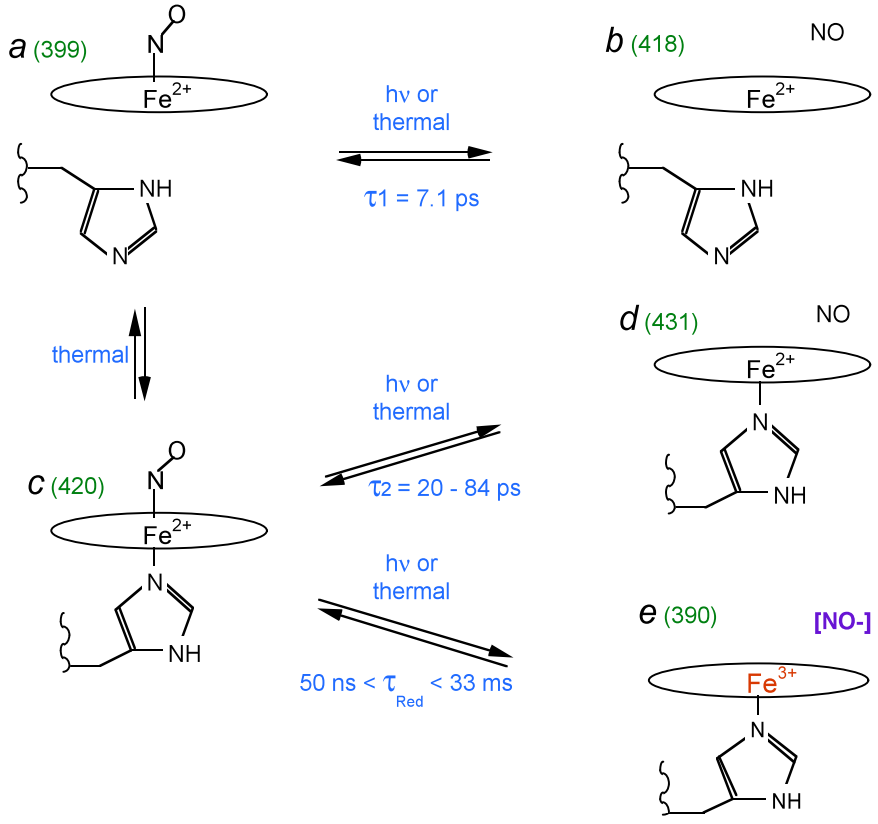

Figure 3.9: Model of the three processes observed after photodissociation of NO from *Tt*-SONO. The maximum of Soret is indicated for each species. The starting species are *b* and *c*, which are in thermal equilibrium. Beside geminate rebinding, photo-oxidation occurred, yielding the ferric species *e*. No other transient species were detected in the 5 ns time-range.

We observed at 5 ns the same spectra than at 200 ps, with only a very slight decay (Figure 3.8), indicating that the ferric species lifetime is much larger, probably >50 ns, but smaller than the period between laser pulses (33 ms). However we did not have enough *Tt*-SONO purified sample to investigate also this time-range. Importantly, the relative amplitude of the first spectral component increased at 65°C (Figure 3.8), indicating that the photo-oxidation

increased with temperature, detrimental to NO geminate rebinding to the ferrous species. The process and interpretation are summarized in Figure 3.9. The reduced species NO^- (nitroxyl anion, also called oxonitrate) can be formed by photochemical reactions[109] and can give rise to peroxynitrite by reacting with O_2[109] which is absent in our experiment. Thus, ferrous nitrosylated *Tt*-SONO can reform from NO^- and Fe^{3+} heme, as it does in ferric hemoglobin[110, 111] and (Cu^{2+})superoxide dismutase[15]. The species NO^- is hypothetical and its identification requires further measurement, such as transient IR. Another possibility (that we did not try) is to trap NO^- with a specific reagent. This property of *Tt*-SONO, not encountered in sGC, suggests that SONO's may have a role in NO or NO derivatives chemistry beyond NO-sensing, in line with the very recently proposed role of the other species *Np*-SONO as a redox switch[106]. It appears that SONO's are not merely NO detectors.

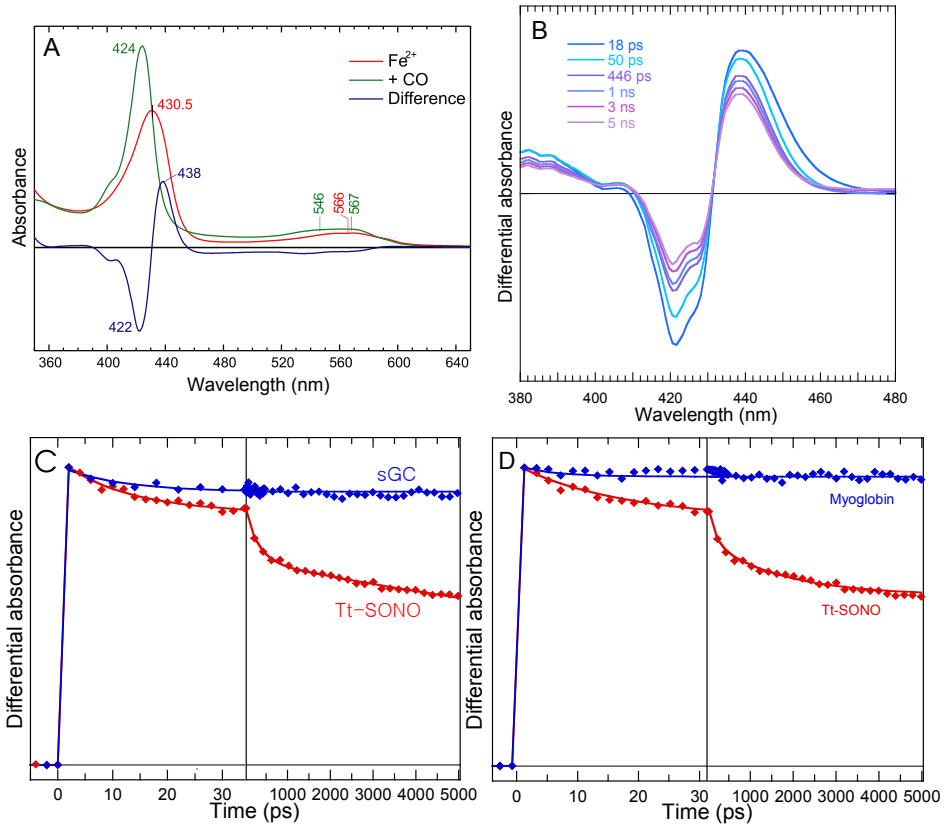

Figure 3.10: A) Electronic absorption and difference spectra of CO-bound *Tt*-SONO at RT, B) Transient spectra at different time delays after photodissociation of CO for ferrous *Tt*-SONO at RT. Normalized kinetics of CO rebinding associated in two time windows upto 5 ns: compared with two proteins, sGC (C) and Myoglobin (D) and at RT. All are ferrous form.

The CO experiment may allow to understand NO data. The raw difference spectra at successive time delays after photolysis of CO are displayed in Figure 3.10-A. The induced absorption and the bleaching decrease until 5 ns due to the formation of the transient 5c-His

from 6c-CO species and the shapes remain without any shift of the maximum and minimum position of peaks. The kinetics associated with geminate rebinding was fitted and contains three decay components (10 ps, 210 ps, and 3.7 ns) and an additional constant term of ∼ 51 % relative amplitude. Unexpectedly, the bleaching discloses a shoulder at ∼ 428 nm (which does not appear in steady-state spectrum but in differential transient one) together with the minimum at 421 nm and there is a slight shift of the isosbestic point at 408-410 nm. This strongly suggests that two rebinding events occurred with different time constants as indicated Table 3.3. The fast process with $\tau_1 = 10$ ps indicates a barrierless process of CO rebinding to the 4c-heme, as measured for the entire sGC in the presence of activators (Table 3.3) but with a larger amplitude in the case of *Tt*-SONO. However the induced absorption of 4c-heme cannot be seen because it overlaps the bleaching of 6c-CO. The component $\tau_2 = 210$ ps is assigned to CO rebinding to 5c-His, CO experiencing a barrier to escape into the solvent as observed in sGC in the presence of BAY and in sensor CooA. *Tt*-SONO is homologous and comprises partially the heme domain in β-subunit of the entire bovine sGC. The geminate rebinding of CO in picosecond time scale does not take place in case of the entire sGC and Mb (Figures 3.10). However, CO geminate rebinding occurs for several bacterial sensors having NO (AXCP), CO (CooA) or O_2 (DOS) as ligands(Table 3.3). Thus, the energy barriers imposed by the side-chains in the heme pocket are as important as the protein tertiary fold for controlling CO dynamics and affinity in diatomic sensors.

Species	τ_1	A_1 %	τ_2	A_2 %	τ_3	A_3 %	Cst %	Reference
	ps		*ps*		*ns*			
Tt-SONO/CO	10	*14*	210	*15*	3.7	*20*	*51*	
AXCP/CO	-	-	218	*4*	1.9	*58*	*38*	Chapter 4
CooA/CO	78	*60*	390	*30*	-	-	*10*	[112]
DosH/CO	-	-	1500	*60*	4.0	*40*	*0*	[107]
sGC/BAY/CO	14	*6*	120	*19*	2.2	*13*	*62*	Chapter 2
sGC/CO	-	-	118	*2*	3.2	*1*	*97*	

Table 3.3: Fit parameters of CO rebinding kinetics of *Tt*-SONO. The kinetic trace in Figure 3.10-B was fitted using the function Parameters obtained with the function $\sum A_i exp(-t/\tau_i)$ + C. The 4 ps component was added to the decay in order to take into account the excited state decay of the heme.

3.2.2 sGC-related bacterial NO-sensor: *Np*-SONO

The SONO domain from *Nostoc punctiforme* shares sequence identity with sGC (39 %). The *Nostoc* is an aquatic form of bacteria that can be found on moist rock, along the bottom of freshwater lakes and springs, and only rarely in marine habitats. *Nostoc* are cyanobacteria[113] and *Nostoc punctiforme* is known to grow preferentially at temperature from ∼15 to ∼ 40°C and it remains mostly 6-coordinate complex with NO[104]. This particular protein displays a thermal equilibrium between 5- and 6-coordination when NO binds to the ferrous heme iron. The particular temperature-dependent equilibrium on the coordination chemistry has been observed for other heme sensor proteins[114, 115]. The interaction of *Np*-SONO with NO will be compared with that of sGC. We present here both spectroscopic and kinetic analysis to characterize the NO rebinding properties for *Np*-SONO.

Because the proportion of 5c- and 6c-NO liganded species depends upon the temperature for *Np*-SONO[104] we will record NO dynamics at different temperatures. Moreover, it is necessary to perform experiments with high signal/noise ratio in order to separate both contributions just as *Tt*-SONO. *Np*-SONO behaves differently than *Tt*-SONO. The Fe(II)-heme of *Np*-SONO remains without oxidation even after several weeks of aerobic storage at 4°C. As purified, the raw protein sample has a Soret maximum at 429 nm and α/β bands at 556 nm which means that the iron is originally in ferrous form for a high proportion. To fully reduce the raw protein we used ascorbate at final concentration 5 mM after adding 10 μL of ascorbate into the sample cell.

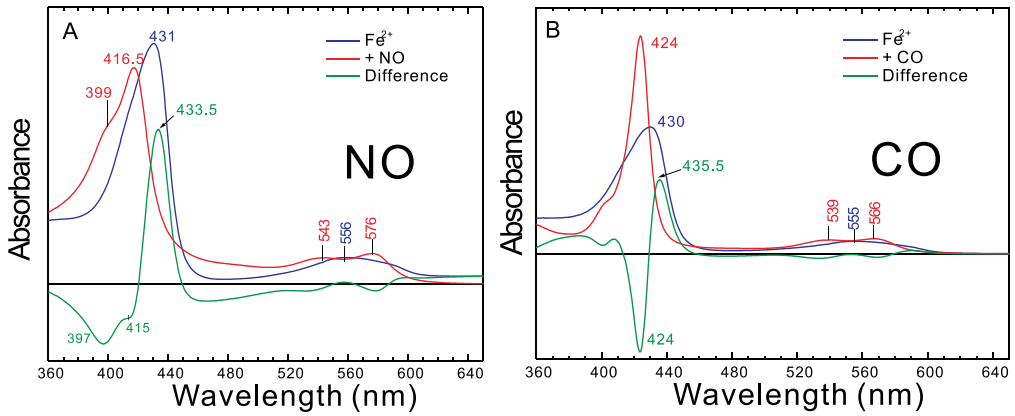

Figure 3.11: Electronic absorption and its difference spectra of *Np*-SONO. A) NO-bound and B) CO bound form at RT. [NO] = 20 μM. [CO] = ∼ 1 mM.

The static absorption and difference spectra in the presence and absence of NO/CO are displayed in Figure 3.11. The spectra of unliganded *Np*-SONO after adding ascorbate exhibit Soret band at 431 nm and broad one α/β band around 556 nm similarly with sGC. Formation

of NO-liganded *Np*-SONO was done by the input of 1 % NO diluted in N_2 directly into the cell through the gas train at a total pressure of 1.3 bar (about 20 μM NO in the aqueous phase). Electronic absorption profiles of *Np*-SONO after the addition of NO resulted in a bathochromic shift of the Soret maximum with the extinction coefficient decreasing at 416.5 nm and a small shoulder at 399 nm (Figure 3.11-A). The characteristic Soret maximum at 416.5 nm is assigned to the 6c-NO heme species and that of 399 nm to the 5c-NO heme species. CO (100 % in gaseous phase) was introduced to the cell to form CO-liganded *Np*-SONO, resulting in a sharp Soret band at 424 nm with an increased extinction coefficient ($\epsilon = 61\ cm^{-1} \cdot mM^{-1}$). A small shoulder at 405 nm appears and its evolution needs to be verified at transient absorption data. Absorption peaks of Soret and α/β band of *Np*-SONO are very similar with those of full-length bovine sGC. In Table 3.4, the spectroscopic parameters of *Np*-SONO are compared with other relevant proteins.

Proteins	**Coordination**	**Soret**	$\epsilon\ (cm^{-1} \cdot mM^{-1})$	**Q-band**
		nm		nm
sGC	5c-His	431.5	108	555
Np-SONO	5c-His	431	39	556
Fe(II)-CO complexes				
sGC	6c-CO	424	159	541/570
Np-SONO	6c-CO	424/405	61/12	546/567
β (1-190) sGC	6c-CO	419	25	541/585
Fe(II)-NO complexes				
sGC	5c-NO	398	91	-
Np-SONO at RT	6c-NO/5c-NO	416.5/399	35/26	543/576
β (1-190) sGC	5c-NO	400	15	-
Ferric protoporphyrin IX	5c-His	390	-	-
Myoglobin	6c-NO	420	144	547/582

Table 3.4: *Np*-SONO and other proteins. Peak positions of UV/Vis spectra of given protein with/without gaseous ligand.

At room temperature, the difference spectrum of NO-bound species shows a maximum located at 433.5 nm and two different characteristic minima are located at 397 and 415 nm. The maximum at 397 nm is due to the minor contribution of 5c-NO species which is seen as a shoulder in spectrum of *Np*-SONO + NO (Figure 3.11-B). Contrary to sGC, the equilibrium changes and the contribution of 6c-NO and 5c-NO species varies as a function of the temperature.

We performed kinetic measurements at different temperatures and the raw difference spectra at successive time delays after NO photolysis disclose very different patterns at three different temperatures (Figure 3.12). At RT the maximum of induced absorption is centered

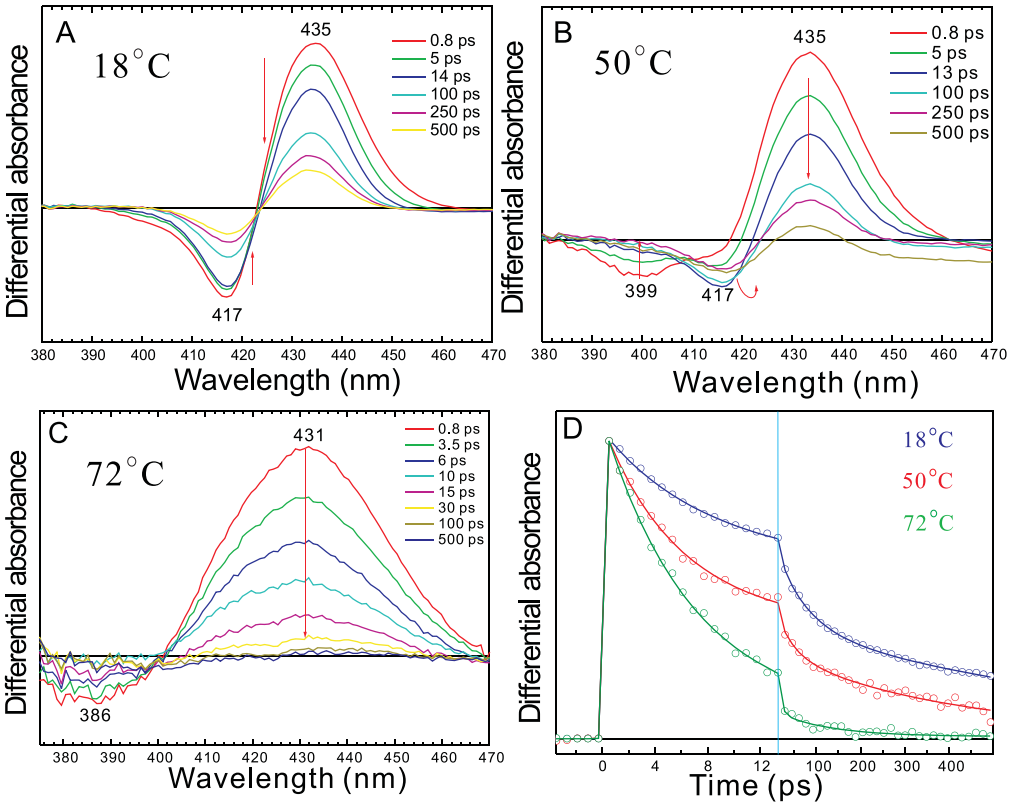

Figure 3.12: A) Transient spectra (raw data) at different time delays after photodissociation of 10 % NO for ferrous *Np*-SONO at RT, B) at 50°C, C) at 72°C, D) Comparison of SVD1 kinetic components for three different temperatures. These are normalized for comparison.

at 435 nm and the minimum of bleaching at 417 nm. A small shift of isosbestic points until 14 ps appears due to the very minor contribution of 5c-NO species but NO rebinding to 5c-His to form 6c-NO represents considerably larger contribution. SVD calculation resulted in two individual spectral components. The first one corresponds to the NO rebinding to the heme and the second one corresponds to the excited state decay. The other components, which have small amplitudes, were excluded. At RT, the main component corresponds to geminate recombination of NO leading to the 6c-His-NO formation identified by the bleaching at 417 nm. But the formation of 5c-NO species brings very small contribution near 400 nm. At 50°C the transient spectra have very different aspect from that at RT: A bleaching recovery in the early time kinetics is detected at 399 nm, which implies that there is rebinding of NO to the 4c-heme to become 5c-NO species. On the other hand, second bleaching that has a slower decay process appears after 30 ps. When the temperature goes up to 72°C unexpectedly it is extremely difficult to detect the transient absorption signal. The induced absorption, whose maximum is located at 431 nm is much broader than at RT and 50°C. The characteristic bleaching at 386 nm appears due to disappearance of 5c-NO bound heme species.

In Figure 3.13-B, the transient raw spectra at two different decay times were compared with the equilibrium difference spectrum and indicate transient 4c-heme. Figure 3.13-A shows that the static absorption spectra after the laser experiments. These spectra clearly indicate that the proportion of 5c-NO increases with temperature.

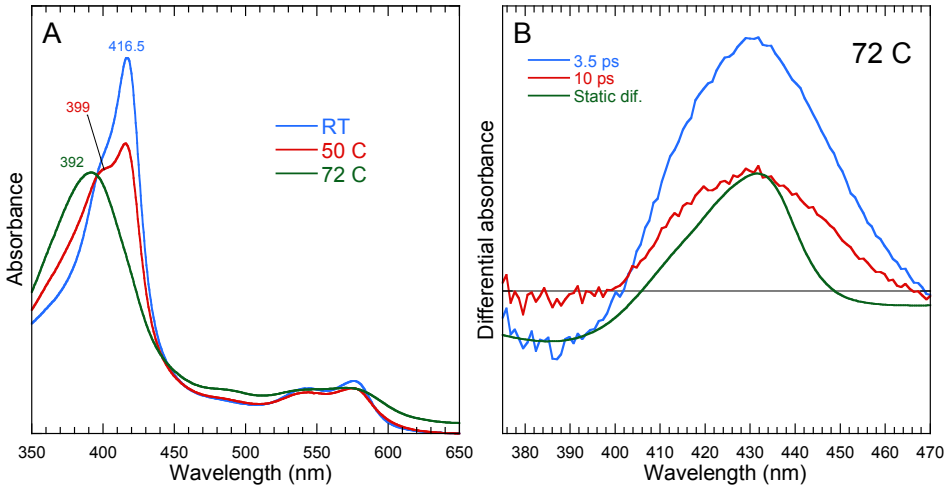

Figure 3.13: A) Static absorption spectra of *Np*-SONO (blue: before laser at RT, red: after laser at 50°C, green: after laser at 72°C), B) Static difference spectrum and transient raw spectra at 3.5 ps and 10 ps. Starting with *Np*-SONO at RT (blue), we performed laser experiment at 50°C for $\sim$ 2 hours. Right after, we measured the equilibrium absorption. Then, we performed same kinetic experiments at 72°C for another 2 hours. After laser experiment, we verified the equilibrium absorption.

SVD calculations were performed for the three temperature measurements. The SVD spectral components and associated kinetics are displayed in Figure 3.14. The kinetic components were fitted and summarized in Table 3.5. The fastest (7 ps) is due to the 5c-NO species formation; the slower (25-65, 250-290 ps) are due to the 6c-NO species formation. For all three temperatures, these time constants were mixed but the relative amplitudes clearly change. Because *Np*-SONO has small contribution of 5c-NO even at RT, 7 ps component was detected. The amplitude of this component increases at higher temperature (50°C; 0.63, 72°C; 0.93). The decay component due to the 6c-NO species formation is major at RT and 50°C but is minor at 72°C. The fast component (7 ps) becomes dominant in case of 72°C at which 5c-NO species is dominant, which the two characteristic peaks appear at 399 and 415 nm (Figure 3.14-C) demonstrate the existence of a mixture at 50°C.

From the spectral and kinetic information of two components, we calculated the decay associated spectra of rebinding of NO to the heme. DAS spectra are gathered in Figure 3.15-A,B,C. Two DAS spectra (25, 250 ps) are dominant because NO rebinding to form 6c-NO is dominant at RT. Due to the small contribution of 5c-NO, we detected DAS spectrum (7 ps)

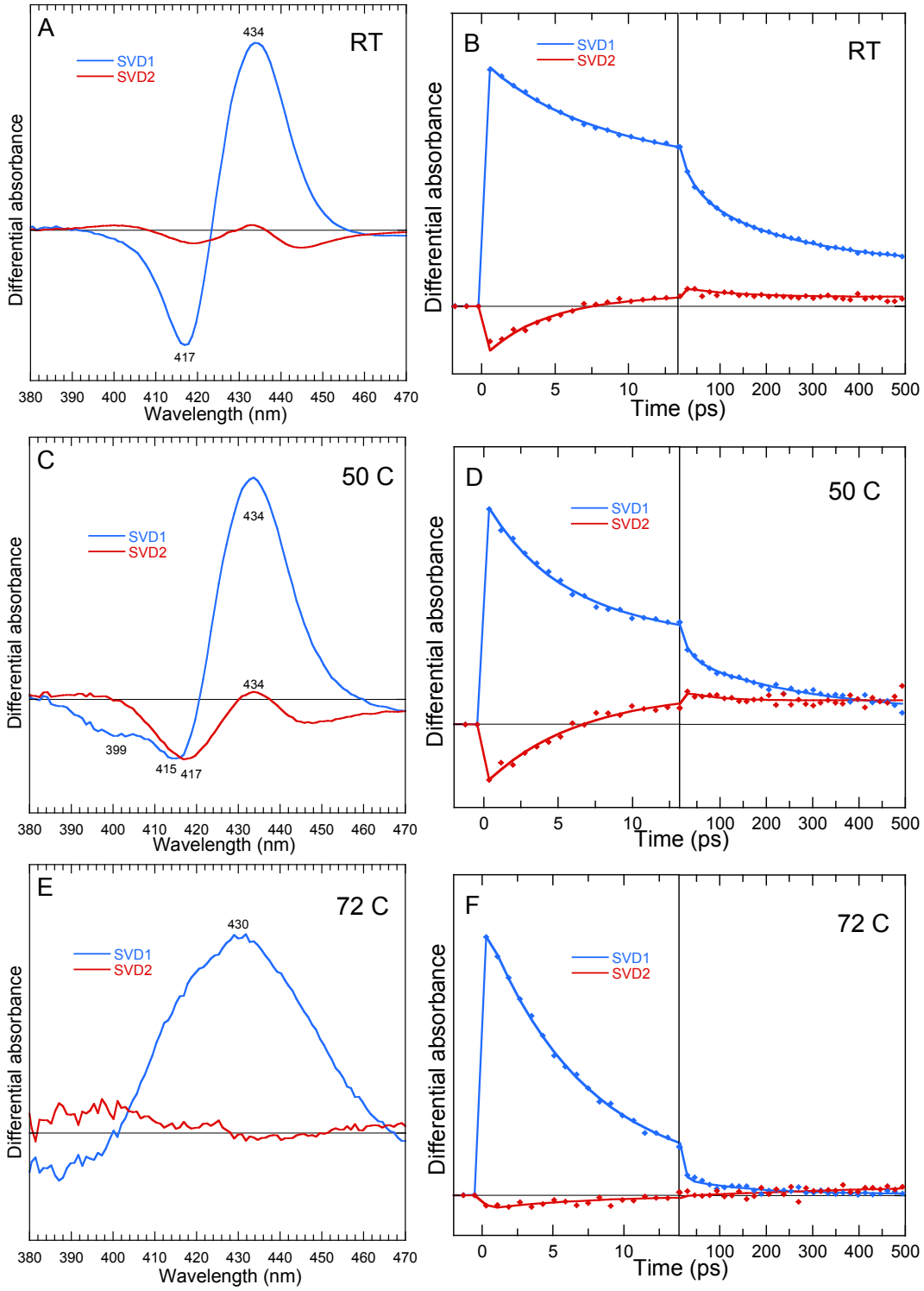

Figure 3.14: SVD analysis for *Np*-SONO. Two SVD spectral components and their corresponding kinetics at RT (A and B), 50°C (C and D), and 72°C (E and F).

as well at RT. The fast component is quite dominant at 50°C together with two minor DAS of slow components (65, 290 ps). The contribution of 5c-NO and 6c-NO are well separated except small bleaching recovery of DAS (65 ps). At 72°C, the dominant DAS of the fast component (7 ps) is similar with the DAS of fast component at 50°C and with the fast 7 ps component of sGC which has the same coordination property than *Np*-SONO at 72°C.

	SVD1 component				SVD2 component		
Species, Temperature	τ_1 (ps) A_1	τ_2 (ps) A_2	τ_3 (ps) A_3	Cst	τ_1 (ps) A_1	τ_2 (ps) A_2	Cst
Np-SONO at RT	7.0 *0.29*	25 *0.20*	250 *0.36*	*0.15*	7.0 *0.60*	250 *0.27*	*0.13*
Np-SONO at 50°C	7.0 *0.63*	65 *0.06*	290 *0.26*	*0.05*	7.0 *0.69*	65 *0.11*	*0.20*
Np-SONO at 72°C	7.0 *0.93*	141 *0.06*	-	*0.01*	7.0 *0.47*	671 *0.01*	*0.52*
sGC at RT	7.5 *0.91*	56 *0.05*	-	*0.04*	-	-	-

Table 3.5: Fit parameters of NO rebinding kinetics to *Np*-SONO displayed in Figure 3.14. The contribution of excited state decay (4.5 ps) was excluded.

Fast component (τ_1 = 7 ps) does not depend upon the temperature, so that there is no energy barrier but slower components (τ_2 = 25-65, 250-290 ps) do depend on the temperature, indicating that there exists an energy barrier for NO rebinding to 5c-His. The fast component τ_1 (= 7 ps) is remarkably equal to values measured in sGC, AXCP, and porphyrin XI Fe (heme alone) and should represent the fastest and thus the limit for NO rebinding without energy barrier from the heme pocket to the 4c-heme due to its planar configuration. Moreover, the affinity of NO towards *Np*-SONO is strongly modulated by small change of temperature[104]. Thus the change of the proportion between the 5c-NO and 6c-NO species and consequent change of NO rebinding governs the NO affinity. These dynamic properties of *Np*-SONO could represent an adaptation to temperature changes. In Figure 3.15-D, the transient spectral contribution decaying with a 7 ps time constant of *Np*-SONO was compared with those of AXCP and sGC. It is clearly different from that of Mb which represents NO rebinding to the 5c-His transient state leading 6c-NO Mb. The photodissociation of NO induces a bleaching at 394 nm for sGC and generates a 4-coordinate transient species whose induced absorption maximum is centered at 425 nm. The transient photodissociated *Np*-SONO species at 72°C does not result in the same spectrum as sGC and AXCP, but results in a broad induced absorption centered at 430 nm.

This band corresponds to a 5c-His heme mixed with that of 4c-heme (see Chapter 2), so that we suggest the very fast rebinding of His to the 4c-heme. This conclusion seems

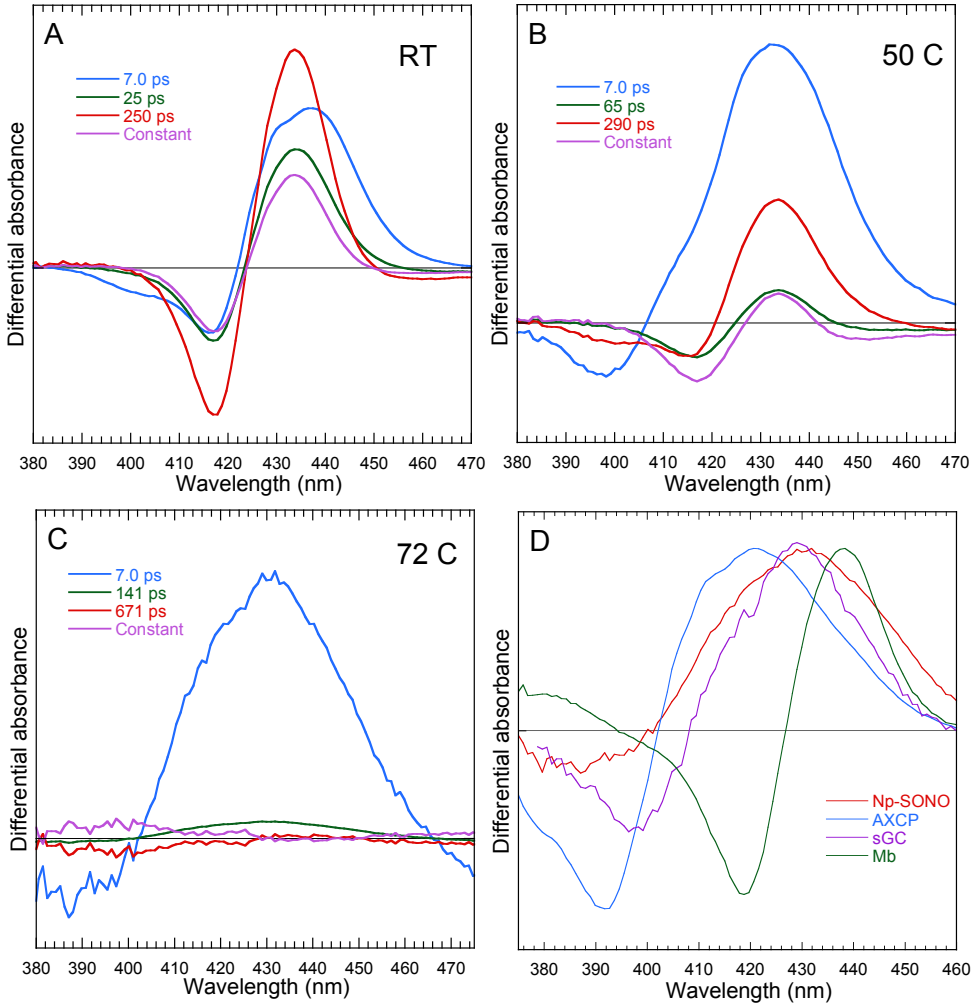

Figure 3.15: DAS spectra at RT (A), 50°C (B), and 72°C (C). D) Comparison of spectral component corresponding to NO geminate rebinding to *Np*-SONO at 72°C and those of relevant proteins.

logical because in the case of *Np*-SONO at 72°C, the trans effect leading to cleavage of Fe-His bond is thermally induced, and not favored by strains within the protein. In the case of sGC, conformational changes follow the Fe-His bond cleavage, which can slow down the His rebinding to $\sim$ 70 ps, but not in the case of heated *Np*-SONO for which the energy barrier to His rebinding should be very low. Another hypothesis could be the photo-reduction of *Np*-SONO, because its spectrum after heating at 72°C is similar to that of oxidized unligated heme[116] and the induced absorption is that of reduced unligated heme. This implies that re-oxidation occurs in 7 ps, at 72°C in the presence of NO, which is much too fast for a process involving NO from the solution. Third hypothesis: the rebinding of NO to a 5c- to form a 6c-NO ferric heme, but this does not result in the same transient spectrum[117] and must be discarded also. Thus, we favor the hypothesis of a very fast His rebinding, but we do not

have a direct proof, which awaits further experimental evidence. We will now compare with a SONO from a third species.

3.2.3 sGC-related bacterial NO-sensor: *Cb*-SONO

It is established that NO is toxic to the bacteria *Clostridium botulinum* though its molecular targets are unknown. *Cb*-SONO is a heme protein sensor that has a femtomolar affinity for NO[27]. The structural modelling study of *Cb*-SONO reveals an important tyrosine residue in the heme pocket that regulates heme-NO coordination. This tyrosine residue in the distal heme pocket participates in hydrogen bonding network with NO and *Cb*-SONO can form a 5c-NO complex[27]. Thus, the femtomolar affinity with NO can be explained by the strong hydrogen bonding character. This property is very unique because SONO proteins from other bacteria and mammalian sGC have a hydrophobic distal pocket. Therefore, we can assume the interaction *Cb*-SONO with NO is different from the previous two SONO proteins and our TA study of *Cb*-SONO aims at comparing the NO dynamics and interaction between them and sGC.

A very interesting property of *Cb*-SONO is its ability to become 5c-NO even at RT, which resembles sGC the most among other SONO proteins. Experimental procedures for both static and TA spectroscopy are same with previous SONO proteins except the temperature range for modulating the coordination states. As purified, the raw protein has a Soret maximum at 408 nm characteristic of ferric heme. Instead of using ascorbate, it was necessary to use dithionite (1 mM) to fully reduce the protein and the Soret drastically moves to 433.5 nm. We initially tried 1 % NO to obtain nitrosylated *Cb*-SONO, but we could not get 100 % 5c-NO species but a mixture of 5c- and 6c-NO species. Therefore, 10 % NO (about 200 μM NO in the aqueous phase) was needed and the Soret moves readily at 400 nm, which indicates the 5c-NO *Cb*-SONO, similarly with sGC (Figure 3.16). Absorption peaks of Soret and α/β band of *Cb*-SONO are also similar with those of our purified bovine sGC. We measured kinetics with the sample thermostated in the range of 4-40°C. The corresponding raw transient spectra of NO rebinding to *Cb*-SONO at three temperatures (4°C, 18°C, 40°C) are displayed in Figure 3.16. Among three temperatures, the behavior at 40°C provides similar spectral shape most similarly with sGC.

The spectral and kinetic SVD1 components as a function of temperature are compared in Figure 3.18-A,B. At 4°C the maximum of induced absorption is centered at 435 nm and the minimum of bleaching at 415 nm. The induced absorption part does not move significantly but the bleaching area changed as the temperature goes up to 40°C. The small contribution of 6c-NO disappears partly at RT and completely at 40°C as shown in Figure 3.18-A. We also

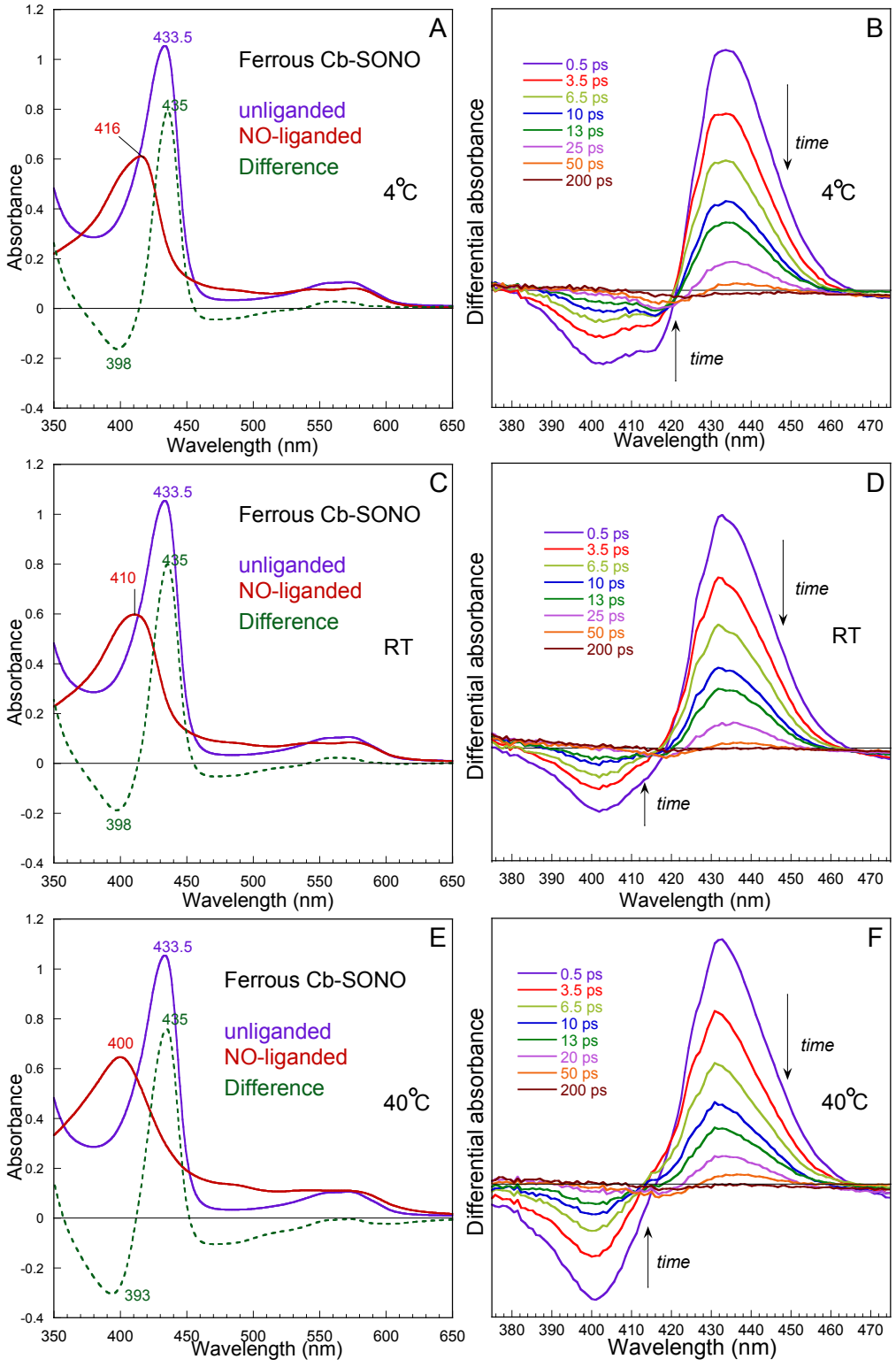

Figure 3.16: UV-visible spectra of *Cb*-SONO in unliganded(violet) and NO-liganded(red) and its difference spectrum and raw transient absorption spectra at different time delays after photodissociation of NO at A) and B) 4°C, C) and D) at RT, E) and F) at 40°C. The spectrum of unliganded species was measured at RT and NO-liganded species at given temperatures. We used 1 % NO at 4°C and RT but 10 % NO was used at 40°C because the solubility of NO decreases with increasing temperature.

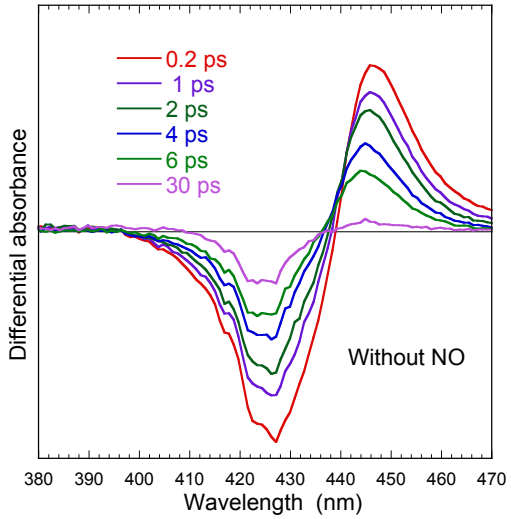

Figure 3.17: Raw TA spectra of ferrous *Cb*-SONO without any ligand at given time delays after photo-excitation.

compared the equilibrium difference spectra with SVD1 spectral component at 40°C. A calculated 4c-heme (absolute spectrum obtained from transient spectrum) was used to calculate its difference with 5c-His which is closer to the SVD1 spectrum as shown in Figure 3.18-A. We recorded the transient spectral evolution (Figure 3.17) for unliganded SONO, which is analogous to sGC[21] and corresponds to the excited state decay whose time constant is 4.4 ps for all three SONO proteins analogous to sGC (4.2 ps). This was done with the purpose of knowing the component due to excited state decay. This contribution was taken into account for fitting the SVD kinetics but was excluded for calculating the relative amplitudes of NO rebinding components from SVD kinetics. Three decay components associated with geminate rebinding of NO to the 5c-His heme were fitted with mono-exponential component and a zero constant as shown in Figure 3.18-B. We obtained 11.2 ps for 4°C and 9.7 ps for 18°C respectively. Remarkably we could obtain dominant 8.5 ps time constant for NO geminate rebinding at 40°C.

SVD calculation resulted in two representative spectral components at 40°C (Figure 3.18-C). SVD1 corresponds to the NO rebinding to become 5c-NO *Cb*-SONO species and SVD2 to the His rebinding to *Cb*-SONO as we discussed for sGC in Chapter 2. We fitted the SVD kinetics as displayed in Table 3.6. The τ_1 (8.5 ps) corresponds to the fast rebinding of NO to 4-coordinate heme and τ_2 is assigned to the histidine rebinding based on the similarity of spectrum with SVD2 component already discussed for sGC (see also the case of cytochrome c' in Chapter 4). The His rebinding component ($\tau_2 = 54$ ps) of *Cb*-SONO is faster than that of sGC (62 ps) but measured at 20°C. Among SONO proteins, we can say that *Cb*-SONO has the most likeness with sGC because of its spectral and kinetic properties. Amazing resemblance to sGC can be found if we compare the spectral SVD1 component with that of sGC (Figure 3.17-A) which is clearly distinguishable from that of Mb. The peak for the

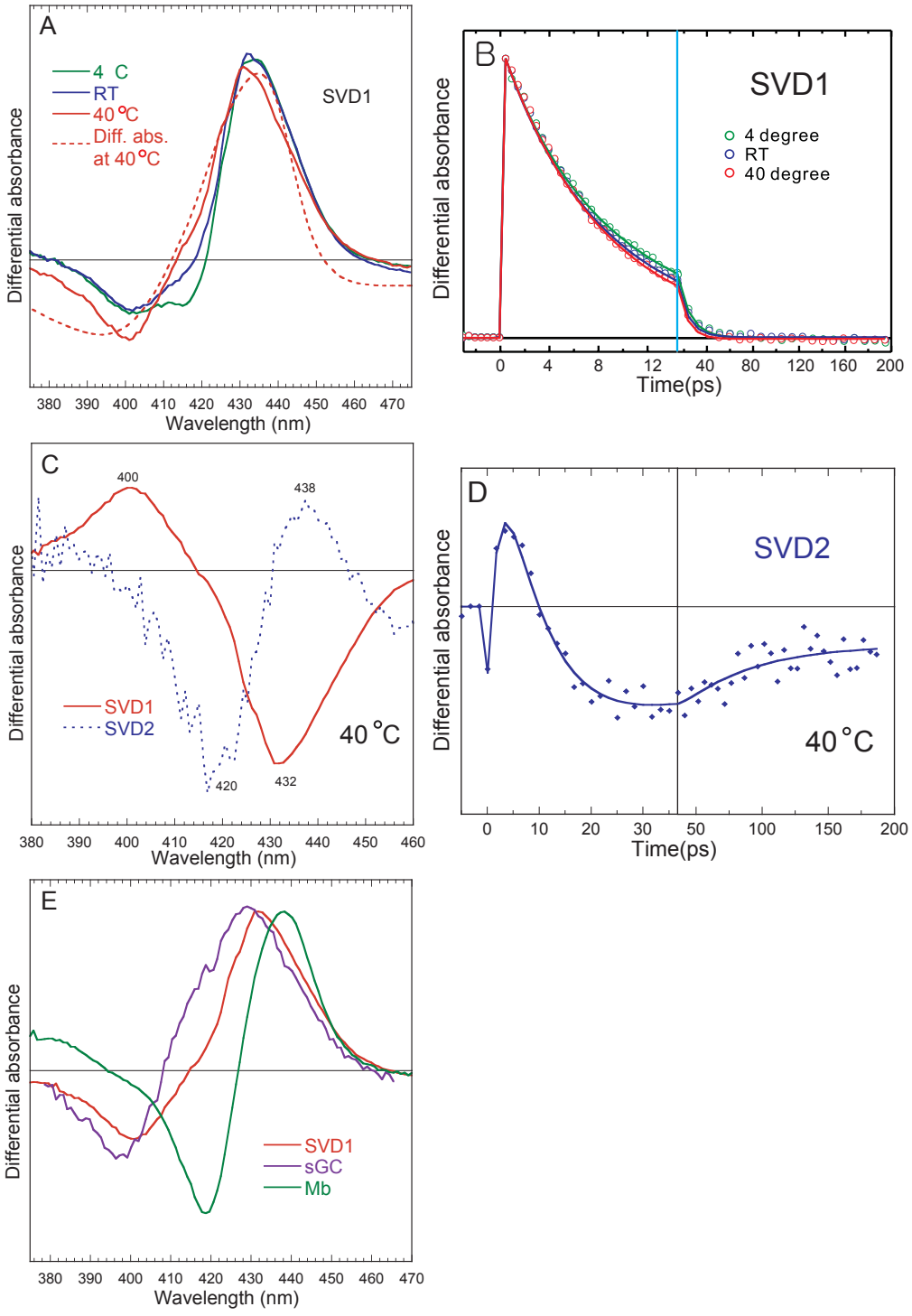

Figure 3.18: A) Comparison of SVD1 A) spectral and B) kinetic components of *Cb*-SONO for three different temperatures. Static difference absorption spectra (5c-His minus 5c-NO and 5c-His minus 4c-heme) were included and all the traces were normalized for comparison. C) Two spectral SVD component at 40°C. D) SVD kinetic trace with fitted curve at 40°C. E) Transient spectral component from SVD analysis associated with the kinetics of Figure 3.16-F is compared with that of sGC and Mb.

minimum of bleaching for *Cb*-SONO (397 nm) is also located at the near wavelength of sGC (395 nm) and clearly distinguishable from Mb (418 nm). Furthermore, 5c-NO is $\sim$ 96 % of the population at 40°C with NO rebinding similar with sGC.

Our results show that the temperature range for modulating the ratio 5c-NO / 6c-NO in *Cb*-SONO is lower than for *Tt*- and *Np*-SONO and that at 40°C *Cb*-SONO behaves like sGC, with a 97 % NO rebinding to the 4c-heme. We did not observed a redox evolution like in *Tt*-SONO or dynamics interpreted as very fast proximal histidine rebinding, like in *Np*-SONO. One must notice that *Cb* is a heat resistant bacteria and the similarity of NO dynamics at RT and 40°C is in line with this property. *Cb*-SONO has 15 % amino-acid identity with sGC β1-subunit, a value similar to that of *Tt*-SONO, 17 %, and yet, their respective interaction with NO appears very different, as measured by NO dynamics after NO dissociation.

	SVD1 component			SVD2 component		
Species, Temperature	τ_1 (ps) A_1	τ_2 (ps) A_2	Cst	τ_1 (ps) A_1	τ_2 (ps) A_2	Cst
Cb-SONO at 40°C	8.5 *0.97*	- -	*0.03*	8.5 *0.74*	54 *0.19*	*0.07*

Table 3.6: Fit parameters of NO rebinding kinetics of *Cb*-SONO at 40°C. 4.4 ps (excited state decay) was excluded.

3.2.4 Discussion: the reactivity of bacterial NO-sensors

From our analyses for three different prokaryotic SONO proteins, we can conclude that: 1) the fast component of rebinding (7.0 ps) of NO is due to the 4c-heme like in sGC. This shows the very high reactivity of Fe^{2+} when it is only 4-coordinate in a planar configuration. This property is used in the functioning of NO-sensors. 2) The affinity of NO towards SONOs is strongly modulated by small temperature change by a modification of the proportion between the 5c-NO and 6c-NO species. In other words, the cleavage of Fe^{2+}-His bond in presence of NO is modulated by temperature. Figure 3.19 describes the temperature-dependent NO activation mechanism, compared to CO which yields only 6c-CO species. The temperature dependence of the equilibrium varies for the different SONO species. NO-sensors from the thermophilic bacteria, having a wide range of affinity for NO, have developed and original strategy for adaptation to varying NO concentrations at different temperatures. The sensitivity of the equilibrium P-NO $\leftrightarrows$ P + NO allows only to detect a narrow range of NO concentration. In these sensors, the equilibrium His-Fe-NO $\leftrightarrows$ His + Fe-NO depends upon the temperature and considerably amplifies the sensitivity towards NO.

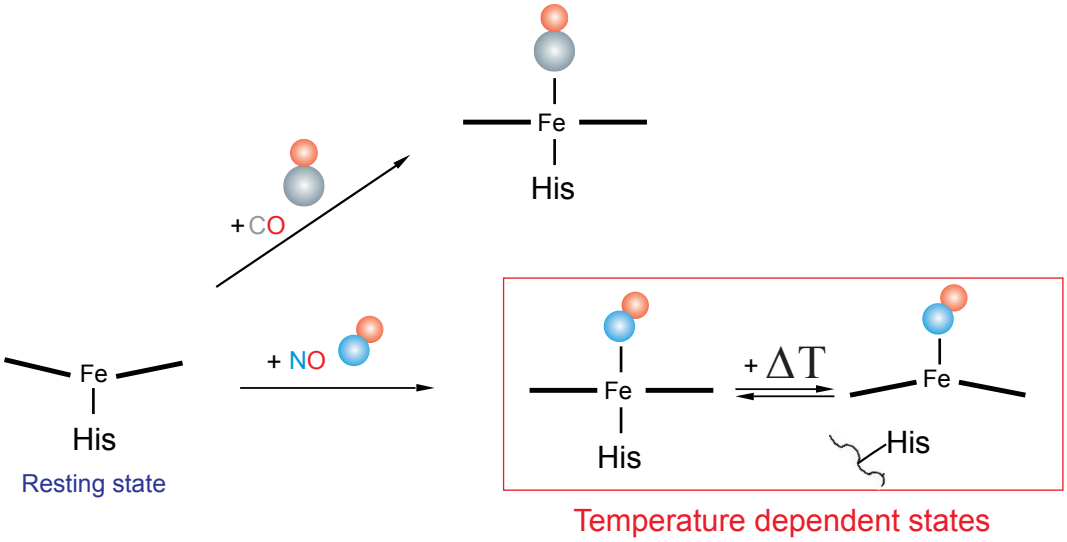

Figure 3.19: CO and NO activation mechanims of bacterial SONOS. The temperature dependence of the equilibrium in case of NO varies for the different SONO species.

We must notice that the bacteria *Thermoaneaerobacter tencongensis* and *Nostoc punctiforme* have their optimum of growth at high and medium temperature respectively; so, we suggest that these dynamic properties of two SONOs represent an adaptation to temperature changes. We may hypothesize that SONO proteins transfer information to trigger or to block an adaptive mechanism. Contrary to Mb, SONO present a very sensitive energy barrier in the heme pocket, which regulates NO release into the solution. This barrier could be either steric or electrostatic, and probably plays a role in the function of this protein because these heme domains of *Cb*-SONO and *Np*-SONO seem coupled to MACP and HK-HATPase domains, respectively (Figure 3.20). SONO proteins have been discovered very recently, and the identification by mutagenesis of the amino-acid side-chains responsible for the energy barrier has yet to be performed.

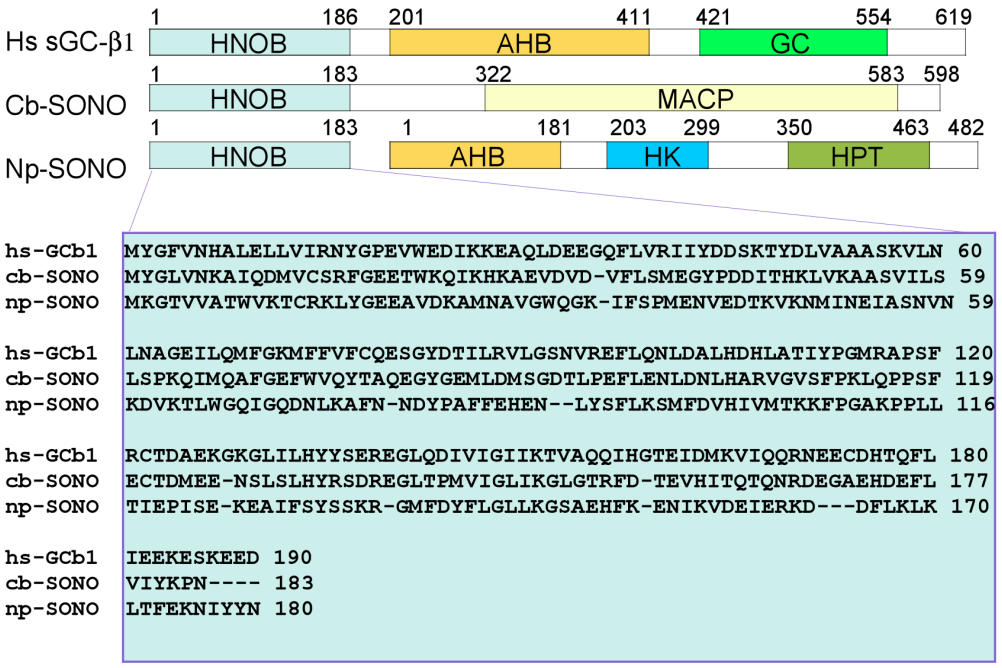

Figure 3.20: Comparison of functional domains in sGC and SONO from *Clostridium botulinum* and *Nostoc punctiform*. HNOB: Heme Nitric Oxide Binding domain. AHB: Associated Heme Binding domain. GC: Guanylate Cyclase domain. MACP: Methyl-Accepting Chemotaxis Protein domain. HK: Histidine Kinase domain. HPT: Histidine Phospho-Transferase domain. The domains colored in light blue are studied in the present Chapter. The SONO proteins from *Np* species do not contain the AHB, HK and HPT domains but their genes are adjacent to these additional functional domains[27, 118]. Source of sequences is obtained from NCBI protein data base.

3.3 Interaction of bacterial NO-sensors with sGC activators

3.3.1 *Np*-SONO with CO in the presence of sGC effectors

Since *Np*-SONO is homologous with the heme domain of β-subunit of the whole sGC, we wonder whether sGC activators exert any effect on *Np*-SONO. Because YC-1 and BAY activate sGC in synergy with CO, we probed the CO dynamics in *Np*-SONO in the presence of these effectors. In the same way for sGC, we incubated overnight YC-1 and BAY 41-2272 with the protein in the presence of CO. We measured the static absorption spectra for each species but we could not find any significant spectral shift. The spectra were the same after the injection of effectors as shown in Figure 3.21. For BAY compound we put CO first and incubated BAY after but there was no change in Soret and α/β bands. For YC-1, we first incubated the sample with effector and then injected CO into the sample. We found a small

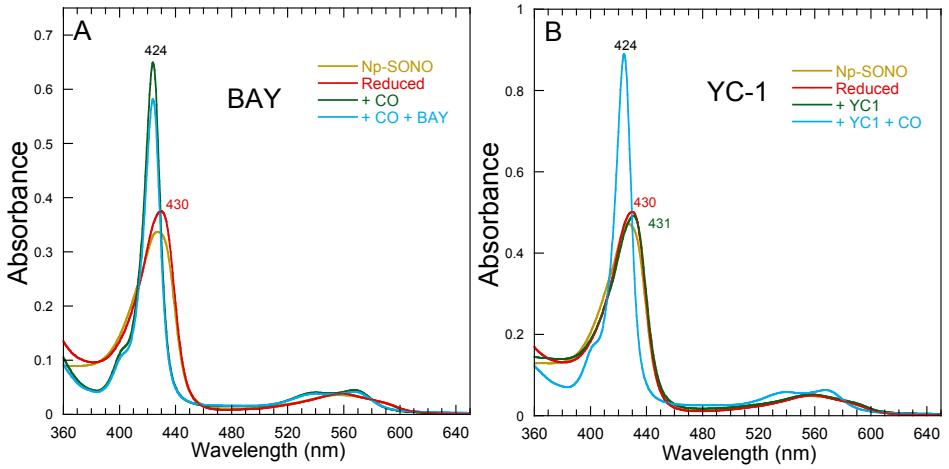

Figure 3.21: Equilibrium absorption spectra in the absence and presence of A) BAY and B) YC-1 for CO bound *Np*-SONO.

shift (431 nm) at Soret band but α/β bands did not change in presence of the effector. Right after, we performed TA measurements for *Np*-SONO at RT and 50°C with the same sample.

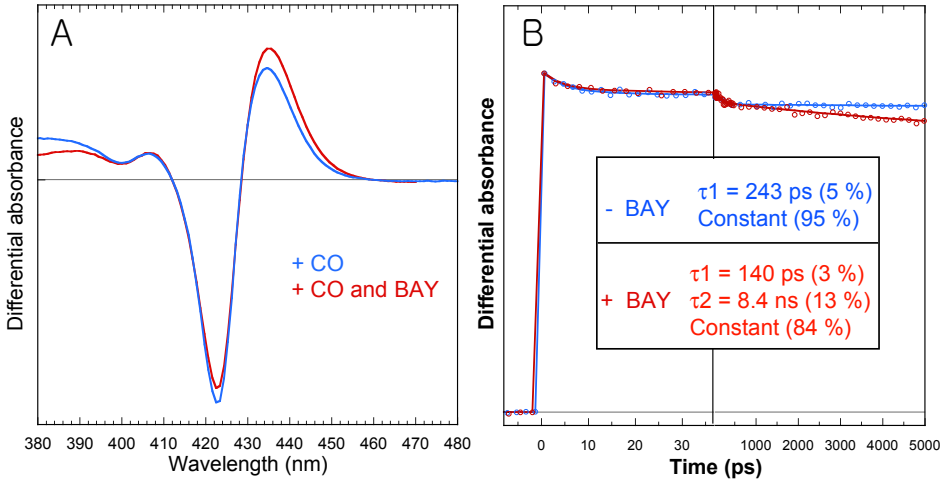

Figure 3.22: Comparison of A) spectral and B) kinetic SVD1 component of *Np*-SONO/CO in the absence and presence of BAY 41-2272 at RT.

Small spectral shift at 435 nm was shown for SVD1 component of *Np*-SONO in the presence of BAY as shown in Figure 3.22-A. This corresponds to geminate rebinding of CO to the *Np*-SONO species as shown by the minimum of bleaching at 423 nm together with the maximum of the induced absorption at 435 nm. A faster decay is apparent in the nanosecond time-range and the SVD1 kinetic was fitted (Figure 3.22) with two decay constants (140 ps and 8.4 ns) for CO rebinding to *Np*-SONO in the presence of BAY. The effect is smaller than for sGC but clearly BAY compound has an effect on the *Np*-SONO heme domain homologous

to sGC with the same measurements at higher temperature for YC-1 and BAY compounds. Figure 3.23 compares of the fitted kinetic traces in the absence (blue) and presence (red) of the two effectors at 50°C. Kinetics was fitted either to a bi-exponential function or to a tri-exponential function (Table 3.7).

Species	T(°C)	τ_1	A_1 %	τ_2	A_2 %	τ_3	A_3 %	Cst %
		ps		*ps*		*ns*		
Np-SONO/CO	20	-	-	243	*5*	-	-	*95*
Np-SONO/CO/BAY	20	-	-	140	*3*	8.4	*13*	*84*
Np-SONO/CO/YC-1	50	-	-	8	*6*	1.6	*9*	*85*
Np-SONO/CO/BAY	50	10	*6*	79	*1*	1.1	*9*	*84*

Table 3.7: Fit parameters of CO rebinding kinetics of *Np*-SONO with and without effectors. The kinetic traces in Figure 3.23 were fitted using the function Parameters obtained with the function $\sum A_i exp(-t/\tau_i)$ + C. The 4 ps component was added to the decay in order to take into account the excited state decay of the heme.

Upon heating from 20 to 50°C, a fast rebinding component appeared (10 ps, 6 %) that we assign to the increased population of 5c-CO heme, as we have observed in the case of NO, but much less pronounced for CO due to its lower ability to promote a trans effect. We conclude that BAY activator binds to *Np*-SONO to a site homologous to that it occupies in sGC.

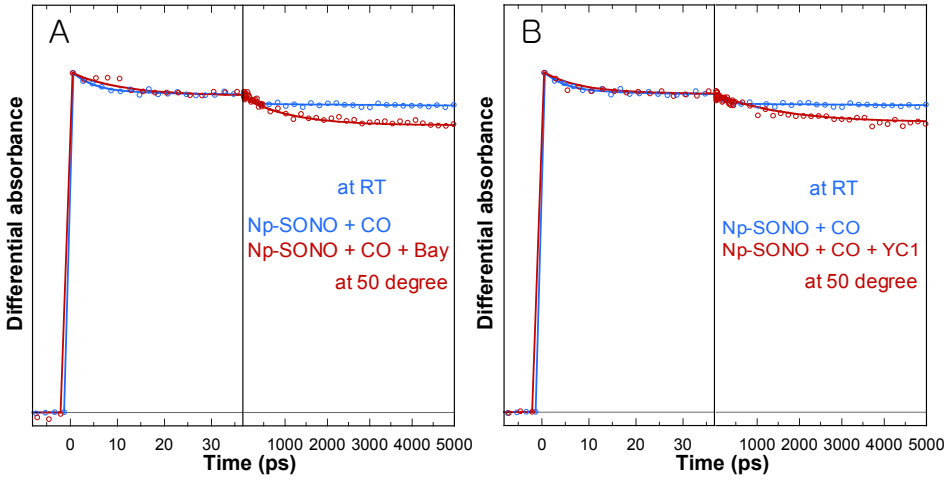

Figure 3.23: Comparison of SVD1 kinetic trace of *Np*-SONO in the absence and presence of A) YC-1 and B) BAY 41-2272 at 50°C. Kinetic data for CO only was done at RT.

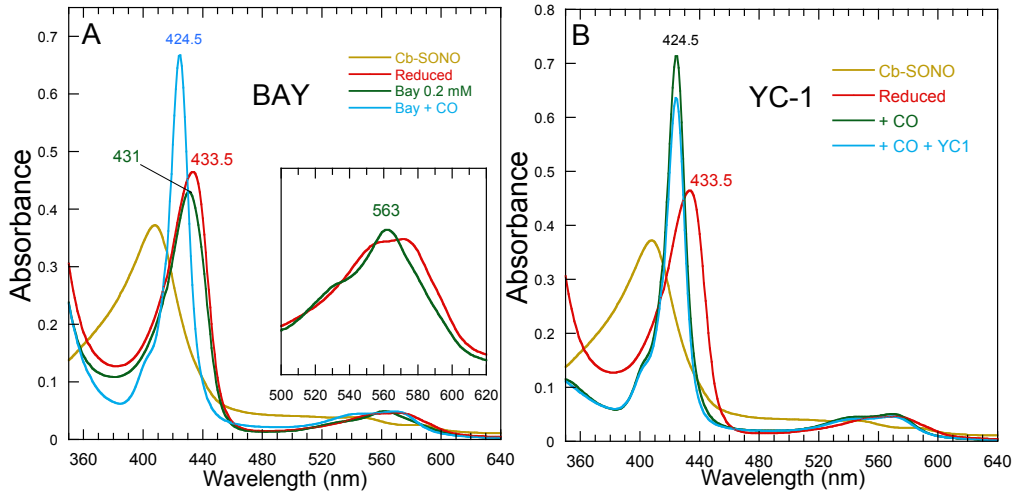

Figure 3.24: A) UV-visible spectra of *Cb*-SONO in ferric (yellow), reduced (red), reduced in the presence of BAY (green), and CO-liganded in the presence of BAY (blue). B) YC-1 in ferric (yellow), reduced (red), CO-liganded (green), and CO-liganded in the presence of YC-1 (blue).

3.3.2 *Cb*-SONO with CO in the presence of sGC effectors

In the same way as for *Np*-SONO and sGC, we incubated YC-1 and BAY 41-2272 with *Cb*-SONO in the presence of CO during one day. The static absorption spectra for each species can be found in Figure 3.24. Whatever was introduced first the effector (YC-1 or BAY 41-2272) and CO, the spectra were the same in both cases. Contrary to other SONO proteins, we observed a shift of Soret maximum at 431 nm for the reduced species after the addition of BAY compound together with a change of shape of the Q-band with a maximum at 563 nm (inset). However, the Soret maximum for final CO-bound *Cb*-SONO with BAY has the same wavelength as in absence of BAY. Right after the measurements of equilibrium absorption spectra, we performed TA spectroscopy for *Cb*-SONO. We incubated effector after putting CO for YC-1 case to verify the difference. As shown in Figure 3.24-B, there is no change in Soret after injection of YC-1 except the decrease due to the dilution of YC-1 solution.

TA spectra at given time delays are displayed for the CO rebinding to the *Cb*-SONO in the presence of YC-1 in Figure 3.25-A. We do not observe a shift for the bleaching and induced absorption as it was seen for sGC in the presence of effectors. The bleaching of the ground state at 423 nm decay continuously until 5 ns parallel with the decay of the induced absorption at 437 nm. Comparing of fitted SVD1 kinetic components corresponding to the CO rebinding in the presence and absence of YC-1 are shown in Figure 3.25-B. The CO nanosecond geminate rebinding to *Cb*-SONO is clearly faster in the presence of YC-1 and this is very similar with sGC (Chapter 2) and *Np*-SONO. This change of kinetic decay induced

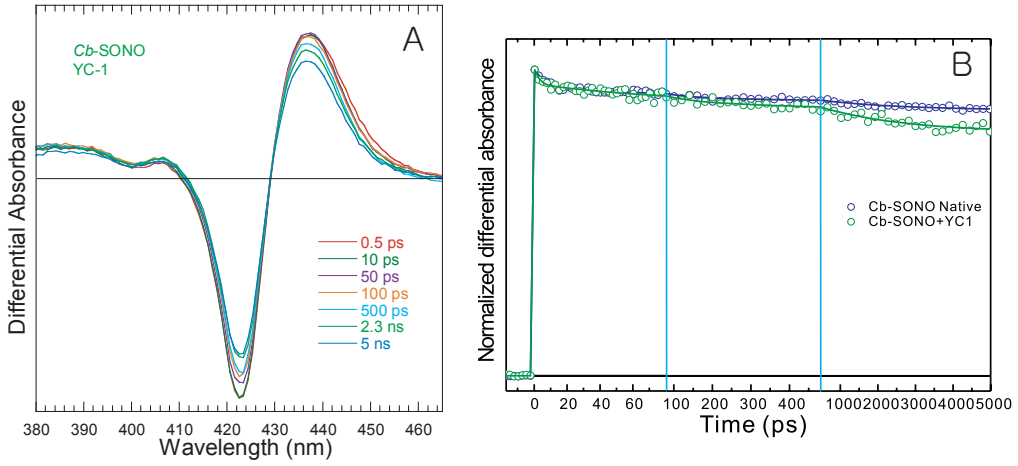

Figure 3.25: A) Raw transient spectra of CO-bound *Cb*-SONO with YC-1, B) Comparison of SVD1 kinetic components in the absence and presence of YC-1.

by YC-1 effector is even more pronounced in the presence of the other effector BAY 41-2272. Figure 3.26-A shows the raw transient spectra at given time delays. Slight shift of induced bleaching appears in the presence of BAY and the more pronounced decay of two peaks is observed (Figure 3.26).

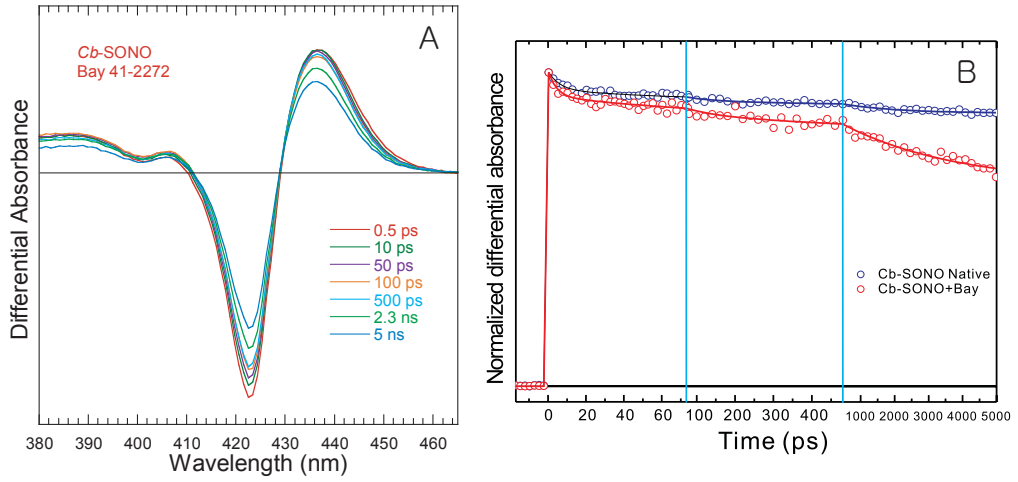

Figure 3.26: A) Raw TA spectra of CO-bound *Cb*-SONO with BAY 41-2272 at given time delays, B) Comparison of SVD1 kinetic components in the absence and presence of BAY 41-2272.

Because the nanosecond phase of CO rebinding is prolonged beyond 5 ns, we performed TA measurements from 5 ns to 0.1 s with electronically delayed lasers (IBPC) with the same sample. Figure 3.27 shows spectral and kinetic comparison for *Cb*-SONO in the presence and absence of BAY compound. For both figures, we can notice the difference in amplitudes at the very beginning, which corresponds exactly to that measured on the ps-ns time range.

We then compare the spectra at 15 ns in the presence and absence of BAY (Figure 3.27-A). Both are identical to the spectrum recorded a 5 ns so that the spectral difference due to the binding of BAY is only detected at early time (Figure 3.26) showing that the same species are involved after 15 ns. Thus, the difference in amplitude detected from 5 ns to 0.1 s is only due to increased CO rebinding before 5 ns.

This is a direct proof that the action of BAY is to increase the energy barrier to CO escape in the nanosecond time scale, so that a structural change can be inferred. To illustrate this crucial result, the two kinetic measurements were merged and displayed (Figure 3.27-C), showing broad dynamic range from 1 ps to 0.1s time scale.

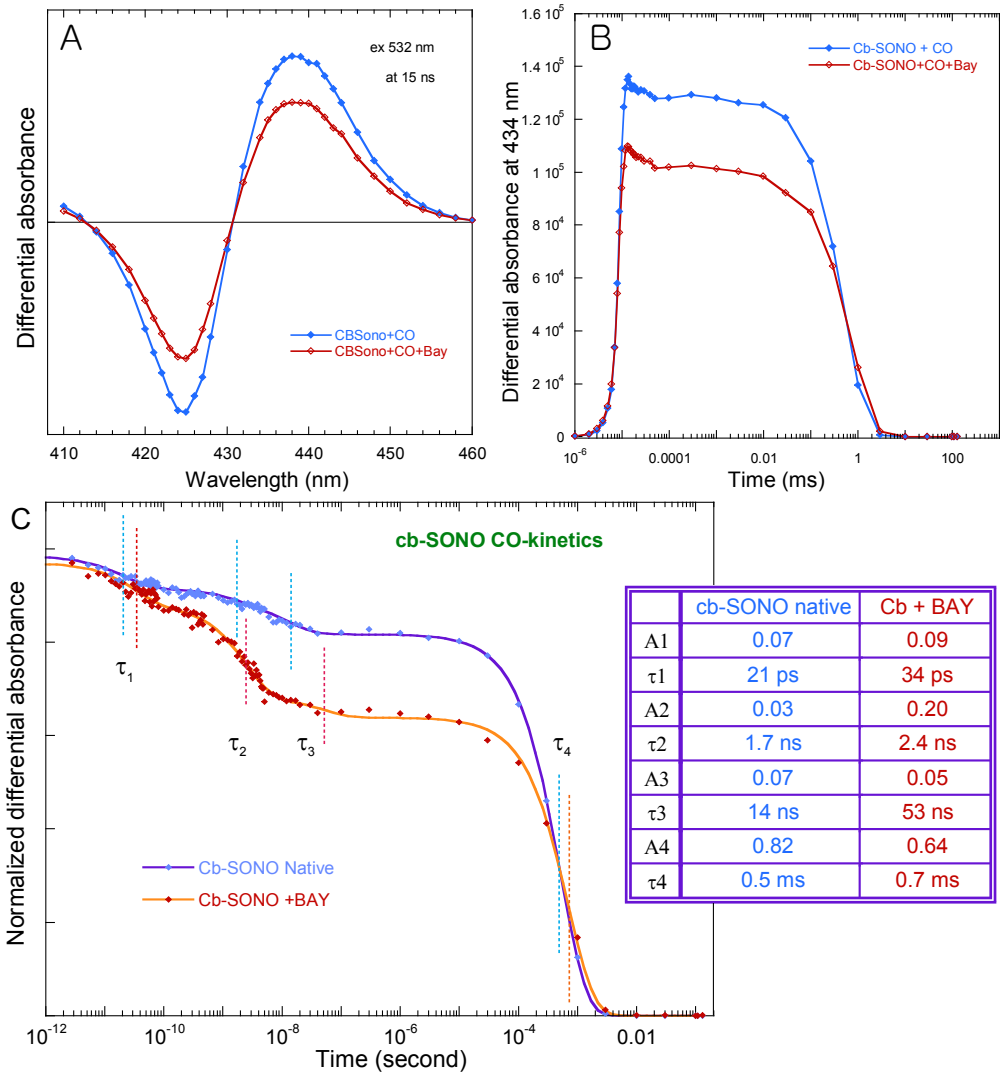

Figure 3.27: Broad range kinetics for *Cb*-SONO. A) Comparison of difference spectra at 15 ns in presence and absence of the effector BAY. The samples are the same as those used for ps-ns measurements and are identical except the presence of BAY. Spectra were recorded point by point. B) Corresponding kinetics from 5 ns to 0.1 s for CO recombination to *Cb*-SONO. C) Reconstructed kinetics of CO recombination on eleven orders of magnitude

3.3.3 Discussion: SONO versus sGC; Where do the effectors bind?

Which domain of sGC harbours the binding site of the activator? The comparison of CO geminate rebinding among the entire sGC, its isolated heme domain part, and SONO's will bring the answer. Various results have been reported about this important issue. It was reported that YC-1 has its enhanced activation effect by the interaction with the catalytic cyclase domain of sGC[35]. Stasch and coworkers reported that YC-1 binds to the N-terminal domain of α1-subunit of sGC[36]. More recently, Monfort and coworkers showed that YC-1 also binds to the two-thirds of rat sGC (1-471 α1 plus N-terminal His-tag, 1-400 β1)[62]. Raman studies suggested that the binding of YC-1 to the heme pocket of entire sGC[119]. On the other hand, Marletta group introduced two partial β1-subunits (1-194, 1-217) of rat sGC to compare with the entire sGC and concluded that there is no interaction between β1-subunit of sGC and YC-1 (or BAY) compound using EPR and Raman methods[120]. Thus, these reports are contradictory.

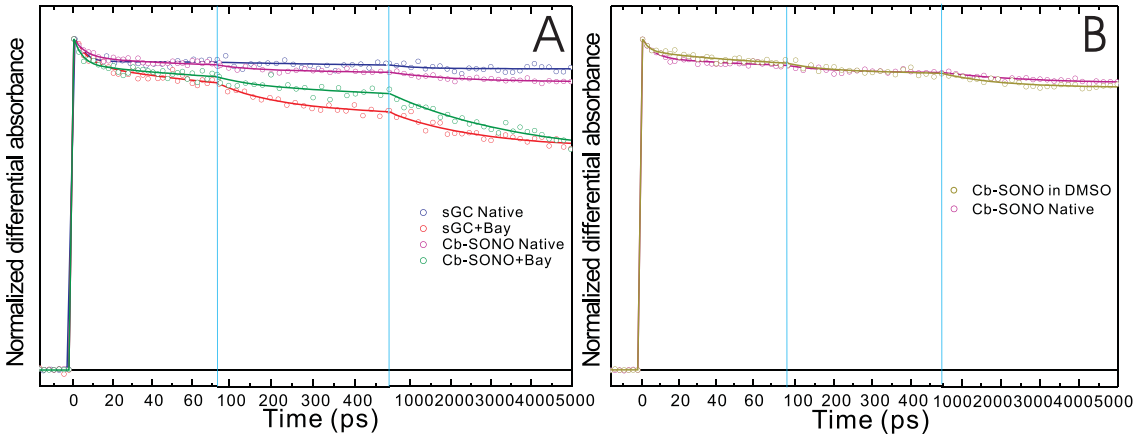

Figure 3.28: A) Comparison of SVD1 kinetics of CO dynamics in *Cb*-SONO with sGC in the absence and presence of BAY 41-2272 recorded in two time windows, B) SVD1 kinetics of CO dynamics for *Cb*-SONO in the presence of DMSO only (i.e. without activators), compared with that in absence of DMSO.

Figure 3.28-A shows the kinetics of CO in the absence and presence of BAY compound for sGC and *Cb*-SONO. CO geminate rebinding in the presence of BAY compound is changed exactly in the same manner for both entire sGC and *Cb*-SONO. Because *Cb*-SONO and sGC β1 subunit are homologous, this is a direct proof that BAY compound binds and exerts its structural effect on the heme domain. Therefore, our results strongly supports that BAY compound binds to β-subunit, more precisely on the restricted region of 1-190 of the sGC heme domain. We performed an extra TA measurement to verify if there is any effect only from the solvent (DMSO) used to dissolve BAY compound ($\sim$ 250 μM of BAY, 3 % of DMSO).

Clearly, there was no difference induced by DMSO alone on the CO dynamics and thus on *Cb*-SONO conformation, as shown in Figure 3.28-B. We observed CO geminate rebinding phase in both sGC and *Cb*-SONO with similar amplitude at 5 ns. BAY compound is involved in structural change both in *Cb*-SONO and sGC, and consequently there is a higher energy barrier for CO escape does exist in both proteins in the presence of BAY compound.

3.4 The isolated heme domain from sGC subunit: β1(1-190)

As discussed in the previous chapter, the exact binding site of YC-1 and BAY compounds in sGC is not known yet. To elucidate this issue it is necessary to interact these activators with a fractional portion of the full-length sGC and it should contain minimum numbers of amino acid residues to retain the original sGC structure. Since we know from X-ray data that bacterial SONO's provide a functional heme domain folding[27], the minimum truncated sGC should correspond to the same domain as SONO's. Such sGC heme domain β1(1-190) constituted of first 190 amino acid residues has been genetically engineered from the human sGC sequence and overexpressed in *E. Coli* by P. Nioche (INSERM S747). β1 (1-190) subunit of sGC is overexpressed as a pure heme domain protein, reducing the possible binding region of the effectors. A lot of biochemical studies were performed with the entire α1β1 sGC coordinating NO and CO in the presence of YC-1 and BAY compounds but no studies were carried out with the heme domain only. We thus evaluated the effects of BAY 41-2272 and YC-1 on CO dynamics in the isolated heme domain β1(1-190) of sGC with the aim of comparing with the entire sGC and with the homologous domains from *Tt*- and *Np*-SONO's. Firstly, comparison of the static absorption spectra for both CO and NO is displayed in Figure 3.29-A.

3.4.1 Interaction of NO with sGC-β1(1-190)

A recent study concerning sGC activation described a possible activation mechanism induced by the transition of the six- to five-coordinated NO only based on crystal structures obtained from a SONO homologue of sGC, not from the entire sGC[72]. This putative activation mechanism is based on heme distortions (pivoting and bending) induced by NO binding to homologous SONO. However, we saw in Section 3.2 that NO interaction and dynamics with SONO's are different, not only among SONO's but also between SONO's and sGC. Because SONO's are homologous to sGC heme domain, we must verify whether NO interaction with the restricted domain β1 (1-190) is similar with that occurring in entire sGC. Here, we describe a direct and clear proof that the NO binding to sGC and β1 (1-190) subunit of sGC

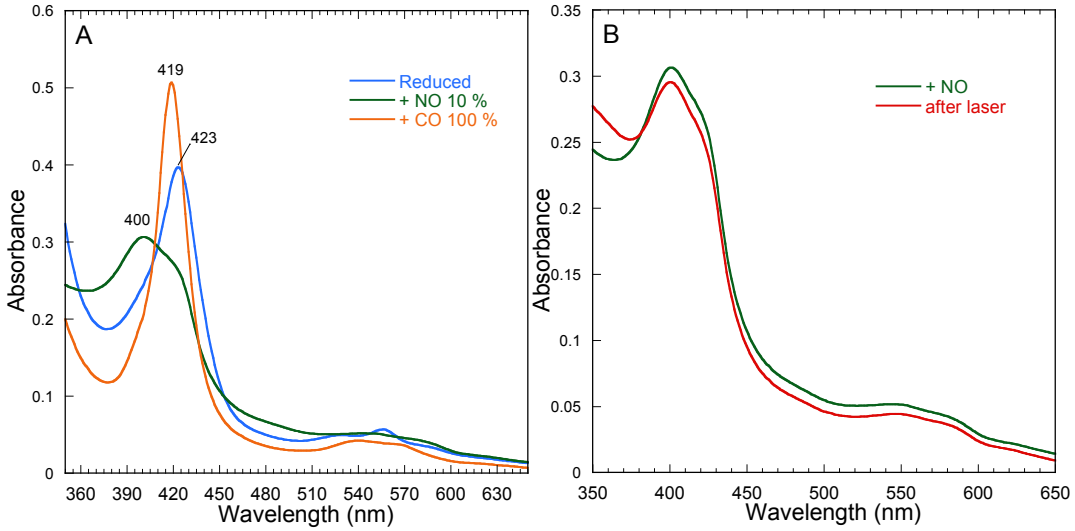

Figure 3.29: A) UV-visible spectra of reduced β1(1-190) subunit of sGC with different ligands, CO (orange) and NO (green). B) Static spectrum of the same sample before and after laser experiment in case of NO.

are in several aspects different one with the other. The steady state spectrum of β1 (1-190) shows that this isolated domain exists in both forms 5c-NO and 6c-NO at RT (Figure 3.29), contrary to entire sGC, but similarly with *Tt*- and *Np*-SONO. As demonstrated in Figure 3.30, the transient raw spectra of both proteins and the dynamic behavior of NO in both proteins is dramatically different.

Raw transient spectra of entire sGC in Figure 3.30-A show only NO rebinding to 4c-heme and the 5-ns spectrum is that of 5c-His rebinding. Compared to entire sGC, two characteristic bleaching recoveries appeared in case of isolated β1 (1-190) subunit (Figure 3.30-D). When we examine the SVD spectral components for entire sGC in Figure 3.30-C, we clearly distinguish the two different processes; geminate rebinding of NO (7.5 ps) and His rebinding (70 ps) as seen in the previous chapter. Transient spectra after NO dissociation from β1 (1-190) (Figure 3.30-D) reveal two bleaching minima corresponding to the disappearance of 5c-NO and 6c-NO (395 nm and 426 nm respectively). However only one induced absorption band is shown at $\sim$ 445 nm. The SVD spectral components have very different shape in case of β1 (1-190) subunit of sGC, compared to that of entire sGC, whereas the first kinetic component has a picosecond rise and a nanosecond decay component (Figure 3.30-F). This corresponds to the 6-coordinate species of β1 (1-190), which is not found in case of entire sGC.

The two kinetic traces (SVD1 and SVD2) were fitted with three exponential components and we calculated DAS from SVD components (Figure 3.31-A). DAS (6.7 ps) corresponds to the geminate rebinding of NO to 4c-heme and is dominant. However, two other components correspond to the bleaching centered at 425 nm but without prominent induced absorption.

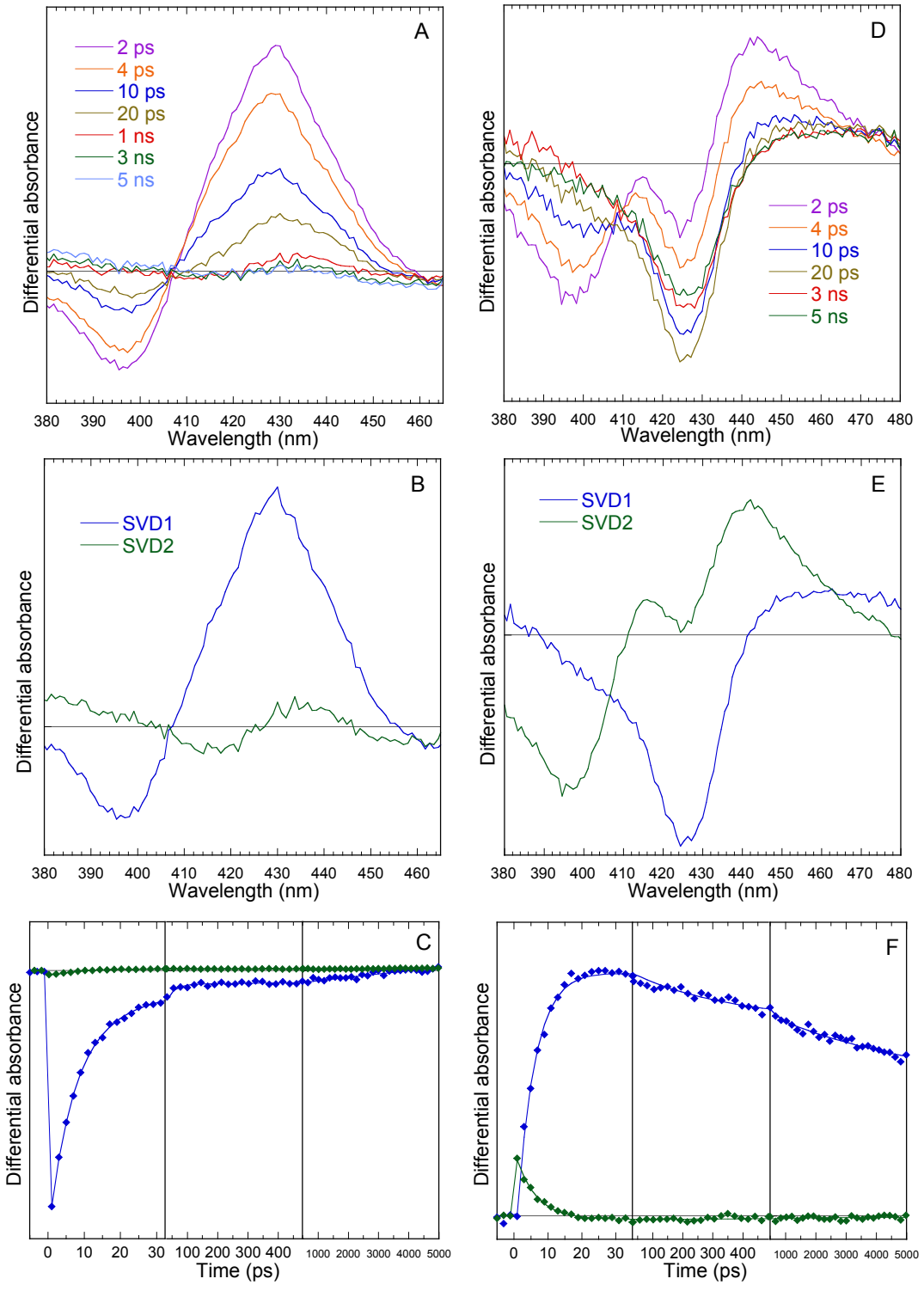

Figure 3.30: Comparison of NO dynamics in the entire sGC (left column, A-C) and β1 (1-190) subunit of sGC (right column, D-F). A and D: raw transient spectra. B and E: SVD spectral components. C and F: SVD kinetic components.

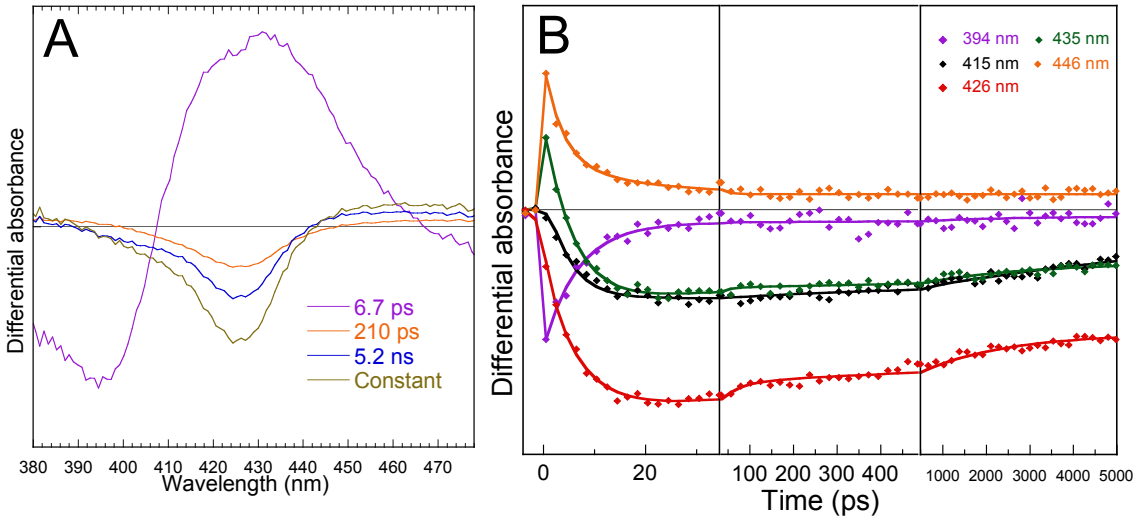

Figure 3.31: A) Difference TA spectra associated with each exponential decay components for β1 (1-190) subunit of sGC, B) Kinetics at single wavelengths for β1 (1-190) subunit of sGC.

These DAS components centered at 425 nm arise from the contribution of 6c-NO, but because it is a mixture of the two different species 5c-NO and 6c-NO, their respective spectral contribution could not be resolved by SVD calculation. SVD calculation should allow to obtain orthogonal vectors which represent spectral species evolving with particular kinetics. This leads to identify processes, for example in the case of CO rebinding to sGC in the presence of activators. However this is not always so, especially when close spectral contributions are entangled. In the case of NO rebinding to β1 (1-190), the bleaching due to the dissociation of 6c-NO at $\sim$ 420 nm mostly overlaps the induced absorption of 4c-heme at 418 nm (see Chapter 2) due to dissociation of 5c-NO. Consequently, the signal is "missing" in this region and the kinetic SVD components are not correctly defined. Only the kinetics of bleaching at 396 nm are correctly defined when we calculate the spectra associated with the 6.7-ps decay (Figure 3.31-A). This DAS has an induced absorption with two maxima, at $\sim$ 420 nm and 430 nm corresponding respectively to 4c- and 5c-His species, showing that the spectral contributions cannot be separated by SVD. Therefore, we further analyzed kinetics at single wavelengths.

Figure 3.31-B shows the NO dynamics within heme domain of β1 (1-190) subunit of sGC at separate wavelengths in three time windows upto 5 ns and corresponds the raw transient spectra in Figure 3.30-D. Each kinetic curve was fitted as indicated in Table 3.8. All kinetic traces included the $\sim$ 4 ps which is the excited state decay. We must notice that an isosbestic point exists at 410 nm in differential transient spectra (Figure 3.30-D) which corresponds to the 6c-NO/5c-NO, close to that measured by stopped-flow for the entire sGC[19, 45].

Wavelength	τ_1	A_1	τ_2	A_2	τ_3	A_3	Cst
	ps		*ps*		*ns*		
394 nm	6.8	*-0.91*			2.0	*-0.05*	*-0.04*
415 nm	7.1	*0.48*			2.1	*-0.27*	*-0.25*
426 nm	6.8	*0.32*	43	*-0.06*	2.0	*-0.09*	*-0.53*
435 nm	7.3	*0.65*			2.4	*-0.09*	*-0.26*
446 nm	7.0	*0.75*	42	*0.16*			*0.09*

Table 3.8: Fit parameters of NO rebinding kinetics of β1 subunit of sGC. The kinetic traces in Figure 3.31 were fitted using the function $\sum A_i exp(-t/\tau_i)$ + C.

However, at this isosbestic, the disappearance of 4c-heme contributes to the signal.

All together, fitting the kinetics resulted in three exponential components: the fastest component is due to NO rebinding to the 4c-heme (similarly to entire sGC) whereas the two slower components ($\tau_2 = 42 \sim 3$ ps and $\tau_3 = 2.0 \sim 2.4$ ns) are assigned to NO rebinding to the 5c-His heme (contrary to entire sGC). After 20 ps, the contribution of 4c-heme + NO $\rightarrow$ 5c-NO process is very small (3 lifetimes, about 5 % remained) while the contribution of 5c-His + NO $\rightarrow$ 6c-NO has decreased by a factor of $\sim$ 1.6 ($\tau_2 = 42$ ps). The evolution of bleaching at 426 nm gives the proportion of $\sim$ 53 % of NO not rebound at 5 ns, which is higher than in myoglobin (10 %). Another difference is the presence of a nanosecond phase for NO rebinding to the 5c-His heme, contrary to myoglobin but similarly to the endothelial NO-synthase[121]. NO dynamics of 5c-His + NO $\rightarrow$ 6c-NO in the isolated heme domain β1 (1-190) do not match those of myoglobin[122], but has a larger proportion of NO diffusing into solution after NO release from the heme.

The binding of NO to the β1 (1-190) heme domain results in a mixture of 5c-NO and 6c-NO species (proportion $\sim$ 0.5/0.5) contrary to the case of entire sGC which gives 100 % 5c-NO. The strain on proximal His, which facilitates the NO trans effect, is considerably decreased. Our results demonstrate that the strains exerted on the heme and its nearby environment are relaxed when the β1 (1-190) domain is isolated. Thus, the other domains (191-619) of βsubunit and the α-subunit exert strains which facilitate NO trans effect and Fe^{2+}-His bond cleavage and consequently play a role in transmitting conformation between the heme domain and other part of the sGC dimer.

3.4.2 Interaction of CO and activators with sGC-β1(1-190)

Steady state spectrum of CO bound β1 (1-190) subunit of sGC is displayed in Figure 3.29. We performed TA measurements of this protein for the purpose of comparing the effect of activators with sGC. Figure 3.32-A presents the transient raw spectra of β1 (1-190) subunit

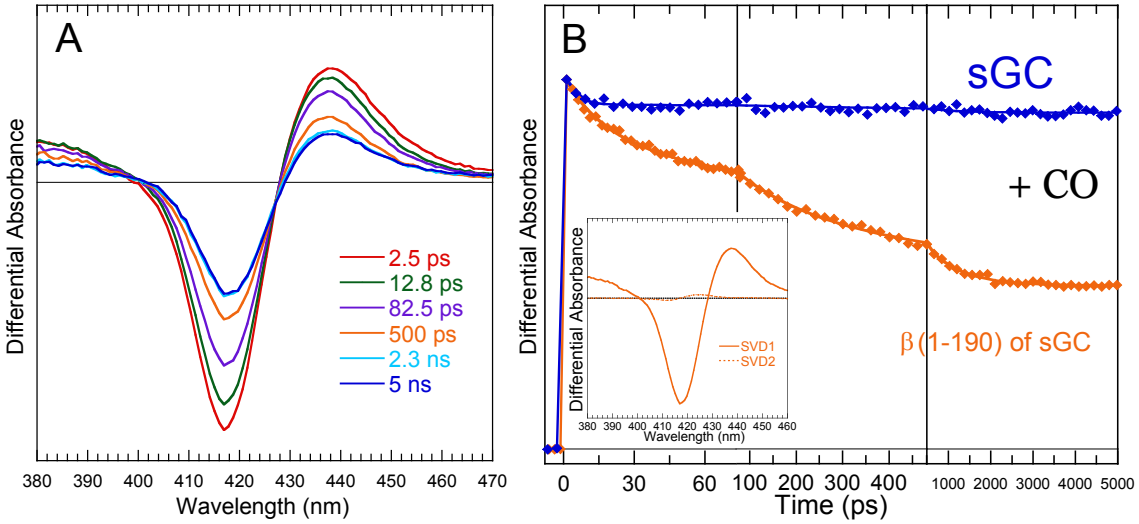

Figure 3.32: A) Transient spectra at given time delays after photodissociation of CO from $\beta 1$ (1-190) subunit of human sGC, B) Kinetic components (SVD1) of CO rebinding to sGC and $\beta 1$ (1-190) subunit of sGC. The associated SVD1 spectrum is displayed in the inset together with SVD2 component.

of sGC after dissociation of CO at given delay times in the absence of effectors. The shape of induced absorption and bleaching recovery does not change from 2.5 ps to 5 ns. Only a very small shift of isosbestic point at 428 nm appeared until 5 ns. But the considerable CO rebinding (almost 50 % at 5 ns) is very unique and not found for entire sGC or Mb. After SVD calculation on these raw transient spectra, we obtained one large component corresponding to CO rebinding. In the inset in Figure 3.32-B, SVD2 spectral component was very small, proportional to its singular value. The kinetic of SVD1 component was fitted with multi-exponential decay components (Figure 3.32-B). Remarkably, there is no geminate rebinding phase in SVD1 upto 5 ns in case of entire sGC, in a similar way with Mb, but we observed a considerable geminate rebinding of CO to $\beta 1$ (1-190) subunit of sGC (Figure 3.32-B and Table 3.9). The energy barriers for CO release into solution appear much higher than in entire sGC, but this is not due to increased steric hindrance from side chains in the heme pocket, as it has been observed in mutated myoglobin[123]. Considering that the sequences of both samples are the same and their steric contribution is thus unchanged, the structural conformation of the heme pocket itself (and/or the distortion of the heme) is modified as a consequence of the absence of α-subunit and of $\beta 1$ (191-619) domains interacting with $\beta 1$ (1-190).

The binding of both YC-1 and BAY did not change the Soret maximum of $\beta 1$ (1-190)-CO complex (Figure 3.33). This implies that in $\beta 1$ (1-190) subunit sGC, the heme iron underwent no changes in heme coordination number in the presence of effectors. We then performed TA measurements of CO dynamics within $\beta 1$ (1-190) in the absence and presence

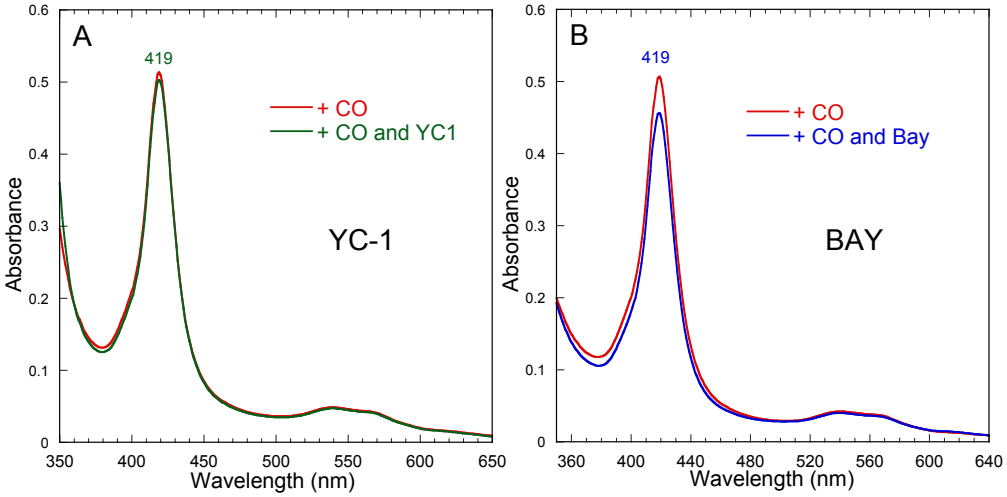

Figure 3.33: UV-visible spectra of β1(1-190) subunit of sGC with CO in the presence and absence of A) YC-1 and B) BAY 41-2272.

of these effectors.

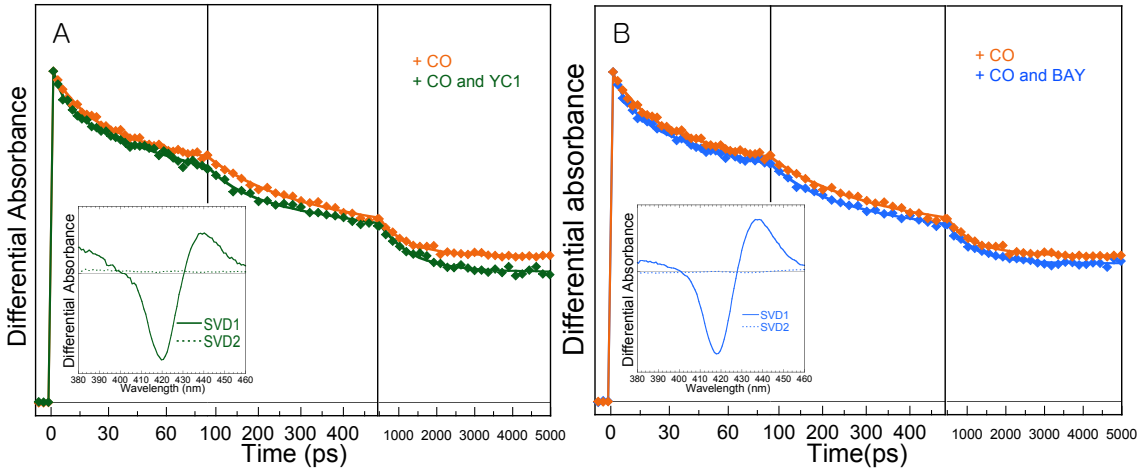

Figure 3.34: Comparison of kinetic components of CO rebinding for β1 (1-190) subunit of sGC in the absence and presence of A) YC-1 and B) BAY 41-2272. The associated SVD1 spectra are displayed in the inset together with SVD2 component which is multiplied by the singular value.

Figure 3.34 are the normalized fitted kinetics for β1 (1-190)-CO in the absence and presence of YC-1 and BAY. Albeit the effect of both stimulators for β1 (1-190) subunit is lower than entire sGC, we can clearly identify fast rebinding phases (Table 3.9). The tendency is similar for both cases and we fitted them with multi-exponential functions (Table 3.9).

We also performed measurements on longer time-scale (5 ns to 0.1 s) for β1 (1-190) subunit of sGC in the presence of both effectors. The comparison with the kinetics at fixed wavelengths (437 nm for sGC and 434 nm for β1 (1-190) subunit of sGC) is displayed in

Species	τ_1	A_1 %	τ_2	A_2 %	τ_3	A_3 %	Cst %
	ps		*ps*		*ns*		
*β*1 (1-190) subunit sGC/CO	18	*16*	165	*20*	0.81	*20*	*44*
sGC/CO	-	-	118	*2*	3.2	*3*	*95*
*β*1 (1-190) subunit sGC/YC-1	6.4	*14*	75	*24*	0.87	*24*	*38*
*β*1 (1-190) subunit sGC/BAY	9.7	*15*	99	*21*	0.73	*23*	*41*
sGC/CO/YC-1	9	*4*	124	*9*	1.7	*10*	*77*
sGC/CO/BAY	14	*6*	120	*19*	2.2	*13*	*62*

Table 3.9: Fit parameters of CO rebinding kinetics to *β*1 (1-190) with and without effectors. The kinetic traces in Figure 3.34 were fitted using the function function $\sum A_i exp(-t/\tau_i)$ + C. The 4 ps component (not listed) was added in order to take into account the excited state decay of the heme.

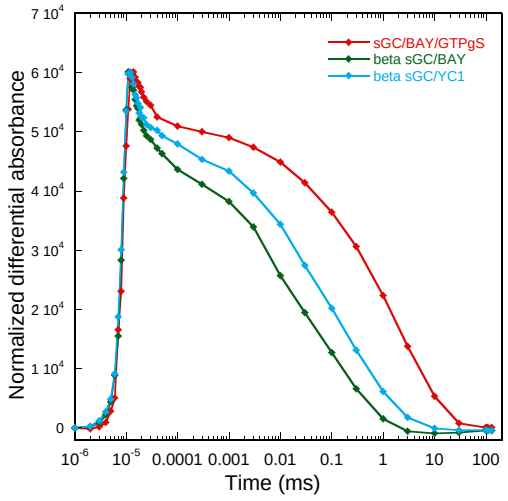

Figure 3.35: Comparison of normalized kinetics in broad time-range at fixed wavelength for sGC and *β*1 (1-190) subunit of sGC in the presence of YC-1 and BAY 41-2272.

Figure 3.35. All three kinetic traces are fitted with multi-exponential functions containing 5 decay components. A fast ($\sim$ 6 ns) decay component for YC-1 and BAY was found and is faster than that of sGC which has 20 ns component. Other time constants are compared and summarized in Table 3.10.

Overall, we observed a faster geminate rebinding phase in case of *β*1 (1-190) subunit of sGC and we can conclude that YC-1 and BAY bind to *β*1-subunit (1-190) heme domain. Due to the difficulty to overexpress *β*1 (1-190), we could not obtain kinetic data for *β*1 in absence of effector in this broad time range. The kinetics were normalized in Figure 3.35 for comparative purposes, but the amplitude of these kinetics directly follow those in Figures 3.32 and 3.34 and represent the evolution of the amplitude fitted as a "constant" term in the 5-ns data (3.34). Firstly, it is obvious that CO rebinding is much faster to *β*1 (1-190) than to entire sGC, in the absence of activators (even in the presence of activators and GTP-*γ*-S bound to entire sGC which were shown to increase CO rebinding in Chapter 2). Secondly, the effect of BAY on *β*1 (1-190) is more pronounced than that of YC-1, exactly as we observed

for sGC. We discuss these two points below.

Species	τ_1	A_1	τ_2	A_2	τ_3	A_3	τ_4	A_4	τ_5	A_5	τ_6	A_6
	ns		*μs*		*μs*		*μs*		*ms*		*ms*	
β1 (1-190) subunit of sGC/CO/YC-1	5.8	*0.59*	0.20	*0.05*	-	-	10	*0.12*	0.15	*0.13*	1.5	*0.11*
β1 (1-190) subunit of sGC/CO/BAY	6.0	*0.58*	0.08	*0.08*	5.0	*0.14*	60	*0.10*	0.50	*0.10*	-	-
sGC/CO/BAY/GTP-γ-S	15	*0.56*	0.20	*0.13*	-	-	22	*0.07*	0.70	*0.11*	7.0	*0.13*

Table 3.10: Fit parameters of CO rebinding kinetics of β1 subunit of sGC. The kinetic traces in Figure 3.35 were fitted using the function Parameters obtained with the function $\sum A_i exp(-t/\tau_i)$ + C.

3.4.3 Discussion: β1 (1-190) versus sGC

Because in the isolated heme domain β1 (1-190), CO rebinds with multiple nanosecond phases and high yield in the absence of any effectors, contrary to the entire sGC, the energy barrier for CO release is much more higher in β1 (1-190), indicating structural changes with respect to the entire dimeric protein. Because the influence of α-subunit is missing in β1 (1-190), this isolated heme domain has different properties than dimeric sGC and consequently structural properties of β1 (1-190) cannot be directly transposed for modeling the activation mechanism in entire wild type sGC. This may call into question a model describing the activation of sGC drawn from an X-ray structure of bacterial SONO (*Nostoc* species) with bound NO[72]. Because our CO dynamics demonstrate a structural change in isolated heme domain, the distortions observed in this structure upon CO and NO binding[72] could be irrelevant with respect to sGC activation mechanism.

Since we observe in β1 (1-190) the same effects induced by the presence of the effectors YC-1 or BAY on the CO dynamics than in entire sGC, we can conclude that these effectors bind to the restricted portion 1-190 of heme domain in the entire sGC. This location of activators binding site agrees with the fact that a shift of the Soret maximum is observed in their presence, indicating a change in heme environment or a slight distortion of the heme itself. Some binding sites have been proposed for YC-1 or BAY, after mutagenesis experiments, for instance the residue β1-Cys541[124] or α1-Cys594[35] but these were ambiguous. One must note that a change of activity in the presence of activators for mutated compared with wild type sGC does not imply that this particular mutated side-chain is involved in YC-1 and BAY binding. Instead, this side-chain can be involved in activation since the entire protein is necessary for activation after NO binding. More rigorously, Rothkegel *et al.*[125] concluded from their mutation experiments that residues β-Asp44 and β-Phe74 are involved in sGC activation and "possibly" in BAY binding.

3.5 Conclusion

We investigated three different homologous SONO and the heme domain $\beta 1$ (1-190) subunit of sGC in order to compare with entire sGC. The heme proteins SONO share partial sequence with the entire sGC but with different sequence identity and thus they have different properties. sGC forms 5c-NO but SONO proteins become either 6c-NO or 5c-NO depending on temperature and depending upon the species. sGC cannot form a complex with O_2 but *Tt*-SONO does. Recently, a study on SONO from *Nostoc* species has revealed that it might function as either a redox or a NO sensor in the cyanobacterium[106]. The authors concluded that *Np*-SONO can be either NO-sensor or redox switch because *Np*-SONO autoxidizes in certain condition. However, this property was not observed in our laser experiments but it was observed for *Tt*-SONO. Binding diatomic gases is a major property of the three SONO proteins but these cannot simply be categorized in a class of heme protein sensor. They have different properties and may have different functions as well. From our results, we can conclude that *Cb*-SONO is the closest to NO-sensor and *Tt*-SONO is the opposite.

Summary of the major findings of this Chapter:

1. SONO's from different species interact differently with NO, displaying redox properties (*Tt*-SONO), adaptation of NO affinity and dynamics as a function of temperature (*Np*-SONO) and high NO affinity (*Cb*-SONO).

2. Binding of NO to the isolated $\beta 1$ (1-190) heme domain results in a mixture of 5c-NO and 6c-NO species contrary to the entire sGC. The remaining part of β-subunit and the α-subunit exert strains which facilitate NO trans effect and Fe-His bond cleavage and which are considerably decreased in their absence.

3. The allosteric activators YC-1 and BAY 41-2272 bind to the isolated sGC heme domain $\beta 1$ (1-190) and to its bacterial counterparts *Np*-SONO and *Cb*-SONO, influencing in the same manner as in entire sGC the dynamics and binding of CO, a diatomic which activates sGC in synergy with activators.

Chapter 4

Nitric Oxide release: Cytochrome c' from *Alcaligenes xylosoxidans*

4.1 Introduction

Cytochromes c' consist of a four α-helical bundle structure which are isolated as homodimers and do not have the same structural fold as mitochondrial cytochrome c[126]. They are high-spin bacterial heme proteins and distinguished from the low-spin mitochondrial cytochromes c since they have the vacant sixth coordination site of the heme iron and are able to bind diatomic ligands such as NO and CO in a different fashion. They are largely found in nature and cytochromes c' homologues have been expressed from various bacterial organisms, which are photosynthetic and denitrifying, and nitrogen-fixing[126, 127]. Although they are structurally well characterized for over 30 years, their physiological function is unresolved. Many studies focus on the possible protection role of cytochromes c' against the toxicity of NO in bacteria[128–130]. In those reports, either NO reductase or NO transporter functions are addressed to explain the behavior of the proteins.

Apart from the general functions of c-type heme proteins whose ability is based on the redox properties, cytochromes c' use heme as a coordination center with the distal side vacant in the unliganded state[131]. Due to the unique heme properties, cytochromes c' from many bacterial organisms have been characterized via crystal structural studies[69, 132]. A very unique heme coordination chemistry with two possible positions for diatomic ligands at the proximal or distal side was revealed by X-ray studies especially from the denitrifier, *Alcaligenes xylosoxidans*[69]. The X-ray structure of AXCP homodimer is displayed in Figure 4.1. The crystal structures for unliganded, CO-, and NO-bound AXCP revealed that CO and NO do not bind to Fe on the same side of the heme. In case of CO, it forms a six-coordinate

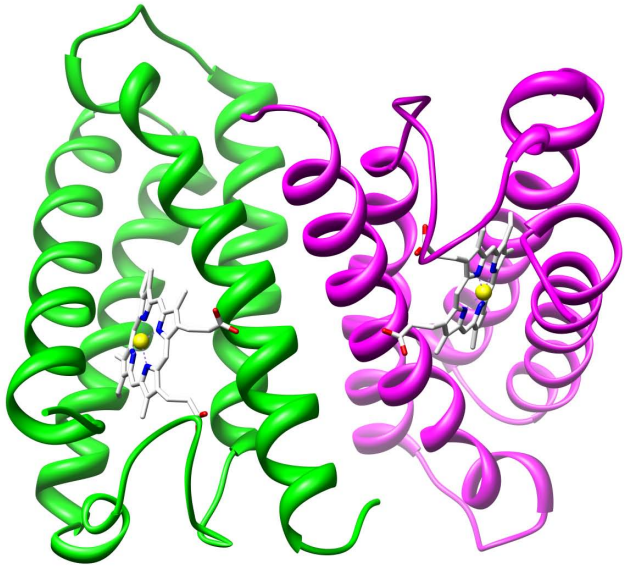

Figure 4.1: Structure of the unliganded (5c-His) ferrous AXCP at equilibrium. The active form of the protein is a homodimer, each monomer being a bundle of four α-helices harboring the heme. The figure was prepared using Chimera. PDB ID: 1E84.

heme complex at the vacant distal side but NO displaces the proximal histidine residue site by occupying it instead.

4.2 AXCP and sGC

One of the proposed mechanisms for sGC activation with NO is that NO can replace the histidine ligand. To support this, crystal structure of AXCP has been the basis for this hypothesis of sGC mechanism. Figure 4.2 shows the superimposed structure of 5c-His and 5c-NO AXCP with NO bound to the proximal side by replacing His residue. Previous TA and Raman studies have shown that fast NO geminate rebinding takes place (7 ps; *sim* 99 %) due to the confined environment of heme pocket but the exact contribution of the minor ($\sim$ 1 %) component escaping and not rebinding remains unknown[67]. So far studies about NO interaction with AXCP focussed on its proximal binding character.

Previous kinetic studies have revealed the existence of transient 6c-NO species prior to forming the **proximal** 5c-NO complex[66, 133, 134]. It was proposed that NO firstly binds to the heme at the distal side to form 6c-NO intermediate species which then convert to the proximal 5c-NO complex. Photolysis of NO with nanosecond pulse detected the ferrous 5c-His species and proposed a fast His reattachment process, suggesting that mechanism is second order. Most of NO-bound heme proteins generally form 6-coordinate complexes with His and NO as axial ligands. However, both AXCP and sGC have the property that NO binding to the heme at the distal side provokes the bond cleavage of the axial Fe-His bond. In sGC, this cleavage of the proximal Fe-His bond triggers the catalytic activity for cGMP production, whereas in AXCP the exact role of the proximal bond formation through a second

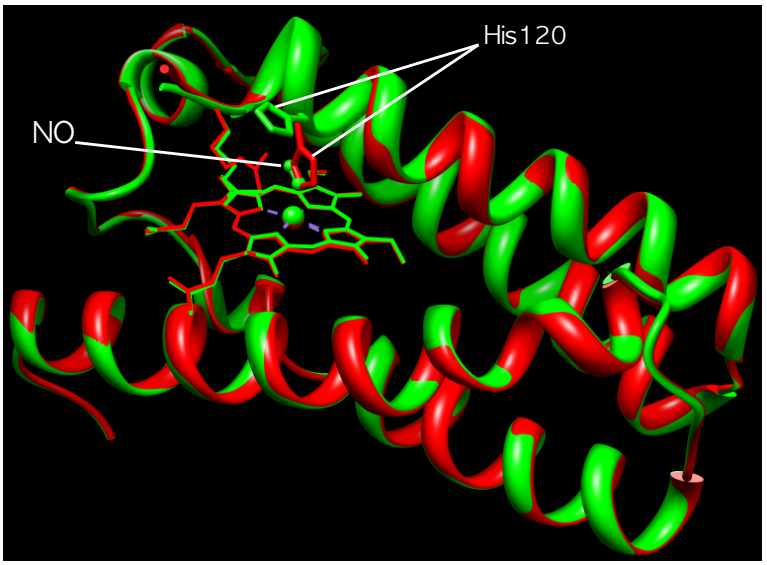

Figure 4.2: Superposition of the equilibrium structures of 5c-His (red) and 5c-NO (green) forms of reduced AXCP showing the strict similarity of tertiary structures. The two positions of His120 and NO are indicated. The figure was generated using Chimera (PDB ID: 1E84 and 1E85).

order reaction is still in question[134]. The formation of 5c-NO complex is thus induced by the trans effect, that is to say the weakening of the Fe-His bond by the trans coordination of NO described by computational method[135]. Disruption of the Fe-His bond is directly related to the conformational change in sGC, but not in AXCP (Figure 4.2). The heme-dinitrosyl intermediate species in the proximal 5c-NO formation mechanism was confirmed[74] and provided a crucial key to the structural mechanism of AXCP. The previous study was focusing on NO rebinding within the heme pocket (99 % population) whereas the present study with TA spectroscopy is performed to follow the dynamics of the transient AXCP after NO release from the protein to the solution (1 % population).

4.3 Steady-state Equilibrium: NO and CO

The equilibrium spectra of ferrous AXCP with NO (Figure 4.3, panels A and B) and CO (Figure 4.4) as a ligand in the Soret region are displayed together with the difference spectra. In Figure 4.4-A, characteristic Soret maxima at 425 and 396 nm reveal the 5c heme with His and NO respectively[67].

AXCP forms 5c-NO complexes rapidly (in seconds) with NO in large excess but the 6c-NO intermediate is long-lived (2 hours) at low concentration of NO since the conversion of 6c-NO to 5c-NO species exhibits a second-order concentration dependence of NO[134]. For

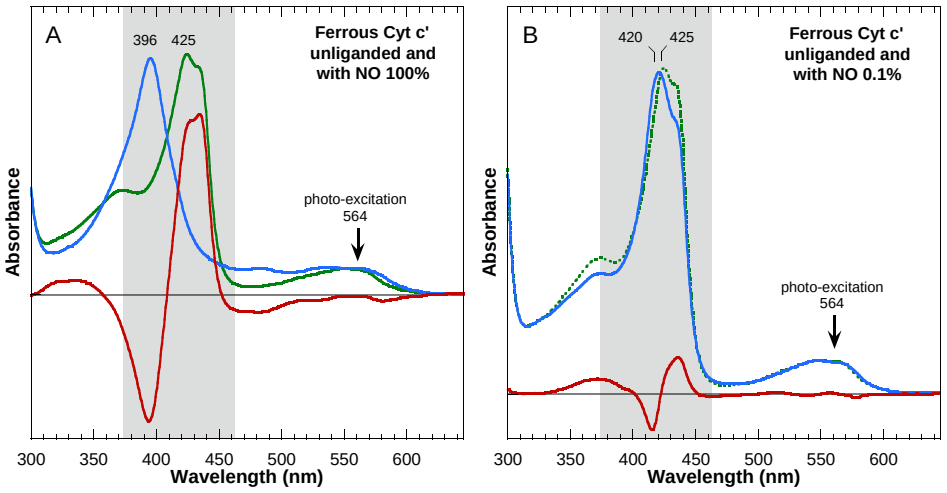

Figure 4.3: Equilibrium absorption and its difference spectra of AXCP showing the Soret maxima, α/β bands; A) 100 % NO-bound, B) 0.1 % NO-bound.

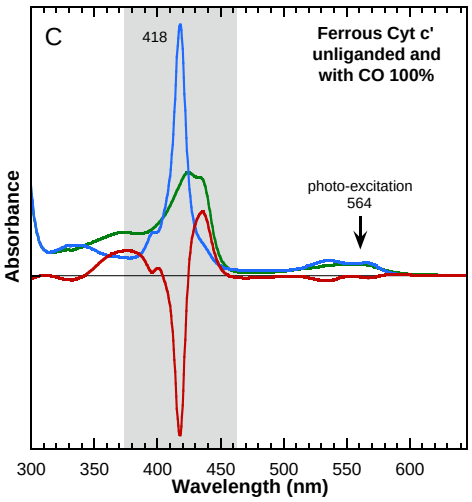

Figure 4.4: Equilibrium absorption and its difference spectra of AXCP of 100 % CO-bound forms.

this reason, we used 0.1 % NO (2 μM in aqueous phase) to obtain the 6c-NO form stable over 2 hours in order to record the 5c-His transient spectrum of AXCP. Soret maximum at 420 nm is assigned to 6c-NO intermediate[136] on the basis of the similarities with myoglobin. Figure 4.4 shows the largely increased Soret maximum at 418 nm for 6c-CO complexes and it is similar to that previously reported[136]. Transient absorption of 6c-CO was also recorded to obtain the 5c-His transient species.

4.4 Geminate Rebinding of NO and CO to AXCP

We will first describe the dynamics of AXCP-NO when [NO] = 2 mM in aqueous phase, then when [NO] = 2 μM, which results in a different AXCP dynamics. CO dynamics will be presented also immediately after results on NO because transient spectra in the three cases

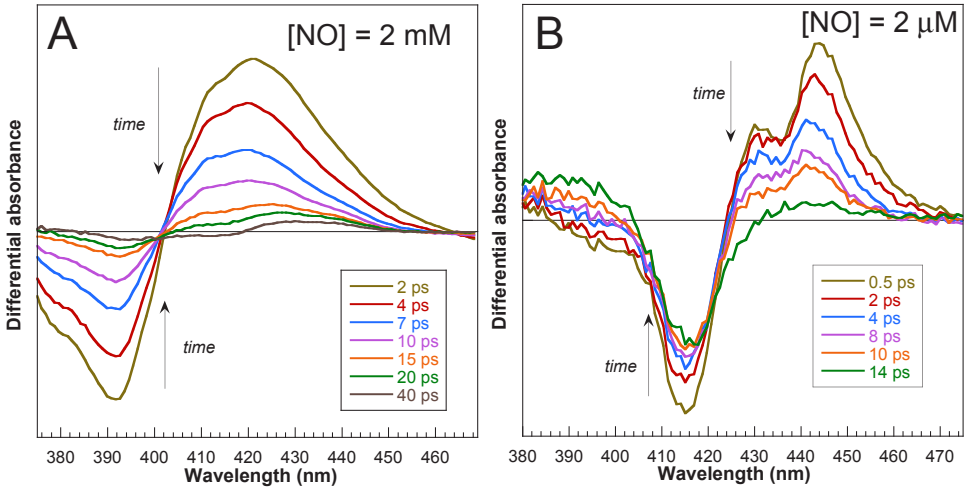

Figure 4.5: Raw spectra at given time delays after photodissociation of A) 100 % NO-bound and B) 0.1 % NO-bound AXCP.

will be used together to infer behavior of AXCP. The raw difference transient absorption spectra at various time delays in high concentration of NO are shown in Figure 4.5-A. After SVD calculation, kinetic trace with fitted curve was obtained together with its corresponding spectral SVD component (Figure 4.7). For 5c-NO AXCP ([NO] = 2 mM), a bleaching appeared at 392 nm reflecting the disappearance of the 5c-NO AXCP (Figure 4.5-A). A broad induced absorption with decreasing intensity from 2 ps to 15 ps due to the rebinding of NO. A small but distinct contribution of the induced absorption at 435 nm starts to appear from 15 ps and this induces a shift of the isosbestic point, showing more than one process takes place.

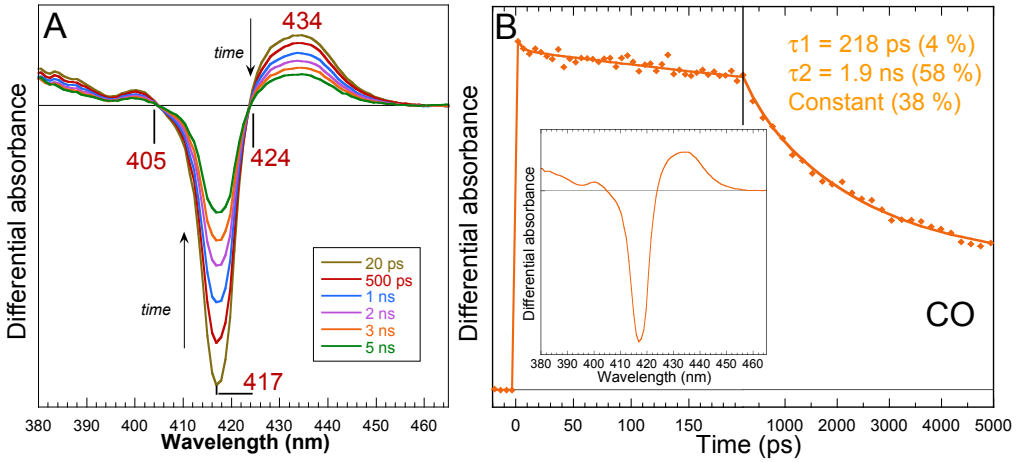

Figure 4.6: A) Raw spectra at given time delays, B) SVD1 kinetic and spectral component of 100 % CO-bound AXCP after photodissociation. Fitted results are included in the figure.

Transient spectra following dissociation of NO from 6c-NO AXCP show a bleaching centered at 415 nm corresponding to the disappearance of the 6c-NO species in Figure 4.5-B. A minor bleaching centered at 395 nm is ascribed to the little contribution from 5c-NO species that is hardly detectable in equilibrium spectrum. This results from the evolution of 5c-NO during kinetic measurements. The isosbestic point moves from 386 nm at 0.5 ps to 404 nm at 14 ps, and the second is displaced from 425 nm to 432 nm in the same time range. The induced absorption at 428-430 nm is due to the truncated 4c-heme spectrum, which rapidly decreases. This is due to the simultaneous presence of 5c-NO and 6c-NO. These considerable shifts of isosbestic points indicate that there are two processes, corresponding to rebinding to 4c- and 5c-His hemes. In Figure 4.5-B, the signal to noise rate is lower because the difference between unliganded and 6c-NO AXCP at Soret region is much lower, as seen in Figure 4.3-B.

We will now discuss the case of CO dynamics in order to compare the induced absorption with the case of NO. The raw transient spectra at successive time delays upto 5 ns after photolysis of CO are displayed in Figure 4.6-A. The maximum of induced absorption centered at 434 nm and the minimum of bleaching at 417 nm clearly decrease without any shift until 5 ns. These characteristic positions are same as the equilibrium difference spectra (Figure 4.4) and are due to the dissociation of CO. Initial contribution of excited state decay before 20 ps is excluded in order to show only CO rebinding to AXCP. Two isosbestic points at 405 and 424 nm do not shift over 5 ns, showing that only one process takes place.

To disentangle the contributions from the different transient species and their associated kinetics, we performed SVD analysis of the raw data matrix. Two main SVD spectral components are displayed in Figure 4.7-A having the larger singular values compared with the equilibrium difference spectrum of unliganded minus 5c-NO AXCP taken from Figure 4.4-A. The main spectral component (SVD1) having the highest singular value has overall similar shape with initial raw transient spectra from Figure 4.4-A. It represents the contribution of geminate rebinding of NO to 4c-heme since it has characteristic bleaching at 392 nm is due to the dissociated 5c-NO species and broad band centered at 421 nm due to 4c-heme. Furthermore, this broad band does not match with that of equilibrium difference spectra (dashed), which show the maximum peak, at 425 nm. The kinetics of absorption associated with the SVD1 component was fitted with a mono-exponential function giving a time constant of 7 ps in the case of SVD1 (Figure 4.7-B, Table 4.1). This corresponds to the geminate rebinding of NO to AXCP 4c-heme. From the raw transient spectrum at 10 ps we calculated the spectrum of the 4c-heme. This spectrum contains both the contribution of photodissociated 4c-heme and of non-dissociated 5c-NO heme. This latter species is assumed to be the only component before zero. We therefore subtracted this weigthed spectrum from that at 10 ps as follows:

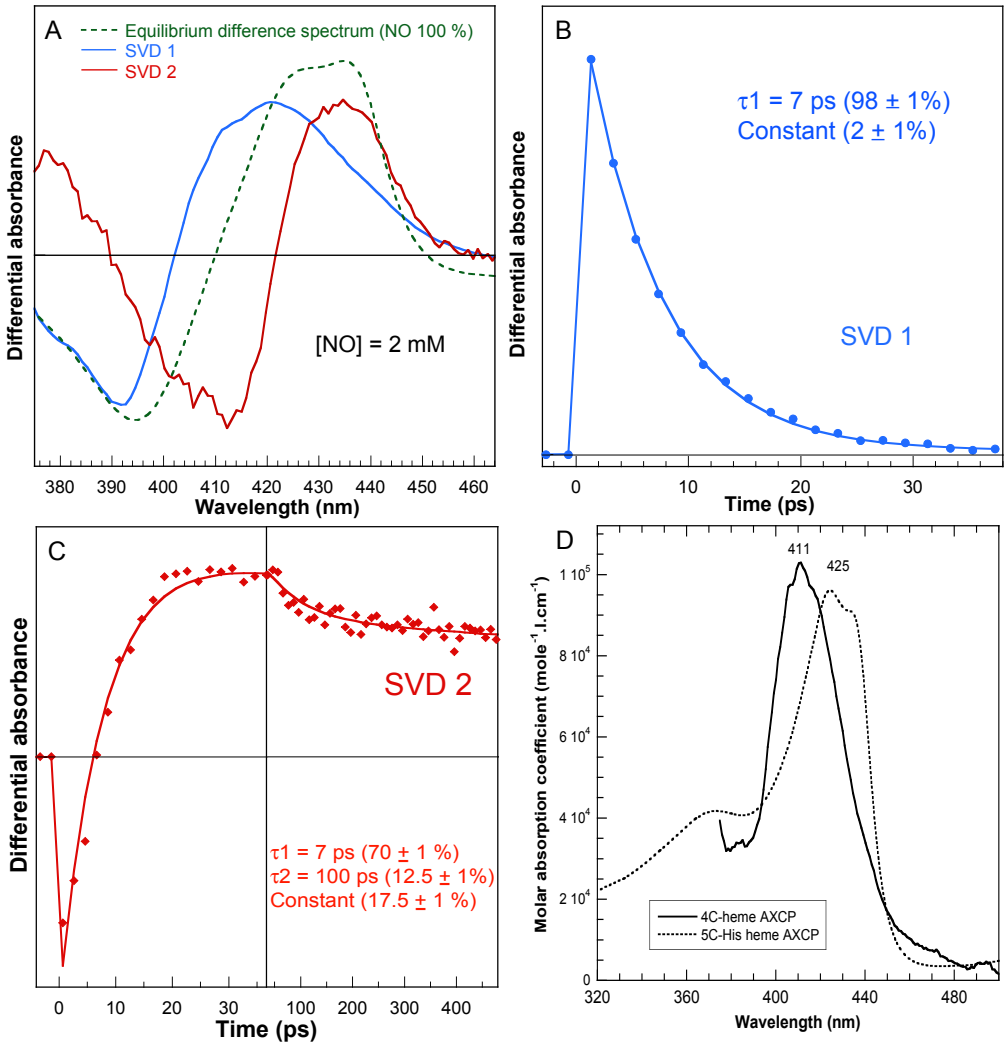

Figure 4.7: A) Normalized transient spectral components for [NO] = 2 mM obtained from SVD analysis are compared with equilibrium difference spectrum. Kinetics of B) SVD1 and C) SVD2 components corresponding to each component from A, D) Calculated spectrum of 4c- and equilibrium 5c-AXCP.

$$\text{4c-spectrum} = \text{spectrum (10 ps)} - 0.93 \times \text{spectrum (-5 ps)}$$

The time delay of 10 ps was chosen to minimize the presence of excited states, which decay with a 3 ps time constant. Since we have observed symmetric bleaching and induced absorption intensities in difference transient spectra after NO photodissociation for two proteins yielding a 4c-heme, AXCP and sGC, we assumed a value of same order of magnitude for 4c- and 5c-AXCP hemes. The coefficient was determined empirically: a higher value results in negative features in the absolute 4c-heme spectrum, whereas the lower value gives rise to a shoulder due to 5c-NO heme. This procedure yields an uncertainty < 10 % for the calculated spectrum and of $\pm$ 1 nm for the position of the Soret maximum (Figure 4.7-D). Interestingly, we observe two

characteristics already seen in the spectrum of a ferric 4c-porphyrin model compound[137]: the Soret band of 4c-species is blue-shifted and slightly higher than that of the 5c-species.

Species	Component	τ_1	A_1 %	τ_2	A_2 %	Cst %
		ps		*ps*		
5c-NO	SVD1	7	*98 ± 1*	-	-	*2 ± 1*
	SVD2	7	*70 ± 1*	100	*12.5 ± 1*	*17.5 ± 1*
6c-NO	SVD1	2	*41*	52	*25*	*34*

Table 4.1: Fit parameters of NO rebinding kinetics of AXCP. The kinetic trace in Figure 4.7-B,C and 4.8-D was fitted using the function Parameters obtained with the function $\sum A_i exp(-t/\tau_i)$ + C. The 3 ps component was added to the decay in order to take into account the excited state decay of the heme.

In the following section we will discuss the origin of SVD2 component.

4.5 His Rebinding

The induced absorption part of SVD2 component (red, Figure 4.7-A) centered at 435 nm is close to that of equilibrium difference spectra and this is characteristic of the formation of 5c-His species. Kinetics associated with SVD2 was fitted with an exponential decay with extremely small amplitude of τ = 100 ps (Table 4.1) which is thus assigned to rebinding of proximal histidine.

To further confirm assignment of the transient SVD2 (at NO 100 %) component precisely it is necessary to compare it with that of CO rebinding to 5c-His since it does not contain 4c-heme species. The bleaching part of SVD2 component is clearly different from the SVD spectral component corresponding to CO dissociation from 6c-AXCP but the two induced absorptions at 435 nm are precisely overlapped one with the other as shown in Figure 4.8-A. Since CO dissociation leads to a 5c-heme, the similarity of induced absorption indicates that SVD2 (NO 100 %) indeed yields the 5c-His species. We will now compare with the case of NO at low concentration (0.1 %) which allows to obtain mainly 6c-NO AXCP. In this case, the characteristic wavelengths of bleaching at 417 nm and induced absorption centered at 434 nm corresponding to 6c-NO are identical with the equilibrium difference spectrum (Figure 4.8-B). The rebinding of NO to the 5c-His heme appears slower (52 ps) than to the 4c-heme of AXCP (Figure 4.8-D). SVD2 component (100 % NO) at bleaching is clearly distinct with the spectral component due to the NO rebinding to 5c-His with the minimum of bleaching at 416 nm. This is a direct proof that SVD2 is not attributable to 6c-NO AXCP. We thus conclude that SVD2 component in the presence of NO 100 % is due to proximal histidine rebinding to the 4c-heme following dissociation of NO.

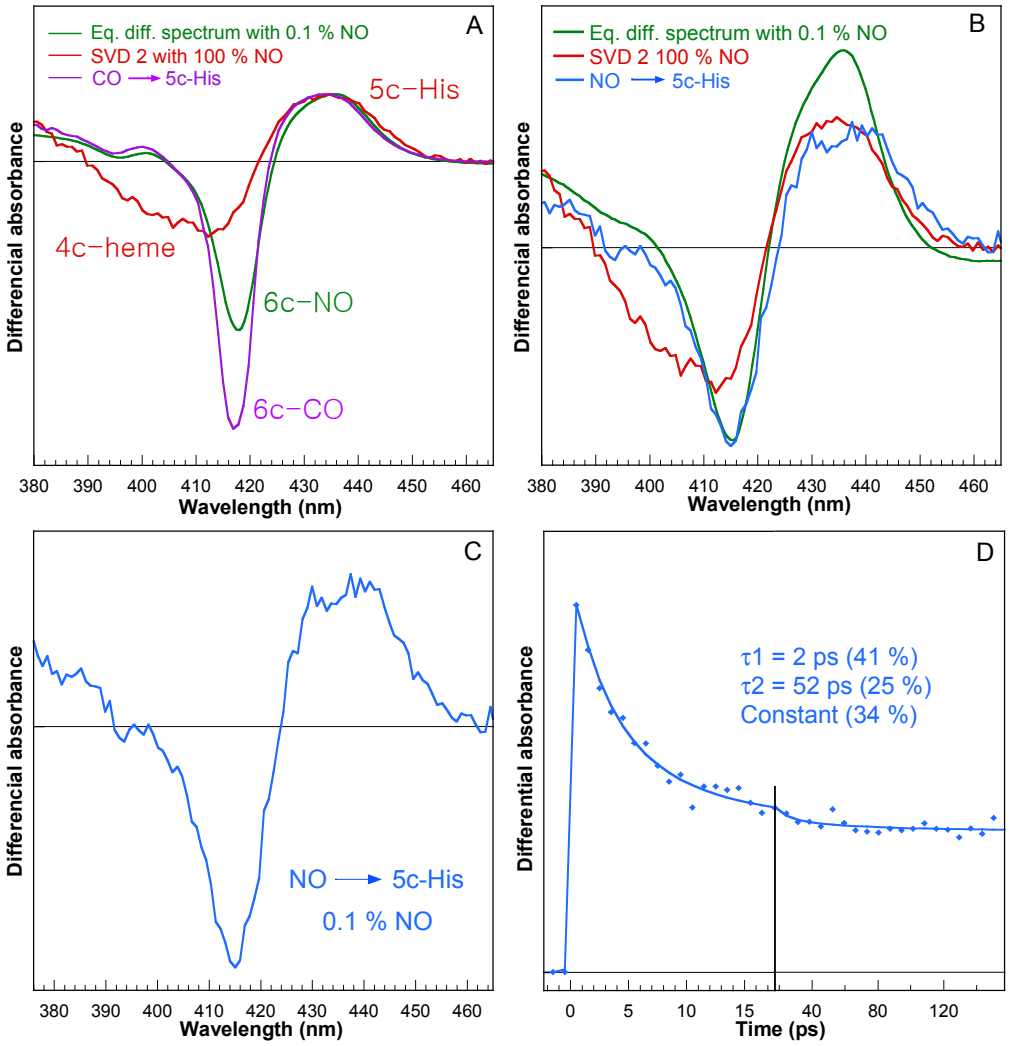

Figure 4.8: A) Equilibrium and normalized transient spectra in the case of CO compared with SVD2 (in presence of 100 % NO), B) Equilibrium and normalized transient spectra in the case of NO compared with SVD2 (100 % NO), C) Spectral and D) kinetic SVD1 component of NO rebinding to the 5c-His AXCP (in presence of 0.1 % NO).

Previously, transient absorption measurements of photodissociated 5c-NO AXCP using ultrafast laser pulse have shown that $\sim$ 99 % NO rebinds to the heme. In this latter study, the proximal His reattachment with heme iron was not detected[67]. Another group reported that $\sim$ 5 % of the photodissociated NO was away from the heme pocket escaping into the solvent, inferring the hypothesis that His rebinding traps the 5c-His ferrous heme and did not measure any time constant below millisecond timescales[66]. Since these two results are not enough to draw complete picture of the implications of proximal versus distal heme-NO coordination, we extended the time scale up to 5 ns. Although two different studies revealed both NO rebinding processes, there is no direct observation of 4c-heme species of AXCP and His reattachment. Our present study demonstrates His reattachment process following NO

geminate recombination within 100 ps to the transient 4c-heme species.

4.6 Gating of NO by Histidine Rebinding: Its putative role in AXCP and sGC

Because both sGC and AXCP form a 5c-NO complex, many groups drew models of sGC functioning with a proximal NO[58, 70, 72, 138], as observed in crystal structure of NO-bound AXCP[69]. We observed His rebinding in both cases in 70-100 ps. However the structures of both proteins are very different and we cannot readily apply AXCP model to sGC. The dynamics of NO from and to the heme of AXCP is unique among heme proteins because AXCP uses both sides of the heme plane. The very minor fractions of NO escaping the heme pocket allows the His to reattach to the heme at the proximal side within 100 ps, precluding NO to rebind directly, creating a "gate" to NO at the proximal side. This leads to a novel mechanism for NO release, which takes advantage of ultrafast rebinding of NO (99 $\pm$ 1 %). The fast rebinding of histidine functions as a gate because it traps NO-dissociated heme and prohibits the NO ligand from direct rebinding. The mechanism in Figure 4.9 explains how two NO molecules are involved during the conversion of Fe-His into the Fe-NO via 6c-NO intermediate. The dissociated NO (thermally or photo-induced) and proximal His compete for the heme iron, whereas the second NO from solution binds the heme iron from the distal direction. Our results demonstrate that the distal side of the heme in AXCP is involved in controlling the initial NO binding. On the other hand, the proximal His ligand controls the release of NO by trapping and gating NO, leading to the proposition that AXCP plays a role as a kinetic trap for NO depending upon NO gradient.

NO is a highly reactive signal molecule so that controlling its reactivity is a key for the function of proteins. Most biological functions of NO are related to the movement of NO and how it reaches its target cell is critical. This can be completed either by free diffusion or specialized delivery with the assistance of proteins. sGC shows the ultrafast and mono-exponential NO geminate rebinding rate providing a high efficiency to trap NO[21]. However, sGC binds NO at the diffusion limit ($k_{off} = 3 \times 10^8 M^{-1} \cdot s^{-1}$, Chapter 2) but the way NO is released and eliminated from sGC is totally unknown. In general, NO can exist as a transportable form by staying at the vicinity of heme proteins with the coordination with non heme proteins. This allows for the delivery of NO to the adjacent cells to reach at the target cells. If NO is efficiently trapped by a certain protein, it can exhibit its biological function, avoiding its toxicity to the cell. Two studies have shown that cytochrome c' from *Chromatium vinosum* and *Rhodobacter sphaeroides* serves to carry NO[140, 141]. According to

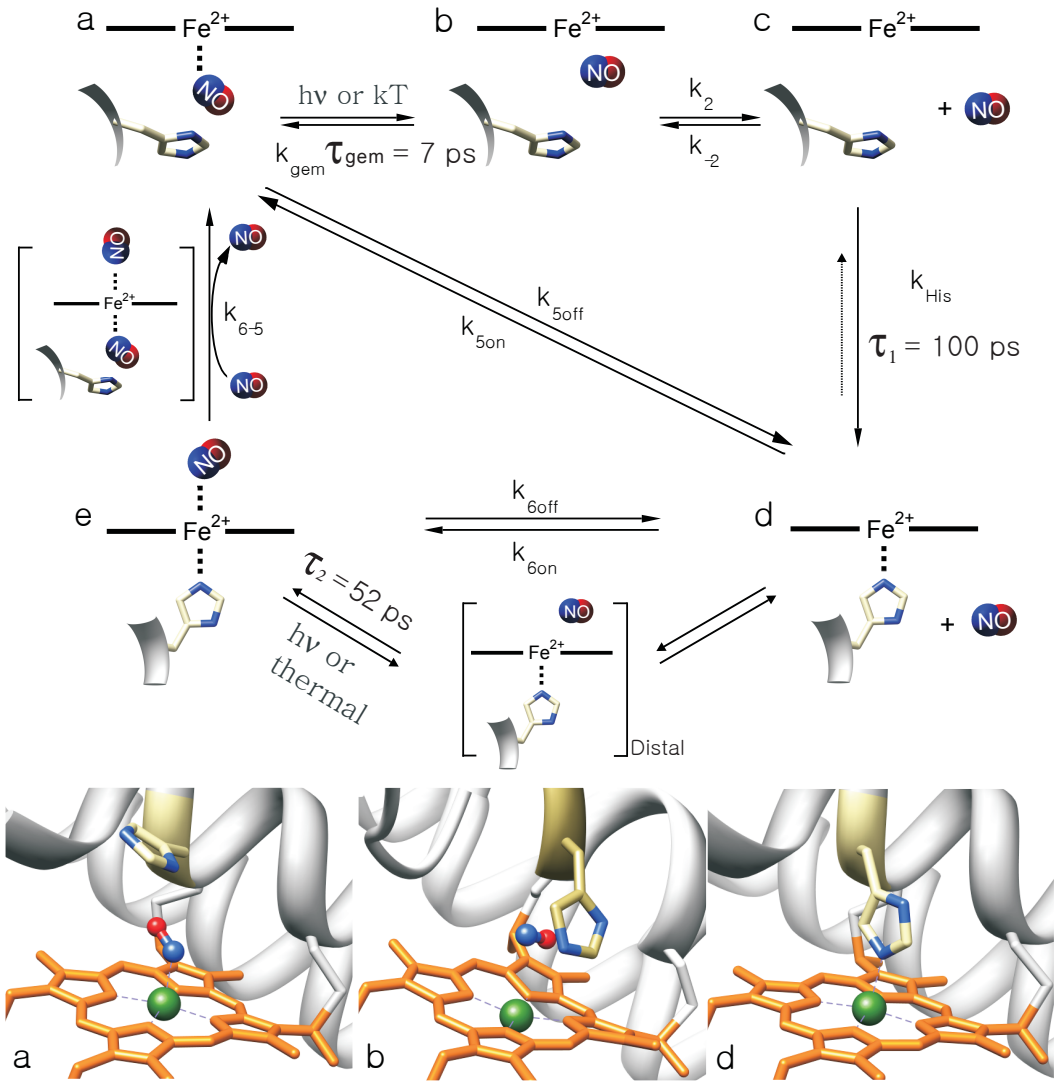

Figure 4.9: A) Model for the binding and release of NO to and from the different transient forms and coordination states of AXCP. The various species are: (a) 5c-NO AXCP with NO at the proximal side which is the starting species of our experiments; (b) transient 4c-AXCP with NO dissociated and located within the heme pocket; (c) transient 4c-AXCP with NO dissociated and located in the solvent; (d) 5c-His resting state AXCP; (e) 6c-His-NO AXCP. The rate constants: k_1, thermal dissociation of NO; k_{-1}, rebinding rate; k_2 and k_{-2}, rates for exiting and accessing the heme pocket of the 4c-AXCP; k_{His}, rate for His rebinding after NO release (the shorter arrow indicates that the back process, albeit formally possible, has a low probability to occur and is not observed); k_{6on}, NO binding rate from the solvent to 6c-His-NO AXCP; k_{6off}, rate of NO release from 6c-His-NO AXCP; k_{6-5}, rate of conversion of 6c-His-NO to 5c-NO AXCP; k_{5off}, overall rate of NO release from 5c-NO AXCP to the solvent; k_{on}, overall rate of NO binding from the solvent leading to 5c-NO AXCP. B) Equilibrium structures of (a) 5c-His and (b) 5c-NO, (c) transient 4c-AXCP at 10 ps after the photodissociation of NO from heme. The files of first two structures from Protein Data Bank are 1E84 and 1E85. The structure of transient 4c-heme of AXCP is determined by molecular dynamics simulation performed with CHARMM and took from the previous result[67]. All figures were generated by Chimera[139].

their proposed shuttling function mechanisms, the increased NO diffusion into the intracellular environment by cytochrome c' allows the cell to respond more easily to NO which could be fatal for the cell. Cells thus take advantage of cytochrome c' by decreasing NO concentration, transporting NO to the membrane. AXCP is an example with its high trapping efficiency for NO exclusion

In sGC, the important step in the molecular process of activation is the change of the heme coordination state. The formation of 6c-NO intermediate and its conversion to the activated 5c-NO species are both dependent on the concentration of NO. The first NO for the formation of 6c-NO functions as a ligand and the second as a catalytic agent for the conversion in the hypothesis of proximal binding[19]. Thus the unique binding properties of cytochrome c' could be an operating model for NO-activated sGC. However, we must remember that proximal NO binding to AXCP is demonstrated by X-ray data and supported by [NO] dependence of 5c-NO formation, whereas proximal NO binding to sGC is only hypothetical (see Chapter 2) and based only on [NO]-dependence of 5c-NO formation. Consequently, His rebinding in AXCP is firmly assigned to the proximal His, whereas in sGC the distal or proximal nature of His rebinding cannot be inferred.

4.7 Conclusion

1. Proximal histidine rebinds in 100 ps after the exit of NO from the heme pocket and thus precludes the rebinding of NO from the solution.

2. Rebinding of proximal histidine functions as a molecular trap for NO dissociated from heme.

Chapter 5

Model for the trans effect in sGC: The myoglobin mutant H93C

5.1 Introduction: trans effect

In heme proteins, a general question is whether and how NO binding produces a five coordinate complex with proximal His-iron bond cleavage. If the His-Fe bond is weak (for example, because of internal constraints), then the rupture of the bond between iron and histidine is accomplished and this produces a 5c-NO species[19, 142]. This event is important for the function of enzymes, especially in the NO-receptor sGC. NO binding to ferrous heme can give rise either to pure 5-coordinate or to pure 6-coordinate complexes with proximal histidine in the second axial coordination but may also yield a mixture of both. Mb (6c-NO) and sGC (5c-NO) are representative examples of these two limit conformations whose change bears important biological roles. The general question of whether NO binding produces a five coordinate complex or not can be investigated by studying NO binding dynamics in myoglobin mutants. Previously it has been reported that H93G Mb whose proximal histidine is replaced by glycine forms 5c- or 6c-NO species depending on the concentration of exogenous imidazole. Our group performed TA measurements for this mutant and found that both 5c- and 6c-NO H93G have bi-exponential character for the geminate recombination of NO with variously different amplitudes. Although H93G at low concentration of imidazole can have 4-coordinate heme right after photolysis, NO rebinding to 4c-heme was not clearly separated as a 7.5-ps mono-exponential component in H93G-Mb.

Our approach for investigating NO binding induced trans effect is to introduce a constraint to the proximal ligand by replacing His with Cys. Likewise the glycine in H93G, cysteine cannot interact with heme when it is reduced[143]. However, the distal histidine (His64) in H93C does bind to the heme iron in the distal side; whereas this coordination

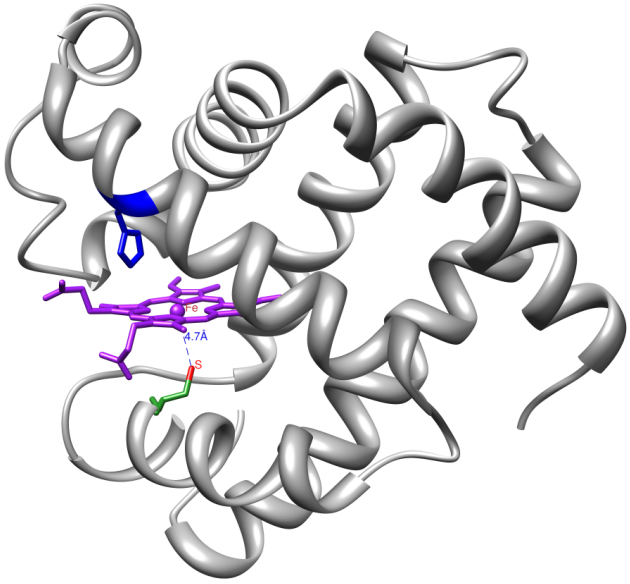

Figure 5.1: Predicted structure of the mutant H93C-Mb from dynamics simulation.

cannot be found in case of H93G and NO can bind to the vacant proximal side since cysteine is not coordinated. Hence we can assume that the NO (CO) rebinding properties of H93C will not be the same as in other Mb mutants. Our aim is to estimate the effects of constraints in H93C-Mb on CO and NO dynamics.

5.2 Structure of H93C-Mb and steady-state equilibrium

The structure of H93C was determined from the result of calculation from dynamics simulation and energy minimization using CHARMM (Figure 5.1). From our predicted structure, we can consider that the mutation H93C does not induce any change of the whole protein fold or the position of the heme. The structural difference between wild-type Mb and its mutant H93C is displayed in Figure 5.2. The distance between heme iron and histidine 93 residue in wild-type Mb is 2.1 $\mathring{A}$ but the distance between heme iron and sulfur atom of cysteine residue is predicted to be 4.7 Å. The superposition of Mb and its mutant H93C structures reveals a slight movement of the distal His 64. However, other residues near the heme remain almost in the same coordinate after mutation.

Hilderbrand *et al.* showed water coordination to ferric heme iron to become five coordinate H93C and this coordination is stabilized through hydrogen bonding with distal histidine residue[143]. In some way, we may consider that there is an inversion of distal and proximal sides, so that His64 became proximal. Small red shift caused by the ligation of water to the ferric heme iron occurred similarly with the wild type myoglobin[116]. NO can bind to both ferric and ferrous wild type myoglobin and to H93C Mb mutant as shown in Figure 5.3. When

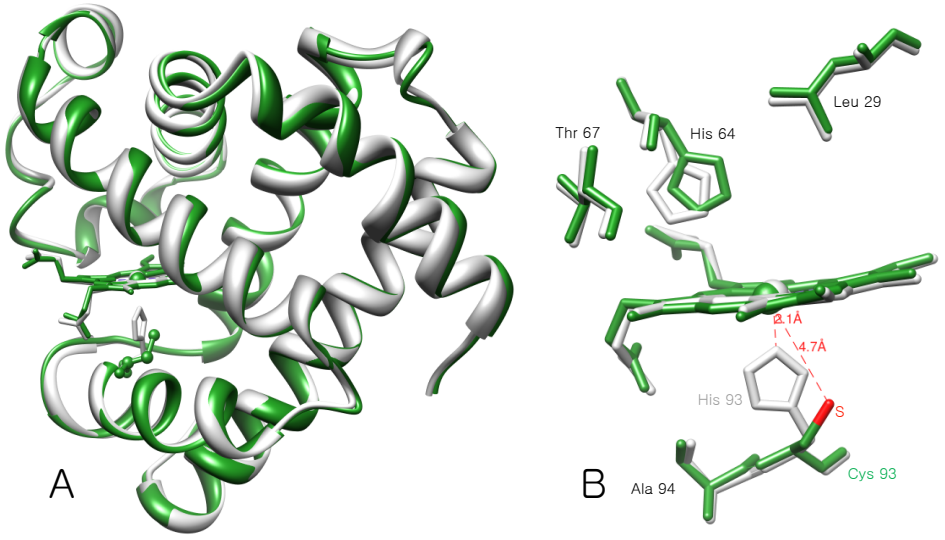

Figure 5.2: A, Superimposed structures of wild type Mb (grey) and H93C-Mb (green). B, Superposition of the heme pocket with closer distal and proximal side-chains.

NO is bound to wild type Mb, the characteristic Soret band appears at 418 nm corresponding NO-6-coordinate species. In Figure 5.3-A and B, a Soret maximum at 400 nm appears on binding of NO to the H93C for both ferric and ferrous heme. We must also note similarity of the Q-bands for both NO species. This means that ferric H93C becomes a reduced and 5-coordinate complex upon binding of NO, similarly with ferrous H93C.

Complexes (ligand)	**Coordination**	**Distance (Å)**	**Reference**
H93C	Cys	4.7	-
eNOS	Cys	2.3	[144]
Chloroperoxidase (NO)	Cys	2.3	[145]
Chloroperoxidase (CO)	Cys	2.4	[145]
P450cam	Cys	2.2	[126]
Mb	His	2.1	-
Cytochrome c'	His	2.1	[69]
Cytochrome c'	NO	2.0	[69]

Table 5.1: Comparison of the distance between S and Fe of H93C-Mb with other relevant proteins.

We can compare the electronic spectra of human Mb mutant with horse heart Mb mutant (89 % sequence identity) to identify the nature of the bond causing the Soret band at 400 nm. It was predicted that NO adducts of H93C and H93Y human Mb mutant are in a five coordinate structure with the coordination of cysteine to the heme iron[146]. But Hildebrand et al. found that horse heart Mb mutant H93C possesses a five-coordinate ferrous iron center with a distally bound water molecule which is stabilized through a hydrogen bonding network and there is no ligation between the heme iron and sulfur atom of cysteine residue[143]. For

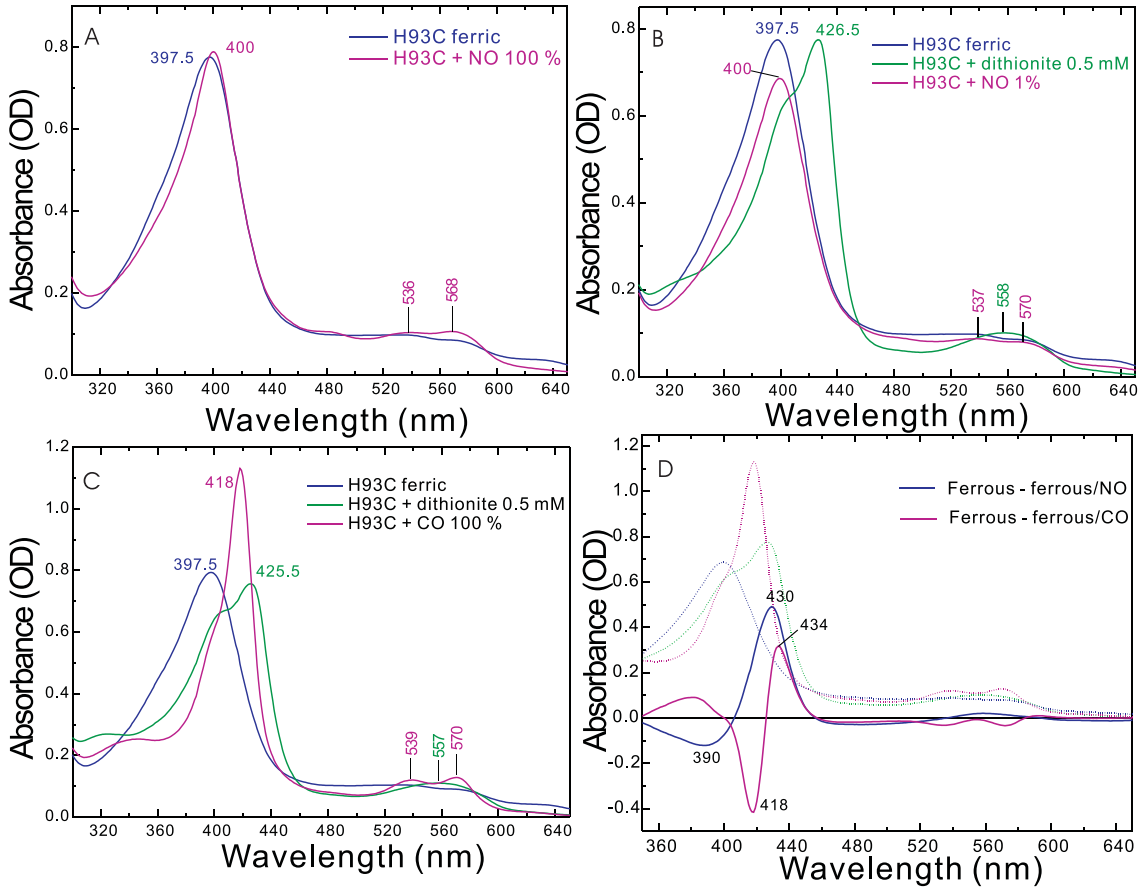

Figure 5.3: A) Electronic absorption spectra of ferric H93C-Mb and with NO. B) Ferrous form of H93C with and without NO. C) Ferrous form of H93C with and without CO. D) Static difference spectra for NO and CO-bound H93C. Note that H93C-Mb/CO was not fully reduced.

this reason, our results show that the origin of the bond between heme iron and cysteine cannot sustain in line with the large distance between Cys and Fe: 4.7 Å. Two different groups found that the iron in the reduced form of both H93C mutants is coordinated by the distal His64 instead of water and this gives a space for proximal binding[143, 146]. Thus, NO replaces His64 to become ferrous 5-coordinate complex, leaving the cysteine unliganded.

In Figure 5.3-C, the absorption maximum of Soret appears at 418 nm which is characteristic for 6c-CO species and this result seems similar to the CO complex of wild type myoglobin. This shows that H93C has a distal coordination by His64 and proximal CO coordination to the heme iron from this similarity and previous results from Hildebrand group. Human Mb mutant H93C and H93Y are known to have 6-coordinate CO heme iron in the proximal rather than distal side on addition of CO to each protein revealed by resonance Raman spectra[146]. In the Table 5.2, the maximum of Soret of H93C is compared with other heme proteins of interest which is similar with that of H93C for the respective ligand.

Proteins	Coordination	Soret	Reference
		nm	
Fe(III) complexes			
H93C	Cys	397.5	[146]
sGC	His	393	[38]
Cytochrome c'	His	401	Chapter 4
Fe(II) complexes			
H93C	His	426.5	
sGC	His	431	Chapter 2
Cytochrome c'	His	425	Chapter 4
Fe(II)-CO complexes			
H93C	His	418	[143]
sGC	His	423	Chapter 2
Cytochrome c'	His	418	Chapter 4
5-coordinate Fe(II)-NO complexes			
H93C		400	
sGC		398	Chapter 2
Cytochrome c'		396	Chapter 4
6-coordinate Fe(II)-NO complexes			
Mb	His	420	
Cytochrome c'	His	420	Chapter 4

Table 5.2: Comparison of the Soret absorption between H93C-Mb complexes and other heme proteins.

5.3 Geminate rebinding of nitric oxide to H93C-Mb

While reduction of H93C with dithionite does not yield 100 % reduced heme (shoulder at 403 mnm), the addition of NO induces 100 % nitrosylated ferrous heme, as observed in the case of wild type Mb[147–149] (Figure 5.3-A and B). This nitrosylated ferrous heme as a Soret maximum at the same position (400 nm) as sGC and AXCP, while the aquo-ferric heme Mb Soret maximum is located at 391 nm[150]. We consequently readily assume that the H93C-NO species is 5c-NO and will produce a 4c-heme upon dissociation.

In Figure 5.4-A, raw transient difference spectra at successive time delays after photodissociation of NO are displayed. Photolysis of NO from the 5c-NO-H93C indeed brings on a bleaching centered at 397 nm and the maximum of broad induced absorption located at about 429 nm. This shape is very much similar with that of AXCP and sGC as seen by the comparison of the main SVD spectral component associated with NO rebinding for the three proteins (Figure 5.4-B). Only a small contribution due to the excited state relaxation, which occurs in 2-3 picoseconds time range, was excluded here. Contrary to Mb, geminate recombination of NO to the 4-coordinate ferrous iron after photodissociation is observed in its H93C mutant. Previously we found that H93G mutant after treating of low concentration of imidazole has a 5-coordinate species with NO[21] and its transient spectral component from main SVD spectral component is also displayed as blue. However, the H93G (imidazole) nitrosylated Mb

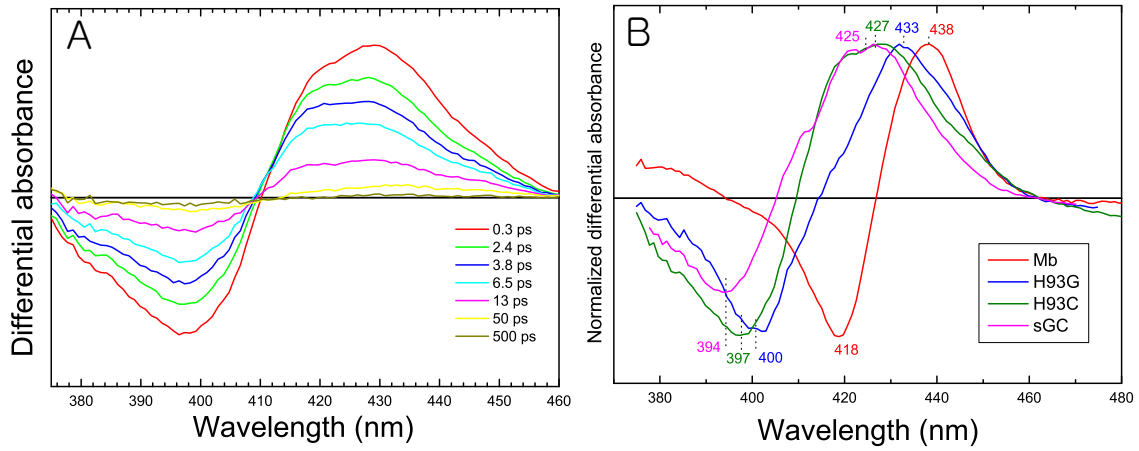

Figure 5.4: A, Transient spectra (raw data) at different time delays after photodissociation of NO for ferrous H93C-Mb. B, Main spectral SVD component of H93C-Mb and other relevant proteins. NO 1 % in gas phase.

mutant did not yield a pure 5c-NO species due to the permanent exchange of imidazole at the proximal position. We assign the bleaching centered at 397 nm to the disappearance of 5c-NO-H93C species based on the similarity with sGC and AXCP and subsequent geminate recombination to form 5-coordinate Fe^{2+}-NO.

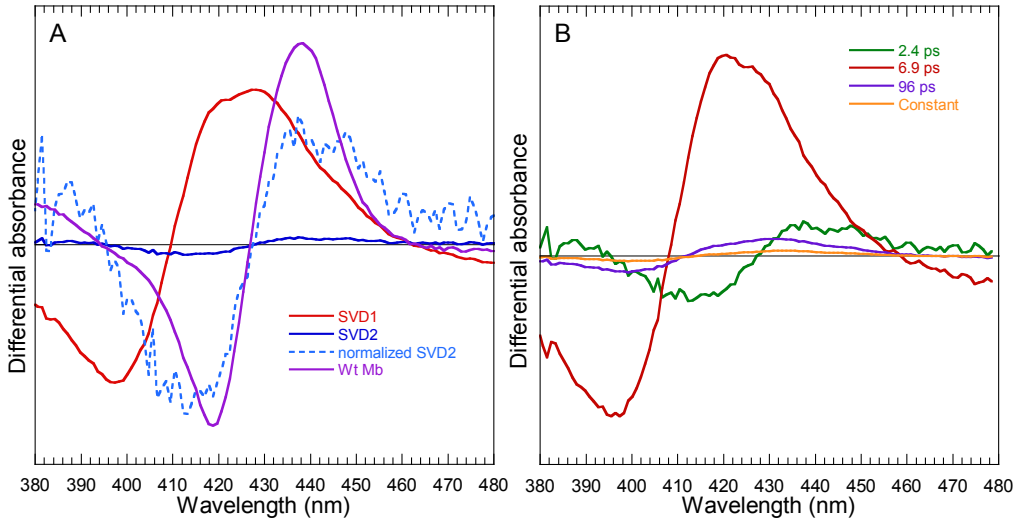

Figure 5.5: A, SVD1 (red) and SVD2 (blue) spectral components for H93C-Mb/NO, obtained from the raw transient spectra in Figure 5.4-A. B, Differential TA spectra associated with each decay components.

SVD analysis of the raw TA data in Figure 5.4-A was performed to detect any contribution other than NO rebinding to 4c-heme (Figure 5.5-A). The rebinding process of NO to 4c-heme causes a broad induced absorption centered at 425 nm and a bleaching recovery at

398 nm as found for sGC, SONO, and AXCP. Figure 5.5-B represents the calculated DAS spectra of each decay components. The decay components for DAS spectra were obtained from the fitting the two SVD kinetic traces of (Figure 5.6). For SVD1 component, two (7.1ps and 95 ps) fast components and a constant term were applied to fit with bi-exponential function. Secondly, SVD2 component was fitted with two fast components (one excited state decay and the other decay for geminate rebinding of NO) and a slower component (120 ps) was detected.

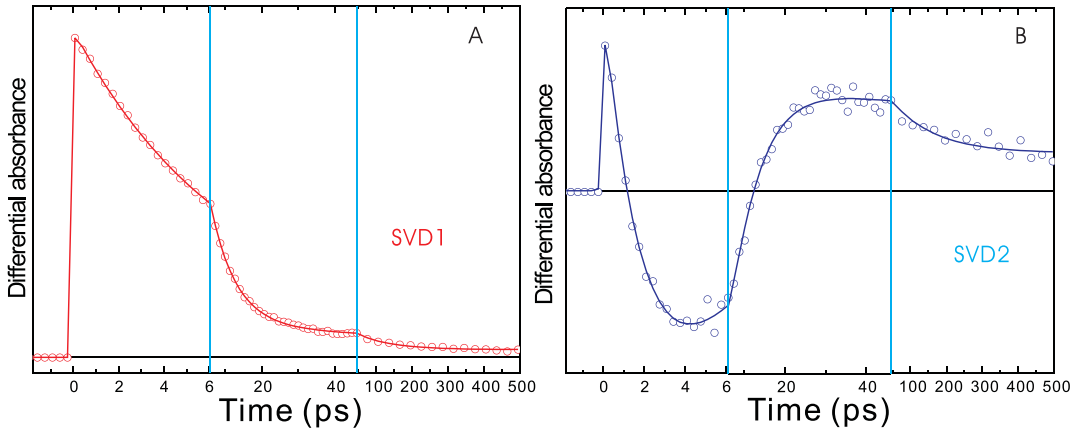

Figure 5.6: NO rebinding kinetics of the A) SVD1 and B) SVD2 for H93C-Mb upto 500 ps.

SVD1 component				SVD2 component				
Singular Value	τ_1 (ps) A_1	τ_2 (ps) A_2	Cst	Singular Value	τ_1 (ps) A_1	τ_2 (ps) A_2	τ_3 (ps) A_3	Cst
0.4938	6.9 *0.89*	96 *0.09*	*0.02*	0.0295	2.4 *0.48*	6.8 *-0.44*	96 *-0.05*	*0.03*

Table 5.3: Fit parameters of NO rebinding kinetics of H93C-Mb.

Kinetic parameters for the two SVD components are given in Table 5.3 with their singular values. DAS spectrum (7.1 ps) composes of mono-exponential NO rebinding to 4c-heme, characteristic and observed in other proteins yielding 4c-heme. On the other hand, SVD2 is clearly different from SVD1 and could correspond to the minor rebinding of NO to become 6c-NO heme. However, this SVD2 spectral component does not correspond to that of NO rebinding to 5c-His WT Mb (violet trace in Figure 5.4-A) but rather matches that of His rebinding to the 4c-heme observed in sGC (Chapter 2) and AXCP (Chapter 4). Thus we assigned the DAS associated with the **120 ps component** only contained in SVD2 to **His rebinding**. The 120 ps time constant makes plausible the existence of the slower 95 ps component of NO rebinding to 4c-heme, which, interestingly, exists also for the His93Gly Mb

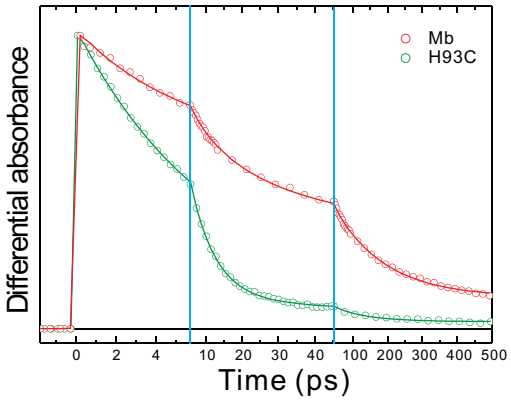

Figure 5.7: Kinetics of NO geminate rebinding to H93C-Mb and Mb obtained by SVD analysis.

mutant. Unfortunately, it is not possible to determine unequivocally whether the side-chain for this 5c- species is the Cys93 or His64 from our results. This needs to be clarified by structural studies such as time-resolved Raman spectroscopy.

The kinetics of NO rebinding to Mb and its mutant H93C is compared in Figure 5.7. The traces are normalized and the kinetic parameters for H93C are compared with other heme proteins in Table 5.4. It appears that the proximal mutant H93**C** contributes a better model than H93**G** to investigate properties of sGC and NO-sensors that we will discuss in light of H93C behavior.

Species	τ_1	A_1	τ_2	A_2	τ_3	A_3	**C**	A_4	Reference
	ps		*ps*		*ns*				
Mb	13	*39.5 %*	147	*46.5 %*			cst	*14 %*	Chapter 7
H93G	15	*63 %*	95	*25 %*			cst	*12 %*	[151]
H93C	7.1	*91 %*	95	*8 %*			cst	*1 %*	-
sGC	7.5	*97 %*					cst	*3 %*	Chapter 2
AXCP	7.0	*99 %*					cst	*1 %*	Chapter 4
NOS	36	*23 %*	400	*14 %*	18	*63 %*			[121]

Table 5.4: Parameters for NO rebinding to selected heme proteins. Kinetics are fitted with the function $\sum A_i exp(-t/\tau_i)$ + C. Excited state decay, included in the fit, is not indicated in the Table.

5.4 Geminate rebinding of carbon monoxide to H93C-Mb

We investigated CO dynamics after photodissociation in H93C because there is a strain on the His and we wish to compare with CO dynamics in sGC in the presence of activators, which also induce a strain on the heme pocket. Figure 5.8-A shows the raw difference transient absorption spectra from 4 ps to 5 ns after CO photodissociation from H93C-CO complex. A

bleaching centered at 419 nm decreases until 5 ns with a small shift of the minimum of bleaching. The induced absorption centered at 435 nm decayed simultaneously with a small shift. This shift appears with the movement of the isosbestic point, showing that more than one process takes place, similarly to the observations in the case of sGC/YC-1. To disentangle the contributions from the different transient species, SVD analysis of the raw data matrix was performed.

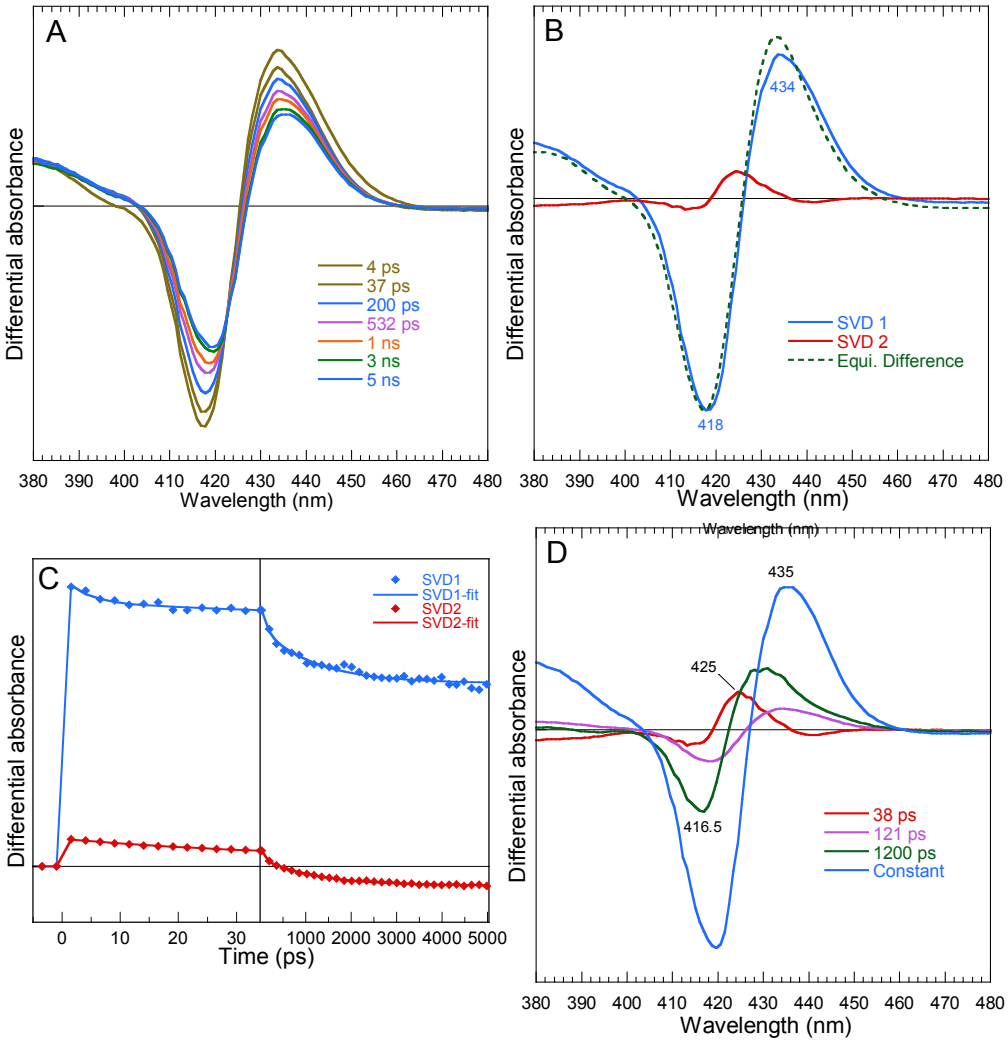

Figure 5.8: A) Raw transient absorption spectra of H93C-Mb at different time delays after photodissociation of CO. B) Two spectral components from SVD analysis. C) Kinetic components associated with the two SVD components. D) Differential TA spectra associated with decay components.

Two distinct SVD spectral components are shown in Figure 5.8-B. For SVD1, bleaching centered at 418 nm together with the induced absorption at 435 nm is similar to equilibrium difference spectrum and corresponds to the rebinding process of CO the 5c-His heme yielding 6c-CO complex. On the other hand, SVD2 is clearly different from SVD1 and may correspond

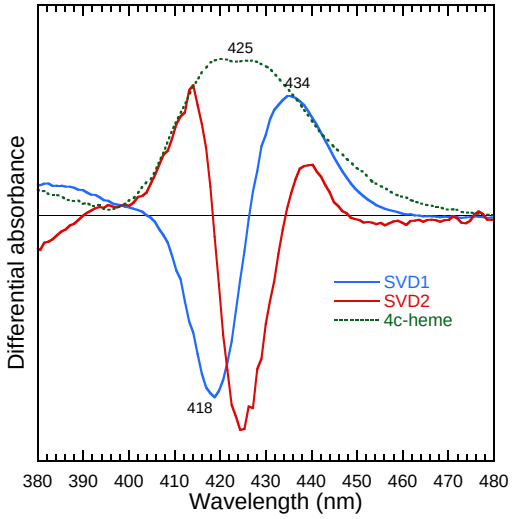

Figure 5.9: Calculated 4c-heme of H93C-Mb and two SVD spectral components obtained from H93C-Mb/CO.

to a minor population of 5c-CO heme. Importantly, we must notice that the shapes of both SVD spectral components are similar to those found in sGC interacting with CO in the presence of activators (Chapter 2), but not their associated singular values. We calculated the absolute spectra from H93C-NO transient spectra before and after pump pulse (Figure 5.9). The two SVD spectral components obtained from H93C-CO were compared with the spectrum of 4c-heme. SVD1 corresponds to the CO rebinding to 5c-His but SVD2 component appears after the subtraction between 4c-heme and 5c-CO. We can notice that the left part of the spectrum matches with the spectrum of 4c-heme. This calculated absolute spectrum of 4c-heme strengthens the existence of 5c-CO. For SVD2, the two lobes of induced absorption, on each side of the bleaching, correspond to the spectrum of the 4c-heme, as calculated in Figure 5.9, so that the bleaching can be assigned to the 5c-CO species whose Soret maximum (425 nm) is close to that of 6c-CO. The steep bleaching at 425 nm in SVD2 is due to the disappearance of 5c-CO complex. SVD2 component arises from CO rebinding to the transient 4c heme and consequently reforming minor contribution of 5c-CO complex. Rebinding of CO to the H93C myoglobin mutant is clearly different from that of wild type of Mb (Figure 5.10). Thus, some key points need to be mentioned when the ligand is CO. First of all, trans effect differ in two cases, 6-coordinate CO-Fe-His vs 6-coordinate CO-Fe-Cys. Apparently bond between iron and His is stronger than that between iron and Cys. This bond can be broken by either thermal energy or by trans effect due to ligand binding.

Two SVD components with higher singular value were found after calculation on the raw transient spectra (5.8). Raw transient spectra showed a spectral shift both in bleaching and induced absorption, similarly with sGC with activators. For SVD1 component, the excited state component (4 ps) is included but not in SVD2 (its amplitude vanished). A slower component (121 ps) was detected only in SVD1 but longest one (1.2 ns) was found for both

SVD1 component					SVD2 component			
Singular Value	τ_1 (ps) A_1	τ_2 (ps) A_2	τ_3 (ns) A_3	Cst	Singular Value	τ_1 (ps) A_1	τ_2 (ns) A_2	Cst
4.21	4.0 *0.10*	121 *0.09*	1.2 *0.19*	*0.62*	0.41	38 *0.29*	1.2 *0.42*	*0.29*

Table 5.5: Fit parameters of CO rebinding kinetics of H93C-Mb.

components. Kinetic parameters for the two SVD components are given in Table 5.5 with their singular values. The decay associated spectra (DAS) for each exponential component were calculated from the SVD spectra and the amplitudes of exponential components (Figure 5.8-D). DAS (121 ps) and constant represent CO rebinding to 5c-His because the position of bleaching and induced absorption well matches with the static absorption difference spectrum (Figure 5.3-D). However, DAS (38 ps) does not follow the static difference spectrum and this can be assigned to the CO rebinding to 4c-heme. A longer component (1.2 ns) can be due to His rebinding to 4c-heme because it is slower than the previous component. This lifetime seems quite large for a 4-ccordinate ferrous heme, but it can be due to a protected environment and to particular constraints in this protein. Future experiments are necessary to strengthen this explanation.

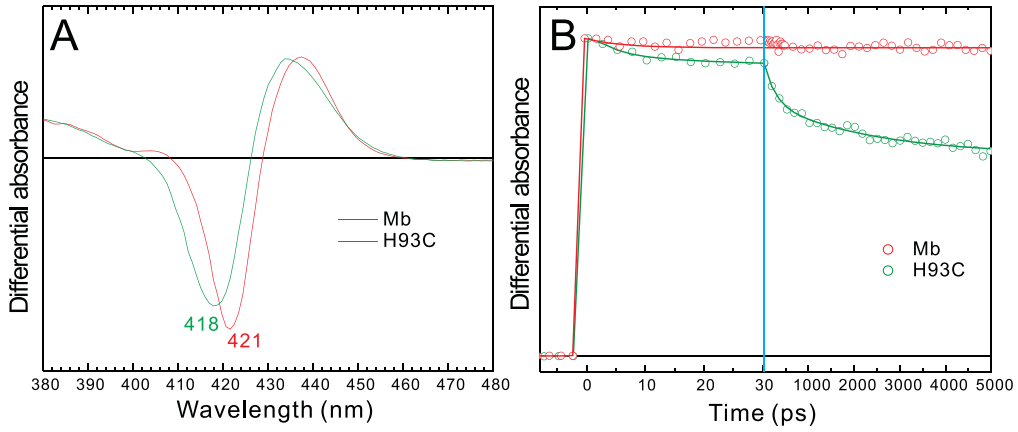

Figure 5.10: A, Spectral component from SVD analysis associated with the geminate rebinding of CO the the wild type and H93C-Mb. B, Kinetic component associated with the SVD1 spectral component of CO rebinding for the wild type Mb and H93C-Mb.

Difference between WT-Mb and H93C relevant to CO dynamics are shown in Figure 5.10-A. The main SVD1 spectral component and kinetic traces are normalized and the parameters of the fits are listed in Table 5.6 with other values. These spectral contributions represent the transition from 5-coordinate minus 6c-CO ferrous heme and the difference in position of Soret maximum reflects different strains exerted on the hemes of both proteins. The small

proportion of protein still in ferric form (Figure 5.3-C) does not contribute to the transient signal because CO does not bind to ferric Mb. Rebinding of CO to the H93C is clearly different from that of wild type of Mb. It is known that the rebinding of CO to the ferrous heme iron is slower than that of NO and O_2 due to the different electronic interaction between the ligand and heme iron[152]. CO rebinding processes have multi-phase character in some heme proteins but geminate rebinding of CO is scarcely observed in heme proteins on the picosecond time scale. In wild type Mb, CO after photo-dissociation does not escape from the heme pocket on the picosecond time scale[153], whereas two time constants were found for the H93C which are of same order of magnitude as AXCP (Table 5.6).

Protein	τ_1	A_1	τ_2	A_2	τ_3	A_3	Constant	Reference
	ps		*ps*		*ns*			
H93C			121	*9 %*	1.2	*19 %*	*62 %*	
sGC			118	*2 %*	3.2	*3 %*	*97 %*	Chapter 2
sGC/BAY			120	*13 %*	2.2	*14 %*	*73 %*	Chapter 2
β1 (1-190)/BAY	9.7	*15 %*	99	*21 %*	0.73	*23 %*	*41 %*	Chapter 3
AXCP			218	*4 %*	1.9	*58 %*	*38 %*	Chapter 4
CooA			78	*60 %*	0.39	*30 %*	*10 %*	[112]
DosH					1.5	*60 %*	*40 %*	[154]

Table 5.6: Dynamics of CO with different proteins. Parameters obtained by fitting the kinetic of the two main SVD components with the function $\sum A_i exp(-t/\tau_i) + C$. DosH: isolated heme domain of Dos.

Even for heme proteins disclosing a picosecond geminate rebinding component for CO, like AXCP (Chapter 5), the CO-sensor CooA[107] or the isolated heme domain of the O_2-sensor DOS[154], CO rebinds to only one species, *i.e.*, there exists only one SVD spectral component corresponding to CO rebinding to 5c-His. In the case of H93C-CO there are two SVD spectral components, which are identical to that observed for sGC in the presence of activators. From our SVD analysis, we conclude that, like in sGC, CO rebinds both to the 4c-heme and 5-His heme, leading the 5-CO and 6-CO species. The fast CO recombination to the 4-heme is due to a very low energy barrier to binding as a consequence of the in-plane position of the iron ([152, 155], see also Chapter 7), while the ns-range rebinding is due to a higher barrier for CO escape into the solvent, increasing the probability of interaction with the iron. This increased barrier is provided by modified environment of the heme in the mutant H93C Mb. The distal amino acid residues play an important role in forming a docking site that controls the geminate rebinding rate and orientations of dissociated CO which rapidly rotates and it does not escape from the heme pocket[156, 157]. Rotational freedom of CO can be more restrained in the heme pocket of H93C and consequently increases probability of geminate rebinding of CO.

5.5 The relevance of CO and NO dynamics in H93C-Mb with sGC

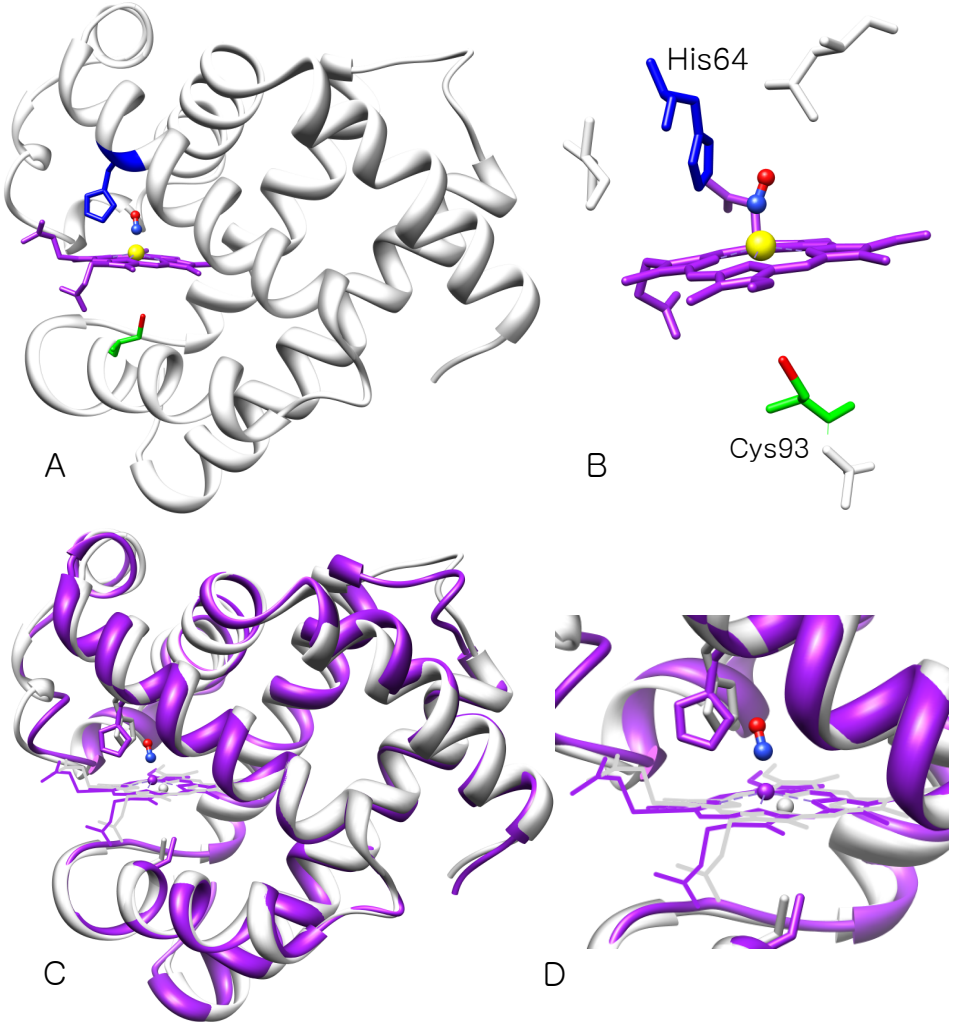

Figure 5.11: A) Structure of H93C-Mb coordinated with NO, B) Close-up view of NO-bound H93C-Mb near heme. C) Superposition of H93C-Mb/NO (violet) and H93C-Mb without NO (grey). D) Superposition of heme ± NO near heme pocket.

In proteins presenting a marked trans effect yielding 5c-NO, the rebinding of NO to the 4c-heme always proceeds with a 7 - 7.5 ps time constant and high amplitude (see also NO-sensors in Chapter 3, not listed in Table 5.6) and this process is mono-exponential. This value seems to be the limiting one for this ultrafast process that is barrierless and only a small population of dissociated NO can go out of the heme pocket. The mono- or bi- exponential character of NO rebinding can be influenced by the protein structure, which provides an energy barrier leading to the second slower component. Two components of NO recombination for H93C are observed ($\tau_1 = 7.1$ ps and $\tau_2 = 95$ ps), the amplitude of the second component being very

low, contrary to H93G that has similar 4-coordinate heme after photo-dissociation. Although many previous results have shown that NO rebinding to any kind of mutants of Mb has bi-exponential components, the origin of two picosecond geminate rebinding components for H93C should be interpreted differently from other mutants of Mb[158–160] which are *distal* mutants, contrary to H93C.

Structural simulation of H93C supports the coordination of NO at the distal side and Fe-S bond cleavage (Figure 5.11). The position of heme residues is apparently different from that of wild-type Mb. Bond strength between Cys93 and heme iron is weaker than in wild type Mb and is broken by external ligands (NO and CO) inducing more 4c-heme. Both H93C and sGC can have 4-coordinate heme after photolysis but the unique mono-exponential rebinding of NO is only seen in sGC and NO-sensors and is not due to the 4-coordinate heme itself but to the heme environment.

From the comparison of both proteins we can infer the following:

1. Because the amplitude of NO rebinding to the 4c-heme is always $\geq$ 90 %, then NO release from the protein (deactivation) involves modulation of energy barriers due to the protein structure (see also the case of AXCP in Chapter 4).

2. Trans effect due to NO (and in a less extent to CO) is amplified by strain exerted on the proximal iron-bound side-chain. In the case of H93C Mb, the increase of Fe^{2+}-S distance weakens this bond, whereas in sGC this strain is due to the protein structure itself, so that the rupture of this bound is sensed by the structure.

3. CO can also induce a trans effect. Its dynamics is governed by a fast phase of geminate rebinding to the 4c-heme and by energy barriers for escape into the solvent due to protein structure.

4. In light of the similar CO dynamics in H93C and in BAY-activated sGC we can infer that the activators BAY 41-2272 and YC-1 induce further strain to proximal His in sGC, in line with their binding to the heme domain deduced from their similar effects observed in the *Clostridium botulinum* NO-sensor homologous to sGC.

Chapter 6

Dynamics of NO in NO-synthase, The endogenous source of Nitric Oxide

6.1 Introduction

The source of NO to be bound to sGC *in vivo* is achieved by the enzyme nitric oxide synthase (NOS) in various cells, which has been identified in mammals as three different isoforms, cloned and expressed[22]. In endothelial cells of arteries, binding of acetylcholin or bradikynin from the blood flow to their specific membrane receptors induces release of Ca^{2+} which induces calmodulin binding to eNOS, triggering the synthase of NO. The biochemistry of eNOS is summarized in Figure 6.1. The generation of NO in the cell requires the presence of several cofactors.

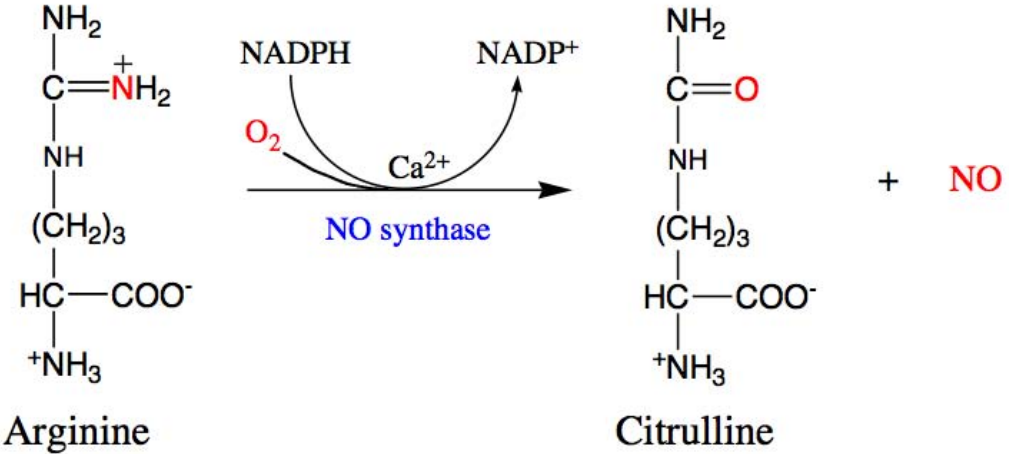

Figure 6.1: Overall production of NO by eNOS. From arginine and dioxygen, NO is generated as a by-product together with citruline. This process needs Ca^{2+}, NADPH, and calmodulin.

NOS catalyzes the oxidation reaction of arginine into citrulline and the produced NO from oxygen near to the heme. The structure of NOS is composed of two distinct domains, a reductase domain that binds the cofactors FMN and FAD and an oxygenase domain that harbors the heme for O_2 ligation. A ribbon diagram of heme domain monomer part of eNOS is displayed in Figure 6.2. When the substrate arginine (Arg) is bound to its specific site of eNOS, the reaction is triggered by the binding of NADPH which provides electrons, which are transferred through the cofactors FMN, FAD, and BH_4. The enzyme is regenerated after NO synthesis by the release of oxidized $NADP^+$ and binding of a reduced NADPH. Because NO is produced close to the heme, there is a large probability for binding to the heme and this role in the regulatory mechanism of eNOS must be taken into account.

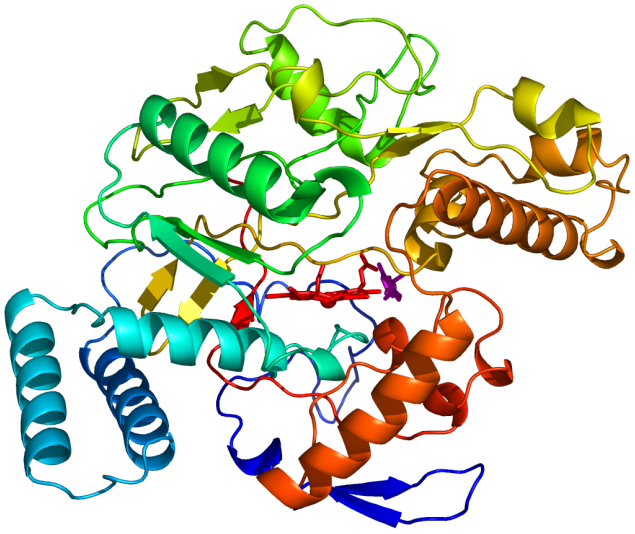

Figure 6.2: Ribbon diagram of eNOS heme domain monomer. The atomic coordinate files were taken from the Protein Data Bank (ID: 1NSE, [144]) and the figure was generated using PYMOL.

A previous report examined the kinetics of NO rebinding after photodissociation in the heme pocket of human eNOS by means of TA spectroscopy[121]. It was found that geminate recombination of NO occurs in all conditions and states of eNOS and that this process was strongly modulated by the substrate binding of L-Arg. One fast ps geminate rebinding phase and the other slower ns phase appears in both ferric and ferrous states. The rates of the two phases became lower and their relative amplitudes were altered in the presence of L-Arg. Importantly, the nanosecond kinetic component is assigned to the rebinding of NO that is still located in the protein core but not in the heme pocket. Such a ns geminate rebinding component is not observed in other heme proteins and in particular in case of the NO receptor sGC, Mb, and SONO's. In the previous chapters, we found that the geminate rebinding of NO to the heme is closely controlled by the protein structure. When we compare the geminate

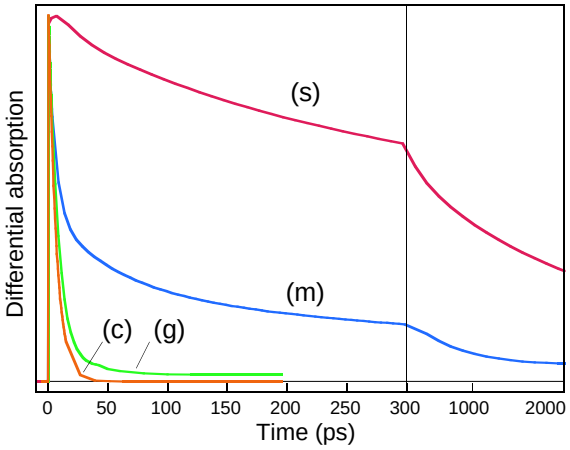

Figure 6.3: The kinetics of NO geminate rebinding are compared for four different heme proteins up to 2 ns, eNOS (s), Mb (m), sGC (g), and AXCP (c).

rebinding kinetics for sGC and eNOS, we can clearly distinguish their differential controls on NO, which are respectively the source of NO and the receptor of NO in cells. Their kinetic profiles for NO rebinding are compared in Figure 6.3 in order to show the influence of the protein structures. For sGC, NO rebinding is extremely fast and mono-exponential (7.5 ps, 97 %), whereas it is multi-phasic and relatively slow for eNOS[121]. Whereas, the geminate rebinding process appears bi-exponential for the 6c-NO-His Mb and Hb, it occurs with three exponential phases for the 6c-NO-Cys eNOS. Large dynamic range for NO in eNOS depends upon the state of the enzyme[121]. Hence, we designed our study of eNOS from the fact that NO geminate recombination will be dependent on the redox state, presence of substrate, allosteric effectors and cofactors. Since the enzyme turn-over depends upon the presence of cofactors and since eNOS changes its redox state during turn-over, we aimed at comparing the influence of cofactors, inhibitors and redox states on NO release. We will try to separate the purely steric effects from the allosteric effects.

6.2 Regulation of eNOS: NO dynamics

We present here the NO dynamics in eNOS under different conditions. It covers the effects of substrate analog (NMA), cofactor (BH_4), the reaction intermediate L-hydroxy-arginine (L-NHA) and an inhibitor (SEITU). These effectors bind close to the heme site and may change the energy barrier for NO rebinding and release either by providing a direct steric hindrance or by modulating the conformation of the heme pocket. All kinetic figures from now on show the normalized kinetics of NO rebinding in two time windows up to 5 ns, whose parameters were obtained by fitting with a multi-exponential function the SVD kinetic component associated with geminate rebinding. The raw transient spectra are compared in Figure 6.4 in the presence of several effectors. For the ferrous eNOS (Figure 6.4-A) the spectrum keeps its shape in the presence of BH_4 (Figure 6.4-B) with slight difference of decay time. For the ferrous species,

the transient spectra at 7 ps has an isosbestic point slightly shifted with respect to that of the longer time spectra except Arg-bound eNOS. For NHA and NMA bound eNOS, the shift disappeared as shown in Figure 6.4-C and E. This indicates that the photodissociated excited state heme is different when these two substrates are bound to eNOS. This tendency also appears in case of ferric eNOS species[121]. Because this shift is observed at early times ($<$ 10 ps), we assigned it to the excited state decay. We can notice that the presence of SEITU induces an almost constant bleaching centered at 438 nm as shown in Figure 6.4-D. To analyze the effect on NO release for each species, we performed SVD calculations and displayed the kinetics to demonstrate the effect of each effector in the following section.

6.2.1 Effect of inhibitor: SEITU (S-Ethyl-Isothio-Urea)

We compared here the kinetics in the presence and absence of SEITU. This experiment was performed on the ferrous form eNOS because the ferric form does not bind NO in the presence of SEITU, albeit ferric eNOS binds NO in the absence of SEITU. This implies that SEITU influences the heme conformation, or the electrostatic potential of heme pocket in the ferric form. The ferrous eNOS was prepared from the purified ferric species by reducing with NADPH in the presence of calmodulin, which is actually its natural cofactor for activation. An aliquot, 5 μL of 20 mM NADPH was added to 1 mM final concentration. Concentration of eNOS is about 60 μM. The reduction is followed by recording the steady-state spectrum before to replace argon by 1 % NO. The kinetic traces are displayed in Figure 6.5 and were fitted with three exponential decay components and fitted parameters in Table 6.1.

The amplitudes of all components of geminate rebinding strongly changed when SEITU is bound to eNOS, whereas time constants are slightly slower. The overall decay becomes slower due to the large increase of the constant term in presence of SEITU. For both cases, BH_4 is present. This inhibitor almost abolishes the rebinding of NO. Overall, it shows a dramatic difference of reactivity induced by SEITU and only a small fraction of picosecond rebinding phase occurred in its presence.

Because NO newly synthesized from eNOS is released from the protein in s-ms, we probed also NO dynamics in this time range. Figure 6.6 and 6.7 presents this kinetics recorded (at 437 nm) with the same apparatus as for sGC/CO/activators measurements at IBPC. They are fitted to a bi-exponential function with parameters listed in Table 6.2. The time constant of first component, slower than the pulse duration ($\sim$ 6 ns), is not influenced by the presence of SEITU or BH_4, (slightly increased only in the presence of both) but the amplitude ratio between geminate and bimolecular rebinding has changed. The time constant of bimolecular rebinding is not influenced. The rise of the signal corresponds to the pulse shape which is

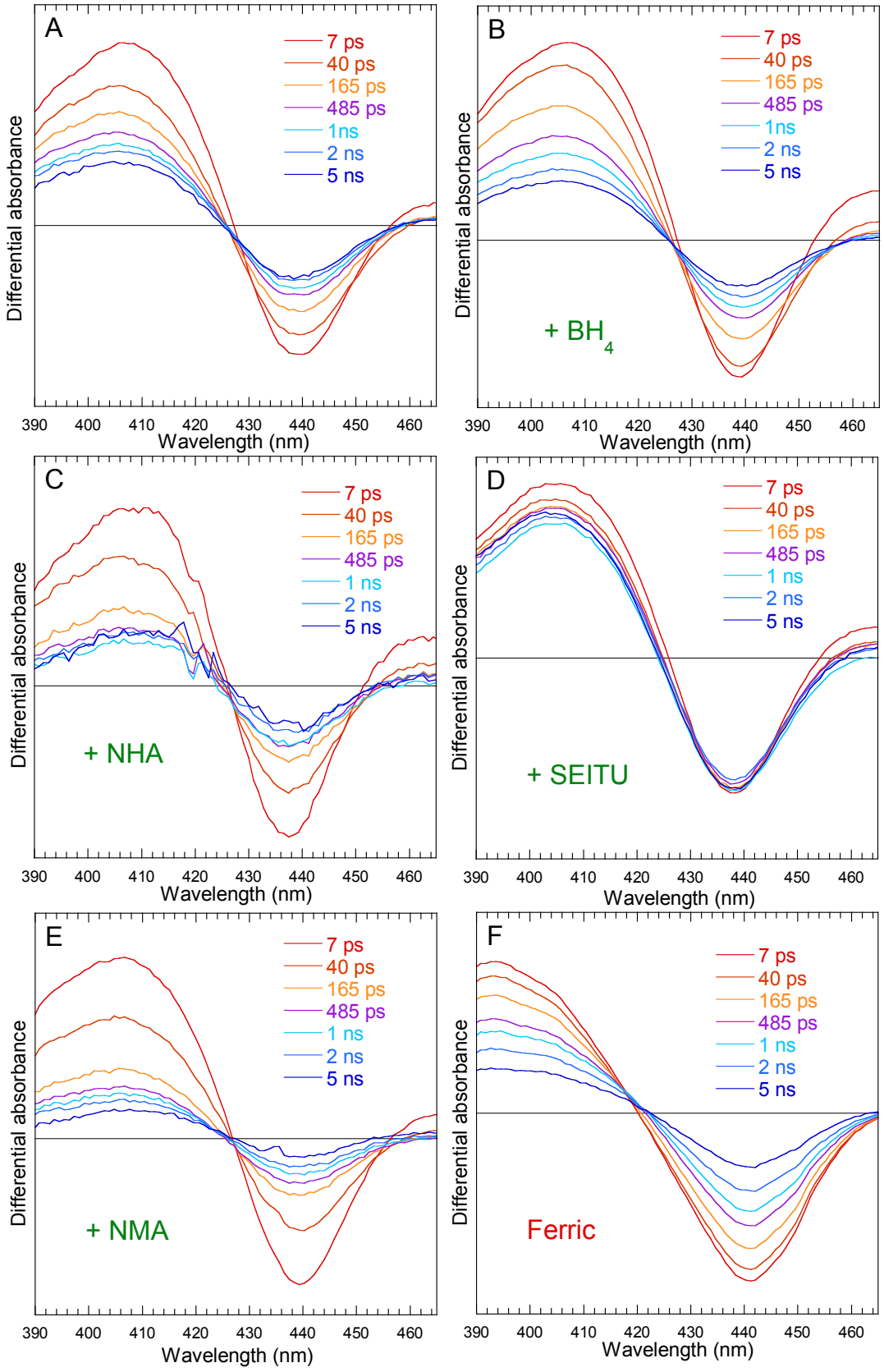

Figure 6.4: Transient spectra (raw data) for the NO rebinding to eNOS for the six species at given times after photodissociation of NO. All the species are ferrous except in F, where ferric eNOS has only BH_4 as cofactor.

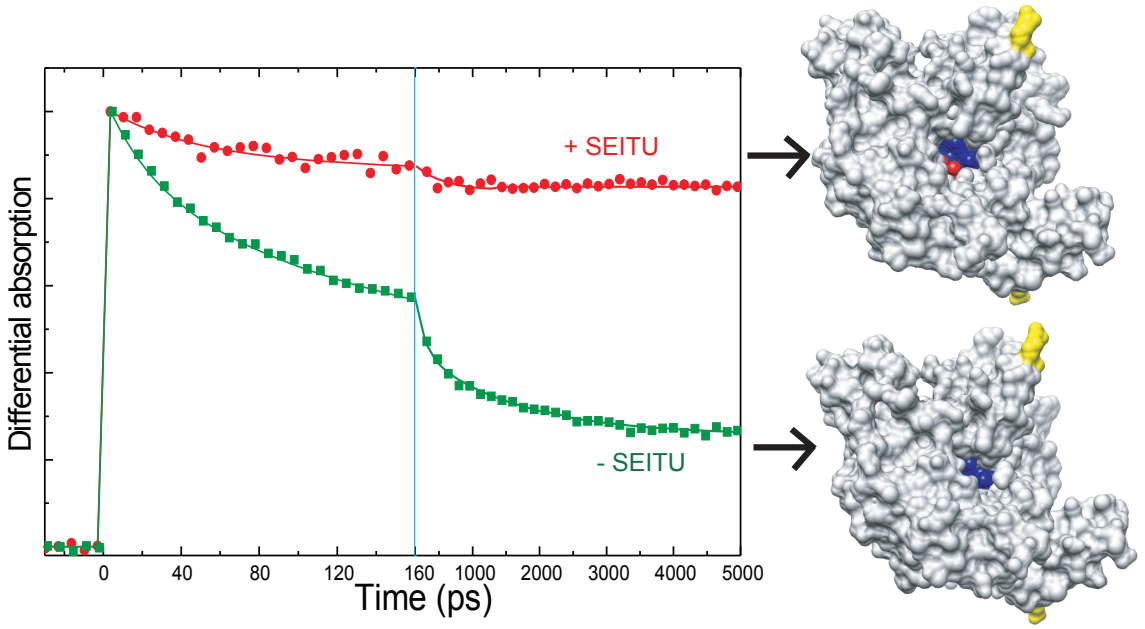

Figure 6.5: Dynamics of NO after photodissociation from ferrous BH_4-bound eNOS in the presence or absence of SEITU and the corresponding structures. Heme is displayed in blue and SEITU in red in the upper structure. Two opposite side-chains are colored in yellow to illustrate the similar position of both structures. Images are created by Chimera.

adjusted to a gaussian function (see Chapter 2) and the fited time constants (8.3 - 14.6 ns) are well defined with respect to the pulse duration of 6 ps. It must be emphasized that the 20 200 ps and the 1.5 ns geminate recombination occured within the 6 ns pulse so that NO photodissociation can occur several times for the same molecule during this 6 ns pump pulse. This leads to an apparent higher yield for NO dissociation and we must consider that the total amplitude of this broad time range kinetics (Figure 6.6) represents the amplitude of the constant term of the ps-ns kinetics (Figure 6.6). Thus, the main influence of SEITU on NO kinetics is observed in the 0 to 1.5 ns time range, that is to say in the heme pocket, not due to overall protein changes, as measured in broader time range (Table 6.2).

Ferrous eNOS	τ_1 (ps)	A_1 (%)	τ_2 (ps)	A_2 (%)	τ_3 (ns)	A_3 (%)	Cst (%)
-SEITU	22	*16*	131	*39*	1.5	*20*	*25*
+SEITU	30	*8*	206	*10*	1.6	*2*	*80*

Table 6.1: Parameters corresponding to the fitted curves in Figure 6.5.

The spectrum shape does not change, neither as a function of time (10 ns versus 10 μs) nor induced by the presence of SEITU and is the same as that measured previously on a ps-ns time scale[121]. No change in the protein structure is detected in this time range. Because the spectra are similar, the process probed with the time constants 8 - 14 ns and 11 - 33 ms

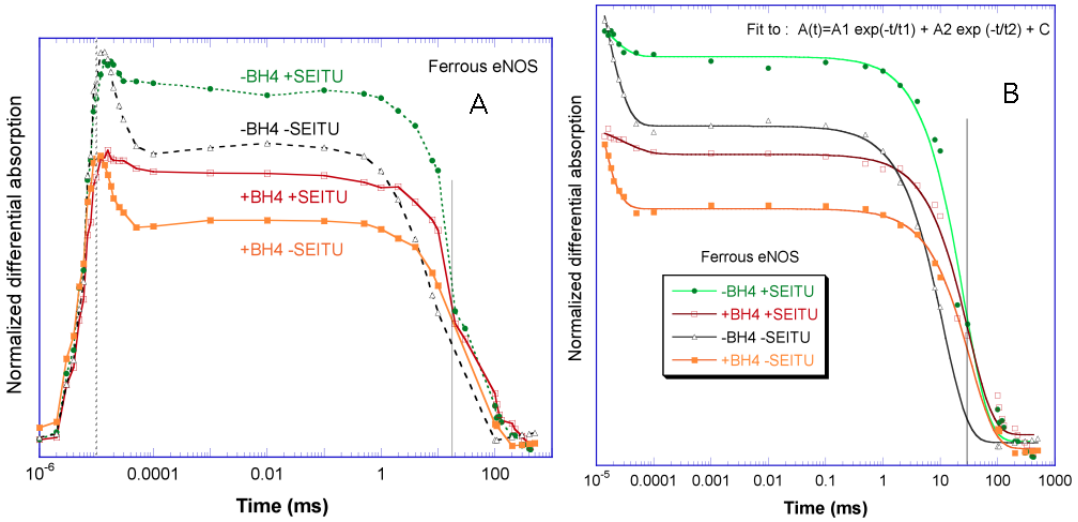

Figure 6.6: Kinetics of NO rebinding to the ferrous eNOS in the presence and absence of the cofactor BH_4 and the inhibitor SEITU. A) Raw data. B) Fitted curves to a bi-exponential function.

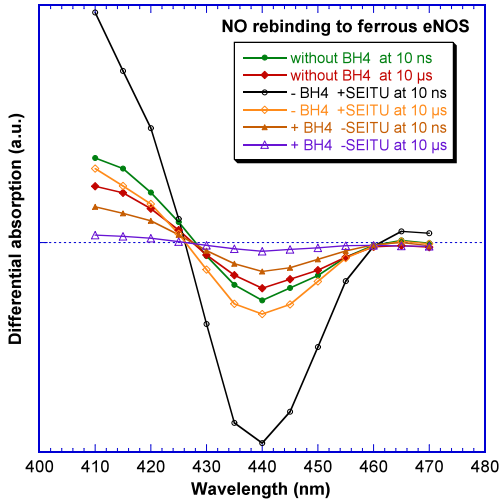

Figure 6.7: Transient spectra for NO rebinding to ferrous eNOS at two different time delays.

corresponds also to rebinding of NO, but 8 - 14 ns is geminate recombination of NO still in the protein core while 11 - 33 ms is bimolecular binding of NO from solution. SEITU is a rather small molecule and occupies the Arg site close to the heme[144]. The effect of SEITU measured here is much larger than that observed for Arg bound to the same site[121], the substrate Arg being a larger molecule than SEITU. This is a clue for an allosteric effect. Indeed, there is cooperativity between the Arg site and the BH_4 site : Arg occupies the pterin site only when SEITU is bound at the Arg site and SEITU promotes pterin binding[144]. This is a achieved through hydrogen bondings observed in the X-ray structure[144].

The corresponding structures of eNOS (without SEITU:2NSE, with SEITU:3NSE, from protein data bank) with and without SEITU (in red) bound close to the heme (in blue) are

Species	τ_1 **(ns)**	A_1 (%)	τ_2 **(ms)**	A_2 (%)	Cst (%)
-BH_4-SEITU	12.8 ± 1	*24*	11 ± 1	*71*	*5*
-BH_4+SEITU	14.6*	*6*	26 ± 2	*88.5*	*5.5*
+BH_4-SEITU	8.3 ± 1.2	*22.5*	33 ± 2	*72.5*	*5*
+BH_4+SEITU	32*	*8*	31 ± 3	*85*	*7*

Table 6.2: Parameters corresponding to the fitted curves in Figure 6.6 for ferrous eNOS. *These components are badly defined due to their low amplitude.

shown in Figure 6.5. To recognize the structural change and orientation of the molecule, two amino acids (Arg99 and Glu323) on opposite sides are displayed in yellow. We can notice that the accessibility to the heme is modified due to the structural change induced by SEITU. Thus, the presence of SEITU altered the heme pocket and decreases the energy barrier for exiting the heme pocket, resulting in decreased rebinding probability.

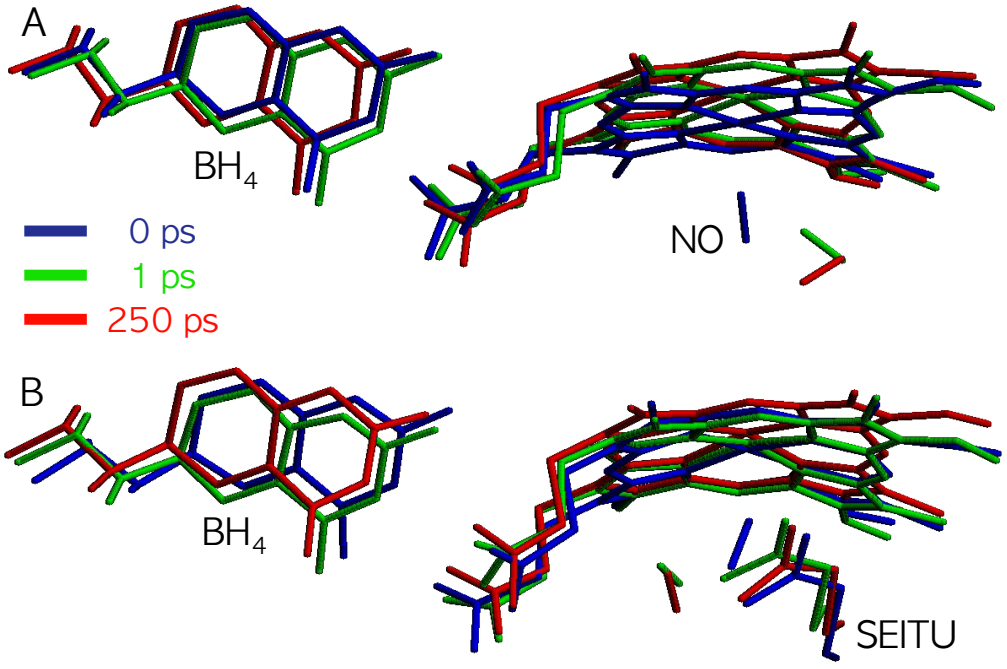

Figure 6.8: Superposition of structure of eNOS near heme in the absence (A) and presence (B) of SEITU at three different times: 0 ps, before photodissociation (blue), 1 ps after the photodissociation (green), and 250 ps (red). Dynamics simulation performed with CHARMM.

Dynamic simulation is another approach to investigate how SEITU is involved in the inhibiting on the NO rebinding. Figure 6.8 is the superposition of the structures of eNOS heme and BH_4 at three times after NO dissociation, obtained by molecular modeling. SEITU is located in the distal side and this position is same with NO[144]. In both cases, NO is still located in the heme distal pocket and did not yet migrate away. The overall result of the

simulation is a more rigid heme structure in the presence of SEITU, in line with an allosteric induced change of the heme pocket (but limited to heme pocket).

6.2.2 Effect of reaction intermediate (NHA) and redox state

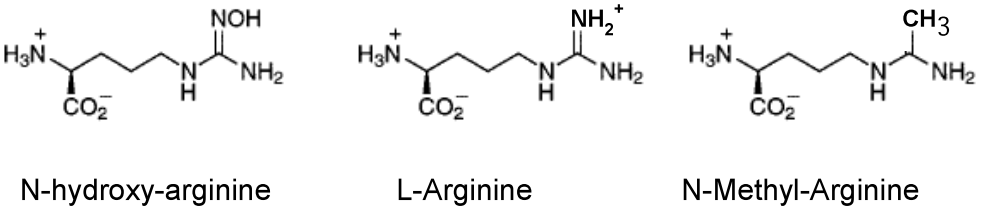

Figure 6.9: Comparison of the structures of the substrate Arg, the inhibitor NMA and the reactional intermediate NHA.

The first step in the NO production reaction by eNOS involves the hydroxylation of one of the amidine nitrogen atoms of L-Arginine. N_ω-Hydroxy-L-Arginine (L-NHA, Figure 6.9) is the reaction intermediate and we investigate its influence on the rebinding to eNOS of newly synthesized NO. The effect of the substrate L-Arg is a large retardation of recombination for both ferric and ferrous eNOS[121]. This effect was smaller than that of SEITU. L-NHA binds to the active site of nNOS in a similar way to that of L-Arg as seen in crystal structure[161] and its binding mode is identical in nNOS and human eNOS[162]. Thus, we can consider that in eNOS the binding mode of L-NHA is the same as L-Arg. Detailed structural information of L-NHA bound to bovine eNOS is available in the protein data bank website (PDB entry: 5NSE).

Figure 6.10-A displays the kinetics of NO rebinding to the ferrous eNOS in the presence or absence of the L-NHA and is compared with the effect of SEITU. On the contrary with the result shown in case of L-Arg, there is no major change in the presence of L-NHA. Three time components (21 ps, 122 ps, 0.8 ns) were obtained and are slightly faster than that those (25 ps, 260 ps, 2.1 ns) in the absence of L-NHA (Figure 6.10-B, blue). Importantly, the effect due to L-NHA is only seen in the range 0.1 to 2 ns, but the asymptotic kinetics (5 ns) is the same as that measured in the absence of L-NHA, contrary to the case of L-Arg[121]. L-NHA and SEITU bind both to the substrate (Arg) catalytic site but have opposite effects on NO dynamics (conspicuous on Figure 6.10-A). The effect of L-NHA is limited to the heme pocket and, when compared to Arg[121] is obviously due to the presence of the OH^- group which can exert an electrostatic barrier for NO motion. Because the amplitude of kinetics is the same after 2.5 ns this is the only effect due to L-NHA and we conclude that there is not induced structural changes. We conclude that L-NHA does not exert a regulatory effect on

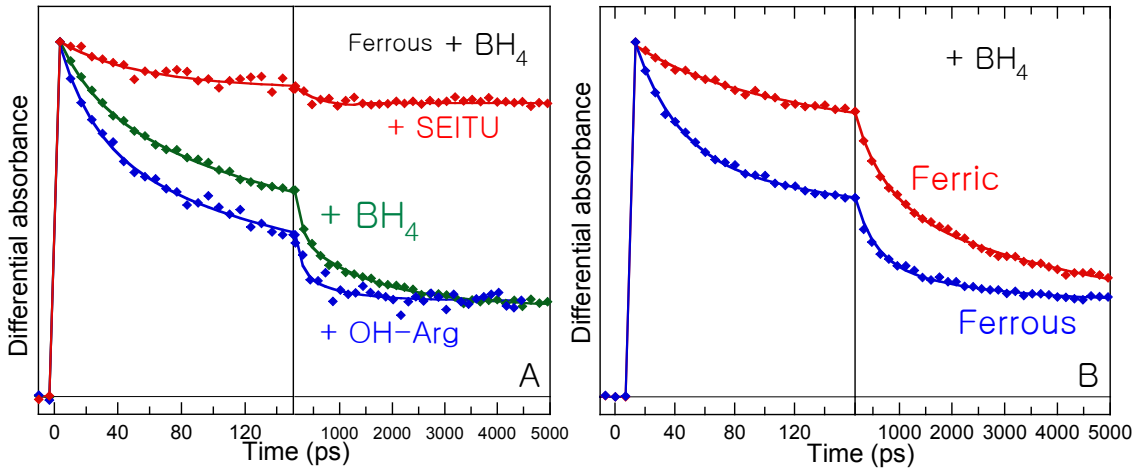

Figure 6.10: A) Dynamics of NO after photodissociation from ferrous eNOS bound with BH_4 in the presence of SEITU or OH-Arg (L-NHA), B) Comparison of the NO dynamics to ferric and ferrous eNOS.

newly-synthesized NO binding as does L-Arg. We consider here NO present in the cell and possibly diffusing to eNOS as does O_2, not NO in the current catalytic cycle, since L-NHA is the reactional intermediate and NO cannot come from the same catalytic cycle than that producing L-NHA. The small effect up to 2 ns most probably arises from electrostatic (steric) barrier. We observed an increased rate of NO rebinding when the oxidation state is ferrous (Figure 6.10-B).

Importantly, X-ray structural data have shown that SEITU binds in the Arg site[144] and that SEITU participates to hydrogen bonding with Glu363 residues. The barrier to NO release is modulated by the occupancy of substrate binding site by Arg L-NHA or SEITU. However, the effect of L-NHA that we observe on NO dynamics in the picosecond time-scale is the contrary to that measured in the presence of L-Arg for which NO rebinds with a larger yield for L-NHA and a lower yield for Arg[121]. The three molecules L-Arg (substrate), SEITU (inhibitor) and L-NHA (reaction intermediate) bind to the catalytic site of eNOS, and yet have very different effects on NO dynamics. We conclude that the heme structural environment is not influenced in the same manner for the three cases, the reaction intermediate inducing very little change. We can conclude that SEITU acts by changing the heme environment, probably by changing the hydrogen bond pattern leading to a very high-energy barrier for rebinding, once NO is dissociated from the iron but a low barrier to NO escape.

Species	τ_1 (ps)	A_1 (%)	τ_2 (ps)	A_2 (%)	τ_3 (ns)	A_3 (%)	Cst (%)	Reference
Ferrous, + BH_4	16	*22*	90	*28*	1.0	*23*	*27*	
Ferrous, + BH_4 + SEITU	30	*8*	206	*10*	1.6	*2*	*80*	
Ferrous, + BH_4 + OH-Arg	21	*27*	122	*38*	0.8	*9*	*26*	
Ferric, + BH_4	65	*17*	598	*23*	-	-	*60*	
Ferric, + NMA	35	*16*	200	*20*	0.9	*5*	*59*	
Ferric, – NMA	36	*7*	196	*21*	2.2	*44*	*28*	
Ferric	15	*7*	200	*30*	2.0	*53*	*10*	
Ferric, + L-Arg	53	*27*	300	*17*	17	*56*	[a]	[121]
Ferrous, + L-Arg	36	*23*	400	*14*	18	*63*	[a]	

Table 6.3: Parameters corresponding to the fitted curves in Figures 6.10,11. [a]Although τ_3 may contain a constant term, the fit was not improved by adding it, or Cst tended to vanish.

6.2.3 Effect of the inhibitor N-methyl-arginine and of the cofactor tetrahydrobiopterin

In this section, we investigated the effects of the substrate analogue inhibitor N_γ-methyl-L-arginine (NMA) and BH_4 cofactor in ferric eNOS. The study of the ferric state is highly relevant for eNOS mechanism since the heme, which starts the catalytic cycle in the ferrous state, becomes ferric in numerous steps during the cycle[163]. NMA has been designed to bind at the substrate site as a mechanism-based inhibitor for NOS[164]. NMA and L-Arg behave in a very similar way in terms of binding affinity for ferric nNOS and the UV-visible absorption spectral properties of both complexes are also similar[165]. As for BH_4 one role is the stabilization of NOS in its active homodimer form by forming a bond in the dimer interface on the proximal side, and a second role is to transfer electron. The presence of BH_4 can influence the binding of substrate, the heme spin state, and the stability of the protein[166]. Especially we have studied the influence of the inhibitor NMA on the dynamics of NO within the core of eNOS in its ferric state together with the cofactor BH_4. The choice of the ferric state is motivated by the characteristic of the catalytic cycle of eNOS, which ends in the ferric state when newly synthesized NO is released. This ferric state binds BH_4 which participates in the electron transfer from the cofactors FMN and FAD, and is also able to bind arginine analogs, acting as inhibitors.

Figure 6.11 shows the NO rebinding to eNOS in the absence or presence of NMA. The effect is clearly pronounced in nanosecond time scales and a very small effect is detected in early few hundreds of picoseconds in absence of BH_4. This overall effect is very similar to that observed in the case of the substrate Arg[121] and this allows to infer that the effect of NHA is indeed due to electrostatic influence from the OH group rather than from a structural influence on the heme pocket.

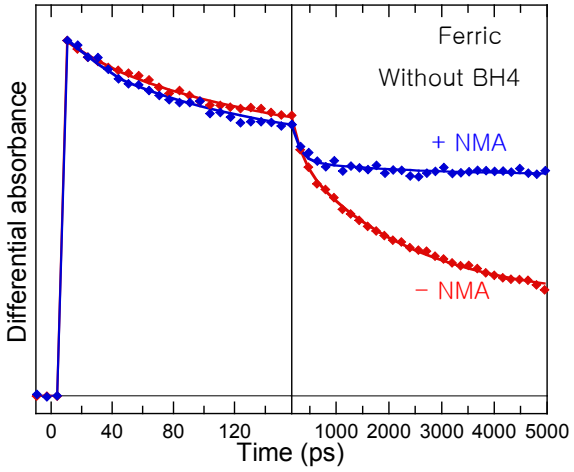

Figure 6.11: Comparison of the dynamics of NO after photodissociation from ferric eNOS in the presence and absence of NMA, A) without BH_4.

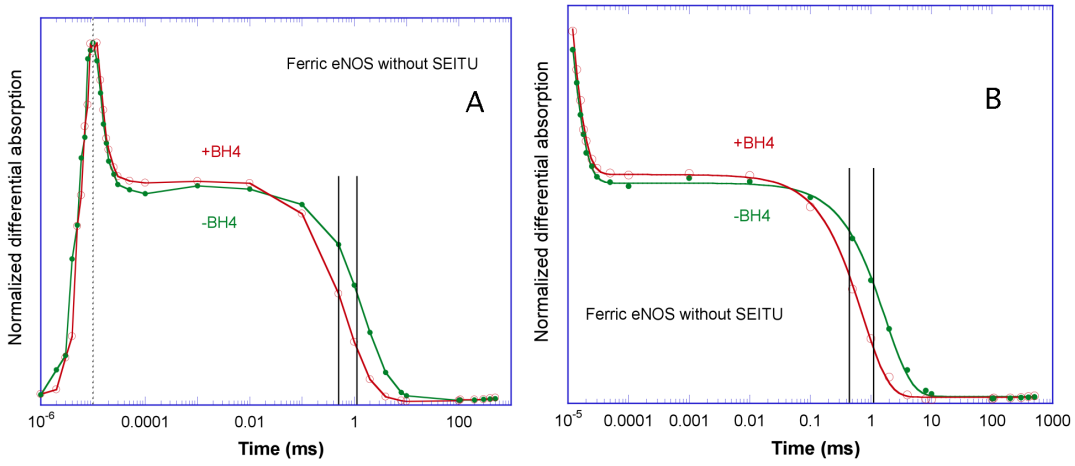

Figure 6.12: Kinetics of NO rebinding to the ferric eNOS in the presence or absence of the cofactor BH_4. A) Raw data at 437 nm (bleaching inverted). B) Fitted curves to a bi-exponential function.

We will now investigate the effect of BH_4 independently of any other effectors. NO rebinding dynamics to ferric eNOS are similar with or without BH_4 in the ns-μs-ms time range exactly as it is observed in the ps-ns time range (Figure 6.14). Only the time constant of bimolecular rebinding is increased by a factor of $\sim$2.5 in the presence of BH_4 (Figure 6.12 and Table 6.4). The amplitude ratio between geminate and bimolecular rebinding did not change. The time constant of the first component is 5.8 $\pm$ 0.1 ns, which is larger than the falling edge of the probing pulse (see in Chapter 2 the case of sGC-CO measurements). The bleaching is similar at 10 ns and at 10 μs (Figure 6.13). However, the shape of the induced absorption at 380-420 nm is changed in the presence of BH_4, indicating an influence of the cofactor on the heme surroundings, in line with previous conclusions.

The cofactor BH_4, located in the heme pocket, will not affect the catalytic turn-over of

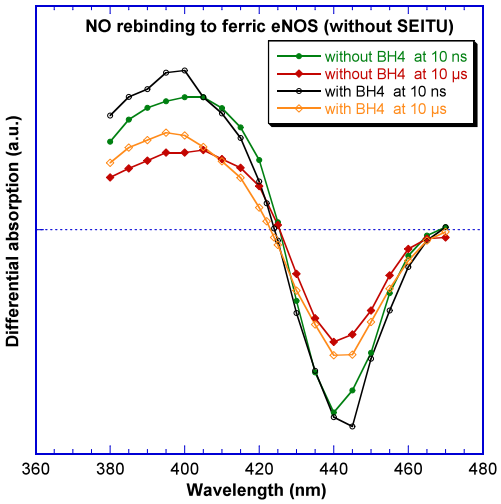

Figure 6.13: Transient spectra for NO rebinding to ferrous eNOS at two different time delays.

Ferric eNOS	τ_1 **(ns)**	A_1 (%)	τ_2 **(ms)**	A_2 (%)	Cst (%)
$+BH_4$	5.6	*40*	0.7	*60*	$\sim$ *1*
$-BH_4$	5.8	*42*	1.7	*58*	$\sim$ *1*

Table 6.4: Parameters corresponding to the fitted curves in Figure 6.12.

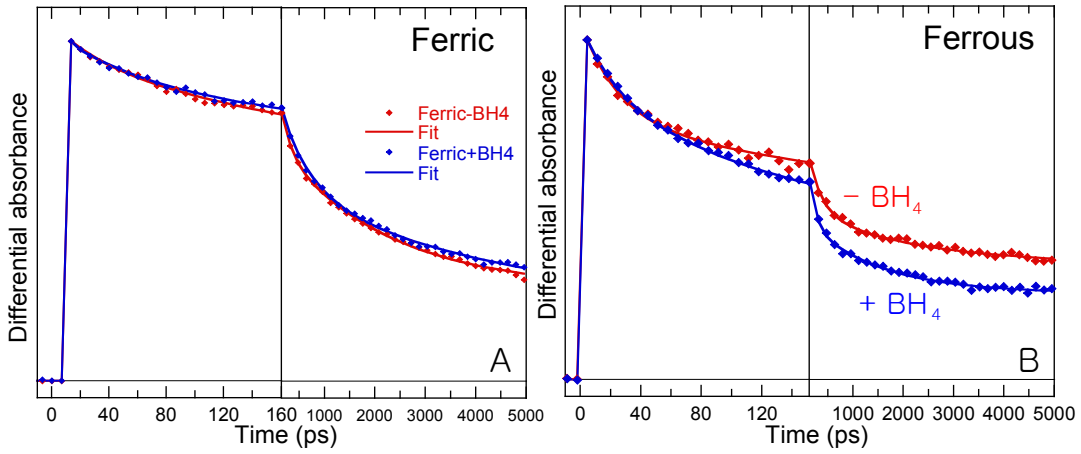

Figure 6.14: Comparison of the NO dynamics after photodissociation from A) the ferric eNOS in the presence and absence of BH_4, B) the ferrous eNOS.

the enzyme in a steric manner, but only by its ability to transfer electrons. BH_4 had no major effect on NO rebinding to the ferric eNOS, however BH_4 does change NO dynamics for ferrous heme (Figure 6.14). Only the longest nanosecond component is affected, which concerns NO out of the heme pocket but still in the protein core. The effect of BH_4 depends upon the redox state of the heme. This means that BH_4 is necessary to maintain the correct conformation of the heme pocket for catalysis and that redox state influences this conformation. We found a faster geminate rebinding phase for the ferrous eNOS species in the presence of BH_4 as shown

in Figure 6.14-B. If we consider that BH_4 does not induce a change in NO dynamics in the ferric state but it does in the ferrous state, then the origin of the effect can not be purely steric, but a conformational modification occurred in the presence of BH_4 in the ferrous state.

6.3 Conclusion

In this chapter, we have shown that the occupancy of the substrate binding site of the enzyme NO-synthase has a large effect on NO release which depends upon the nature of the effector bound, so that in eNOS may control the dynamics of NO once it has been synthesized. This concerns not only NO still in the protein core but also NO which has already been released into the cytosol and diffuses randomly as does O_2 during the catalytic cycle. We showed that both steric and allosteric effects take place to control diatomic dynamics. The inhibitors NMA (Nγ-Methyl-L-arginine) and SEITU (S-ethylisothiourea), and of the cofactor BH_4 (tetrahydrobiopterin), differently influence the heme surrounding structure as well as the redox state of eNOS. We conclude that the inhibitor SEITU and the cofactor BH_4 induce structural changes in the vicinity of the heme. Importantly, BH_4 effect on heme pocket depends on the redox state of the heme iron.

Chapter 7

The movement of the heme iron: Probing band III in hemoglobin and myoglobin

7.1 Introduction

As discussed for sGC in previous chapter, the binding and release of diatomics (O_2, NO or CO) to their heme sensor domain triggers changes in protein structure. The signaling mechanisms between diatomics and protein are based on an allosteric structural alteration of the receptor/sensor protein coupled to a change of activity or affinity. Binding and release of diatomics, the first events of activation and deactivation are transmitted into the entire protein structure by the movement of the heme iron. For example, this iron motion occurs from the **proximal out-of-plane** to the **distal out-of-plane** position for sGC activation, while this motion occurs from **out-of-heme** plane to **in-plane** position of the iron for O_2 and NO binding to the O_2-carriers Hb and its monomeric counterpart Mb. For Hb, the out-of-plane iron motion induced by NO or CO dissociation occurs in less than 0.6 ps as measured by transient absorption[167] or by Raman spectroscopy[168] and this represents the very first event of the allosteric R $\rightarrow$ T transition[83]. When O_2 or NO binds to the heme iron, the iron moves toward the heme plane and this initial iron motion was considered quasi-instantaneous up to now. However, since the iron motion is coupled to protein backbone dynamics, the in-plane motion induced by ligand binding is not necessarily instantaneous and has actually never been directly measured.

Band III is a near-infrared electronic transition at $\sim$ 760 nm in heme proteins which was studied as a marker of conformational relaxation of heme proteins after photodissociation of the ligands[169]. It appears only in the unliganded ferrous form, thus the dynamics of its

reappearance gives an indication of relaxation back to the ground state when the heme is excited by the laser pulse. The absorption coefficient (ϵ = 250-350 $M^{-1} \cdot cm^{-1}$) is extremely small compared to the Soret and Q bands. For this reason not so many absorption studies has been done both for Hb and Mb. Anfinrud and co-workers reported the temporal behavior of band III position of Mb (763 nm) after CO photodissociation using femtosecond near IR absorption probing the heme relaxation of unliganded heme. However measurement for Hb or Mb with NO has never been done.

Recently, Kruglik et al.[122] measured the intensity kinetics of Fe-His stretching band after NO dissociation in five heme proteins, including myoglobin and hemoglobin. This kinetics was systematically slower than those of Soret absorption. This slow down was interpreted as a retarded iron in-plane motion occurring in the range 7 $\sim$ 40 ps after NO binding, depending upon the nature of the protein, as depicted in Figure 7.6. These findings were rationalized by theoretical calculations[170] describing the coupling between the Fe-His stretching intensity and the iron position through heme absorption and resonance Raman enhancement depending upon the iron position. In line with this Raman study, we investigate another possible manifestation of the heme iron motion.

A theoretical study focused on the absorption of band III in 5-coordinate ferrous heme, assigned to a charge transfer transition from π-porphyrin molecular orbital to a d_{yz} iron orbital[171]. This study concluded that intensity of band III is sensitive to the iron-heme plane distance, but the rebinding of NO to heme was never investigated by probing band III absorption kinetics. We aimed at measuring the band III intensity kinetics in the picosecond time-range in order to compare it with Soret intensity, which reflects only the evolution of heme iron coordination, whereas band III reflects the iron position with respect to the heme plane during the rebinding of NO. We also measured band III spectral shift kinetics in the picosecond time-range aiming at verify hypothesis about band III behavior inferred from theory[171]. We compare the kinetics of band III spectral shift, with those of Soret band and Q-band and to iron-histidine stretching and compared its behavior for tetrameric Hb and monomeric Mb.

7.2 Heme iron motion in myoglobin probed by band III kinetics

The static absorption spectra of ferrous Mb and Hb in the presence and absence of NO in the band III region are displayed in Figure 7.1-A. The strong Soret band is not shown and only the very end of Q band, close to band III, appears for the ferrous Mb and Hb. The

maximum of band III peak is located at 760.6 nm for Mb and 758 nm for Hb. This charge transfer transition is observed for unliganded 5c-His ferrous heme but is almost absent in the spectra of 6c-His-NO species.

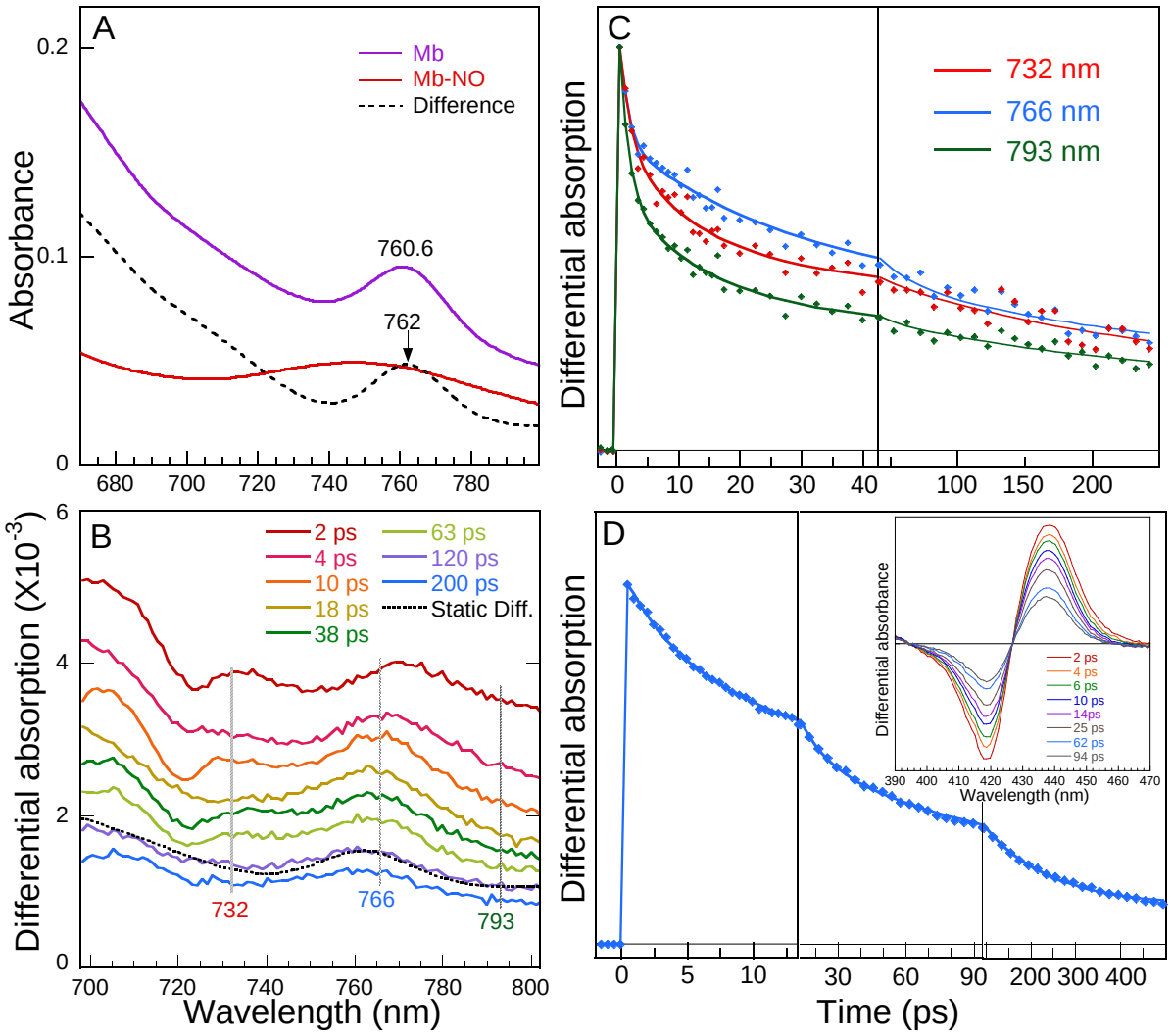

Figure 7.1: A) Equilibrium absorption spectra of Mb in the absence and presence of NO at the near IR region. [Mb] = 4 mM, NO 10 % in gas phase. B) Raw transient spectra at selected time delays, these spectra are not offset. Static absorbance difference spectrum (dotted) is included. C) Normalized kinetics at selected wavelengths, indicated by the dotted lines in panel B. D) Kinetics of NO rebinding probed by Soret absorption. SVD analysis of the entire time-wavelength matrix data and raw transient spectra (inserts) at given time delays for Mb in water.

We have performed TA measurements of the band III region for Mb and Hb with the same samples used to measure static absorption. Firstly, the raw transient spectra after photolysis of MbNO are displayed in Figure 7.1-B and reveals the picosecond spectral evolution of MbNO. After photo-dissociation using a pump pulse at same wavelength as used for Soret

measurement (564 nm), a spectral blue shift of band III from 2 ps to 10 ps is detected as it was observed in the case of Mb-CO[169]. However, in the case of Mb-CO, the shift corresponds to unliganded heme relaxation because CO does not rebind, while in our experiment the situation is more complex because NO rebinds with kinetics defined by the Soret evolution. At 2 ps we observe a broadening of band III due to vibrational excitation. At three different wavelengths (dotted lines in raw transient spectra), kinetics were fitted and compared as shown in Figure 7.1-C. Just by inspecting the figure, the kinetics at band III maximum (766 nm) is slower than that of the background due to Q-band (732 nm and 793 nm). The latter follows the kinetic trace of Soret band region as probed by our TA measurement and represents the NO rebinding event to heme iron. The raw transient spectra and its kinetics of NO rebinding from SVD analysis for Soret are displayed in Figure 7.1-D.

Spectral region	NO rebinding phases				
	τ_1	A_1	τ_2	A_2	Constant
	ps		*ps*		
band III at 766 nm	27.5	*0.42*	293	*0.33*	*0.25*
Q-band at 732 nm	12	*0.40*	205	*0.37*	*0.23*
Q-band at 793 nm	14	*0.45*	204	*0.37*	*0.18*
Soret	13	*0.40*	148	*0.50*	*0.10*

Table 7.1: Kinetic parameters obtained from TA measurements. The kinetic traces were fitted with the function $\sum A_i exp(-t/\tau_i)$ + C. [2 ps: excited state decay].

For band III, we fitted the kinetics at fixed wavelengths instead of performing SVD analyses. Fitting parameters are given in Table 7.1. All the curves were fitted with two decay components and one constant term. The fast components at 732 and 793 nm are similar with the decay constants of MbNO at Soret band region, having time components of 13 ps and 148 ps. Thus kinetics at the region of Q-band tail follows those at Soret band region, whereas those at band III appear slower (27.5 ps) and clearly different from the decay from NO geminate rebinding. Recently the retardation of the iron motion toward the heme after NO binding has been reported in our group[122]. The time constant for domed-to-planar transition induced by NO binding in Mb was determined to be $\sim$ 30 ps. The first component (27.5 ps) at the band III region is very close to this reported time constant (30 ps) and largely different from the time constant of NO rebinding (13 ps).
Considering that:

1. theory predicts a dependency of band III intensity upon iron position[171]

2. kinetics of Fe-His stretching intensity, also predicted to depend upon iron position[170], is slower than Soret kinetics[122]

3. we measured a time constant in band III (27.5 ps) similar to that of Fe-His stretching intensity (30 ps) and slower than Soret kinetics (13 ps, Table 7.1)

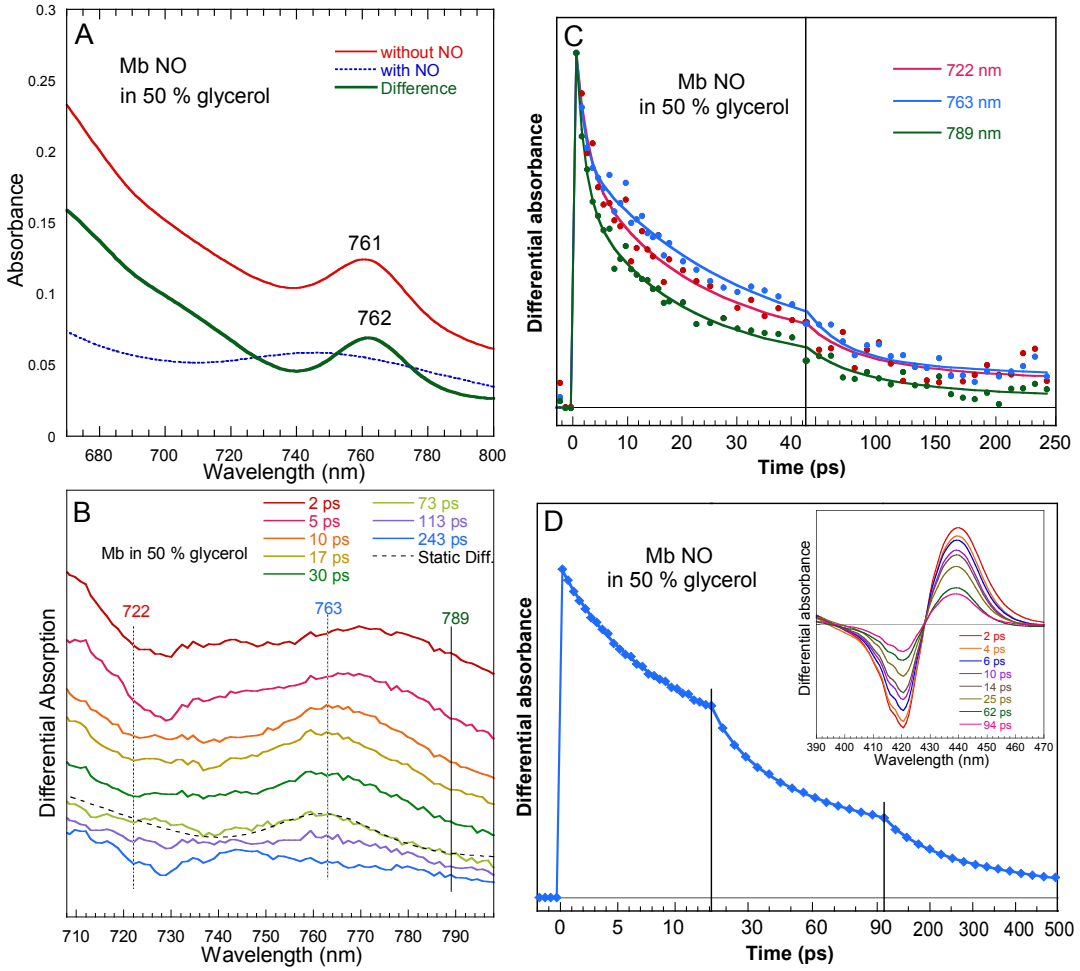

Figure 7.2: A) Equilibrium absorption spectra of Mb in the absence and presence of NO at the near IR region in 50 % glycerol solution. B) Raw transient spectra at selected time delays, these spectra are not offset. C) Normalized kinetics at selected wavelengths, indicated by the dotted lines in panel B. D) Kinetics of NO rebinding from SVD analysis of the entire time-wavelength matrix and raw transient spectra (inserts) at given time delays for Mb in 50 % glycerol solution.

then we conclude that our band III kinetics measured the iron motion toward the heme plane induced by NO binding. Our TA results at separate regions provide a direct mean to separate the NO rebinding and iron movement toward the heme plane.

Theoretical study predicted that the solvent viscosity could have an effect on the band III shape[171]. For this reason, we have performed TA measurements on Mb in 50 % glycerol solution after photolysis of MbNO instead of 100 % water (Figure 7.2). First observation is that all spectra at given time delays have broader shapes than those of Mb in 100 % water

(Figure 7.2-B). It is known that the rate of the rapid phase is not dependent on the solvent viscosity, studied for the Soret band region[151]. However, the relative amplitudes and the rates of phase are influenced by the solvent viscosity. Secondly, we found a slower decay component (27 ps) at band III, similarly with 100 % water. Kinetic parameters obtained from the fitting of three traces (Figure 7.2-C and D) are given in Table 7.2. Thus, as in water, band III kinetics do not have the same time constant as Soret. However, we did not find a difference between water and 50 % glycerol, as it was observed in Raman, albeit with large estimated error (Table 7.5).

Spectral region	NO rebinding phases						
	τ_1	A_1	τ_2	A_2	τ_3	A_3	Constant
	ps		*ps*		*ps*		
band III at 763 nm	27	*0.68*	60	*0.15*	336	*0.07*	*0.10*
Q-band at 722 nm	16	*0.56*	63	*0.32*	300	*0.03*	*0.09*
Q-band at 789 nm	13	*0.53*	53	*0.36*	345	*0.08*	*0.03*
Soret	15	*0.42*	71	*0.36*	378	*0.21*	*0.01*

Table 7.2: Kinetic parameters for Mb-NO in 50 % glycerol. The kinetic traces were fitted with the function $\sum A_i exp(-t/\tau_i)$ + C. [2 ps: excited state decay].

7.3 Band III of Hb

The steady-state spectra of hemoglobin in the presence and absence of NO are displayed in Figure 7.3. The same procedures are applied to investigate the band III kinetics of Hb (Figure 7.4). A spectral blue shift of band III is observed from 1 ps to 6 ps as in Mb together with a broadening of band III. The kinetics at band III wavelength 765 nm was fitted to a multi-exponential function, containing a fast (18 ps) and a slow (140 ps) component together with a constant (Figure 7.4-C). However, when kinetics are fitted at Q-band wavelength (705 nm and 785 nm) the fast component τ_1 = 11 ps, is identical to that measured in the Soret band (10.8 ps) and assigned to NO geminate rebinding. The second component in Q-band (96 ps) is also closer to that in Soret band (61 ps). In a similar way with Mb, the time evolution at band III was slower than that of kinetics of NO rebinding at Soret region. Fitting parameters are given in Table 7.3.

The reported value (15 ps) for the heme iron motion in Hb as measured by Raman spectroscopy[122] is also very close to the fast component (18 ps) of band III decay which is clearly slower than that at Soret. The Q-band fast component (11 ps) represents the coordination of the heme after photodissociation while the band III should represent the motion of the iron (18 ps) according to the theoretical study on band III intensity[171]. Because this

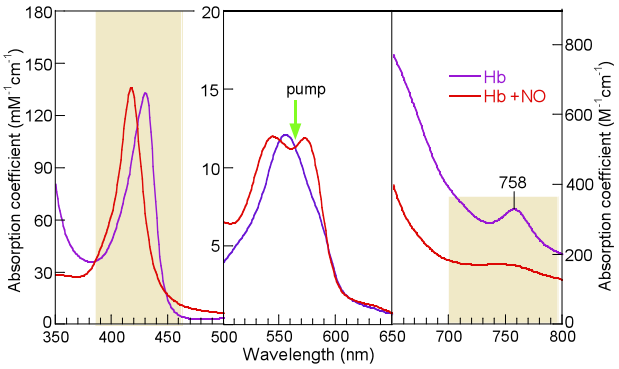

Figure 7.3: Steady-state absorption spectra of unliganded ferrous hemoglobin and liganded with NO. The three panels disclose successively the Soret absorption band (or γ-band), the Q-bands (or α- β-bands) and the band III. The shaded areas are those probed by our experiments and the arrow indicates the wavelength photodissociating pulse.

latter kinetics is slower, we can deduce that the iron does not move instantaneously upon NO binding due to the protein constraints which influences on this motion. This will be discussed in "Structural implications". Let us now analyze the spectral shift.

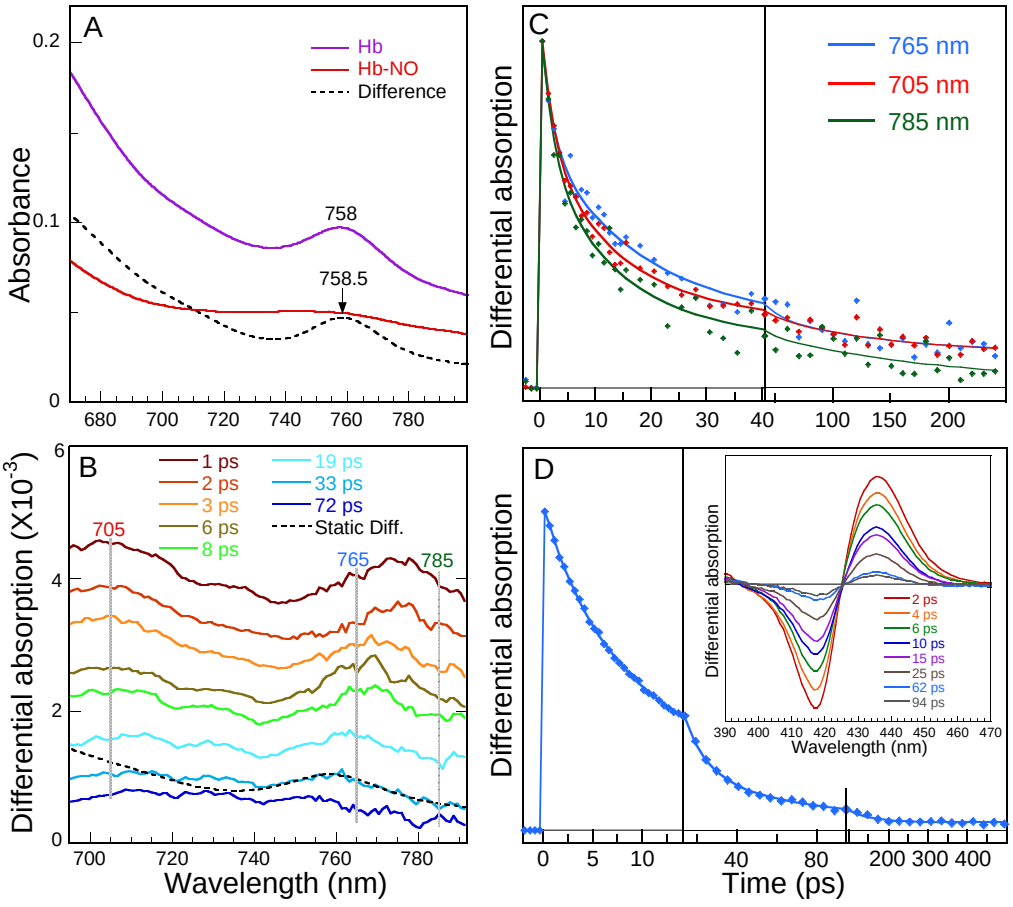

Figure 7.4: A) Equilibrium absorption spectra of Hb in the absence and presence of NO at the near IR region. B) Normalized kinetics at selected wavelengths, indicated by the dotted lines in panel C. C) Raw transient spectra at selected time delays, these spectra are not offset. Static absorbance difference spectrum (dotted) is included. D) Kinetics of NO rebinding from SVD analysis of the entire time-wavelength matrix and raw transient spectra (inserts) at given time delays for Hb in water.

Spectral region	NO rebinding phases				
	τ_1	A_1	τ_2	A_2	Constant
	ps		*ps*		
band III at 765 nm	18	*0.61*	140	*0.24*	*0.15*
Q-band at 705 nm	11	*0.60*	96	*0.25*	*0.15*
Q-band at 785 nm	12	*0.74*	114	*0.24*	*0.02*
Soret	10.8	*0.74*	61	*0.22*	*0.04*

Table 7.3: Kinetic parameters obtained from TA measurements. The kinetic traces were fitted with the function $\sum A_i exp(-t/\tau_i)$ + C. [2 ps: excited state decay].

7.4 Spectral shift of band III

As shown in the raw transient spectra for Mb and Hb, we found a spectral shift immediately after NO dissociation. Each transient spectrum was fitted with a gaussian function to model the band III plus a second order polynomial (or an exponential) function to model the tail of Q-band (Figure 7.5). The central position of the fitted gaussian curves was plotted as a function of time. Then, the kinetics of this spectral shift was fitted to a sum of three exponentials (Table 7.4). The grey vertical dotted line in transient spectra and the grey horizontal dotted line in kinetics correspond to the steady-state difference central position of the band III. After fitting the kinetics of band III spectral shift, we found that τ_1' is remarkably different for each protein but τ_{ex} and τ_2' are similar. The fast component τ_{ex} = 3.3-4.2 ps is similar to those observed by probing band III of photodissociated Mb-CO[169] or unliganded photo-excited Mb[172, 173] and is assigned to excited state decay, which follows the same process after photo-dissociation of NO from Mb and Hb. The amplitude of this ex component is similar for both proteins (Table 7.4). Two important observations emerge from these measurements:

1. for both proteins, there is a component of band III spectral shift with similar time-constant (τ_1' = 11 ps for Hb and 15 ps for Mb) as that obtained by Soret kinetics for fast NO geminate rebinding (τ_1 = 10.8 ps and 13 ps), but not similar to band III intensity decay.

2. although the band III shift due to excited state decay has similar amplitude for Mb and Hb (9.7 and 10.8 nm), the shift of the second component is more important for Hb (8.5 nm) than for Mb (4.6 nm) as is the shift of third component (Table 7.4). Within our time range, the time constant of the third shift component (τ_2' = 650 ps) is badly defined and will not be discussed.

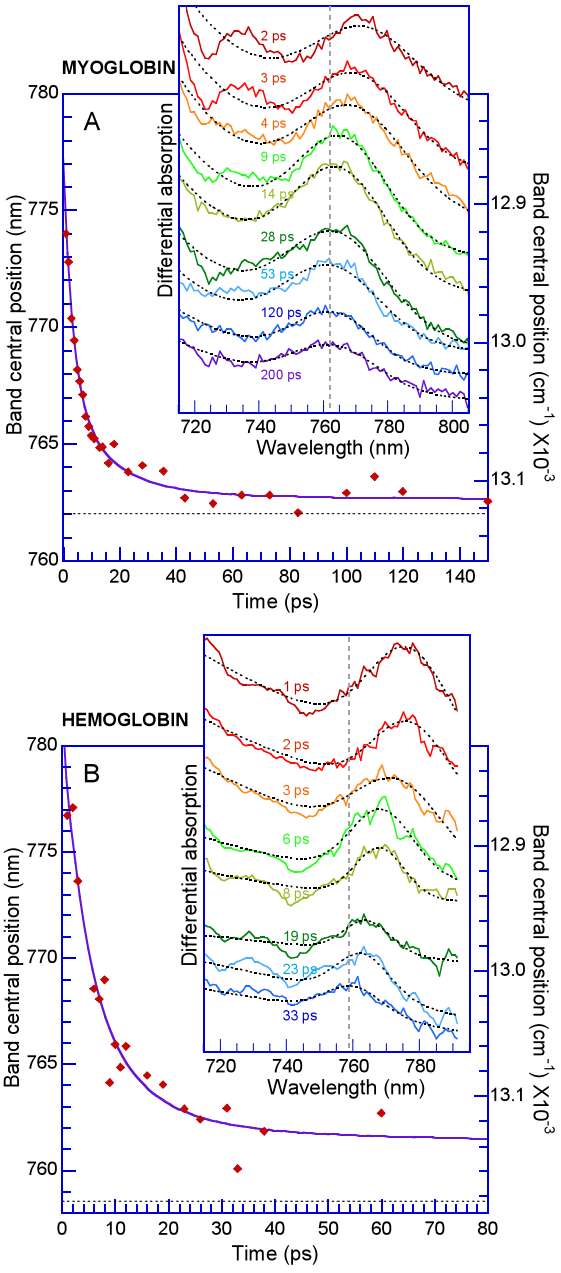

Figure 7.5: Spectral shift of transient absorption band III for Mb-NO (A) and Hb-NO (B). Each difference transient spectra was fitted with a gaussian function to model the band III and the central position of the fitted gaussian was plotted as a function of time. Then, the kinetics of this spectral shift was fitted to a sum of three exponentials (Table 7.4). The grey vertical dotted line in transient spectra and horizontal one in kinetics correspond to the central position of the band III in difference steady-state spectrum. The spectra are not offset and their relative absorption is that experimentally obtained.

When extrapolating the kinetics to t=0, the total amplitude of the band III frequency shift including the thermal relaxation[169] is $\sim$ 253 cm^{-1} for Mb and $\sim$ 380 cm^{-1} for Hb (sum of amplitudes of the three components). This overall larger energy shift of the transition is thus due to NO binding and structural relaxation, not to excited states relaxation. Quaternary structures are different for both proteins because Mb is a homologous monomeric counterpart of the tetrameric Hb. Thus, the structural constraint exerted on Hb heme is higher than in Mb from our band III results.

Previous published measurements of band III spectral shift[169] were performed on unliganded Mb or on Mb-CO for which the photodissociated CO rebinds on ms time scale, whereas we probed the heme during NO rebinding, so that comparative discussion is limited. The measurement of band III evolution during the NO rebinding was rendered very difficult, especially after $\sim$ 100 ps, because the intensity quickly decreased both for

Mb and Hb, but the spectral shift is conspicuous. The comparison of kinetic parameters obtained from transient absorption at Soret and band III and from Raman intensity kinetics is summarized in Table 7.5.

We observed that band III shifts with a time constant similar to NO rebinding, but different from that assigned to iron motion. Since the band III corresponds to a charge transfer transition, it depends on the Fe^{2+} spin state and on the d_{yz} orbital energy[174], but also on other factors such as vibronic interactions or electric field exerted on the heme[171, 175], so that its position (energy of the transition) depends on the iron coordination state. This is sufficient to explain the presence of a component in spectral shift kinetics similar to Soret kinetics during NO rebinding, directly due to the change of iron coordination, provided that band III shift is much less influenced by the iron position, contrary to its intensity.

Protein	Component 1	Component 2	Component 3
Myoglobin	τ_{ex} = 3.3 ps 9.7 nm 163 cm^{-1}	τ_1' = 15 ps 4.6 nm 78 cm^{-1}	τ_2' = 650 ps 0.8 nm 12 cm^{-1}
Hemoglobin	τ_{ex} = 4.2 ps 10.8 nm 180 cm^{-1}	τ_1' = 11 ps 8.5 nm 145 cm^{-1}	τ_2' = 650 ps 3.2 nm 55 cm^{-1}

Table 7.4: Time constants and amplitudes of band III spectral shift components.

The spectral shift due to excited state decay (τ_{ex} = 3.6-4.2 ps) is similar for Mb and Hb ($\Delta\lambda$ = 10.4 and 11 nm, equivalent to $\Delta\nu$ = 176 and 185 cm^{-1} with respect to 760 nm), reflecting the same energy of relaxation in both proteins. An important observation is the much larger spectral shift associated with NO rebinding to Hb (8 nm; 134 cm^{-1}) than to Mb (3.3 nm; 38 cm^{-1}). Given that band III is a charge transfer transition from porphyrin orbitals and d iron orbitals[174, 176], a larger change of the transition energy reflects a larger rearrangement influencing molecular orbitals in Hb induced by NO release and binding than in monomeric Mb. A much more important structural change occurs in the heme surroundings upon NO release and binding in Hb than in Mb, despite a smaller energy barrier for iron motion back to the heme plane (smaller τ_D). Because it is more important in tetrameric Hb than in monomeric Mb, this structural change in heme vicinity should be associated with allosteric transitions in the Hb.

Structural implications

The T $\rightarrow$ R (T = tensed state, unliganded; R = relaxed state, diatomic liganded, Ref. [83]) allosteric transition in hemoglobin is triggered by the iron motion toward the heme

plane, induced by diatomic binding. The time constant (τ = 18 ps) faster in Hb than in Mb (27.5 ps), shows that the interaction between Hb monomers does not increase the constraints exerted on the heme iron in the T state of Hb with respect to its homologous monomeric counterpart Mb. We must note that if the iron motion is detected, this implies that NO can bind to a domed 5-coordinate high-spin ferrous heme. Such a possibility has indeed been hypothesized[155] from the absence of energy barrier for NO rebinding and also agrees with theoretical calculation concluding that NO can bind to an out-of-plane iron[152].

Another important point is that the delayed iron motion reveals structural constraints exerted by the protein on the heme. Such constraints imply that structural changes of the heme pocket and/or its close vicinity have taken place after the dissociation of diatomics, faster than iron motion. A time-resolved circular dichroism study on Mb-CO[177] reported a motion of the proximal histidine with 7-ps time constant after CO dissociation and a TR^3 study[178], probing the aromatic Mb side-chains in the heme vicinity, observed localized structural motions with 8-ps time constant. These two latter studies revealed relaxation due to diatomic release (R $\rightarrow$ T transition) while our observations concern the T $\rightarrow$ R transition due to binding. The removal of constraints in the heme vicinity during the T $\rightarrow$ R transition, first proposed by Perutz for Hb[83], necessitates to overcome an energy barrier and cannot be immediate, but requires some time. This causes the retardation of iron movement exactly as we observed in the present study for Hb-NO. This iron motion back into the heme plane represents the first step of the allosteric transition T $\rightarrow$ R in hemoglobin upon NO binding (Figure 7.6).

Protein	NO rebinding phases (from Soret transient absorption)			Iron motion τ_D from Raman data in Ref[122]	Iron motion τ_D from Band III kinetics
	τ_1 (amplitude)	τ_2 (amplitude)	Constant		
Myoglobin	13 ps (*0.40*)	148 ps (*0.50*)	*0.10*	30 ± 10 ps	27.5 ps
Myoglobin in 50 % glycerol	15.3 ps (*0.42*)	71 ps (*0.36*) τ_3 = 378 ps (*0.21*)	*0.01*	40 ± 15 ps	27 ps
Hemoglobin	10.8 ps (*0.74*)	61.3 ps (*0.22*)	*0.04*	15 ± 6 ps	18 ps

Table 7.5: Kinetic parameters obtained from transient absorption measurements at Soret and Band III, and from Raman intensity kinetics[122]. We found a third component only for Mb in 50 % glycerol.

7.5 Conclusion

Similarly to transient Raman of Fe-His intensity, the transient absorption measurements at band III show retarded kinetics with respect to NO rebinding. Both, ν_{Fe-His} intensity and

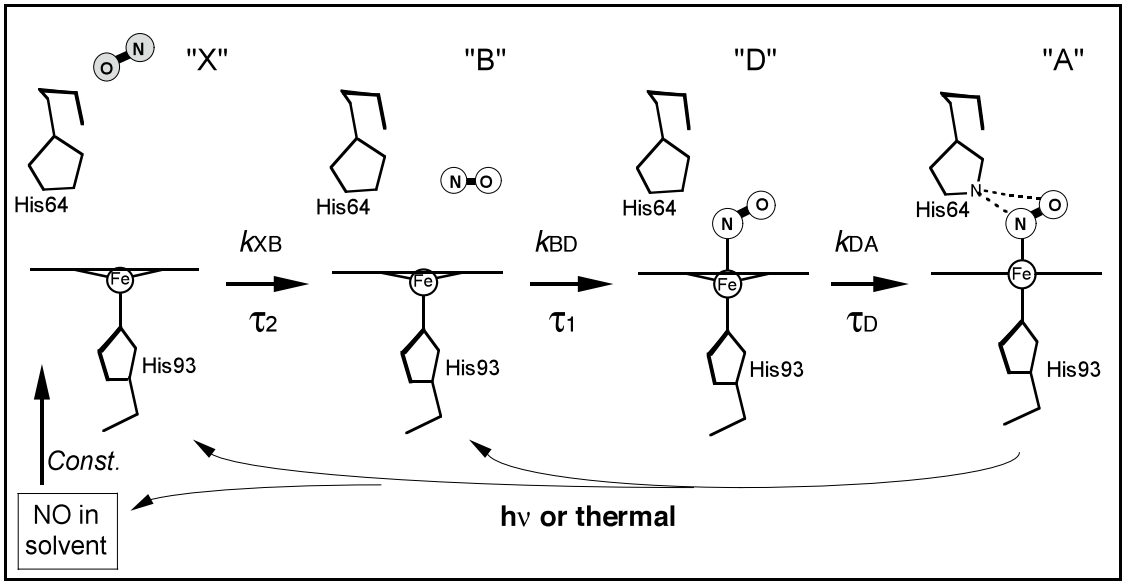

Figure 7.6: Scheme of NO recombination to Hb and Mb with relevant transient species within the picosecond time range. The positions of His side-chains are obtained from structures (2FRK and 2V1K) in the Protein Data Bank. After dissociation (thermal or photo-induced) or diffusing from solution, NO can bind to a domed heme whose iron is displaced toward the proximal His. The letters (X, B, D, A) refer to the kinetic model in Ref [155]. This scheme is applicable to all proteins. τ_D is the domed-to-planar heme time constant. The bimolecular rebinding, occurring in microsecond time scale, is represented as a constant term.

band III intensity have been theoretically shown to depend upon the out-of-plane position of the heme iron, which thus does not move instantaneously but is retarded after NO binding to the ferrous heme. We conclude that band III indeed constitutes a marker of iron motion. Through the study of band III of two representative heme proteins, we have illustrated that TA spectroscopy allows to identify the very first structural events which induce allosteric transitions triggered by NO binding in heme binding sites and consequently the activation or deactivation of 6c-NO heme proteins. We also observed a spectral shift of absorption band III after NO dissociation, assigned to heme relaxation. The kinetics of band III intensity does not follow that of Soret band and Q-band but its time-constant is similar to that of ν_{Fe-His} stretching intensity decay induced by NO rebinding after photodissociation. The iron motion inside the heme plane after NO binding to the domed heme is definitively not instantaneous. Our results confirm the theoretical calculations showing the dependence of band III intensity upon the heme iron position, which thus constitutes a marker of iron position with respect to the heme plane. Band III position appears sensitive to the iron coordination, but not to iron motion, contrary to its intensity.

Chapter 8

Overview and Perspectives

As described in Introduction and in Methods, the time-resolved "pump-probe" technique allows to study a system by perturbing it, in our case by shifting the closed system protein-ligand out of equilibrium with respect to ligand binding and position. This methodology, which was initiated about three decades ago, can bring numerous information if we push it to its limits: extending time-scale; trying to detect small signals; taking into account all the components of the time-wavelength data matrix; choosing pertinent model proteins and experimental conditions. We tried to follow these general guidelines as much as possible during this thesis work.

This thesis mainly focuses on the soluble guanylate cyclase, a crucial heme protein in cell signaling. Up today, while it has not been possible to have a crystal structure of sGC, our approach with transient absorption method aimed at bringing fundamental bases for understanding sGC activation and deactivation mechanisms. We also extended our research to other relative heme proteins. We obtained 1) an allosteric model (mainly with CO) of the functioning of sGC and 2) a kinetic model of the regulation processes with NO in sGC ranging from picosecond to second time scales. We studied allosteric effectors of sGC in a NO-independent way and we demonstrated the mechanism of synergistic activation of sGC by CO by detecting 5c-CO transient species in the presence of activators YC-1 and BAY 41-2272, which are starting point of pharmaceutical researches. Biochemical approaches including an inhibitor study (hypericin) and preliminary adaptation of SPR methodology to find an endogenous ligand of sGC were also described. Extra studies to complete this issue by SPR method are necessary to reveal the nature of unknown endogenous effectors, which act on the different steps of the NO-cGMP signaling pathway and may have therapeutic implications.

In the third chapter, we explored NO sensors from three different prokaryotic sources and the human $\beta 1$ heme domain (1-190) subunit of sGC. We concluded that the adaptation of SONO to temperature changes is not achieved by a simple temperature-dependent NO binding

equilibrium, but by a change of the proportion between 5c-NO and 6c-NO heme coordinated species. This amplifies the response to temperature changes since a fast NO rebinding is only the property of a 5c-NO heme leading to 4c heme after dissociation. We demonstrated that YC-1 and Bay 41-2272 drugs bind to the heme domain part (1-190) in β1-subunit of sGC. Similarly with sGC, we investigated AXCP and we demonstrated that the proximal histidine rebinds in about 100 ps after the exit of NO from the heme pocket, and thus precludes the rebinding of NO from the solution, so that the rebinding of proximal histidine functions as a molecular trap for NO-dissociated heme. This behavior represents a unique kinetic trap, and has not been observed among other heme proteins.

In the fifth chapter, we expanded our study about the trans effect by introducing one myoglobin mutant (H93C) which has similar trans effect found in sGC but with a different structure. NO(CO) rebinding dynamics was similar with sGC due to its 4c-heme property. We concluded that the factors which control the trans effect were limited to the heme pocket and surrounding structure of H93C. This Mb mutant allowed us to reproduce structural effect of effectors in sGC.

The interaction of NO with the enzyme NO-synthase, whose function is to provide NO to the cell, is strikingly different from thos described for the various NO-sensors. We observed that the occupancy of the effectors on the enzyme NO-synthase has a large effect on NO dynamics and release. We studied the effects of a variety of effectors such as two inhibitors (NMA, SEITU), a substrate analog (NHA) and one cofactor (BH_4) bound to the NO-releasing eNOS enzyme. They differently influenced the heme surrounding structure and NO dynamics and the challenge here was to discriminate simple steric effects from physiological allosteric effects with the help of molecular simulation. Parameters in mechanisms which regulate NO-synthase are numerous and NO release from eNOS responds differently with respect to effectors.

In the seventh chapter, we put our step in a somewhat different way. Instead of probing the intense Soret band, we probed the extremely small charge transfer band III (755-760 nm). This band reflects the iron position with respect to the heme plane during the rebinding of NO. By measuring its absorption change, we measured the very first structural event, namely the iron motion, which induce allosteric transitions in heme proteins whose coordination is 6c-NO (or 6c-O_2) such as myoglobin and hemoglobin. We compared our results at band III with our recent published data that demonstrated the retardation of the transition from the 6-coordinated domed heme to planar heme due to the protein relaxation.

Concluding this survey of dynamics in several heme proteins that become 5-coordinate with NO, we see that fast NO rebinding in $\sim$7.5 ps is not a unique property of sGC but of the 4c-heme. Its existence in a heme protein depends upon the strains exerted by the protein

structure on the heme and more specifically on the proximal ligand (usually a histidine), taking advantage of the trans effect of NO. However, the proportion 5-NO/6-NO is dependent on the facility of breaking the Fe-His bond and can vary from 30/70 to 99/1 and is modulated by protein structure and heme surroundings, as seen by the comparison between sGC, SONO's, H93C-Mb, and AXCP. This fast time constant (∼7.5 ps) of barrierless NO recombination does not necessarily mean that the affinity for NO is high, depending on the energy barrier to NO escape from the heme pocket which will determine k_{off}.

We saw through our study that all these parameters are strongly controlled by the protein and adapted to their function (or putative function). For example the trans effect is modulated within SONO's family despite their strong homology, and for a particular SONO can be also modulated as a function of temperature (some are thermophiles). The modulation of trans effect for CO is also clearly observed by the binding of artificial compounds to sGC which shift its energy minimum to a conformation increasing tension on the proximal histidine. This demonstrates that drugs can allosterically activate sGC by another mean than NO. The modulation of the affinity is obtained by the heme pocket architecture, which defines the energy barriers for ligand motion from and to the iron-binding site. An extreme case of modulation is exemplified by the binding of NO at the proximal position in AXCP, replacing the His previously detached by trans effect. Given the very fast rebinding of proximal histidine to the 4c-heme (70-100 ps), NO thermally released from the 5c-NO heme iron and leaving the heme pocket cannot rebind to the proximal heme side from outside the heme pocket (but in protein core), but must bind first to the distal side from solution, ensuring an efficient gating mechanism. Remarkably, in this case of modulation, all parameters are involved: trans effect, NO proximal binding (concentration dependent), rate of His rebinding, energy barriers from and to the heme both at distal and proximal sides. Despite this very particular mechanism, the exact biochemical function of AXCP is still unknown! We must also remember that NO proximal binding was demonstrated so far only in AXCP, not in sGC or other proteins.

Albeit our time-resolved experiments probed only NO/CO dynamics through the heme absorption, we have access to some protein structure dynamics. The most striking example is that the same transition (the cleavage of Fe-his bond equivalent to the conversion 6c-NO → 5c-NO, independent from NO concentration), is observed in sGC with two different time constants (∼0.7 μs and 250 μs) because the protein is not in the same allosteric state in both cases, so that allosteric transition occurred between 0.7 μs and 250 μs. As a promising perspective, this transition should be probed by time-resolved circular dichroism.

Through these studies, we have illustrated that time-resolved spectroscopy allows to identify the very first structural events which induce allosteric transitions in heme binding proteins and consequently the activation and deactivation mechanisms at molecular level.

Importantly, to trigger these transitions, we have used the light absorption properties of the heme, which allows one to cleave the chemical bond between the heme site and the diatomic ligand, synchronizing the population of molecules to be observed. Such a methodology has also been applied to non-naturally absorbing proteins such as photosystems, rhodopsin and fluorescent proteins[179, 180]. Now, time-resolved spectroscopy is awaiting its adaptation to unnaturally absorbing proteins, for example by using photo-activatable effectors or by introducing light-sensitive constituents in the protein by bio-engineering.

Chapter 9

Materials and Methods

9.1 Transient Absorption (TA) spectroscopy: Pump-probe method

Transient absorption measurements were performed with the pump-probe laser system previously described[181]. Basic idea of time-resolved pump-probe experiment is to perturb a system then to measure spectroscopically the consequence of the perturbation. Using a visible light pulse, the perturbation is always through electronic excitation, which leads in the case of a liganded heme to breaking the bound between the heme iron and the diatomic, and thus to release the diatomic. The system ligand/protein is put into in a non-equilibrium state and then structural dynamics measurements can take place. The sample experiences a change toward a new unknown equilibrium. Reaching this new equilibrium may take place in tens of picoseconds as well as in the ns-μs time-range. This change can be monitored at different time delays and probed with a low-energy second light probe pulse. This pulse should be harmless to the sample. The source of ultra-short pulse (<100 fs) is a dye laser pumped by a continuous wave Argon laser ($\sim$2.5 W) providing pulses at 620 nm at a repetition rate of $\sim$95 MHz. These pulses are amplified by a YAG laser at 30 Hz (only 30 pulses on 95×10^6 pulses are amplified), and the amplified pulse train is split in two equal beams used respectively for pumping and probing the sample. The splitting of the pulse train is thus the origin of the time delay in such time-resolved experiment. After this splitting, each pulse train is separately modulated to obtain precisely shaped pulses (energy, wavelength, duration, and spectrum).

In a typical pump-probe experiment, the delayed probe pulse is used to detect the optical difference ΔA induced by the perturbation triggered with the pump pulse. Measuring the evolution of ΔA at different time delays allows us to detect structural changes. The appearance of the unliganded species is monitored by probing the amplitude of the induced

transient absorption in the given region. The observed spectral changes in the 2 ps–5 ns time window are due to ligand rebinding, but thermal relaxation of the protein and contributions from the short lifetime-excited state may be detected before 5 ps. The temporal range can be directly determined by the repetition rate and duration of the lasers of pump and probe pulses. The photodissociation of NO was achieved with an excitation pulse at 564 nm whose duration was ∼40 fs with a repetition rate of 30 Hz. White light continuum for obtaining a broad band probe pulse was created after passing 8-mm cell that contained H_2O (Soret) or D_2O (band III measurement). Probe and pump beams were focused to a spot of ∼50 μm and $\sim$ 200 μm respectively and spatially overlapped in the sample cell, which was continuously moved perpendicular to the beams to ensure sample renewal between the shots. Two beams are used to measure the absorbance. The reference beam does not go through the sample but the probe beam does go through the sample to calculate the ratio and this allows us to eliminate the influence of intensity fluctuations and is mandatory to obtain a good signal to noise ratio. Both beams, whose spectral width is about 200 nm, go through a spectrometer, and then are measured as two channels on a CCD detector. Thus the reference pulse is taken into accountat each individual pixel.

9.1.1 Description of our setup for TA measurement

Figure 9.1 shows the experimental setup currently employed in our laboratory for TA measurements[181, 182]. All experiments were carried out at room temperature except for some bacterial NO-sensors. The absorption spectra of the samples were verified before and after time-resolved experiments using a spectrophotometer (Shimadzu 1601). We used quartz cell from Hellma with a 1-mm optical path length. The same cell was used to record steady state and transient spectra. The optical density can be in the range 0.1 to 1, but below OD = 0.1 the signal is too small and above OD = 1 there is a distortion of the transient spectrum due to the low intensity of the probe pulse. If the absorbance is too high, the signal is close to the noise level and a small change in OD will not appear significantly above the noise. Thus the best working range for our set-up is 0.4<OD<0.8; however, we may have a lower value for a rare protein or a higher value if we cannot estimate the final absorbance, because the extinction coefficient is always higher for liganded heme proteins than for unliganged. Mb is used as a standard in its CO-liganded form to align the delay line and to adjust the colinearity and overlap between the pump and probe beams. In its NO-liganded form we use it for checking the alignment and as a comparison for the unknown proteins. Since we record a series (40 to 60) of transient spectra (375-475 nm) at different time delays, the result consists of a matrix of differential absorption as a function of time and wavelength. Measurement of

transient absorption data and control of delay line was done by the same software whereas analysis of data was performed by specific software.

9.1.2 Special setup for band III measurements

For Band III measurements, we used our femtosecond absorption spectroscopy setup with minor modifications. We changed the light path of the probe beam with different position of the prisms. We also employed RG650 filters to attenuate 620 nm light from continuum. We tried this setup from the scratch with trial and error approach and got enough signal for detecting the band III signal of Mb with NO for the first time. We varied the excitation wavelength (564, 590, and 610 nm) according to published protocol[169] but the best possible pump pulse had the same wavelength as in Soret measurement at 564 nm (pulse duration ∼40 fs; repetition rate 30 Hz). White light continuum probe pulses of about 50 fs duration was generated after focusing in a 8-mm cell that contained D_2O to shift the Raman emission induced in H_2O. Both beams were focused to spots of 100 μM and 200 μM. Concentration of Mb and Hb is much higher than the Soret because band III has an extremely low extinction coefficient (250-350 $M^{-1} \cdot cm^{-1}$). The global analysis of the data at band III and Q-band was performed both by SVD of the time-wavelength matrix or at single wavelengths in the multiple time windows ranging from 25 ps to 250 ps. Up to 160 scans were recorded and averaged with a dwell time of 2 s at each point.

9.2 Molecular dynamics simulation - CHARMM

Molecular simulation studies can provide the details concerning individual particle motions as a function of time. Our experimental results are given priority than those by simulation for significance but the results of the simulations can detect impossibilities. In our cases, molecular simulation studies are applied to compare our experimental results in order to provide structural information, which is usually missing, for some proteins studied in this thesis. In 1977, the first molecular dynamics simulation study of a macromolecule was published[183]. Jean-Christophe Lambry in our lab is the specialist in molecular dynamics study and helped me for the molecular simulation studies. We frequently use the program CHARMM (Chemistry at HARvard Molecular Mechanics), which is suitable for macromolecular energy minimization and dynamics calculations[184], for our studies of sGC and its related proteins.

The first step to do MD simulation is to prepare the 3D structure of given proteins obtained from the Protein Data Bank website with PDB format. If the crystal structure is

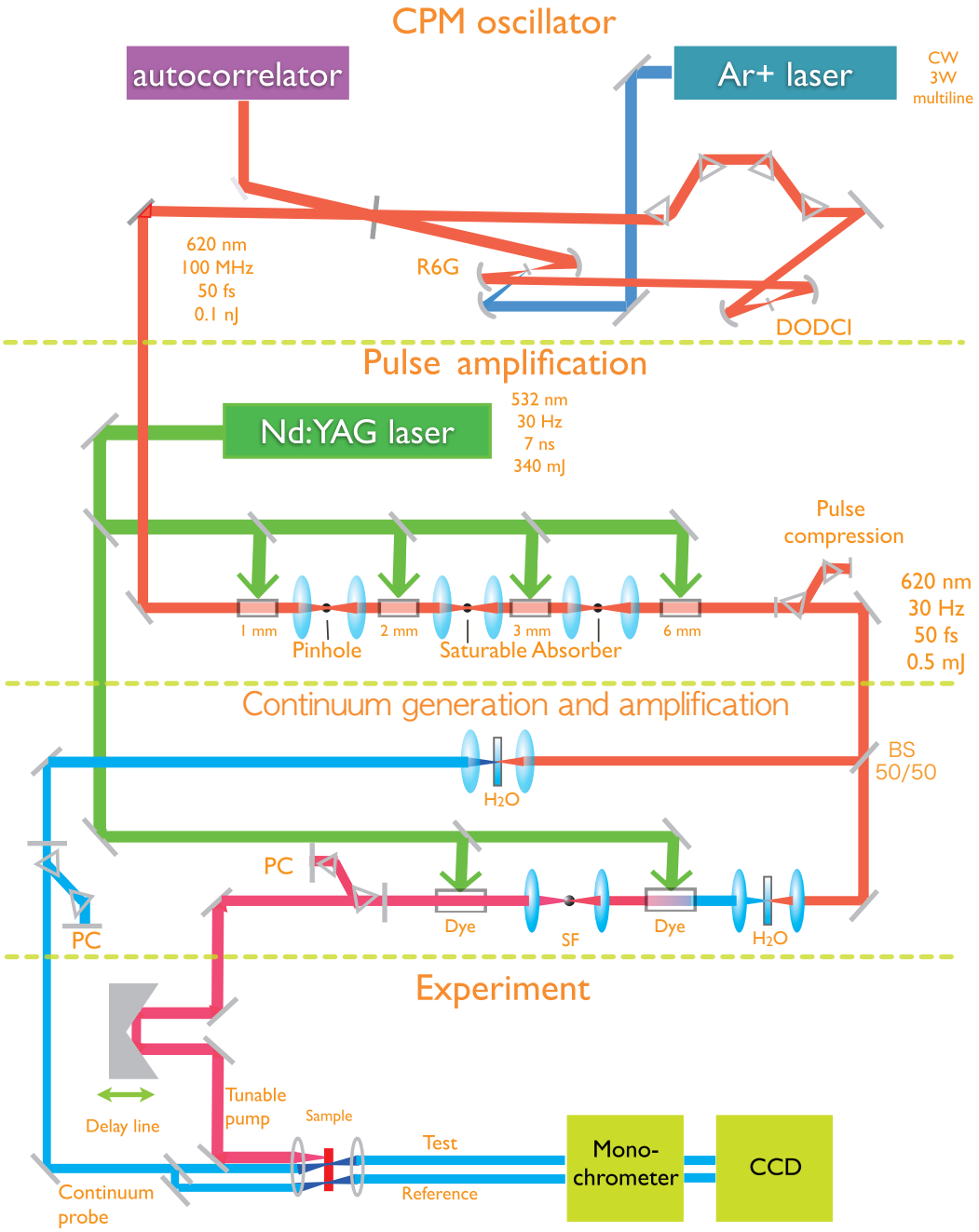

Figure 9.1: Scheme of the experimental setup used for femtosecond transient absorption spectroscopy. The spectrum of the pump pulse is tunable by the choice of the dyes in the amplification of the continuum. The temporal length of the pulses depends on the spectrum and generally is shorter than the fundamental pulse. Abbreviations are: SA, saturable absorber; SF, spatial filtering; PC, pulse compression with two prisms.

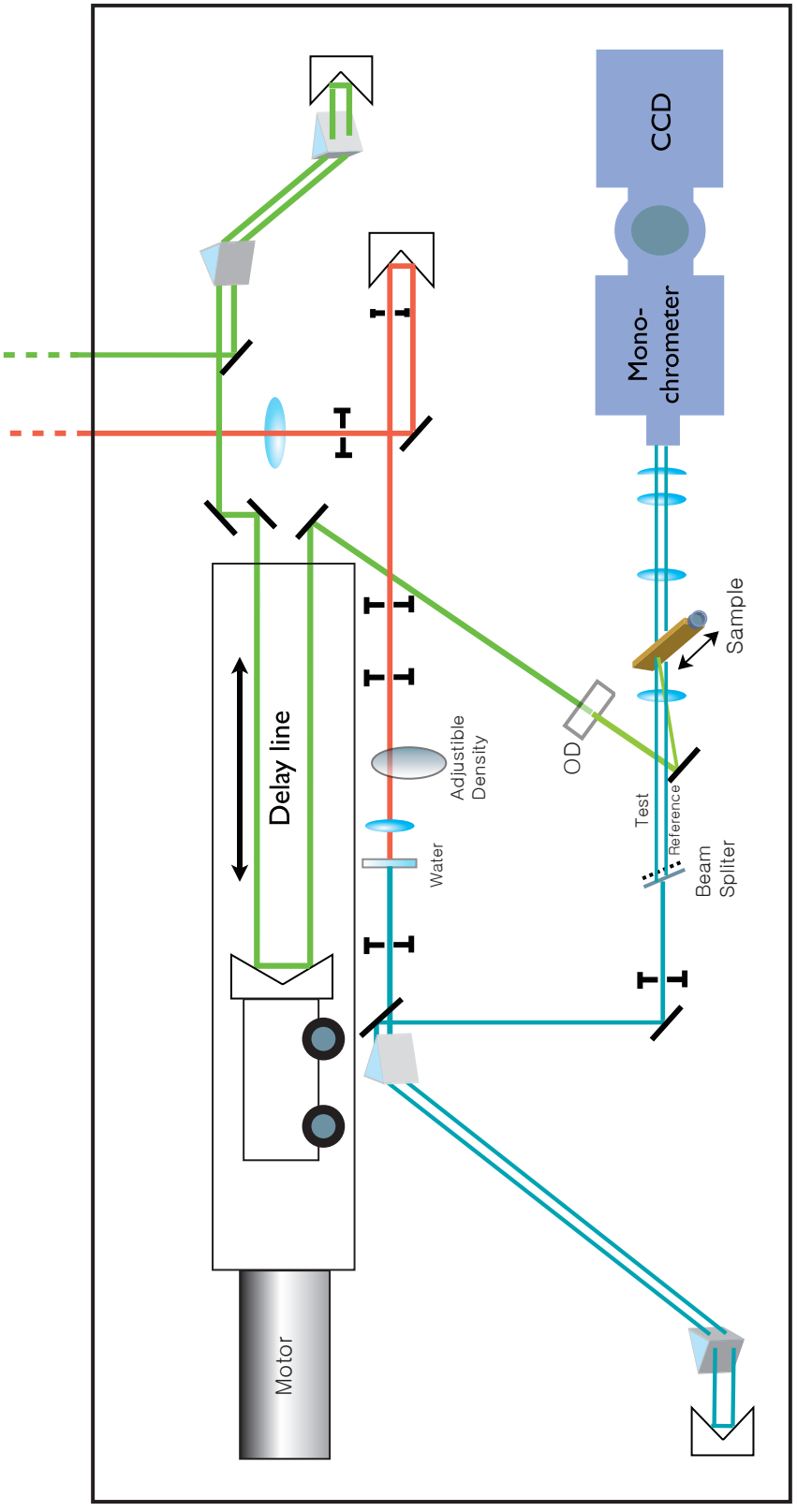

Figure 9.2: In detail part of measuring the transient absorption of the sample.

not available, we obtained it from homology modelling method. In our case, we applied this method for sGC heme domain in Chapter 2 and Mb mutant H93C in Chapter 5. Secondly, we put water molecules into the system because the atomic coordinate from PDB files usually does not include water. Therefore, we introduce a water molecule box around the proteins to have realistic environment. This increases the number of total atoms of the system and it causes long time of calculations. The next step is to do the energy minimization of the system. The general form of the potential energy function used in CHARMM for proteins is shown in equation below.

$$U_{CHARMM} = \sum_{bonds} K_b(b - b_0)^2 + \sum_{angles} K_0(\theta - \theta_0)^2 + \sum_{dihedrals} K_\phi[1 + \cos(n\phi - \delta)]$$

$$+ \sum_{impropers} K\omega(\omega - \omega_0)^2 + \sum_{Urey-Bradley} K_{UB}(S - S_0)^2 + \sum_{residues} U_{CMAP}(\phi, \psi)$$

$$+ \sum_{non-bonded-pairs} \left[\varepsilon_{ij} \left[\left(\frac{R_{\min,ij}}{r_{ij}} \right)^{12} - 2 \left(\frac{R_{\min,ij}}{r_{ij}} \right)^{6} \right] + \left(\frac{q_i q_j}{4\pi\varepsilon_0 \varepsilon r_{ij}} \right) \right]$$

More details of this potential function with force fields can be found in the reference[185]. Then we increased the temperature during several picoseconds by heating the system upto 300 K together with equilibration process to distribute the heat over the system. After the energy minimization process (MINImize command), main calculation is performed by molecular simulation and it requires the integration of Newton equations of atomic motion with the function of time. Briefly, for each atom the potential energy U is calculated taking into account the positions of atoms involved in interactions within the equation above, allowing to know its velocity. From this velocity, its new position is calculated after 1 fs (or 2 fs). After having completed this step for every atom, then the potential energy U is again calculated with the new positions of atoms. And so on. Basic step for this calculation is 1 or 2 fs and we need millions of integration of the step to have a few ns simulation time. MD trajectories are controlled by the DYNAmics command and the data (new structures) are saved every ps. Two different softwares such as Chimera or Pymol are used to visualize the calculated structures afterwards. We used CHARMM both for obtaining relaxed structures after homology modeling, or for calculating NO trajectories after removing the bound between NO and Fe^+ (NO-synthase).

9.3 Homology modelling - MODELLER

Homology modelling is often used for the protein tertiary structure prediction. If the sequence for the unknown protein of our interest is similar with the sequence of the protein with the known structure, we can use this homology modelling method. In this thesis, we applied this method to unknown heme domain of β1 subunit of sGC and known *Cb*-SONO. We used the powerful program MODELLER, which is the representative tool for the so-called restraint-based method[186]. In this method, the program measures the distance between atoms or amino acid residues of the template protein (in our case: *Tt*-SONO) and it builds the 3D structure of unknown structure using this distance as the restraint. The process of using MODELLER can be summarized as below.

- Searching for a template protein, usually the PDB file of the protein
- Alignment between the sequence of template protein and the sequence of protein of our interest
- Inserting relevant amino-acids in gaps
- Building the 3D structure of the protein of our interest

```
>P1;1xbn181nooxy
structureX:1xbn181nooxy.pdb:   1 :A:+193 : :MOL_ID  1; MOLECULE
METHYL-ACCEPTING CHEMOTAXIS PROTEIN; CHAIN  A; ENGINEERED  YES:MOL_ID
1; ORGANISM_SCIENTIFIC  THERMOANAEROBACTER TENGCONGENSIS; STRAIN
MB4T; GENE  TAR4; EXPRESSION_SYSTEM  ESCHERICHIA COLI;
EXPRESSION_SYSTEM_COMMON  BACTERIA; EXPRESSION_SYSTEM_STRAIN
BL21(DE3); EXPRESSION_SYSTEM_VECTOR_TYPE  PLASMID;
EXPRESSION_SYSTEM_PLASMID  PET24D: 2.50:-1.00
MKGTIVGTWIKTLRDLYGNDVVDESLKSVGWEPDRVITPLEDIDDDEVRRIFAKVSEKTGKNVNEIWREVGRQNI
KTFSEW-FPSYFA--GRRLVNFLMMMDEVHLQLTKMIKGATPPRLIAKPVAK-DAIEMEYVSKRK-MYDYFLGLI
EGSSKFFKE-EISVEEVERGEKDGFSRLKVRIKFKNPh/wwwwwwwwwww*

>P1;sGCbeta
sequence:sGCbeta:     : :     : ::: 0.00: 0.00
MYGFVNHALELLVIRNYGPEVWEDIKKEAQLDEEGQFLVRIIYDDSKTYDLVAAASKVLNLNAGEILQMFGKMFF
VFCQESGYDTILRVLGSNVREFLQNLDALHDHLATIYPGMRAPSFRCTDAEKGKGLILHYYSEREGLQDIVIGII
KTVAQQIHGTEIDMKVIQQRNEE-CDHTQFLIEEKESh/.....*
```

For the first step, we took the PDB file of *Tt*-SONO form the protein data bank and put it into the PIR format file, displayed as a text file and easily edited using simply text editor. After performing the align2d command file, the resulting file for the next step in case of the heme domain of β1 subunit of sGC is displayed as above. The reconstituted file (saved as $filename.ali$) should always have $*$ at the end and the first line contains the tens fields separated by colons indicating the information about the structure file if available. The amino

acid sequences are represented by capital one-letter code, while other groups are represented by small letters. In the source file, h means the heme and w means water. Using the alignment file, we can start building a model (*model-single* command) with a pdb file format having the atomic coordinate information. The energy of the built model is minimized by using CHARMM. The 3D structure of the heme domain of $\beta 1$ subunit of sGC was displayed in Chapter 2 with this protocol.

9.4 Preparation of the proteins

9.4.1 Purification and characterization of soluble guanylate cyclase

We purified sGC from bovine lung using a modified method from Mulsch and Gerzer[187], Stone and Marletta[38]. All steps were performed at 4°C. One kg of bovine lung was homogenized in 1 L of buffer (TEA 25 mM, pH 7.4, NaCl 50 mM, DTT 5 mM, PMSF 1 mM, EDTA 1 mM, benzamidine 1 mM, pepstatin A 1 μM, leupeptin 1 μM, aprotinin 1 μM). The homogenate was centrifuged at 40 000 X g for 30 min. The supernatant was filtered through 8 layers of gauze and then centrifuged again at 40 000 X g for 2 h. One liter of this surpernatant was loaded by means of a peristaltic pump (3 mL/min) onto a column (2.5 cm x 90 cm) containing Q-Sepharose Fast Flow (Sigma Chemical) previously equilibrated with homogenizing buffer. The column was then washed with two volumes of same buffer. All the following chromatographic steps were performed using an Akta Purifier FPLC system (Amersham Biosciences). The column was eluted with a linear gradient from 50 to 400 mM NaCl (flow 2.5 mL/min). The elution profile was continuously monitored for absorption at 280, 430 nm and 460 nm, as well as for pH and conductivity. The fractions (10 mL each) were assayed for cyclase activity (see below) and the active ones were pooled and diluted 3 times in buffer without NaCl to get about 85 mM NaCl.

This solution (about 220 mL) was then loaded either onto a high-resolution anion exchange column (Source 30Q; 2.6 × 30 cm; Pharmacia Biotech) which was subsequently washed with two volumes of buffer A (TEA 25 mM, pH 7.4, NaCl 50 mM, DTT 5 mM, PMSF 0.1 mM, benzamidine 0.2 mM). The proteins were eluted by means of a linear gradient from 50 mM to 400 mM NaCl (2.5 mL/min). The 10 mL fractions were assayed for GMP cyclase activity: the more active ones were pooled (60 mL totally) and concentrated in a stirring concentrator with a 50 kDa cut-off membrane (Millipore) under argon at a positive pressure of 1.5 bar. The solution was supplemented with additional DTT (5mM) and 8 mL were injected onto a high resolution gel filtration column (Superdex 200pg, Amersham Biosciences, 2.6 × 60 cm) from which proteins were separated using an isocratic elution with buffer A at a

flow of 1mL/min. The active fractions (25 mL totally) were concentrated in a centrifugation device with a 50 kDa cut-off membrane (Ultrafree-15, Millipore) to 3 mL. The buffer A was exchanged for buffer G (same as A but without NaCl and containing 5 mM $MnCl_2$).

This last solution concentrated to 1.5 mL was loaded onto a GTP-agarose affinity column (Sigma, 2.6 × 3 cm) equilibrated with buffer G, which was immediately eluted (0.5 mL/min) with a linear gradient from buffer G to buffer C (TEA 25 mM, pH 7.4, ATP 6 mM, NaCl 50 mM, DTT 5 mM, PMSF 0.1 mM, benzamidine 0.2 mM). The purified sGC was eluted as a single peak at 62 % of buffer C (about 3.7 mM ATP). The active fractions (9 mL) were pooled and concentrated to $\sim$ 75 μL. For spectroscopic measurements the buffer was exchanged for only TEA 25 mM, NaCl 50 mM, pH 7.5 by means of successive dilutions and centrifugations in order to obtain less than 50 nM of ATP and DTT. The specific activity (see below) was measured and the presence of two subunits was checked on 7.5 % polyacrylamide-SDS electrophoresis.

Figure 9.3 and 9.4 show the chromatograms of the four columns. The elution was followed by recording continuously the absorption at 280 nm for the absorption of total proteins (blue line) and at 431 nm (red) and 552 nm (purple), which are the absorption maxima of guanylate cyclase, but also located within absorption bands of other heme proteins. The separated fractions are indicated in light blue. The pH (green) and the ionic strength (brown) were also recorded. The black straigtht line is the theoretical NaCl gradient for the two first columns, shifted from the brown curve by the dead volume of the respective column. The Superdex molecular filtration column was eluted in isocratic mode, keeping constant the ionic strength. For the last GTP-agarose column, the gradient was obtained by increasing ATP, which absorbs also at 280 nm, leading to a strong absorption. Purified sGC was never frozen or stored, but was used within two days for spectroscopic experiments.

Properties of the columns used:

- Q-Sepharose: anion exchange, high capacity, high flow
- Source 30Q: anion exchange, high resolution
- Superdex 200pg: molecular size filtration
- GTP-Agarose: specific affinity (or ATP-agarose)

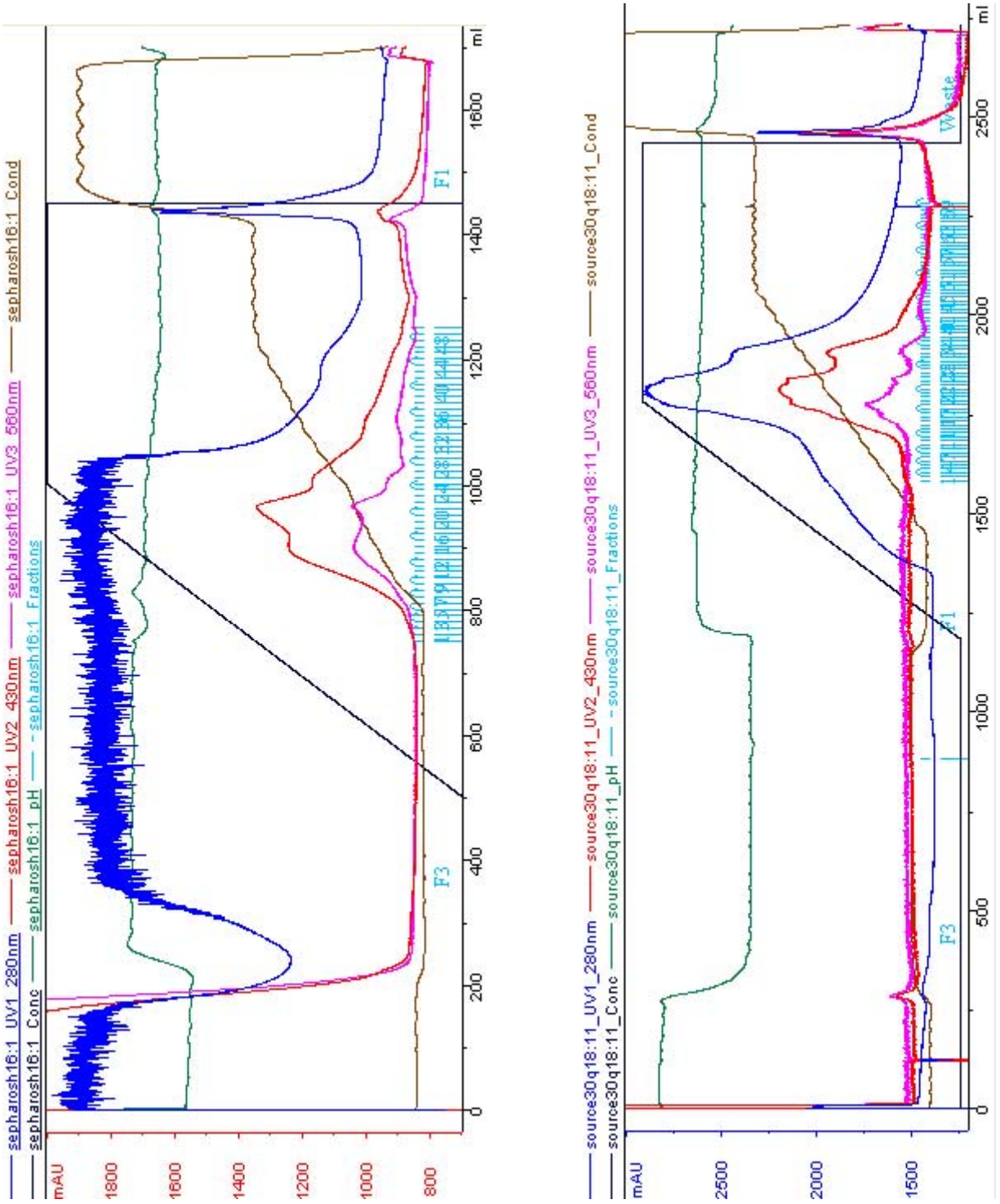

(a) Sepharose Fast Flow

(b) Source 30Q

Figure 9.3: Chromatograms of (a) Sepharose Fast Flow and (b) Source 30Q columns

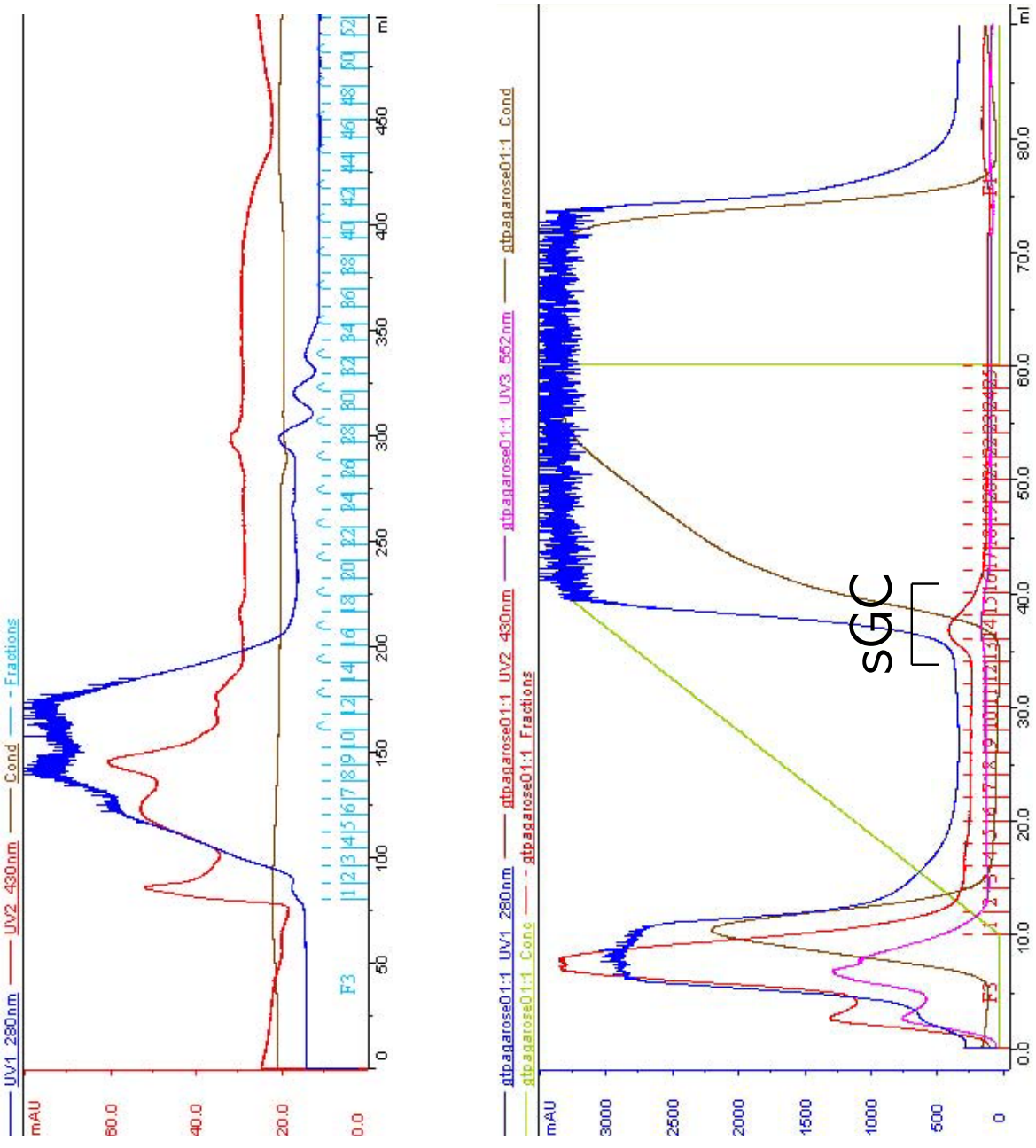

(a) Superdex

(b) GTP-agarose

Figure 9.4: Chromatograms of (a) Superdex and (b) GTP-agarose columns

9.4.1.1 Assays of the fractions

The sGC activity assay for first two columns is displayed in Figure 9.5. On each panel the fractions pooled are indicated. These fractions presented at least 75 % of the peak of activity and are concentrated to be injected at the next step. For the Superdex column, a peak of lower activity is eluted before the main peak, maybe containing monomers of sGC, as sGC is mainly purified as dimers[188] thus located in the main peak.

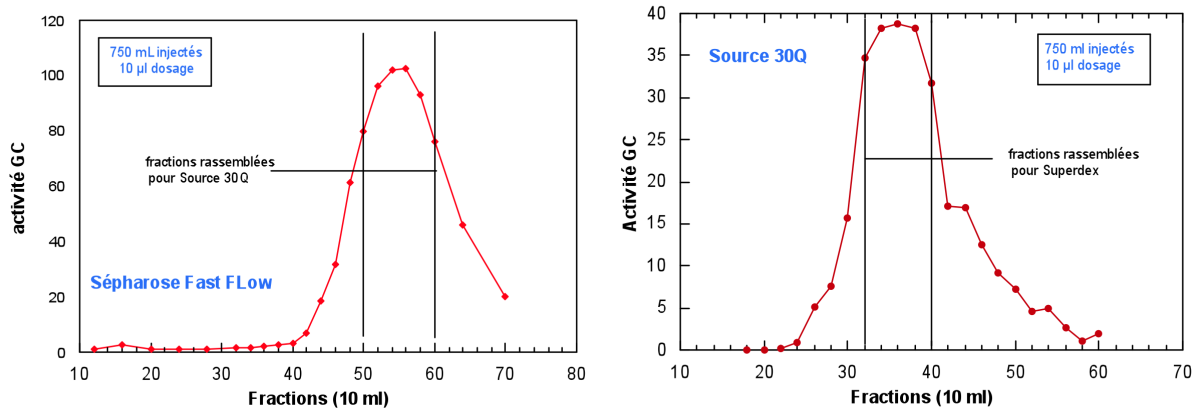

(a) Sepharose Fast Flow

(b) Source 30Q

Figure 9.5: Activity profile of the fractions for (a) Sepharose Fast Flow and (b) Source 30Q columns. The volume of supernatant injected into the column is indicated together with the volume of aliquot taken for the activity assay. The fractions pooled for the next purification step are indicated by vertical lines.

We used in the second step a Source 30Q column, which has the same chemical nature as the Q-Sepharose anionic exchange column. However, instead of having a broad range of bead size (50-300 μm for Q-Sepharose) it possesses calibrated beads of exactly 30 μm. This ensures a very high resolution, because the path of the proteins being eluted (which depends both upon bead size and protein size) interferes minimally with the elution pattern due to the gradient of ionic strength. Usually, one chooses columns of different chemical nature within a purification process, in order to have different separation mechanisms at each step. However, the first chromatographic step of guanylate cyclase purification is particular because the solution injected into the column is a high amount of crude cell extract in which sGC is very diluted among other major proteins at high concentration. This requires a fast and broad "sorting" which does not allow us to exploit the highest possible resolution of an anionic exchange. For this purpose, the Q-Sepharose fast flow chromatography allowed the rapid processing of a large amount of crude supernatant and was followed by the very high resolution anionic exchange Source 30Q. The GTP-affinity medium used in the fourth step was slowly degraded by sGC (and maybe slow spontaneous hydrolysis), and was used only

twice for this reason. The sGC activity assay for the remaining two columns is displayed in Figure 9.6.

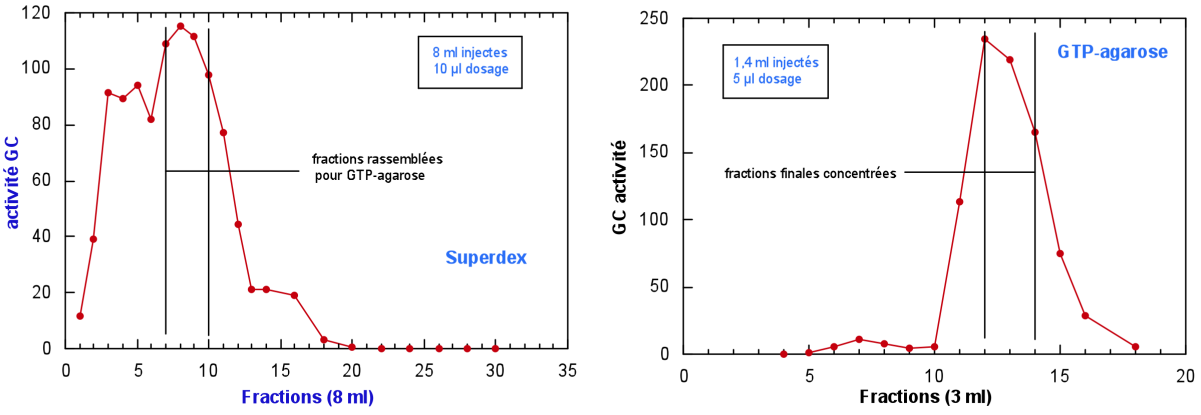

(a) Superdex (b) GTP-agarose

Figure 9.6: Activity profile of the fractions for (a) Superdex and (b) GTP-agarose columns. The volume of supernatant injected into the column is indicated together with the volume of aliquot taken for the activity assay. The fractions pooled for the next purification step are indicated by vertical lines.

9.4.1.2 Measurement of guanylate cyclase catalytic activity: cyclic GMP assay

The activity of sGC in the fractions was measured after each column and at the end of the purification, together with the protein content. The method has been adapted from the paper by Mulsch and Gerzer[187]. In a first step cGMP was synthesized by sGC from GTP, then the cGMP was assayed by immuno-detection using a commercial kit and 96-wells micro-titration plates (General Electric Healthcare) and a BioRad plate reader.

1. Formation of cGMP

   Incubation buffer: TEA 100 mM, pH 7.4, EGTA 0.1 mM, DTT 1 mM, MnCl2 3 mM, GTP 0.2 mM, creatine phosphate 5 mM, creatine phosphokinase 150 U/L, isobutyl-methylxanthine 1 mM, Na nitroprusside 0.1 mM (stock solution freshly prepared every day).

   Nitroprusside provides NO, which is slowly released in the solution and activates sGC. Mn^{2+} is necessary for the functioning of the enzyme, but its role is unknown. Isobutyl-methylxanthine is an inhibitor of phosphodiesterase, which hydrolyses cGMP. Creatine phosphokinase regenerates GTP from GDP creatine phosphate because of its slow hydrolysis.

   An aliquot (5 to 20 μL depending upon the step and the expected activity) of the fractions to be assayed is mixed with 90 μL of this buffer previously warmed at 37°C.

Incubation was performed for 10 min, then stopped by placing the tubes on ice and immediately adding 400 μL of Zn acetate followed by 500 μL of Na_2CO_3. The precipitate was separated by centrifugation at 4°C (10 min, 14000 rpm) and 10 μL of the supernatant are put in polypropylene tubes simultaneously to the cGMP standards (2 to 512 femtomoles of cGMP) and diluted with buffer to 500 μL. All the samples were then acetylated by adding 50 μL of acetic anhydride/triethylamine (1/2 mixture).

2. Assay of cGMP

   Antiserum (100 μL) was added in all wells then 50 μL of the acetylated samples were deposited into the wells of the antibody-coated micro-titration plate. Incubation for 2 h at 4°C. cGMP-peroxydase complex (100 μL) was added to each well except in blanks. Incubation for 1 h at 4°C. All the wells were washed and rinsed three times and the color substrate in added to each well (200 μL). Incubation for 30 min at 20°C. Sulfuric acid (100 μL) was added to the wells and the optical density at 450 nm was read in a micro-titration plate reader.

3. Assay of total protein content

   The total protein content was assayed by means of the bicinchoninic acid method (Pierce) adapted for a micro-titration plate with bovine serum albumin as a standard. Variable amounts of samples (5 to 20 μL) were deposited in the wells, then 10 μL of NaOH 0,3 M. After a 20 min incubation, 200 μL of BCA reactive were added to each well. After one hour of incubation at 37°C, incubate each well (200 μL) for 30 min at 20°C. Sulfuric acid (100 μL) was added to the wells and the optical density at 570 nm was read in the plate reader.

   For assaying the catalytic activity, we choose standard conditions: 37°C, pH 7.4, Mn^{2+} as the required divalent metal cofactor and nitroprusside as the NO donor. It must be noted that the result was dependent upon the concentration of available NO. We always performed the assays using several dilutions of GC samples in order to obtain values within the linear range of the cGMP standards (Figure 9.7). The linear range of the measurement corresponds to the absolute amount of 3 to 300 femtomoles of cGMP for one well. Outside of this range there was either saturation of binding or no binding.

   During the purification, we performed an activity assay between each column. Because we only needed to compare the fractions, the assay was not absolute, omitting the cGMP standard, and the activity was expressed as a value proportional to the amount of cGMP produced, which is linear for log[cGMP] only within a range of two orders of

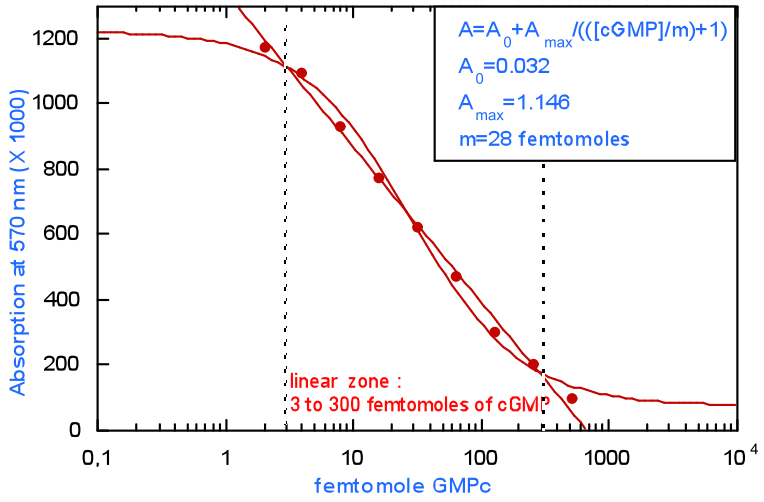

Figure 9.7: Assay of cGMP standard. Absorption (A) of wells containing the increasing amount of cGMP. This assay must be performed for each different plate coated with anti-body anti-cGMP in order to determine the linear zone. The points were fitted to the curve $A=A_0+A_{max}/(([cGMP]/m)+1)$. A_0 and A_{max} are respectively the absorbance in absence of cGMP (blank) and the maximum of absorbance. m is the cGMP concentration for which $A=A_0+A_{max}/2$, defining the middle of the linear range.

magnitude: [cGMP] $\propto 10^{(A-A_{max})}$-1. Plotting directly the absorption of the well versus the fraction number would lead to a distortion of the eluted peak activity. After the last column and wash, for the final samples used in spectroscopic measurements, we obtained specific activities in the range 0.5-1.0 $\pm$ 0.3 μmole cGMP/min/mg of protein in the presence of Mn^{2+}(3 mM) and Nitroprusside (0.1 mM) as NO donor.

4. SDS-Polyacrylamide Gel Electrophoresis

SDS-PAGE using a discontinuous buffer system was performed according to the method of Laemmli using slab gels (1.0 mm thick).

Stacking gel: 50 μL 0.1 M SDS, 80 μL 0.1M Ammonium Persulfate, 5 μL TEMED, 670 μL of bis-acrylamide, 1.25 mL of Tris-HCl 0.5 M pH 6.8, 3.0 mL of water.
Running gel: 100 μL of 0.1 M SDS, 100 μL of 0.1 M APS, 5 μL TEMED, 2.7 mL of bis-acrylamide, 1.25 mL of Tris-HCl 1.0 M pH 8.8, 1.2 mL water.

For the detection of alpha and beta subunits with resolution in the range 70-80 kDa, we used a 7.5 % acrylamide gel. The amount of sample loaded to each well was 15 to 25 μL at a concentration of about 2 mg/ml. Standard protein molecular weight markers (Promega) ranging in size from 10 kDa to 250 kDa were used. A second home-made marker was used combining myoglobin and Bovine Serum Albumin (BSA) to

unambiguously identity the range of our protein (72 to 84 kDa). The gel was run on a BioRad apparatus at a constant voltage (110 V). The gels were then either stained using Commassie Brilliant Blue dye or processed for western blot analysis and were photographed with a digital camera.

5. Western Blot

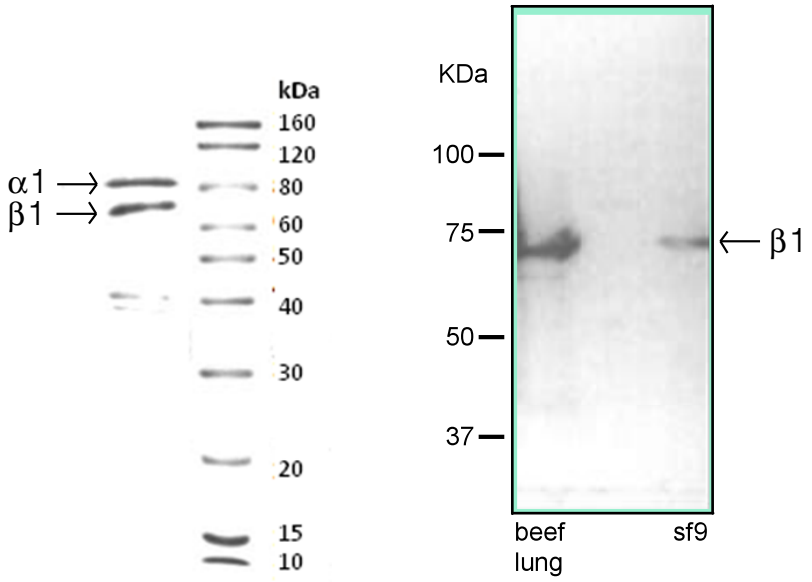

(a) α1 and β1-sGC (b) Beef lung vs sf9

Figure 9.8: (a)- Western-blot with anti-α-sGC and anti-β-sGC subunits specific antibodies from 10 % (w/v) SDS/polyacrylamide gel. (b)- Western-blot with anti-β-sGC subunit and anti-hexa-histidine antibodies from 8 % (w/v) SDS/polyacrylamide gel comparing sGC purified from beef lung and overexpressed in a sf9/baculovirus system. In this system the yield was not sufficient from obtaining a protein amount allowing spectroscopic experiments. Monoclonal Anti-polyHistidine - Peroxidase antibody - Sigma A7058. In both cases proteins were detected by colorimetric development Opti-4N (BIO-RAD).

For immuno-detection, the proteins were transferred from polyacrylamide gel to a membrane (nitrocellulose filter, Millipore, 0.2 μm pore size) by electroblotting (80 V; $\sim$ 1 hour). The membrane was then dyed using red Ponceau. The non-specific sites for proteins binding to the membrane were then blocked by a one-hour incubation in 10 % non-fat dry milk dissolved in 20 mL of PBS/Tween (0.10 M PBS, 0.001 M Tween 20). After three washings with PBS/Tween, the membranes were incubated and slowly agitated overnight at 4°C in the presence of the primary antibodies anti-β-sGC or anti-α-sGC. Both were mouse monoclonal antibodies and were purchased from Sigma-Aldrich. Antibodies were diluted according to manufacturer's recommendations. The working dilution of monoclonal anti- bodies was 1:1000 in PBS/Tween. Following overnight

incubation of membrane with antibodies, each membrane was washed and incubated with a secondary antibody (goat anti-mouse IgG conjugated with horseradish peroxidase, BioRad Opti4CN substrate kit). Secondary antibodies were diluted to a working concentration of 1:5000 in PBS/Tween. Each membrane was then slowly agitated for 1.5 hours at 4°C. Following a double wash, the membrane was lastly incubated with the colorimetric reagent. The membranes were then photographed using a digital camera.

9.4.2 Preparation of samples for transient spectroscopy

As general procedure employed for all samples, the proteins thawed from –80°C or from liquid N_2 are centrifuged to remove precipitated material and may be diluted in buffer if necessary. 75-100 μL of sample are placed in a 1 mm optical path quartz cell and the steady-state spectrum is recorded. A gas-tight rubber stopper is placed on the cell. The sample is degassed under vacuum using three cycles of vacuuming and filling with pure argon. Purified sGC is already in the reduced state. Other proteins must be reduced. For reduction we use Na-dithionite ($Na_2O_4S_2$) when working with CO or ascorbate when working with NO because dithionite reacts with NO. In a small gas-tight vial, firstly we degassed 500 μL of water and added reductant to get 20 mM and degassed again. Finally put 10 μL of degassed dithionite in the cell containing the protein using a gas-tight Hamilton syringe. The final concentration is about 2 mM. After that, we recorded absorption spectrum and degassed to replace argon by CO or NO and wait for 10 min for equilibration between the gas phase and the solution. Immediately after removing the cell from the gas train, we placed a drop of vacuum grease on the rubber stopper and a second stopper. Depending upon the k_{on} of the protein, the full equilibration may take a variable duration and is verified until the absorption spectrum is stable. When NO is 100 % in the gas phase (1 bar) the concentration of NO in the aqueous phase is 2 mM at 20°C

To obtain CO-liganded sGC we used 100 % CO, at 1.4 bar, leading to a 1.5 mM CO concentration in the solution. All the gases were purchased from Air Liquide. At each step, absorption spectra were recorded for monitoring the evolution of the protein. Equilibrium spectra were recorded using a Shimadzu-1601 UV-Visible spectrophotometer. The same sample in the same quartz cell (1-mm optical path length) was used to measure equilibrium spectra and transient spectra at room temperature. All steps of sample preparation were monitored by absorption and steady-state spectrum was always measured after each kinetic measurement to verify the integrity of the sample in the laser beam. The cell can be thermostated for measurements as a function of temperature. Particularities for each protein are described below.

1. Preparation of NO-liganded sGC samples for spectroscopy

   An aliquot of freshly purified sGC solution (70 μl at about 30 μM) was put in a 1-mm optical path length cell in quartz. It was sealed and degassed. Guanylate cyclase was purified directly in its ferrous state, and it was not necessary to reduce it, at variance with the other heme proteins. For preparing NO-liganded sGC, NO diluted at 1 % in N_2 was directly introduced in the quartz cell at a pressure of 1.4 bar, corresponding to about 20 μM of free NO in the solution, and a second stopper was put on the cell. The concentration of sGC was 30 $\pm$ 10 μM. Its affinity for NO is very high ($K_D < 50$ nM), leading to a depletion of free NO in solution. However, NO was supplied constantly to the gas phase during the equilibration, ensuring the saturation of sGC by NO.

2. Binding of the activators: YC1 and BAY 41-2272

   The effector YC1 was obtained commercially from RBI-Sigma and BAY 41-2272 is a gift from Dr Johannes-Peter Stasch, Bayer. Their solubility in water is very low (this is one reason why they cannot be used as drugs because of unfavorable parmaco-kinetics) and it was dissolved in DMSO at a stock concentration of 4 mM. An aliquot of 5 μL of this solution was added to 95 μL of sGC solution in an Eppendorf centrifugation tube to give 200 μM, then mixed thoroughly. Incubation was performed overnight in the dark at 20°C. A first trial of incubation at 4°C led to partial precipitation of YC1, and increasing the temperature to 20°C allowed to minimize precipitation without damage of the protein. After incubation, the solution was centrifuged (13000 rpm, 5 min) and 80 μL of sGC with bound activator were introduced in the spectroscopic cell. The final concentration of DMSO was 3 %. We tried also to introduce aliquot of stock solution in DMSO directly in the cell to incubate overnight. The slight precipitate did not preclude spectroscopic measurements.

3. Binding of the non-hydrolysable substrate analog: GTP-γ-S

   GTP-γ-S was obtained from SIGMA (1 mg) and kept at – 20°C. Since it is highly soluble in water we dissolved it in water in the original bottle of the product. 100 μL of buffer with 1 mg sample gave rise to $\sim$ 10 mM and was transferred to a vial for degassing. After degassing the vial under argon, 10 μL of the solution was added to the 90 μL of sGC or SONOs in solution. The final concentration of GTP-γ-S is 1 mM.

9.4.2.1 Preparation of SONOs

Three different SONOs were obtained from Pierre Nioche in Paris. SONO from *C. botulinum* was well expressed in growing *C. botulinum* cells. By using *E. coli* as the host protein,

which constitutes the N-terminal heme domain with 186 amino acids from the *C. botulinum* DNA source was overproduced. The procedure was the same for *Np*-SONO (1-183) and *Tt*-SONO (1-191). His-tagged SONO proteins were purified by Nickel affinity chromatography followed by gel filtration. Proteins thus produced were over 98 % pure as determined by SDS-PAGE (Sodium Dodecyl Sulfate-Poly Acrylamide Gel Electrophoresis).

9.4.2.2 Preparation of AXCP

AXCP was purified as previously described[189] by Colin Andrew (Eastern Oregon University). The stock solution of protein was concentrated to 0.47 mM in heme in MES buffer (pH 6). Aliquots were kept frozen (– 80°C), thawed immediately before the spectroscopic measurements, and diluted to the working concentration. The solution of ferric AXCP (100 μL, 75 μM) was degassed. The heme iron was reduced by the addition of 10 μL of degassed sodium ascorbate solution (5 mM final concentration). For preparing NO-liganded AXCP, gas phase 100 % or 0.1 % NO diluted in N_2 was directly introduced into the spectroscopic cell (2 mM and 2 μM NO in the aqueous phase respectively). To obtain the 100 % CO-bound form, it was equilibrated with 1 atm of CO gas. Equilibrium spectra were recorded at each step for monitoring the evolution of the Soret band. The absorbance of the sample was in the range $0.7 \sim 1$ at the Soret maximum for 1-mm path length.

9.4.2.3 Preparation of H93C

The original horse heart myoglobin mutant H93C was a gift from Stefen Franzen and Michael Davis in North Carolina University. The construction and expression of a synthetic gene coding for wild-type and mutant horse heart myoglobin in *Escherichia coli* has been described previously[190]. The H93C from horse heart was overexpressed and purified as described[143]. Preparation of H93C Mb mutant was performed exactly as the wild type protein.

9.4.2.4 Preparation of eNOS

Endothelial NO-synthase was prepared by Dr Ah-Lim Tsai (Houston Medical School). Preparation of samples for spectroscopy is well described in a previous paper[121]. After thawing, 100 μL of eNOS (75 μM) were put in a 1-mm cell and degassed. 8 μL of 60 mM L-Arg were added using a gas-tight syringe (Hamilton) previously rinsed with argon (final concentration, 5 mM; K_D of L-Arg for eNOS is 2 μM). For preparing NO-liganded ferric eNOS, we used a pure NO (99.99 %) was directly introduced in the cell. For reduction of L-Arg bound eNOS, 5 μL of a 20 mM β-NADPH solution, degassed under vacuum and argon,

were added to the sample (final concentration, 1 mM; [NADPH]/[heme] = $\sim$ 17). Calmodulin (10 μL) and $CaCl_2$ (1 mM) were added to activate the reduction. To get NO-liganded ferrous eNOS, 1 or 10 % NO (diluted in nitrogen; total pressure, 1.3 bar) was introduced in the cell yielding a NO concentration of 10 μM in the aqueous phase. For substrates bound eNOS, we chose the concentrations: SEITU (2 mM), NHA (2mM), and NMA (2 mM).

9.4.2.5 Preparation of Mb and Hb for band III measurements

Horse heart myoglobin and human hemoglobin type A (Sigma) were dissolved in phosphate buffer (pH 7.4). The solution of ferric proteins (100 μL, 5 mM) was put in a 1-mm quartz cell and degassed. Two ferric proteins were reduced by the addition of 10 μL degassed sodium dithionite to obtain 2 mM final concentration. The ferrous samples yield absorbance of 2.9 (Mb) and 2.1 (Hb) at 564 nm, the wavelength used to photoexcite the sample. Equilibrium spectra were recorded at each step to verify the stability of the sample. For preparing NO-liganded proteins, gas phase 10 % NO diluted in N_2 was directly introduced into the spectroscopic cell (0.2 mM NO in the aqueous phase). Because the concentration of Mb and Hb was 5 mM and 10 % NO in gas phase equilibrates with 0.2 mM NO in aqueous phase, it was necessary to incubate ($\sim$ 15 min) the solution in the cell still connected to the gas train to ensure an "infinite" reservoir of NO during binding equilibration and avoid depletion of NO, so that yield is $\sim$ 100 % of nitrosylated proteins.

9.5 SVD analysis

In most systems designed for picosecond and nanosecond timescales, the transient absorption is monitored as entire spectra as a function of time and results of TA setup consist of a two-dimensional array of induced absorbances, A(λ, t). λ is wavelength of probe pulse and t is the time after excitation. These raw transient spectra can be treated with Singular Value Decomposition (SVD) approach of this time-wavelength matrix which is a sophisticated mathematical method[191]. SVD is a well-known technique for the analysis of data having two or more variables. This method is very useful for the initial characterization of the data. For our case of TA setup, ΔA(λ, t) the matrix obtained can be decomposed into:

$$\Delta A(\lambda, t) = \Delta A^{SVD}(\lambda) S K^{SVD}(t)$$

where $\Delta A^{SVD}(\lambda)$ contains the spectral component matrix, S is the diagonal singular value, and $K^{SVD}(t)$ is the matrix containing the associated kinetic matrix. This procedure allows to separate the spectral components and their kinetic evolution within the data matrix together

with the reduction of the time-correlated noise components induced by baseline fluctuations. The kinetic components $K^{SVD}(t)$ were fitted with a multi-exponential function, where the minimal number of exponents was determined iteratively. The decay associated spectra for each individual exponential component can be calculated. This is important in order to separate populations of proteins species which behave differently and to separate the elementary structural steps of relaxation after photodissociation of the ligand.

SVD analysis has many advantages compared to the spectral (or kinetic) information at fixed time (or wavelength). SVD allows to identify spectral species (usually associated with one process) and their evolution. Transient species and processes can thus be identified. Moreover, SVD can be used to discover an extremely low signal, which is difficult to detect. If a small but significant signal does not show up well in the first SVD1 component, it can be found in another SVD components. Indistinguishable TA spectra from our experimental setup were disentangled by the SVD method. We could successfully apply this powerful methodology to identify the minor contribution of histidine rebinding of sGC and AXCP, which convey key information of the mechanism and we also could identify by SVD analysis the existence of 5c-CO hemes.

Appendix A

Summary of Soret absorption maxima of proteins discussed

Ferrous protein	**Coordination state**	**Soret position**	**Reference**
b-type hemes			
sGC	5c-His	431.5	Chapter 2
β (1-190) sGC	5c-His	423.5	Chapter 3
Mb	5c-His	435	[192]
Mb (H93G)	5c-Imidazole	434	[151]
Mb (H93C)	5c-Cys	397.5	Chapter 5
DHP	5c-His	430.5	
Cb-SONO (a)	5c-His	433.5	
Np-SONO (b)	5c-His	431	Chapter 3
Tt-SONO (c)	5c-His	431	
eNOS	5c-Cys	412	[121]
sGC-NO	5c-NO	399	Chapter 2
Mb-NO	6c-His-NO	420	Chapter 5
Mb (H93G)-NO	5c-NO	399	[151]
Mb (H93G)-NO	6c-Imidazole-NO	421	[151]
Mb (H93C)-NO	5c-NO	400	Chapter 5
DHP-NO	6c-His-NO	420	
β (1-190) sGC	5c-NO	400	
Cb-SONO-NO	5c-NO	400	Chapter 3
Np-SONO-NO	6c-NO/5c-NO	399/416.5	
Tt-SONO-NO	6c-His-NO	420	
eNOS	6c-Cys-NO	412	[121]
sGC-CO	6c-CO	424	Chapter 2
Hb-CO	6c-CO	424	[192]
Mb-CO	6c-CO	420	[192]
Mb (H93G)-CO	6c-imidazole-CO	418	[151]
Mb (H93C)-CO	6c-CO	418	Chapter 5
β (1-190) sGC-CO	6c-CO	419	
Cb-SONO-CO	6c-CO	424	Chapter 3
Np-SONO-CO	6c-CO	424.5	
Tt-SONO-CO	6c-CO	424	
c-type hemes			
Cyt c' (d)	5c-His	425	
Cyt c'-NO	5c-NO	396	Chapter 4
Cyt c'-CO	6c-CO	418	
Cyt c (e)	6c-His/Met	415	[193]
Cyt c-NO	6c-His-NO	411	[194]

a, from *Clostridium botullinum*. b, from *Nostoc punctiform*.

c, from *Thermoanaerobacter tencongensis*. d, from *Alcaligenes xylosoxydans*.

e, mammalian mitochondrial.

Ferric protein	**Coordination state**	**Soret position**	**Reference**
b-type hemes			
sGC	5c-His	391 nm	[195]
Mb (H64V)	5c-His	395 nm	[196]
Mb (H93Y)	5c-Tyr	403 nm	[143]
HR peroxidase	5c-His	402 nm	[197]
Dehaloperoxidase	6c-His/OH^-	406 nm	
Chloroperoxidase	6c-His/OH^-	406 nm	
Mb	6c-His/OH^-	409 nm	
eNOS	5c-Cys	398 nm	[121]
Fe-PP IX-NO	6c-His-NO	390 nm	[197]
eNOS-NO	6c-Cys-NO	441 nm	[121]
c-type hemes			
Cyt c' (a)		395 nm	[127]
Cyt c' (b)		400 nm	[198]
Cyt c' (d)		403 nm	Chapter 4
Cyt c (e)	6c-His/Met	409 nm	[193, 194]
Cyt c (e)	transient 5c-His	∼390-395 nm	
Cyt c-NO (e)	6c-His-NO	416 nm	

a, from *Rhodospirillum rubrum*.

b, from *Rhodobacter capsulatus*.

d, from *Alcaligenes xylosoxydans*.

e, mammalian mitochondrial.

Bibliography

[1] Lehninger, A. L., Nelson, D. L., and Cox, M. (2005) *Principles of Biochemistry*. Fourth edition, p. 1119.

[2] Smith, M., Drummond, G., and Khorana, H. (1961) Cyclic phosphates. IV. Ribonucleoside-3', 5' Cyclic Phosphates. a general method of synthesis and some properties. *J Am Chem Soc 83*, 698–706.

[3] Kauffman, Brock, G. B., Jensen, W. H., Jorgensen, K. A., and Klixbull, C. (1983) Ligand. *Journal of Chemical Education 60*, 509–510.

[4] Frieden, E. (1985) New perspectives on the essential trace elements. *Journal of Chemical Education 62*, 917.

[5] Eaton, W., Henry, E., Hofrichter, J., and Mozzarelli, A. (1999) Is cooperative oxygen binding by hemoglobin really understood? *Nature Structural Biology 6*, 351–358.

[6] Monod, J., Wyman, J., and Changeux, J. (1965) On the nature of allosteric transitions: A plausible model. *Journal of Molecular Biology 12*, 88–118.

[7] Perutz, M. F., Wilkinson, A. J., Paoli, M., and Dodson, G. G. (1998) The stereochemical mechanism of the cooperative effects in hemoglobin revisited. *Annu Rev Biophys Biomol Struct 27*, 1–34.

[8] Ghosh, A., ed. (2008) *The smallest biomolecules: diatomics and their interactions with heme proteins*. p. 603.

[9] Rodgers, K. R. (1999) Heme-based sensors in biological systems. *Curr Opin Chem Biol 3*, 158–67.

[10] Chan, M. K. (2001) Recent advances in heme-protein sensors. *Curr Opin Chem Biol 5*, 216–22.

[11] Uchida, T. and Kitagawa, T. (2005) Mechanism for transduction of the ligand-binding signal in heme-based gas sensory proteins revealed by resonance raman spectroscopy. *Acc. Chem. Res 38*, 662–670.

[12] Traylor, T. G. and Sharma, V. S. (1992) Why NO ? *Biochemistry 31*, 2847–9.

[13] Furchgott, R. F. and Vanhoutte, P. M. (1989) Endothelium-derived relaxing and contracting factors. *FASEB J 3*, 2007–18.

[14] Hartsfield, C. (2002) Cross talk between carbon monoxide and nitric oxide. *Antioxidants and Redox Signaling 4*, 301–7.

[15] Lancaster, J. R. (1996) *Nitric oxide: principles and actions*. p. 355.

[16] Schmidt, H. H. H. W., Hofmann, F., and Stasch, J.-P. (2008) *cGMP: Generators, Effectors and Therapeutic Implications*. p. 583.

[17] Kim, H., Ryter, S., and Choi, A. (2006) CO as a cellular signaling molecule. *Annual Review of Pharmacology and Toxicology 46*, 411–449.

[18] Ignarro, L. J., Ballot, B., and Wood, K. S. (1984) Regulation of soluble guanylate cyclase activity by porphyrins and metalloporphyrins. *Journal of Biological Chemistry 259*, 6201–7.

[19] Zhao, Y., Brandish, P. E., Ballou, D. P., and Marletta, M. A. (1999) A molecular basis for nitric oxide sensing by soluble guanylate cyclase. *Proc Natl Acad Sci USA 96*, 14753–8.

[20] Siebert, F. and Hildebrandt, P. (2008) *Vibrational spectroscopy in life science*. p. 310.

[21] Négrerie, M., Bouzhir, L., Martin, J. L., and Liebl, U. (2001) Control of nitric oxide dynamics by guanylate cyclase in its activated state. *Journal of Biological Chemistry 276*, 46815–21.

[22] Bredt, D. S. and Snyder, S. H. (1994) Nitric oxide: a physiologic messenger molecule. *Annu Rev Biochem 63*, 175–95.

[23] Schonhoff, C. M., Gaston, B., and Mannick, J. B. (2003) Nitrosylation of cytochrome c during apoptosis. *Journal of Biological Chemistry 278*, 18265–70.

[24] Fraser, M., Chan, S. L., Chan, S. S. L., Fiscus, R. R., and Tsang, B. K. (2006) Regulation of p53 and suppression of apoptosis by the soluble guanylyl cyclase/cGMP pathway in human ovarian cancer cells. *Oncogene 25*, 2203–12.

[25] Blaise, G. A., Gauvin, D., Gangal, M., and Authier, S. (2005) Nitric oxide, cell signaling and cell death. *Toxicology 208*, 177–92.

[26] Evgenov, O. V., Pacher, P., Schmidt, P. M., Haskó, G., Schmidt, H. H. H. W., and Stasch, J.-P. (2006) NO-independent stimulators and activators of soluble guanylate cyclase: discovery and therapeutic potential. *Nat Rev Drug Discov 5*, 755–68.

[27] Nioche, P., Berka, V., Vipond, J., Minton, N., Tsai, A., and Raman, C. (2004) Femtomolar sensitivity of a NO sensor from clostridium botulinum. *Science 306*, 1550–1553.

[28] Derbyshire, E. R. and Marletta, M. A. (2009) Biochemistry of soluble guanylate cyclase. *Handb Exp Pharmacol* pp. 17–31.

[29] Winger, J. A., Derbyshire, E. R., Lamers, M. H., Marletta, M. A., and Kuriyan, J. (2008) The crystal structure of the catalytic domain of a eukaryotic guanylate cyclase. *BMC Struct Biol 8*, 42.

[30] Eswar, Eramian, D., Webb, B., Shen, M., and Sali, A. (2008) Protein structure modeling with MODELLER. *Methods in Molecular Biology 426*, 145–159.

[31] Brandish, P. E., Buechler, W., and Marletta, M. (1998) Regeneration of the ferrous heme of soluble guanylate cyclase from the nitric oxide complex: Acceleration by thiols and oxyhemoglobin. *Biochemistry 37*, 16898–16907.

[32] Bellamy, T. C. and Garthwaite, J. (2001) Sub-second kinetics of the nitric oxide receptor, soluble guanylyl cyclase, in intact cerebellar cells. *Journal of Biological Chemistry 276*, 4287–92.

[33] Yoo, B., Martin, J., Andrew, C., and Negrerie, M. (2009) Rebinding of proximal histidine in the cytochrome c' from alcaligenes xylosoxidans acts as a molecular trap for nitric oxide. *Ultrafast Phenomena XVI 92*, 556–558.

[34] Makino, R., Obayashi, E., Homma, N., Shiro, Y., and Hori, H. (2003) YC-1 facilitates release of the proximal his residue in the NO and CO complexes of soluble guanylate cyclase. *Journal of Biological Chemistry 278*, 11130–7.

[35] Lamothe, M., Chang, F.-J., Balashova, N., Shirokov, R., and Beuve, A. (2004) Functional characterization of nitric oxide and YC-1 activation of soluble guanylyl cyclase: structural implication for the YC-1 binding site? *Biochemistry 43*, 3039–48.

[36] Stasch, J. P., Becker, E. M., Alonso-Alija, C., Apeler, H., Dembowsky, K., Feurer, A., Gerzer, R., Minuth, T., Perzborn, E., Pleiss, U., Schröder, H., Schroeder, W., Stahl, E., Steinke, W., Straub, A., and Schramm, M. (2001) NO-independent regulatory site on soluble guanylate cyclase. *Nature 410*, 212–5.

[37] Denninger, J. W., Schelvis, J. P., Brandish, P. E., Zhao, Y., Babcock, G. T., and Marletta, M. A. (2000) Interaction of soluble guanylate cyclase with YC-1: kinetic and resonance Raman studies. *Biochemistry 39*, 4191–8.

[38] Stone, J. R. and Marletta, M. A. (1994) Soluble guanylate cyclase from bovine lung: activation with nitric oxide and carbon monoxide and spectral characterization of the ferrous and ferric states. *Biochemistry 33*, 5636–40.

[39] Russwurm, M. and Koesling, D. (2005) Purification and characterization of NO-sensitive guanylyl cyclase. *Methods in Enzymology 396*, 492–501.

[40] Mathis, K., Emmons, T., Curran, D., Day, J., and Tomasselli, A. (2008) High yield purification of soluble guanylate cyclase from bovine lung. *Protein Expression and Purification 60*, 58–63.

[41] Koglin, M. and Behrends, S. (2004) Native human nitric oxide sensitive guanylyl cyclase: purification and characterization. *Biochem Pharmacol 67*, 1579–85.

[42] Tomita, T., Tsuyama, S., Imai, Y., and Kitagawa, T. (1997) Purification of bovine soluble guanylate cyclase and ADP-ribosylation on its small subunit by bacterial toxins. *Journal of Biochemistry 122*, 531–536.

[43] Lee, Y. C., Martin, E., and Murad, F. (2000) Human recombinant soluble guanylyl cyclase: expression, purification, and regulation. *Proc Natl Acad Sci USA 97*, 10763–8.

[44] Hoenicka, M., Becker, E. M., Apeler, H., Sirichoke, T., Schröder, H., Gerzer, R., and Stasch, J. P. (1999) Purified soluble guanylyl cyclase expressed in a baculovirus/Sf9 system: stimulation by YC-1, nitric oxide, and carbon monoxide. *J Mol Med 77*, 14–23.

[45] Martin, E., Berka, V., Tsai, A., and Murad, F. (2005) Soluble guanylyl cyclase: the nitric oxide receptor. *Methods in Enzymology 396*, 478–492.

[46] Emmons, T. L., Mathis, K. J., Shuck, M. E., Reitz, B. A., Curran, D. F., Walker, M. C., Leone, J. W., Day, J. E., Bienkowski, M. J., Fischer, H. D., and Tomasselli, A. G. (2009) Purification and characterization of recombinant human soluble guanylate cyclase produced from baculovirus-infected insect cells. *Protein Expr Purif 65*, 133–9.

[47] Zabel, U., Weeger, M., La, M., and Schmidt, H. (1998) Human soluble guanylate cyclase: functional expression and revised isoenzyme family. *Biochemical Journal 335*, 51–57.

[48] Shah, S. and Hyde, D. (1995) Two drosophila genes that encode the alpha and beta subunits of the brain soluble guanylyl cyclase. *Journal of Biological Chemistry 270*, 15368–15376.

[49] Harteneck, C., Koesling, D., Söling, A., Schultz, G., and Böhme, E. (1990) Expression of soluble guanylyl cyclase. catalytic activity requires two enzyme subunits. *FEBS Lett 272*, 221–3.

[50] Brandish, P. E., Buechler, W., and Marletta, M. A. (1998) Regeneration of the ferrous heme of soluble guanylate cyclase from the nitric oxide complex: acceleration by thiols and oxyhemoglobin. *Biochemistry 37*, 16898–907.

[51] Ko, F. N., Wu, C. C., Kuo, S. C., Lee, F. Y., and Teng, C. M. (1994) YC-1, a novel activator of platelet guanylate cyclase. *Blood 84*, 4226–33.

[52] Straub, A., Stasch, J. P., Alonso-Alija, C., Benet-Buchholz, J., Ducke, B., Feurer, A., and Fürstner, C. (2001) NO-independent stimulators of soluble guanylate cyclase. *Bioorg Med Chem Lett 11*, 781–4.

[53] Hobbs, A. J. (2002) Soluble guanylate cyclase: an old therapeutic target revisited. *Br J Pharmacol 136*, 637–40.

[54] Miller, L. N., Nakane, M., Hsieh, G. C., Chang, R., Kolasa, T., Moreland, R. B., and Brioni, J. D. (2003) A-350619: a novel activator of soluble guanylyl cyclase. *Life Sci 72*, 1015–25.

[55] Martin, E., Czarnecki, K., Jayaraman, V., Murad, F., and Kincaid, J. (2005) Resonance Raman and infrared spectroscopic studies of high-output forms of human soluble guanylyl cyclase. *J Am Chem Soc 127*, 4625–31.

[56] Schmidt, H. H. H. W., Hofmann, F., Stasch, J.-P., and Hobbs, A. J. (2009) *NO-Independent, Haem-Dependent Soluble Guanylate Cyclase Stimulators*. (Springer Berlin Heidelberg) Vol. 191, pp. 277–308.

[57] Pal, B., Tanaka, K., Takenaka, S., and Kitagawa, T. (2010) Resonance Raman spectroscopic investigation of structural changes of CO-heme in soluble guanylate cyclase generated by effectors and substrate. *Journal of Raman Spectroscopy 41*, 1178–1184.

[58] Pal, B. and Kitagawa, T. (2005) Interactions of soluble guanylate cyclase with diatomics as probed by resonance Raman spectroscopy. *J Inorg Biochem 99*, 267–79.

[59] Tomita, T., Ogura, T., Tsuyama, S., Imai, Y., and Kitagawa, T. (1997) Effects of GTP on bound nitric oxide of soluble guanylate cyclase probed by resonance Raman spectroscopy. *Biochemistry 36*, 10155–10160.

[60] Pal, B., Li, Z., Ohta, T., Takenaka, S., Tsuyama, S., and Kitagawa, T. (2004) Resonance Raman study on synergistic activation of soluble guanylate cyclase by imidazole, YC-1 and GTP. *J Inorg Biochem 98*, 824–32.

[61] Beal, D., Rappaport, F., and Joliot, P. (1999) A new high-sensitivity 10-ns time-resolution spectrophotometric technique adapted to in vivo analysis of the photosynthetic apparatus. *Rev Sci Instrum 70*, 202–207.

[62] Hu, X., Feng, C., Hazzard, J. T., Tollin, G., and Montfort, W. R. (2008) Binding of YC-1 or BAY 41-2272 to soluble guanylyl cyclase induces a geminate phase in CO photolysis. *J Am Chem Soc 130*, 15748–9.

[63] Russwurm, M., Mergia, E., Mullershausen, F., and Koesling, D. (2002) Inhibition of deactivation of NO-sensitive guanylyl cyclase accounts for the sensitizing effect of YC-1. *Journal of Biological Chemistry 277*, 24883–8.

[64] Bellamy, T. C. and Garthwaite, J. (2002) Pharmacology of the nitric oxide receptor, soluble guanylyl cyclase, in cerebellar cells. *Br J Pharmacol 136*, 95–103.

[65] Silkstone, G., Kapetanaki, S. M., Husu, I., Vos, M. H., and Wilson, M. T. (2010) Nitric oxide binds to the proximal heme coordination site of the ferrocytochrome c/cardiolipin complex: formation mechanism and dynamics. *Journal of Biological Chemistry 285*, 19785–92.

[66] Andrew, C. R., Rodgers, K. R., and Eady, R. R. (2003) A novel kinetic trap for NO release from cytochrome c': a possible mechanism for NO release from activated soluble guanylate cyclase. *J Am Chem Soc 125*, 9548–9.

[67] Kruglik, S. G., Lambry, J.-C., Cianetti, S., Martin, J.-L., Eady, R. R., Andrew, C. R., and Negrerie, M. (2007) Molecular basis for nitric oxide dynamics and affinity with alcaligenes xylosoxidans cytochrome c'. *Journal of Biological Chemistry 282*, 5053–62.

[68] Roy, B. and Garthwaite, J. (2006) Nitric oxide activation of guanylyl cyclase in cells revisited. *Proc Natl Acad Sci USA 103*, 12185–90.

[69] Lawson, D. M., Stevenson, C. E., Andrew, C. R., and Eady, R. R. (2000) Unprecedented proximal binding of nitric oxide to heme: implications for guanylate cyclase. *EMBO J 19*, 5661–71.

[70] Russwurm, M. and Koesling, D. (2004) NO activation of guanylyl cyclase. *EMBO J 23*, 4443–50.

[71] Poulos, T. L. (2006) Soluble guanylate cyclase. *Curr. Opin. Struct. Biol. 16*, 736–43.

[72] Ma, X., Sayed, N., Beuve, A., and van den Akker, F. (2007) NO and CO differentially activate soluble guanylyl cyclase via a heme pivot-bend mechanism. *EMBO J 26*, 578–88.

[73] Garthwaite, J. (2010) New insight into the functioning of nitric oxide-receptive guanylyl cyclase: physiological and pharmacological implications. *Mol Cell Biochem 334*, 221–32.

[74] Pixton, D. A., Petersen, C. A., Franke, A., van Eldik, R., Garton, E. M., and Andrew, C. R. (2009) Activation parameters for heme-NO binding in alcaligenes xylosoxidans cytochrome c': the putative dinitrosyl intermediate forms via a dissociative mechanism. *Journal of the American Chemical Society 131*, 4846–53.

[75] Wayland, B. B. and Olson, L. W. (1974) Spectroscopic studies and bonding model for nitric oxide complexes of iron porphyrins. *J Am Chem Soc 96*, 6037–41.

[76] Lorkovic, I. and Ford, P. (2000) Nitric oxide addition to the ferrous nitrosyl porphyrins Fe(P)(NO) gives trans-Fe(P)(NO)(2) in low-temperature solutions. *J Am Chem Soc 122*, 6516–6517.

[77] Lim, M. D., Lorkovic, I. M., and Ford, P. C. (2005) NO and NOx interactions with group 8 metalloporphyrins. *J Inorg Biochem 99*, 151–65.

[78] Bellamy, T. C., Wood, J., and Garthwaite, J. (2002) On the activation of soluble guanylyl cyclase by nitric oxide. *Proc Natl Acad Sci USA 99*, 507–10.

[79] Cary, S. P. L., Winger, J. A., Derbyshire, E. R., and Marletta, M. A. (2006) Nitric oxide signaling: no longer simply on or off. *Trends Biochem Sci 31*, 231–9.

[80] Halvey, E. J., Vernon, J., Roy, B., and Garthwaite, J. (2009) Mechanisms of activity-dependent plasticity in cellular nitric oxide-cGMP signaling. *Journal of Biological Chemistry 284*, 25630–41.

[81] Hofrichter, J., Sommer, J., Henry, E., and Eaton, W. (1983) Nanosecond absorption spectroscopy of hemoglobin: elementary processes in kinetic cooperativity. *Proc Natl Acad Sci USA 80*, 2235.

[82] Cammarata, M., Levantino, M., Wulff, M., and Cupane, A. (2010) Unveiling the timescale of the R-T transition in human hemoglobin. *Journal of Molecular Biology 400*, 951–962.

[83] Perutz, M. F. (1970) Stereochemistry of cooperative effects in haemoglobin. *Nature 228*, 726–39.

[84] Paoli, M., Dodson, G., Liddington, R. C., and Wilkinson, A. J. (1997) Tension in haemoglobin revealed by Fe-His(F8) bond rupture in the fully liganded t-state. *Journal of Molecular Biology 271*, 161–7.

[85] Kim, T. D. and Burstyn, J. N. (1994) Identification and partial purification of an endogenous inhibitor of soluble guanylyl cyclase from bovine lung. *Journal of Biological Chemistry 269*, 15540–5.

[86] Murthy, K. S. (2004) Modulation of soluble guanylate cyclase activity by phosphorylation. *Neurochemistry International 45*, 845–51.

[87] Louis, J. C., Revel, M. O., and Zwiller, J. (1993) Activation of soluble guanylate cyclase through phosphorylation by protein kinase c in intact pc12 cells. *Biochim Biophys Acta 1177*, 299–306.

[88] Sayed, N., Baskaran, P., Ma, X., van den Akker, F., and Beuve, A. (2007) Desensitization of soluble guanylyl cyclase, the NO receptor, by S-nitrosylation. *Proc Natl Acad Sci USA 104*, 12312–7.

[89] Mayer, B., Kleschyov, A. L., Stessel, H., Russwurm, M., Münzel, T., Koesling, D., and Schmidt, K. (2009) Inactivation of soluble guanylate cyclase by stoichiometric S-nitrosation. *Mol Pharmacol 75*, 886–91.

[90] Flamigni, F., Facchini, A., Stanic, I., Tantini, B., Bonavita, F., and Stefanelli, C. (2001) Control of survival of proliferating L1210 cells by soluble guanylate cyclase and p44/42 mitogen-activated protein kinase modulators. *Biochem Pharmacol 62*, 319–28.

[91] Chan, S. L. and Fiscus, R. R. (2003) Guanylyl cyclase inhibitors NS2028 and ODQ and protein kinase G (PKG) inhibitor KT5823 trigger apoptotic DNA fragmentation in

immortalized uterine epithelial cells: anti-apoptotic effects of basal cGMP/PKG. *Mol Hum Reprod 9*, 775–83.

[92] Haramis, G., Zhou, Z., Pyriochou, A., Koutsilieris, M., Roussos, C., and Papapetropoulos, A. (2008) cGMP-independent anti-tumour actions of the inhibitor of soluble guanylyl cyclase, ODQ, in prostate cancer cell lines. *Br J Pharmacol 155*, 804–13.

[93] Mujoo, K., Sharin, V. G., Martin, E., Choi, B.-K., Sloan, C., Nikonoff, L. E., Kots, A. Y., and Murad, F. (2010) Role of soluble guanylyl cyclase-cyclic GMP signaling in tumor cell proliferation. *Nitric Oxide 22*, 43–50.

[94] Punathil, T., Tollefsbol, T., and Katiyar, S. (2008) EGCG inhibits mammary cancer cell migration through inhibition of nitric oxide synthase and guanylate cyclase. *Biochemical and Biophysical Research Communications 375*, 162–167.

[95] Sauviat, M.-P., Colas, A., Chauveau, M.-J., Drapier, J.-C., and Négrerie, M. (2007) Hypericin activates L-type Ca^{2+} channels in cardiac myocytes. *J Nat Prod 70*, 510–4.

[96] Hölzl, J. and Ostrowski, E. (1986) Analysis of the essential compounds of hypericum perforatum. *Planta Med 52*, 531.

[97] Miskovsky, P. (2002) Hypericin–a new antiviral and antitumor photosensitizer: mechanism of action and interaction with biological macromolecules. *Curr Drug Targets 3*, 55–84.

[98] Galeotti, N., Vivoli, E., Bilia, A. R., Vincieri, F. F., and Ghelardini, C. (2010) St. John's Wort reduces neuropathic pain through a hypericin-mediated inhibition of the protein kinase Cγ and ϵ activity. *Biochemical Pharmacology 79*, 1327–36.

[99] Foster, B., Sockovie, E., Vandenhoek, S., Bellefeuille, N., Drouin, C., Krantis, A., Budzinski, J., Livesey, J., and Arnason, J. (2004) In vitro activity of St. John's wort against cytochrome P450 isozymes and P-glycoprotein. *Pharmaceutical Biology 42*, 159–169.

[100] Pajonk, F., Scholber, J., and Fiebich, B. (2005) Hypericin - an inhibitor of proteasome function. *Cancer Chemother Pharmacol 55*, 439–46.

[101] Karow, D. S., Pan, D., Davis, J. H., Behrends, S., Mathies, R. A., and Marletta, M. A. (2005) Characterization of functional heme domains from soluble guanylate cyclase. *Biochemistry 44*, 16266–74.

[102] Andrew, C. R., Green, E. L., Lawson, D. M., and Eady, R. R. (2001) Resonance Raman studies of cytochrome c' support the binding of NO and CO to opposite sides of the heme: implications for ligand discrimination in heme-based sensors. *Biochemistry 40*, 4115–22.

[103] Pellicena, P., Karow, D., Boon, E., Marletta, M., and Kuriyan, J. (2004) Crystal structure of an oxygen-binding heme domain related to soluble guanylate cyclases. *Proc Natl Acad Sci USA 101*, 12854–12859.

[104] Boon, E. M., Davis, J. H., Tran, R., Karow, D. S., Huang, S. H., Pan, D., Miazgowicz, M. M., Mathies, R. A., and Marletta, M. A. (2006) Nitric oxide binding to prokaryotic homologs of the soluble guanylate cyclase beta1 H-NOX domain. *Journal of Biological Chemistry 281*, 21892–902.

[105] Boon, E. M., Huang, S. H., and Marletta, M. A. (2005) A molecular basis for NO selectivity in soluble guanylate cyclase. *Nat Chem Biol 1*, 53–9.

[106] Tsai, A.-L., Berka, V., Martin, F., Ma, X., van den Akker, F., Fabian, M., and Olson, J. S. (2010) Is Nostoc H-NOX a NO sensor or redox switch ? *Biochemistry 49*, 6587–99.

[107] Liebl, U., Bouzhir-Sima, L., Negrerie, M., Martin, J.-L., and Vos, M. H. (2002) Ultrafast ligand rebinding in the heme domain of the oxygen sensors FixL and Dos: general regulatory implications for heme-based sensors. *Proc Natl Acad Sci USA 99*, 12771–6.

[108] Bao, Q., Tian, Y., Li, W., Xu, Z., Xuan, Z., Hu, S., Dong, W., Yang, J., Chen, Y., Xue, Y., Xu, Y., Lai, X., Huang, L., Dong, X., Ma, Y., Ling, L., Tan, H., Chen, R., Wang, J., Yu, J., and Yang, H. (2002) A complete sequence of the T. tengcongensis genome. *Genome Research 12*, 689–700.

[109] Donald, C., Hughes, M., Thompson, J., and Bonner, F. (1986) Photolysis of the nitrogen-nitrogen double bond in trioxodinitrate: reaction between triplet oxonitrate (1-) and molecular oxygen to form peroxonitrite. *Inorganic Chemistry 25*, 2676–2677.

[110] Gow, A. J. and Stamler, J. S. (1998) Reactions between nitric oxide and haemoglobin under physiological conditions. *Nature 391*, 169–73.

[111] Fago, A., Crumbliss, A. L., Peterson, J., Pearce, L. L., and Bonaventura, C. (2003) The case of the missing NO-hemoglobin: spectral changes suggestive of heme redox reactions reflect changes in NO-heme geometry. *Proc Natl Acad Sci USA 100*, 12087–92.

[112] Kumazaki, S., Nakajima, H., Sakaguchi, T., Nakagawa, E., Shinohara, H., Yoshihara, K., and Aono, S. (2000) Dissociation and recombination between ligands and heme in a CO-sensing transcriptional activator CooA. *Journal of Biological Chemistry 275*, 38378–83.

[113] Castenholz, R. W. and Waterbury, J. B. (1989) Group I. cyanobacteria. *Bergey's manual of systematic bacteriology 3*, 1710–1728.

[114] Clark, R., Lanz, N., Lee, A., Kerby, R., Roberts, G., and Burstyn, J. (2006) Unexpected NO-dependent DNA binding by the CooA homolog from carboxydothermus hydrogenoformans. *Proc Natl Acad Sci USA 103*, 891–896.

[115] Huston, W. M., Andrew, C. R., Servid, A. E., McKay, A. L., Leech, A. P., Butler, C. S., and Moir, J. W. B. (2006) Heterologous overexpression and purification of cytochrome c' from rhodobacter capsulatus and a mutant (K42E) in the dimerization region. mutation does not alter oligomerization but impacts the heme iron spin state and nitric oxide binding properties. *Biochemistry 45*, 4388–95.

[116] Cao, W., Christian, J. F., Champion, P. M., Rosca, F., and Sage, J. T. (2001) Water penetration and binding to ferric myoglobin. *Biochemistry 40*, 5728–37.

[117] Benabbas, A., Ye, X., Kubo, M., Zhang, Z., Maes, E. M., Montfort, W. R., and Champion, P. M. (2010) Ultrafast dynamics of diatomic ligand binding to nitrophorin 4. *J Am Chem Soc 132*, 2811–20.

[118] Ma, X., Sayed, N., Baskaran, P., Beuve, A., and van den Akker, F. (2008) PAS-mediated dimerization of soluble guanylyl cyclase revealed by signal transduction histidine kinase domain crystal structure. *J Biol Chem 283*, 1167–78.

[119] Li, Z., Pal, B., Takenaka, S., Tsuyama, S., and Kitagawa, T. (2005) Resonance Raman evidence for the presence of two heme pocket conformations with varied activities in CO-bound bovine soluble guanylate cyclase and their conversion. *Biochemistry 44*, 939–46.

[120] Derbyshire, E. R., Gunn, A., Ibrahim, M., Spiro, T. G., Britt, R. D., and Marletta, M. A. (2008) Characterization of two different five-coordinate soluble guanylate cyclase ferrous-nitrosyl complexes. *Biochemistry 47*, 3892–9.

[121] Negrerie, M., Berka, V., Vos, M., Liebl, U., Lambry, J., Tsai, A., and Martin, J. (1999) Geminate recombination of nitric oxide to endothelial nitric-oxide synthase and mechanistic implications. *Journal of Biological Chemistry 274*, 24694–24702.

[122] Kruglik, S. G., Yoo, B.-K., Franzen, S., Vos, M. H., Martin, J.-L., and Negrerie, M. (2010) Picosecond primary structural transition of the heme is retarded after nitric oxide binding to heme proteins. *Proc Natl Acad Sci USA 107*, 13678–13683.

[123] Sugimoto, T., Unno, M., Shiro, Y., Dou, Y., and Ikeda-Saito, M. (1998) Myoglobin mutants giving the largest geminate yield in CO rebinding in the nanosecond time domain. *Biophysical Journal 75*, 2188–2194.

[124] Friebe, A., Russwurm, M., Mergia, E., and Koesling, D. (1999) A point-mutated guanylyl cyclase with features of the YC-1-stimulated enzyme: implications for the YC-1 binding site? *Biochemistry 38*, 15253–7.

[125] Rothkegel, C., Schmidt, P. M., Stoll, F., Schröder, H., Schmidt, H. H. H. W., and Stasch, J.-P. (2006) Identification of residues crucially involved in soluble guanylate cyclase activation. *FEBS Lett 580*, 4205–13.

[126] Messerschmidt, A., Huber, R., Wieghardt, K., Cygler, M., Poulos, T., and Bode, W. (2001) *Handbook of Metalloproteins*. Vol. 1-2, p. 1472.

[127] Yoshimura, T., Fujii, S., Kamada, H., Yamaguchi, K., Suzuki, S., Shidara, S., and Takakuwa, S. (1996) Spectroscopic characterization of nitrosylheme in nitric oxide complexes of ferric and ferrous cytochrome c' from photosynthetic bacteria. *Biochim Biophys Acta 1292*, 39–46.

[128] Cross, R., Aish, J., Paston, S. J., Poole, R. K., and Moir, J. W. (2000) Cytochrome c' from rhodobacter capsulatus confers increased resistance to nitric oxide. *Journal of Bacteriology 182*, 1442–7.

[129] Cross, R., Lloyd, D., Poole, R. K., and Moir, J. W. (2001) Enzymatic removal of nitric oxide catalyzed by cytochrome c' in rhodobacter capsulatus. *Journal of Bacteriology 183*, 3050–4.

[130] Anjum, M. F., Stevanin, T. M., Read, R. C., and Moir, J. W. B. (2002) Nitric oxide metabolism in neisseria meningitidis. *Journal of Bacteriology 184*, 2987–93.

[131] Meyer, T. E., Cheddar, G., Bartsch, R. G., Getzoff, E. D., Cusanovich, M. A., and Tollin, G. (1986) Kinetics of electron transfer between cytochromes c' and the semiquinones of free flavin and clostridial flavodoxin. *Biochemistry 25*, 1383–90.

[132] Tahirov, T. H., Misaki, S., Meyer, T. E., Cusanovich, M. A., Higuchi, Y., and Yasuoka, N. (1996) High-resolution crystal structures of two polymorphs of cytochrome c'

from the purple phototrophic bacterium rhodobacter capsulatus. *Journal of Molecular Biology 259*, 467–79.

[133] George, S., Andrew, C., Lawson, D., Thorneley, R., and Eady, R. (2001) Stopped-flow infrared spectroscopy reveals a six-coordinate intermediate in the formation of the proximally bound five-coordinate NO adduct of cytochrome c'. *J Am Chem Soc 123*, 9683–9684.

[134] Andrew, C., George, S., Lawson, D., and Eady, R. R. (2002) Six- to five-coordinate heme-nitrosyl conversion in cytochrome c and its relevance to guanylate cyclase. *Biochemistry 41*, 2353–2360.

[135] Martí, M. A., Capece, L., Crespo, A., Doctorovich, F., and Estrin, D. A. (2005) Nitric oxide interaction with cytochrome c' and its relevance to guanylate cyclase. why does the iron histidine bond break? *J Am Chem Soc 127*, 7721–8.

[136] Andrew, C. R., Kemper, L. J., Busche, T. L., Tiwari, A. M., Kecskes, M. C., Stafford, J. M., Croft, L. C., Lu, S., Moënne-Loccoz, P., Huston, W., Moir, J. W. B., and Eady, R. R. (2005) Accessibility of the distal heme face, rather than Fe-His bond strength, determines the heme-nitrosyl coordination number of cytochromes c': evidence from spectroscopic studies. *Biochemistry 44*, 8664–72.

[137] Fang, M., Wilson, S. R., and Suslick, K. S. (2008) A four-coordinate Fe(III) porphyrin cation. *J Am Chem Soc 130*, 1134–5.

[138] Ballou, D. P., Zhao, Y., Brandish, P. E., and Marletta, M. A. (2002) Revisiting the kinetics of nitric oxide (NO) binding to soluble guanylate cyclase: the simple NO-binding model is incorrect. *Proc Natl Acad Sci USA 99*, 12097–101.

[139] Pettersen, E. F., Goddard, T. D., Huang, C. C., Couch, G. S., Greenblatt, D. M., Meng, E. C., and Ferrin, T. E. (2004) UCSF chimera-a visualization system for exploratory research and analysis. *Journal of Computational Chemistry 25*, 1605–12.

[140] Mayburd, A. L. and Kassner, R. J. (2002) Mechanism and biological role of nitric oxide binding to cytochrome c'. *Biochemistry 41*, 11582–91.

[141] Choi, P., Grigoryants, V., and Abruna, H. (2005) Regulation and function of cytochrome c' in Rhodobacter sphaeroides 2.4.3. *Journal of Bacteriology 187*, 4077–4085.

[142] Yu, A. E., Hu, S., Spiro, T. G., and Burstyn, J. N. (1994) Resonance raman-spectroscopy of soluble guanylate cyclase reveals displacement of distal and proximal heme ligands by NO. *J Am Chem Soc 116*, 4117–4118.

[143] Hildebrand, D., Ferrer, J., Tang, H., Smith, M., and Mauk, A. (1995) Trans effects on cysteine ligation in the proximal His93Cys variant of horse heart myoglobin. *Biochemistry 34*, 11598–11605.

[144] Raman, C. S., Li, H., Martásek, P., Král, V., Masters, B. S., and Poulos, T. L. (1998) Crystal structure of constitutive endothelial nitric oxide synthase: a paradigm for pterin function involving a novel metal center. *Cell 95*, 939–50.

[145] Sundaramoorthy, M., Terner, J., and Poulos, T. L. (1998) Stereochemistry of the chloroperoxidase active site: crystallographic and molecular-modeling studies. *Chem Biol 5*, 461–73.

[146] Adachi, S., Nagano, S., Ishimori, K., Watanabe, Y., Morishima, I., Egawa, T., Kitagawa, T., and Makino, R. (1993) Roles of proximal ligand in heme proteins: replacement of proximal histidine of human myoglobin with cysteine and tyrosine by site-directed mutagenesis as models for P-450, chloroperoxidase, and catalase. *Biochemistry 32*, 241–52.

[147] Cooper, C. E. (1999) Nitric oxide and iron proteins. *Biochim Biophys Acta 1411*, 290–309.

[148] Hoshino, M., Maeda, M., Konishi, R., Seki, H., and Ford, P. (1996) Studies on the reaction mechanism for reductive nitrosylation of ferrihemoproteins in buffer solutions. *J Am Chem Soc 118*, 5702–5707.

[149] Hoshino, M., Ozawa, K., Seki, H., and Ford, P. C. (1993) Photochemistry of nitric oxide adducts of water-soluble iron (III) porphyrin and ferrihemoproteins studied by nanosecond laser photolysis. *J Am Chem Soc 115*, 9568.

[150] Denninger, J. W. and Marletta, M. A. (1999) Guanylate cyclase and the NO/cGMP signaling pathway. *Biochim Biophys Acta 1411*, 334–50.

[151] Negrerie, M., Kruglik, S. G., Lambry, J.-C., Vos, M. H., Martin, J.-L., and Franzen, S. (2006) Role of heme iron coordination and protein structure in the dynamics and geminate rebinding of nitric oxide to the H93G myoglobin mutant. *Journal of Biological Chemistry 281*, 10389–10398.

[152] Franzen, S. (2002) Spin-dependent mechanism for diatomic ligand binding to heme. *Proc Natl Acad Sci USA 99*, 16754–9.

[153] Schotte, F., Lim, M., Jackson, T. A., Smirnov, A. V., Soman, J., Olson, J. S., Phillips, G. N., Wulff, M., and Anfinrud, P. A. (2003) Watching a protein as it functions with 150-ps time-resolved X-ray crystallography. *Science 300*, 1944–7.

[154] Liebl, U., Bouzhir-Sima, L., Kiger, L., Marden, M., Lambry, J., Negrerie, M., and Vos, M. (2003) Ligand binding dynamics to the heme domain of the oxygen sensor DOS from Escherichia coli. *Biochemistry 42*, 6527–6535.

[155] Ionascu, D., Gruia, F., Ye, X., Yu, A., Rosca, F., Beck, C., Demidov, A., Olson, J. S., and Champion, P. M. (2005) Temperature-dependent studies of NO recombination to heme and heme proteins. *J Am Chem Soc 127*, 16921–34.

[156] Silkstone, G., Jasaitis, A., Wilson, M. T., and Vos, M. H. (2007) Ligand dynamics in an electron transfer protein: Picosecond geminate recombination of carbon monoxide to heme in mutant forms of cytochrome c. *Journal of Biological Chemistry 282*, 1638–49.

[157] Kim, S. and Lim, M. (2005) Picosecond dynamics of ligand interconversion in the primary docking site of heme proteins. *J Am Chem Soc 127*, 5786–7.

[158] Petrich, J., Lambry, J., Balasubramanian, C., Lambright, D., Boxer, S., and Martin, J. (1994) Ultrafast measurements of geminate recombination of NO with site-specific mutants of human myoglobin. *Journal of Molecular Biology 238*, 437–444.

[159] Kholodenko, Y., Gooding, E., Dou, Y., Ikeda-Saito, M., and Hochstrasser, R. (1999) Heme protein dynamics revealed by geminate nitric oxide recombination in mutants of iron and cobalt myoglobin. *Biochemistry 38*, 5918–5924.

[160] Brunori, M., Cutruzzola, F., Savino, C., Travaglini-Allocatelli, C., Vallone, B., and Gibson, Q. (1999) Structural dynamics of ligand diffusion in the protein matrix: A study on a new myoglobin mutant Y(B10) Q(E7) R(E10). *Biophysical Journal 76*, 1259–1269.

[161] Li, H., Shimizu, H., Flinspach, M., Jamal, J., Yang, W., Xian, M., Cai, T., Wen, E. Z., Jia, Q., Wang, P. G., and Poulos, T. L. (2002) The novel binding mode of N-alkyl-N'-hydroxyguanidine to neuronal nitric oxide synthase provides mechanistic insights into NO biosynthesis. *Biochemistry 41*, 13868–75.

[162] Fischmann, T. O., Hruza, A., Niu, X. D., Fossetta, J. D., Lunn, C. A., Dolphin, E., Prongay, A. J., Reichert, P., Lundell, D. J., Narula, S. K., and Weber, P. C. (1999) Structural characterization of nitric oxide synthase isoforms reveals striking active-site conservation. *Nat Struct Biol 6*, 233–42.

[163] Santolini, J. (2011) The molecular mechanism of mammalian no-synthases: A story of electrons and protons. *Journal of Inorganic Biochemistry 105*, 127–141.

[164] Olken, N. M. and Marletta, M. A. (1993) Nγ-methyl-L-arginine functions as an alternate substrate and mechanism-based inhibitor of nitric oxide synthase. *Biochemistry 32*, 9677–85.

[165] Olken, N. M., Osawa, Y., and Marletta, M. A. (1994) Characterization of the inactivation of nitric oxide synthase by Nγ-methyl-L-arginine: evidence for heme loss. *Biochemistry 33*, 14784–91.

[166] Crane, B. R., Arvai, A. S., Ghosh, D. K., Wu, C., Getzoff, E. D., Stuehr, D. J., and Tainer, J. A. (1998) Structure of nitric oxide synthase oxygenase dimer with pterin and substrate. *Science 279*, 2121–6.

[167] Petrich, J. W., Lambry, J. C., Kuczera, K., Karplus, M., Poyart, C., and Martin, J. L. (1991) Ligand binding and protein relaxation in heme proteins: a room temperature analysis of NO geminate recombination. *Biochemistry 30*, 3975–87.

[168] Franzen, S., Lambry, J. C., Bohn, B., Poyart, C., and Martin, J. L. (1994) Direct evidence for the role of haem doming as the primary event in the cooperative transition of haemoglobin. *Nat Struct Biol 1*, 230–3.

[169] Lim, M., Jackson, T. A., and Anfinrud, P. A. (1993) Nonexponential protein relaxation: dynamics of conformational change in myoglobin. *Proc Natl Acad Sci USA 90*, 5801–4.

[170] Stavrov, S. S. (1993) The effect of iron displacement out of the porphyrin plane on the resonance raman spectra of heme proteins and iron porphyrins. *Biophys J 65*, 1942–50.

[171] Stavrov, S. S. (2001) Optical absorption band III of deoxyheme proteins as a probe of their structure and dynamics. *Chemical Physics 271*, 145–154.

[172] Petrich, J., Poyart, C., and MARTIN, J. (1988) Photophysics and reactivity of heme proteins: A femtosecond absorption study of hemoglobin, myoglobin, and protoheme. *Biochemistry 27*, 4049–4060.

[173] Li, P., Sage, J., and Champion, P. (1992) Probing picosecond processes with nanosecond lasers: Electronic and vibrational relaxation dynamics of heme proteins. *The Journal of Chemical Physics 97*, 3214.

[174] Eaton, W., Hanson, L., Stephens, P., Sutherland, J., and Dunn, J. (2001) Optical spectra of oxy- and deoxyhemoglobin. *J. Am. Chem. Soc 100*, 4991–5003.

[175] Stavrov, S. (2004) Correct interpretation of heme protein spectra allows distinguishing between the heme and the protein dynamics. *Biopolymers 74*, 37–40.

[176] Sage, J. T., Morikis, D., and Champion, P. M. (1991) Spectroscopic studies of myoglobin at low ph: heme structure and ligation. *Biochemistry 30*, 1227–1237.

[177] Dartigalongue, T. and Hache, F. (2005) Observation of sub-100 ps conformational changes in photolyzed carbonmonoxy-myoglobin probed by time-resolved circular dichroism. *Chemical Physics Letters 415*, 313–316.

[178] Sato, A., Gao, Y., Kitagawa, T., and Mizutani, Y. (2007) Primary protein response after ligand photodissociation in carbonmonoxy myoglobin. *Proc Natl Acad Sci USA 104*, 9627–32.

[179] Kukura, P., McCamant, D. W., Yoon, S., Wandschneider, D. B., and Mathies, R. A. (2005) Structural observation of the primary isomerization in vision with femtosecond-stimulated Raman. *Science 310*, 1006–9.

[180] Aubert, C., Vos, M. H., Mathis, P., Eker, A. P., and Brettel, K. (2000) Intraprotein radical transfer during photoactivation of DNA photolyase. *Nature 405*, 586–90.

[181] Martin, J. and Vos, M. (1994) Femtosecond measurements of geminate recombination in heme-proteins. *Methods in Enzymology 232*, 416–430.

[182] Martin, J. and Vos, M. (1992) Femtosecond biology. *Annual Review of Biophysics and Biomolecular Structure 21*, 199–222.

[183] McCammon, J. A., Gelin, B. R., and Karplus, M. (1977) Dynamics of folded proteins. *Nature 267*, 585–90.

[184] Brooks, B., Bruccoleri, R., Olafson, B., States, D., Swaminathan, S., and Karplus, M. (1983) Charmm: A program for macromolecular energy, minimization, and dynamics calculations. *J. Comput. Chem. 4*, 187–217.

[185] Brooks, B. R., Brooks, C. L., Mackerell, A. D., Nilsson, L., Petrella, R. J., Roux, B., Won, Y., Archontis, G., Bartels, C., Boresch, S., Caflisch, A., Caves, L., Cui, Q., Dinner, A. R., Feig, M., Fischer, S., Gao, J., Hodoscek, M., Im, W., Kuczera, K., Lazaridis, T., Ma, J., Ovchinnikov, V., Paci, E., Pastor, R. W., Post, C. B., Pu, J. Z., Schaefer, M., Tidor, B., Venable, R. M., Woodcock, H. L., Wu, X., Yang, W., York, D. M., and Karplus, M. (2009) Charmm: the biomolecular simulation program. *J. Comput. Chem. 30*, 1545–614.

[186] Fiser, A. and Sali, A. (2003) Modeller: generation and refinement of homology-based protein structure models. *Meth Enzymol 374*, 461–91.

[187] Mülsch, A. and Gerzer, R. (1991) Purification of heme-containing soluble guanylyl cyclase. *Meth Enzymol 195*, 377–83.

[188] Mayer, B. and Koesling, D. (2001) cGMP signalling beyond nitric oxide. *Trends in Pharmacological Sciences 22*, 546–548.

[189] Norris, G. E., Anderson, B. F., Baker, E. N., and Rumball, S. V. (1979) Purification and preliminary crystallographic studies on azurin and cytochrome c' from alcaligenes denitrificans and alcaligenes sp. NCIB 11015. *J Mol Biol 135*, 309–12.

[190] Guillemette, J., Matsushimahibiya, Y., Atkinson, T., and Smith, M. (1991) Expression in Escherichia-Coli of a synthetic gene coding for horse heart myoglobin. *Protein Engineering 4*, 585–592.

[191] Vandegriff, K. D. and Shrager, R. I. (1994) Hemoglobin–oxygen equilibrium binding: rapid-scanning spectrophotometry and singular value decomposition. *Meth Enzymol 232*, 460–85.

[192] Antonini, E. and Brunori, M. (1970) Hemoglobin. *Annu Rev Biochem 39*, 977–1042.

[193] Cianetti, S., Kruglik, S., Vos, M., Turpin, P., Martin, J., and Negrerie, M. (2004) Interaction of cytochrome c with NO studied by time-resolved Raman and absorption spectroscopy. *Biochimica et Biophysica Acta-Bioenergetics 1658*, 219–219.

[194] Negrerie, M., Cianetti, S., Vos, M. H., Martin, J.-L., and Kruglik, S. G. (2006) Ultrafast heme dynamics in ferrous versus ferric cytochrome c studied by time-resolved resonance Raman and transient absorption spectroscopy. *Journal of Physical Chemistry B 110*, 12766–81.

[195] Stone, J. R., Sands, R. H., Dunham, W. R., and Marletta, M. A. (1996) Spectral and ligand-binding properties of an unusual hemoprotein, the ferric form of soluble guanylate cyclase. *Biochemistry 35*, 3258–62.

[196] Ikeda-Saito, M., Hori, H., Andersson, L. A., Prince, R. C., Pickering, I. J., George, G. N., Sanders, C. R., Lutz, R. S., McKelvey, E. J., and Mattera, R. (1992) Coordination structure of the ferric heme iron in engineered distal histidine myoglobin mutants. *Journal of Biological Chemistry 267*, 22843–52.

[197] Ye, X., Yu, A., and Champion, P. M. (2006) Dynamics of nitric oxide rebinding and escape in horseradish peroxidase. *J Am Chem Soc 128*, 1444–5.

[198] Yoshimura, T., Suzuki, S., Iwasaki, H., and Takakuwa, S. (1987) Spectral properties of cytochrome c' from rhodopseudomonas capsulata B100 and its CO complex. *Biochem Biophys Res Commun 144*, 224–31.

Résumé

Le récepteur endogène du NO, la guanylate cyclase (sGC) est l'objet de thèse. Cette enzyme synthétise le GMPc après fixation du NO. L'outil principal utilisé est la spectroscopie d'absorption résolue en temps picoseconde-nanoseconde. Nous avons montré que la fixation simultanée du CO et d'activateurs (YC-1, Bay 41-2272) induisent un hème 5c-CO, à l'instar du NO seul, expliquant l'activation synergique. Nous avons identifié toutes les étapes de l'interaction sGC-NO en mesurant la dynamique du NO de la picoseconde à la seconde. Cette dynamique dans la protéine entière est comparée à celle de la sous-unité beta (1-190) isolée et celle de senseurs de NO bactériens. Un mutant de la myoglobine (H93C) à été utilisé comme modèle pour l'étude de l'hème dans les états 4- et 5-coordonnés. Enfin, nous avons mesuré la variation d'absorption dans la bande III de la Mb et Hb pour mesurer le mouvement du Fer de l'hème aprés fixation du NO. Nous avons cherché un inhibiteur potentiel et un ligand endogène de la sGC.

Mots-clés: transduction d'un signal, guanylate cyclase soluble, monoxyde d'azote, spectroscopie d'absorption résolue en temps, allostérie, hémoprotéines

Abstract

The endogenous NO receptor, soluble guanylate cyclase (sGC) is the subject of this thesis. This enzyme synthesizes cGMP after NO binding. The main tool used is time-resolved picosecond-nanosecond absorption spectroscopy. We have shown that the simultaneous binding of CO and activators (YC-1, Bay 41-2272) induce a 5c heme-CO, like NO, explaining the synergistic activation. We identified all steps of the sGC-NO interaction by measuring the dynamics from picosecond to second. This dynamics of the entire protein is compared with that of the isolated beta subunit (1-190) and bacterial NO sensors. A myoglobin mutant (H93C) was used as a model for the study of heme in the 4- and 5-coordinated states. Finally, we measured the band III absorption of Mb and Hb to measure the movement of the heme iron after NO binding. We also investigated a potential inhibitor and an endogenous ligand of sGC.

Key words: signal transduction, soluble guanylate cyclase, nitric oxide, transient absorption spectroscopy, allostery, heme proteins

초록

본 박사학위 논문의 주제는 내피세포의 일산화질소 수용체인 수용성 구아닐레이트 사이클라제 (sGC) 효소다. 이 효소는 일산화질소가 결합한 후 cGMP를 합성한다. 우리는 시분해 피코-나노초 흡광 분광법을 주된 측정 도구로 사용하여 일산화탄소와 두 활성제 (YC-1, Bay 41-2272) 가 이 효소와 결합할 경우 5배위 헴의 형성을 유도하여 일산화질소와 유사한 상승활성화를 보임을 밝혔다. 이 효소와 일산화질소의 상호작용의 모든 단계를 피코초에서 초단위까지의 동역학을 측정함으로써 알아냈다. 포유류 (소)에서 정제된 이 효소 전체의 동역학은 효소의 일부분 (1-190) 을 따로 떼어낸 헴 단백질과 몇몇 세균에서 만들어 낸 일산화질소 센서 단백질들과 비교되었다. 이 효소는 4배위나 5배위를 형성하는데 이를 연구하기 위한 한 모델로써 미오글로빈의 한 돌연변이 (H93C) 를 선택했다. 마지막으로 우리는 미오글로빈과 헤모글로빈의 한 흡광 영역 (band III) 을 측정함으로써 일산화질소의 결합 이후 헴의 철원자의 움직임을 연구했다. 또한 이 효소의 유력한 저해제와 내생적인 리간드를 찾기 위한 연구도 함께했다.

주제어: 신호전달, 수용성 구아닐레이트 사이클라제, 일산화질소, 순간흡수분광법, 알로스테릭 효과, 헴 단백질